High open-circuit voltage in heterojunction photovoltaics containing a printed colloidal quantum-dot photosensitive layer

by

Alexi Cosmos Arango

Submitted to the Department of Electrical Engineering and Computer Science
in partial fulfillment of the requirements for the degree of

Doctor of Philosophy

at the

MASSACHUSETTS INSTITUTE OF TECHNOLOGY

February 2010

Author . . . .
Department of Electrical Engineering and Computer Science
January 11, 2010

Certified by . . . .
Vladimir Bulović
Associate Professor of Electrical Engineering
Thesis Supervisor

Accepted by . . . .
Terry P. Orlando
Chairman, Department Committee on Graduate Students

High open-circuit voltage in heterojunction photovoltaics containing a printed colloidal quantum-dot photosensitive layer

by

Alexi Cosmos Arango

Submitted to the Department of Electrical Engineering and Computer Science
on January 11, 2010, in partial fulfillment of the
requirements for the degree of
Doctor of Philosophy

Abstract

Within four to seven years, electricity generated from solar cells will cost less than grid electricity, making it the cleanest, cheapest, and most abundant energy source on the planet. The rise of solar energy, however, could come to an untimely end if current solar cell technologies fail to meet the staggering manufacturing volumes needed to sustain current growth rates. Nanostructured donor/acceptor photovoltaics utilizing small molecule organics or conjugated polymers offer processing advantages that might enable high-throughput, large-area production. However, power conversion efficiencies of these structures have remained low, due in large part to low open-circuit voltages (V_{OC}). Using printing methods, we deposit a layer of colloidal cadmium selenide (CdSe) quantum dots (QDs) onto a wide band-gap organic hole-transporting thin film of N,N′-bis(3-methylphenyl)-N,N′-bis-(phenyl)-9,9-spiro-biuorene (spiro-TPD) in order to form a unique planar heterojunction photovoltaic device. This structure is found to produce much higher V_{OC} than previously predicted for donor/acceptor heterojunction photovoltaics. Absorption and charge generation occur primarily in the QD layer and indium tin oxide (ITO) provides the top contact, allowing for exceptional device stability and full transparency below the QD bandgap of 2.0 eV. Overall power conversion efficiencies remain low at 0.03% because only a small percentage of the incident light is absorbed (4% at the first QD excitonic peak of 2.1 eV) and fill factors are near 0.4, yet V_{OC} is 1.3V. The high V_{OC} is remarkable for an architecture with symmetric electrodes and exceeds the offset between the highest occupied molecular orbital (HOMO) of the acceptor (near 5.2 eV) and the lowest unoccupied molecular (LUMO) orbital of the QDs (near 4.6 eV). The internal quantum efficiency (IQE) exhibits a strong dependence on QD film thickness and reaches a maximum of 30% at a thickness of 3-4 monolayers, indicating that transport losses dominate photocurrent generation for QD thicknesses above 4-5 monolayers. From the bias-dependence of quantum efficiency, we identify an intensity-independent compensation voltage V_0 of 1.5 V that represents the maximum attainable V_{OC}. Investigation of the bias-dependence of the photocurrent decay transients identifies charge diffusion as the dominant mechanism responsible for photocurrent generation and reveals a vast discrepancy between the time constant associated with charge extraction (0.6 μs, measured at 0V) and that of recombination (0.4 ms, measured at 2 V). An alternative model for V_{OC} is presented that considers the dark current in forward bias as the critical mechanism determining V_{OC}. We conclude that suppression of recombination across the spiro-TPD heterojunction interface forces recombination to occur predominantly in the QD film. Electroluminescence from the QD layer confirms that hole injection from spiro-TPD into the QD layer and recombination in the QD layer is, in part, responsible for current flow in forward bias. Because the device architecture is straightforward and the fabrication techniques are simple, QD tandem cells are easily attained, furthering the prospect for high conversion efficiencies coupled with the potential for scaleable manufacturability.

Thesis Supervisor: Vladimir Bulović
Title: Associate Professor of Electrical Engineering

Acknowledgments

I am foremost indebted to my cheerful advisor, Vladimir Bulović, who is an extraordinarily supportive and thoughtful professor. Many of the concepts and topics in this thesis are much more well-developed than they would have been without his well-intentioned skepticism.

I would like to thank professor David Oertel, Scott Geyer and Moungi Bawendi, our collaborators who supplied the quantum dot material for this work. I especially thank Scott and David for their commitment, helpful discussions and skill in preparing quantum dot solutions.

I would also like to thank the dedicated graduate students and post-docs who spent years building and maintaining the lab, beginning of course with Conor Madigan, Seth Coe-Sullivan and Debbie Mascaro. In addition, John Ho, Matt Panzer, Tim Osedach, Ian Rousseau and Jill Rowehl were instrumental in helping to set up much of the lab equipment and making improvements that enabled the experimental work in this thesis. In particular, Conor, John, Tim and Jen Yu provided many years of companionship, support and stimulating discussions. Jill deserves special mention for proof-reading this thesis and for her remarkable ability to generate exactly one new question per day about photovoltaics. John Kymissis, Yaakov Tischler, Jen Yu, Scott Bradley, Polina Anikeeva, Vanessa Wood and Ivan Nausieda all added greatly to my experience in the Bulović lab and were a pleasure to work with. Help from summer students Youfeng Xu, Lauren Culver and Ian Rousseau was critical to many experiments. Discussions with all of the above people helped me understand and formulate many of the ideas in this thesis.

I am thankful to Marilyn Pierce, Monica Pegis and Angela Glass for providing indispensable support with many administrative hurdles.

I am particularly indebted to my friends and housemates Ingrid Werge, Bénédicte Mornet, Liza Marcato, P.J. Barry, Ryan Redmond, Brian Hone and Elizabeth, Holly, Violet and Milli Gates for sharing wonderful meals and companionship for so many years.

I'd like to thank my marvelous parents, Pat and Bob Arango, for their enduring support, encouragement and thoughtful advice over the years.

Finally, I'm indebted enormously to the single most influential person in my life, LeeAnn Kim, whose insights, humor, technical knowledge, amazing creativity and awesome hand-grown local produce have contributed in some way to every page of this thesis. I'd also like to thank LeeAnn's family, Eunjoo, Ducksoo, SueAnn and Andrew Kim for their support.

This research was generously supported in part by the Institute for Solder Nanotechnology (ISN) and the Martin Family Society of Fellows for Sustainability.

Contents

List of Figures

List of Tables

Chapter 1

Introduction

A viable way of generating electricity from sunlight – one that is low cost, highly efficient, scalable and reliable – could be an important foundation for the realization of a sustainable human society and the recovery of the world's ecosystems. This thesis falls short of delivering that goal, but does arrive at a number of important conclusions that, I hope, will play a major role in developing solar photovoltaics to the point where they become a significant source of electricity. My intention is that this work provides a clear and discerning guide to a host of critical issues facing the field of donor/acceptor photovoltaics, most importantly the origin of open-circuit voltage, the benefit of employing colloidal quantum-dot semiconductors and the merit of pursuing tandem photovoltaic structures.

In this chapter, we introduce the research field of donor/acceptor photovoltaics and provide a brief survey of device architectures and performance characteristics. We identify the low open-circuit voltage generated by these cells as a major cause of subpar efficiency. We briefly introduce colloidal quantum dots and organic semiconductors and present a new device design that, we believe, has the potential to meet the demanding efficiency requirements necessary for commercial viability.

1.1 Introduction to solar photovoltaics

Photovoltaic devices are one of the most widely used electronic devices of the digital age, constituting the critical component of imaging arrays in digital cameras, high-speed detectors in optical communications, sensors in a television's remote control and even the motion detection system in your optical mouse. With each application, the physical requirements differ, as do performance needs and economic considerations. This thesis addresses the extraordinarily difficult challenges posed by one as yet underdeveloped application - solar electricity generation.

A solar photovoltaic installation is comprised of many components, including solar panels (also called modules, pictured in Figure 1-1), electrical wiring, aluminum support structures (racking), junction boxes and an inverter. Here, we study the portion of a photovoltaic module that consists of a semiconductor device (also called a solar cell) responsible for the actual conversion of light energy into electricity. Typically, 20 to 100 photovoltaic cells are connected in series in order to form a module. The area of each individual cell determines the electrical current output of the module and the number of cells connected in series determines the voltage.

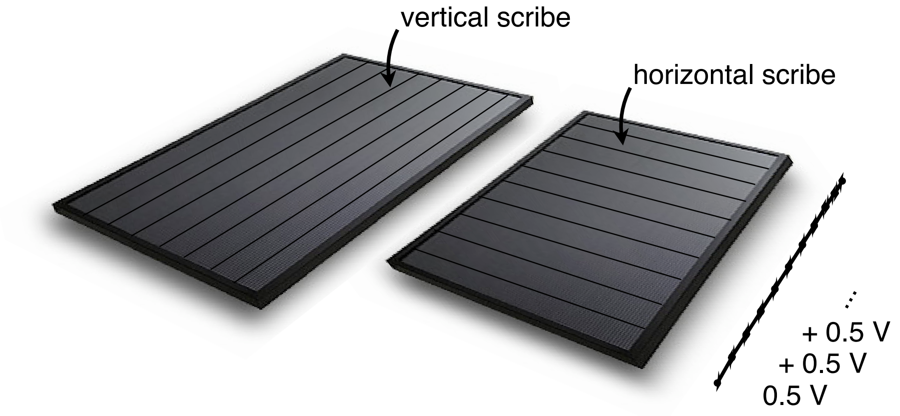

Figure 1-1: Images of vertically and horizontally scribed photovoltaic modules. Each photovoltaic cell, which usually generates ∼0.5 V, is connected in series in order to form a module with an output voltage of 30 V to 60 V.

1.1.1 Can we live off of solar energy?

We begin in Chapter 2 by asking a question that is seldom answered correctly:

> Could solar energy ever supply enough power to significantly impact energy production without destroying pre-existing open space or arable land?

From an analysis of the scale of energy demand in the US and the potential solar resource available from sunlight incident on land area that has already been converted for human use, the answer is a resounding "yes": more than double the amount of total energy used in the US in 2007 could be produced by solar photovoltaics. However, despite the large solar resource and wide-spread interest in solar energy conversion, solar photovoltaic installations currently generate only 1 GW_{peak} (in full sunlight) of the 5 TW_{peak} needed to offset all energy usage in the United States in 2007, or 0.02% of U.S. energy needs.[1] Unfavorable economic and political factors are certainly responsible for low market penetration in the US, yet difficulties in manufacturing scale-up are also at fault. An examination of photovoltaic technologies on the market today suggests that in the next 10-20 years, current solar technologies will struggle to provide modules at the rate needed to supply a significant fraction of the US energy from sunlight.

1.2 Emerging photovoltaic technologies

At least 20 new photovoltaic technologies have emerged that promise to solve the manufacturing bottleneck encountered by conventional photovoltaics. Nearly all employ new materials and some element of nanostructure, for example, a mesoscopic anode,[5] light trapping techniques,[6] a conjugated polymer/fullerene bulk heterojunction,[7] semiconducting organic small molecules[8] or quantum confined semiconductor nanocrystals.[9]

Unfortunately, the solar power conversion efficiency (η_P) of these devices is well below the threshold needed to make solar energy generation practical. Some nanostructured photovoltaics have matured to the point where η_P for laboratory-scale cells is as high as 5% (see Table 1.1) - sufficient for consumer electronics applications, but far from the minimum needed to enter the solar photovoltaic installations market. Even today, 8-10% is considered the lowest practical efficiency for photovoltaic modules[10] and, furthermore, large-scale manufacturing reduces the efficiency of modules by 45% compared to record laboratory-scale devices.[11] The target laboratory efficiency for emerging nanostructured solar cells is, therefore, a soaring 14.5%, much higher than the predicted maximum efficiency of 6% for small molecule cells[12] or 11% for conjugated polymer cells.[13]

1.2.1 Efficiency limitations in donor/acceptor heterojunction photovoltaics

In Chapter 3, we explore the essential background physics needed to understand some of the limitations to reaching higher efficiencies in nanostructured photovoltaics. For instance, the confined nature of the excited state (an exciton) prevents it from spontaneously separating into free charge, a prerequisite for photovoltaic action. Therefore, a heterojunction between two semiconductors with differing electron affinities (where one semiconductor readily donates an electron and the other readily accepts the electron) is often employed to facilitate charge separation. Another limitation is the relatively short distance an exciton can diffuse in order to reach the donor/acceptor heterojunction, compared to the characteristic length needed to absorb an appreciable amount of light.

There are three established ways to solve the problem of short exciton diffusion length relative to the absorption length:

Bulk heterojunction: The donor and acceptor materials can be mixed if they are solution processable [7, 20, 21, 22, 23, 25], co-evaporated if they sublime [29, 24, 30] or one material can be infiltrated into a porous network of the other [31, 32, 28] in order to form optically thick devices comprised of a bulk heterojunction with a high interfacial surface area.

Table 1.1: Survey of notable donor/acceptor photovoltaic devices and performance characteristics.

Device Structure[a]	**Year**	η_P [%]	EQE[b] [%]	FF	E_g[c] [eV]	V_{OC} [V]	$E_g - qV_{OC}$ [eV]	$\Delta_{homo-lumo}$ [eV]
Discrete Layers								
Al/Al2O3/Merocyanine/Ag	1978 [14]	0.7	35	0.25	2.00	1.20	0.80	
ITO/PEDOT:PSS/CuPc/C60/BCP/Al	2001 [15]	3.6	20	0.52	1.70	0.58	1.12	1.60
ITO/CuPc/SnPc/C60/BCP/Ag	2005 [16]	1.0	21	0.50	1.34	0.40	0.94	1.60
ITO/Al2O3/CdTe/CdSe/Ca/Al	2005 [17]	2.9	40	0.49	1.48	0.45	1.03	1.00
ITO/SubPc/C60/BCP/Ag	2006 [18]	2.1		0.57	1.89	0.97	0.92	2.00
ITO/PbSe/Ca/Al	2008 [19]	2.1	35	0.41	0.87	0.24	0.63	
Bulk Heterojunction								
ITO/PEDOT:PSS/APFO-3:CdSe/Al	2006 [20]	2.4	36	0.38	1.92	0.95	0.97	1.20
ITO/PEDOT:PSS/P3HT:PCBM/Ca/Al	2006 [21]	4.0	50	0.66	1.89	0.60	1.29	1.10
ITO/PEDOT:PSS/P3HT:PCBM/TiOx/Al	2006 [22]	5.0	75	0.66	1.93	0.61	1.32	1.10
ITO/PEDOT:PSS/F8TBT/P3HT/LiF/Al	2007 [23]	1.8	26	0.44	1.98	1.20	0.78	1.57
ITO/CuPc/CuPc:C60/C60/BCP/Ag	2007 [24]	4.4	55	0.56	1.57	0.46	1.11	1.60
ITO/PEDOT:PSS/P3HT:TiO2/TiO2/Al	2008 [25]	1.7		0.65	1.97	0.75	1.22	0.80
Mesoscopic Anode								
FTO/TiO2/Ru complex/(electrolyte)/Pt	1991 [5]	7.9	70	0.76	1.80	0.66	1.14	
FTO/TiO2/"black dye"/(electrolyte)/Pt	2006 [26]	11.1	70	0.72	1.44	0.74	0.70	
FTO/TiO2/K68/spiro-MeOTAD/Ag	2007 [27]	5.1	35	0.68	1.87	0.86	1.01	
FTO/TiO2/Z-907/P3HT/Ag	2008 [28]	0.61		0.55		0.65		

---

[a] Al_2O_3 = alumina; PEDOT:PSS = poly(3,4-ethylenedioxythiophene) poly(styrenesulfonate); CuPc = copper phthalocyanine; BCP = bathocuproine; SnPc = tin(II) phthalocyanine; CdTe = cadmium telluride; CdSe = cadmium selenide; SubPc = boron subphthalocyanine chloride; APFO-3 = poly(2,7-(9,9-dioctyl-fluorene)-alt-5,5-(4′,7′-di-2-thienyl-2′,1′,3′-benzothiadiazole)); P3HT = poly(3-hexylthiophene); PCBM = (6,6)-phenyl C61-butyric acid methyl ester; TiO_x = titanium oxide; F8TBT= poly((9,9-dioctyluorene)-2,7-diyl-alt-[4,7-bis(3-hexylthien-5-yl)-2,1,3-benzothiadiazole]-2′,2′′-diyl); TiO_2 = titanium dioxide; ruthenium dye = $RuL_2(\mu\text{-}(CN)Ru(CN)L'_2)_2$,1, where L is 2,2′bipyridine-4,4′-dicarboxylic acid and L′ is 2,2′-bipyridine; K68 = NaRu(4-carboxylic acid-4′-carboxylate)(4,4′-bis[(triethyleneglycolmethylether) heptylether]-2,2′-bipyridine)(NCS)2; spiro-MeOTAD = 2,2′,7,7′-tetrakis(N,N-di-p-methoxypheny-amine)-9,9′-spirobifluorene; Z-907 = RuLL′(NCS)2 where L is 2,2′bipyridyl-4,4′-dicarboxylic acid and L′ is 4,4′-dinonyl-2,2′bipyridine

[b] EQE is a rough estimate of the average EQE over the absorption region of the device

[c] E_g refers to the onset energy of charge generation, determined for all devices by taking the energy corresponding to 20% of device peak EQE

Light-trapping: Employ geometrical or optical light-trapping techniques in order to boost the absorption of otherwise optically thin devices [33, 34, 35, 6, 36, 37]

Tandem cells: Stack multiple optically thin devices on top of one another, connected in series using a transparent intermediate recombination layer [38, 39, 40]

The first solution, the bulk heterojunction, is the most common and the most successful, so far [22]. The second solution, light trapping, generally does not produce enough absorption enhancement alone [37] (see Section 3.2.4) and therefore has been employed in conjunction with bulk heterojunctions and/or tandem cells [22, 41]. Recently, the third solution, tandem cells, has become increasingly common as a way of increasing the efficiency of bulk heterojunction cells [42, 43].

Despite successful implementations of the above techniques, efficiencies remain low. A survey of performance metrics of various nanostructured photovoltaics (Table 1.1 and Table 1.2) reveals that the origin of low efficiency rests predominantly with inadequate open-circuit voltages (V_{OC}, defined in Section 3.5). Some of the most efficient cells have succeeded at maximizing external quantum efficiencies (EQE, defined as the number of electrons generated per incident photon). For example, Kim et al.[22] has achieved an average of 75% EQE over the absorption region of the device. To a lesser extent, fill factors (FF, defined in Section 3.6) have been maximized at 0.56-0.66, but nearly all V_{OC} remain low - in general only 0.6 V for a typical optical bandgap (E_g) of 1.9 eV. This represents a 32% efficiency of converting photon energy into voltage, considerably lower than the detailed-balance limit of approximately 1.5 V for $E_g = 1.9$ eV or 79% (see Section 3.5 for a discussion of detailed balance).[44, 45] Figure 1-2 plots V_{OC} versus E_g for cells listed in Table 1.1. Overcoming low V_{OC} could result in a substantial increase in the conversion efficiency (by as much as a factor of 2.5 for some nanostructured photovoltaics), enough to begin approaching commercial viability.

Tandem donor/acceptor cells exhibit slightly improved power efficiencies (η_P) versus single cells, as shown in Table 1.2 and Figure 1-2, but currently fall short of the major gains in efficiency that are expected theoretically. Two types of tandem cells

Table 1.2: Survey of notable tandem donor/acceptor photovoltaic devices and performance characteristics.

Junction 1	E_g^{1g} [eV]	**Junction 2**	E_g^{2g} [eV]	**Year**	η_P %	EQE^h %	FF	$E_g^1 + E_g^{2g}$ [eV]	V_{OC} [V]	$E_g - qV_{OC}$ [eV]
CuPc/PTCBI[a]	1.57	CuPc/PTCBI	1.57	2002 [39]	2.60		0.43	3.14	0.78	2.36
CuPc:C60[b]	1.57	CuPc:C60	1.57	2004 [46]	5.70	30	0.59	3.14	1.03	2.11
ZnPc:C60[c]	1.55	ZnPc:C60	1.55	2005 [47]	3.80		0.47	3.10	0.99	2.11
MDMO-PPV:PCBM[d]	2.16	MDMO-PPV:PCBM	2.16	2006 [48]	3.10		0.56	4.32	1.34	2.98
P3HT:PCBM[e]	1.90	ZnPc/ZnPc:C60	1.55	2006 [49]	2.30		0.46	3.45	1.02	2.43
PCPCTBT:PCBM[f]	1.38	P3HT:PC70BM	1.90	2007 [41]	6.50	30	0.67	3.28	1.24	2.04

---

[a] ITO/CuPc/PTCBI/Ag/CuPc/PTCBI/Ag

[b] ITO/CuPc/CuPc:C60/C60/PTCBI/Ag/m-MTDATA/CuPc/CuPc:C60/C60/BCP/Ag

[c] ITO/MeO-TPD/ZnPc:C60/C60/Au/MeO-TPD/ZnPc:C60/C60/Al

[d] ITO/PEDOT:PSS/MDMO-PPV:PCBM/ITO/PEDOT:PSS/MDMO-PPV:PCBM/Al

[e] ITO/PEDOT:PSS/P3HT:PCBM/C60/Au/ZnPc/ZnPc:C60/C60/Al

[f] ITO/PEDOT:PSS/PCPCTBT:PCBM/TiOx/PEDOT/P3HT:PC70BM/TiOx/Al

[g] E_g refers to the onset energy of charge generation, determined for all devices by taking the energy corresponding to 20% of device peak EQE

[h] EQE is a rough estimate of the average EQE over the absorption region of the device

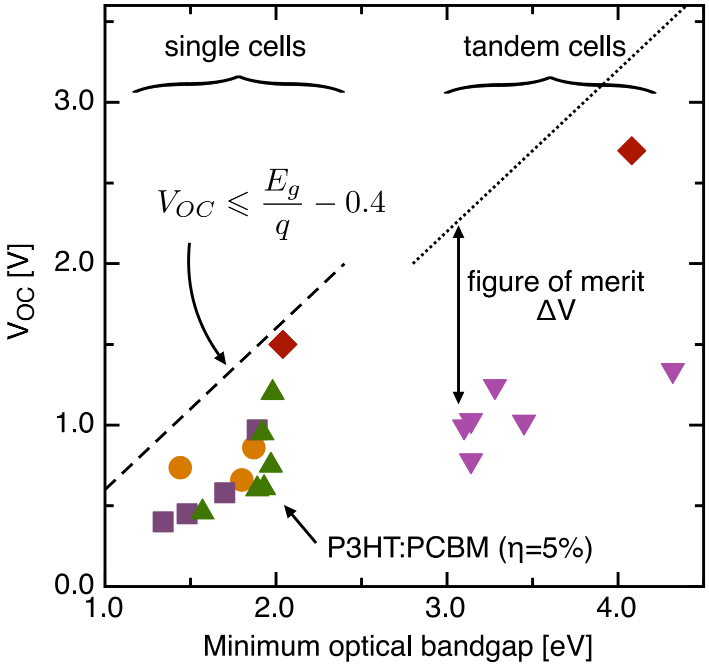

Figure 1-2: Open-circuit voltage V_{OC} versus the minimum optical bandgap for devices listed in Tables 1-2 and 1.2. Also plotted is the theoretical limit, which is the bandgap subtracted by 0.4 eV for single cells or 0.8 eV for tandem double cells. Shown are devices with a mesoscopic anode (●), discrete layers (■), bulk heterojunction (▲), tandem cells (▼) and this work (♦).

have been employed, consisting of either multiple stacked cells of the same bandgap (where the thickness of each cell must be chosen such that the same number of photons are absorbed in each cell) or of different bandgaps (where the bandgaps must chosen such that each individual bandgap absorbs the same number of photons). Both types have been implemented, though with moderate success. Few reports give EQEs, but those that do indicate low EQEs around 30%. FFs are respectable, often above 0.5, but again V_{OC} is at ∼38% of the total bandgap.

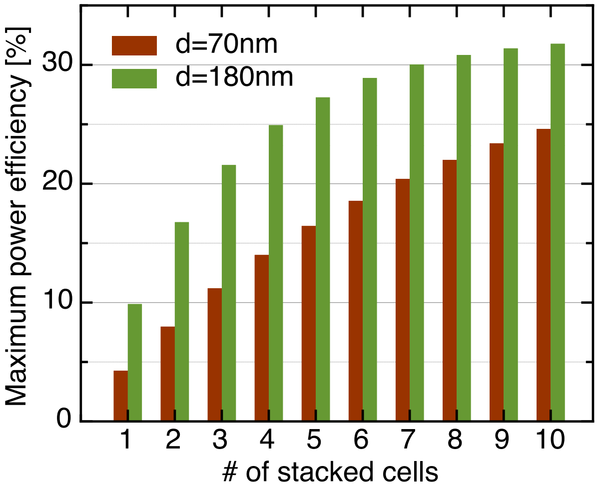

Figure 1-3: Theoretical maximum power efficiency of stacked cells with ideal electrical characteristics, individual cell thicknesses of 70 nm or 180 nm, $E_g = 1.4$ eV and $\alpha = 10^4$ cm^{-1}.

For tandem cells consisting of multiple stacked cells of the same bandgap, the theoretical efficiency of an optically thick tandem cell should be much higher than that of an optically thin single cell. For example, Figure 1-3 shows the expected efficiency for two ideal devices (limited only by absorption ($\alpha = 10^4$ cm^{-1})) with $E_g = 1.4$ eV and an initial single cell thickness of either $d = 70$ nm or $d = 180$ nm. For the 70 nm device, the theoretical efficiency increases from 3.8% for a single cell to 7.6% for two stacked cells and up to 11% for three stacks. For the 180 nm thick device, the theoretical efficiency saturates near 31% after 10 stacks, which is just under the theoretical efficiency of an ideal device with no absorption losses. With greater absorption per cell, the number of cells needed to achieve a given efficiency is reduced. However, the ultimate efficiency is the same, provided that enough cells can be stacked together.

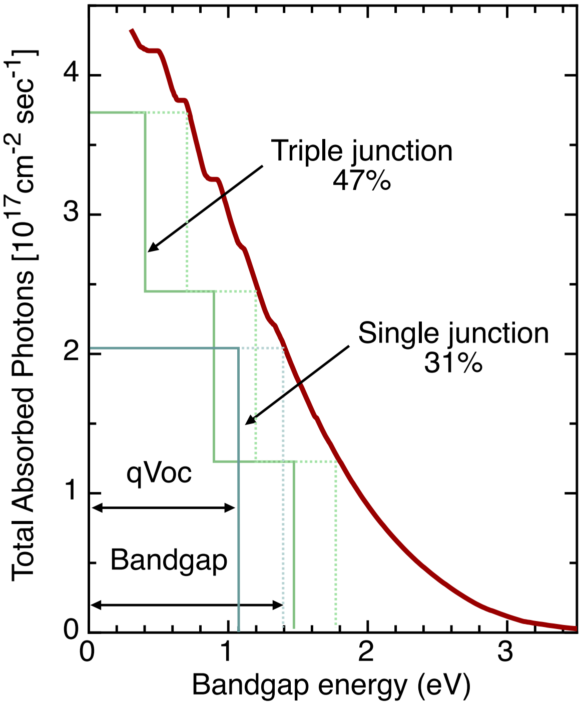

Figure 1-4: The graphical method for the calculation of the power efficiency of a solar cell involves multiplying the total number of absorbed photons with the solar cell's bandgap, less 0.4 eV.

For tandem cells consisting of cells with different bandgaps, a simple graphical analysis shows that the theoretical efficiency of tandem cell should be much greater than cells with a single bandgap [45]. In Figure 1-4, we plot the total number of photons in the solar spectrum that will be absorbed by a solar cell with a given bandgap. For an ideal solar cell with complete absorption and no loss mechanisms, the power produced is the number of photons multiplied by qV_{OC}, which is often 0.4 eV less than the bandgap. For triple cell tandem structures, the optimal bandgaps are approximately 0.7 eV, 1.2 eV and 1.8 eV, which corresponds to a theoretical power efficiency of 47%, much higher than the theoretical power efficiency of 31% for a single bandgap cell with an optimum bandgap of 1.4 eV (a 50% improvement).

Three problems appear to limit increased efficiency in donor/acceptor tandem cells:

- The mechanical instability and rough morphology of multiple spin coated or evaporated layers inhibits stacking of more than two cells
- The bandgap of organic semiconductors is larger than optimal, limiting absorption in the infrared part of the solar spectrum
- The transparent interstitial layer used to make contact between the top and bottom cell often results in reduced EQE, V_{OC} and/or FF

Therefore, achieving high efficiency in tandem structures requires fabrication techniques that are compatible with stacking multiple cells an one another, semiconductors with bandgaps in the range of 0.7 eV to 1.8 eV and transparent conductive interstitial layers that do not sacrifice device performance.

1.3 Our device concept

This thesis investigates a unique photovoltaic device architecture that attempts to satisfy the above requirements in order to achieve efficient tandem photovoltaics. The device employs a pristine layer of colloidally synthesized cadmium selenide (CdSe) quantum dots (QDs) as the principle photo-active species. An organic hole-transporting film, N,N′-bis(3-methylphenyl)-N,N′-bis-(phenyl)-9,9-spiro-bifluorene (spiro-TPD) is used to form the donor/acceptor heterojunction. Below, we briefly introduce quantum dot semiconductors and organic small molecules and explain the potential benefits of our non-traditional device design.

1.3.1 Quantum dots

A semiconducting structure that limits the motion of charge carriers to two, one or zero dimensions is often referred to as a low-dimensional semiconductor. For example, an ultra-thin film allows charge to propagate in the x and y directions, but not in the z direction, resulting in what's called a two-dimensional semiconductor. A zero-dimensional semiconductor constrains an electron in all three dimensions and is often called a quantum dot [50].

Since the early 1980's, low-dimensional semiconductors have appeared in optoelectronic devices such as photodetectors [51], lasers [52] and optical modulators. Their unique optical and electronic properties stem from the physical phenomenon called quantum confinement, which occurs when a semiconductor's dimensions approach the de Broglie wavelength of an electron:

$$\lambda = \frac{h}{p}$$

where h is Planck's constant and p is the electron momentum. With decreasing thickness, the semiconductor's broad energy level bands collapse into discrete energy levels E_n that can be approximated by assuming an infinite square potential well, as in the textbook one dimensional quantum mechanics problem. The energy levels are given by

$$E_n = \frac{\hbar^2}{2m^*}(\frac{n\pi}{L_z})^2$$

where $\hbar = h/2\pi$, m^* is the electron effective mass, L_z is the size of the quantum well and n is an integer. These discrete energy levels can be tuned by changing the width of the well without changing the materials themselves (Figure 1-5).

Modification of the electronic state density and narrow emission from transitions between discrete states have enabled quantum well laser diodes [52]. Quantum wells also exhibit special electronic properties like enhanced electron impact ionization, as seen in low-noise avalanche photodetectors [53]. An important consequence of confinement for photovoltaics is the increase in the absorption coefficient. One way to understand this increase is to consider that the same material volume, unconfined, will experience a similar number of absorption events as the confined volume. The unconfined volume will absorb across a broad range of wavelengths and the confined volume will absorb only at discrete wavelengths, but with greater probability.

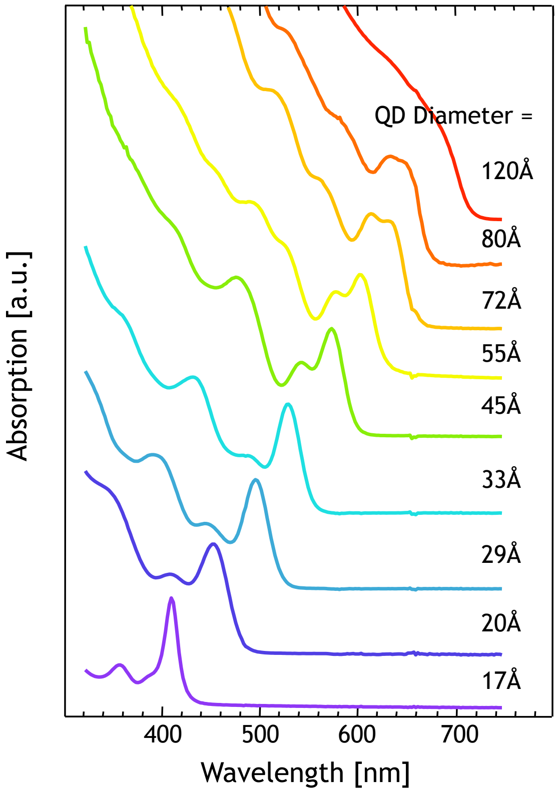

Figure 1-5: Absorption spectra of CdSe nanocrystals. From Chris Murray.

1.3.2 Colloidal quantum dot technology

Colloidal quantum dot technology arose in the early 1980's when scientists at both Bell Labs and in the former Soviet Union noticed that solutions of semiconductor nanoparticles were colored differently although the semiconductor material was the same [54]. Since then, high purity semiconductor nanocrystals have been grown synthetically and processed with organic capping groups so that they can be dispersed in organic solvents and deposited in solution [55].

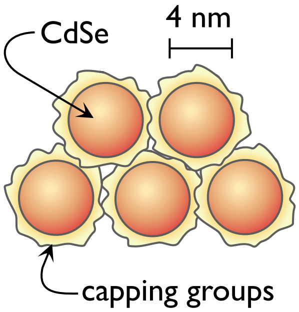

Figure 1-6: Diagram of CdSe QDs with organic ligand capping groups. Typical QD size is ~4 nm with ~1 nm spacing between QDs.

Solution processable colloidal quantum dot systems display many of the special optical and electronic properties associated with epitaxially grown quantum confined systems [56]. Their tunable band gap and their higher absorption relative to the bulk make quantum dots particularly attractive as photogeneration materials. At the same time, colloidal quantum dots offer much greater material system flexibility than epitaxial quantum dots because deposition on any substrate is possible [57]. This flexibility is central to our work because it allows us to independently choose a substrate and a top contact layer that are optically transparent and electrically compatible.

1.3.3 Colloidal quantum-dot photovoltaics

A photovoltaic effect in quantum dot/conjugated polymer blends was first observed by Greenham, et al. [9]. In these devices, CdSe quantum dots are used as both an absorber and electron acceptor. The efficiency was found to be limited in part by poor transport through the network of quantum dots [58]. Larger efficiencies have been reported using CdSe nanorods, in which transport is improved along the extent of the rods [59] [60]. However, resistive losses remain an issue because the nanorods tend to lay flat, perpendicular to the direction of current flow [61]. Sun, et al. [62] have achieved an external quantum efficiency of 15% at the quantum dot absorption edge using branched CdSe tetrapods comprised of four limbs connected at a central core. Their device structure consists of a CdSe tetrapod/conjugated polymer composite film (86% CdSe by weight) spun onto a PEDOT film and covered with aluminum as the top electrode, as shown in Figure 1-7. Recently, Johnston et al. [63] demonstrated a QD only device consisting of lead sulfide (PbS) nanocrystals sandwiched between ITO and aluminum. Efficiencies for these structures have reached 2.1% [19].

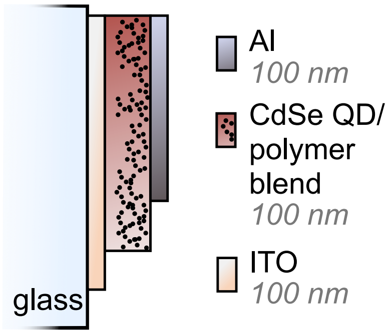

Figure 1-7: Depiction of typical device structure used for CdSe/conjugated polymer blend photovoltaics.

1.3.4 The CdSe quantum dot film

Cadmium selenide (CdSe) forms an ionically bonded semiconducting crystal with a direct band gap of 1.7 eV and an electron mobility of 800 cm^2/Vs. CdSe crystals with perfect stoichiometry and crystal structure are insulating with low intrinsic carrier concentrations. In this work, CdSe nanocrystals are grown synthetically in solution to a diameter of 4 nm. At this size, quantum confinement increases the band gap to 2.2 eV. During synthesis, the surface of the quantum dot is functionalized with the organic molecule trioctylphosphine oxide (TOPO). TOPO capping groups are transparent, insulating and extend about 1-2 nm beyond the nanocrystal surface (Figure 1-6). The resulting large interparticle spacing prohibits interparticle sharing of electron states and hence the mobility is reduced significantly. Ginger, et al. [64] have obtained low mobilites of 10^{-4} to 10^{-6} $\mathrm{cm}^2/\mathrm{Vs}$ from current-voltage characteristics fitted with a trap limited space charge conduction model, but mobility has not yet been measured directly. Annealing CdSe nanocrystal films reduces the interparticle spacing, which in turn increases the mobility [65]. Ridley, et al. [66] found relatively high field-effect electron mobilities of around 1 $\mathrm{cm}^2/\mathrm{Vs}$ in a transistor geometry where the CdSe film was synthesized without organic capping groups and sintered at 350°C.

Jarosz, et al. [67] found that a butylamine treatment of CdSe quantum dot films resulted in enhanced photocurrent. It was shown that interparticle spacing decreases in treated samples. Also, butylamine is thought to passivate recombination centers at the quantum dot surface. In these experiments, Jarosz observed that the photocurrent reached saturation at 60 V applied across a 1 micron channel length (corresponding to an electric field of 6 x 10^5 V/cm) and speculated that all photogenerated charge was being collected in the saturation limit. Electric fields of this magnitude are too high to achieve in a solar cell at low bias. Instead, a heterojunction interface is required to help generate charge, which we will discuss in further detail in Chapter 3.

1.3.5 Organic semiconductors

An organic solid is a molecular material that contains carbon. Research into solid state organic semiconductors appears to have begun around 1906 when Pochettino discovered photoconductivity in solid anthracene [68]. In the past twenty years, the field of organic semiconductors has expanded rapidly, driven largely by the prospect of new materials for light emission, light harvesting, lasing, superconductivity and molecular transistors. Organic molecular solids consist of molecules that are weakly bound to each other by van der Waals forces. They are characterized by low melting points, low conductivity, high absorption and soft structural properties. Organic molecules exhibiting semiconducting behavior are a special class of hydrocarbon molecules that

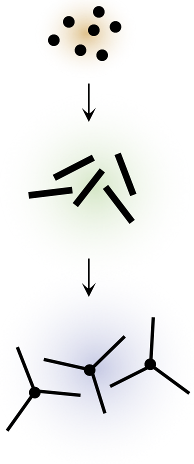

Figure 1-8: Succession of increasingly more sophisticated nanocrystal morphologies, from one-dimensional spheres, to two-dimensional rods and finally branched tetrapods.

contain conjugated bonds. Conjugation refers to the the alternating sequence of single and double bonds, displayed for example by benzene (Figure 1-9), a ring of six hydrogen and six carbon atoms arranged in a hexagon. Such conjugation along chains of atoms often leads to the ability to conduct charge due to the resonant sharing of electrons across atoms along the conjugated chain.

When a carbon atom is brought close to another carbon or hydrogen atom, the electron wavefunctions change their spatial configuration to accommodate the new potential energy situation. In the case of benzene, three electrons of the six total electrons on a carbon atom distribute themselves at roughly 120° increments in the plane of the molecule. These electrons form covalent bonds with other carbon or hydrogen atoms, called σ bonds. A fourth electron remains distributed in the z direction, above and below the plane of the molecule, and loosely binds to other z-distributed electrons from neighboring carbon atoms. These bonds are called π bonds and the resulting π electron system is delocalized over the entire benzene molecule.

Between molecules, van der Waals forces resulting from induced dipole-dipole interactions are responsible for intermolecular attraction. Electron delocalization is

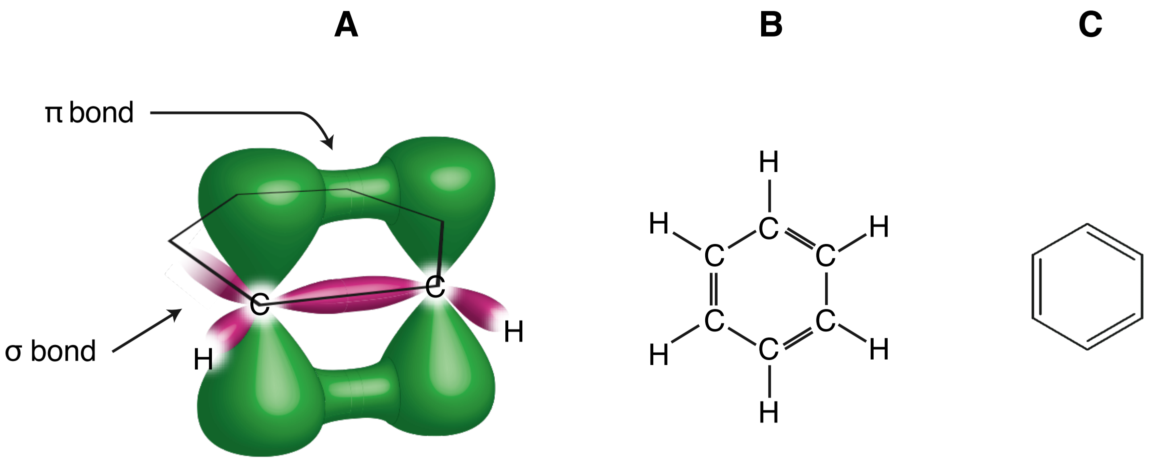

Figure 1-9: Illustration of molecular orbitals in benzene (a) and chemical structure in explicit form (b) and condensed form (c).

not present over intermolecular length scales, but some electron wavefunction overlap leads to the possibility of tunneling between molecules and ultimately charge conduction. Optical absorption occurs when the π electron - which is in the highest occupied molecular orbital (HOMO) - is excited to the next available unfilled state - the lowest unoccupied molecular orbital (LUMO). This excited electron state is called the π^* orbital. For each molecule, π-π^* transitions occur at a well-defined energy level. But over the whole molecular solid, π-π^* transition energies vary broadly because of molecular deformations and local electric field variations due to intermolecular dipole interactions.

1.3.6 The organic hole transport molecule spiro-TPD

For the hole acceptor and hole transporting contact to the CdSe film, we use the organic small molecule spiro-TPD, a spiro-linked variant of TPD, a common organic semiconductor used in electrophotography and organic LEDs. The spiro-TPD film is deposited by thermal evaporation. The molecular structure of spiro-TPD is shown in Figure 1-10. Transport takes place via hopping of holes among spiro-TPD molecules, which occurs relatively efficiently, as reflected in it's mobility of $\sim 10^{-4}\text{cm}^2/\text{Vs}$ [2]

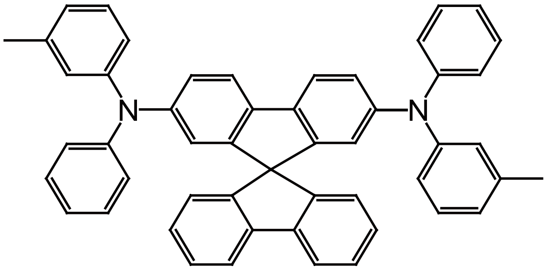

Figure 1-10: Molecular structure of spiro-TPD.

1.3.7 Device fabrication

The prevailing deposition method for colloidal QD systems is spin casting [69], which introduces limitations such as solvent incompatibility with underlying films and the inability to pattern side-by-side pixels for multispectral photodetector arrays. The alternative deposition method of drop casting is applicable to the fabrication of lateral QD devices (such as photoconductors [67] and transistors [70]), but resulting films are generally of non-uniform thickness and unsuitable for vertical heterojunction structures.

In Chapter 4, we describe the two innovative fabrication methods that are critical to our device growth process. First, a thin QD film (∼20 nm) is deposited onto an organic hole transport layer using a non-destructive microcontact printing method [71]. With the non-destructive QD printing process, a distinct planar heterojunction is formed between the neat QD film and the underlying spiro-TPD. Second, a thin film of indium-tin-oxide (ITO) is non-destructively sputter-deposited onto the QD layer as a transparent top electrode. The transparency in the visible part of the spectrum of the ITO ensures that the optical field intensity near the top electrode interface – where the QDs are located – is not suppressed. The thickness of the QD film is kept as thin as possible in order to limit losses associated with exciton diffusion or carrier transport across the QD's insulating capping groups.

Tandem structures (described in Chapter 7) are obtained by simply repeating the device growth process of the single cell. The only difference being that the interme-

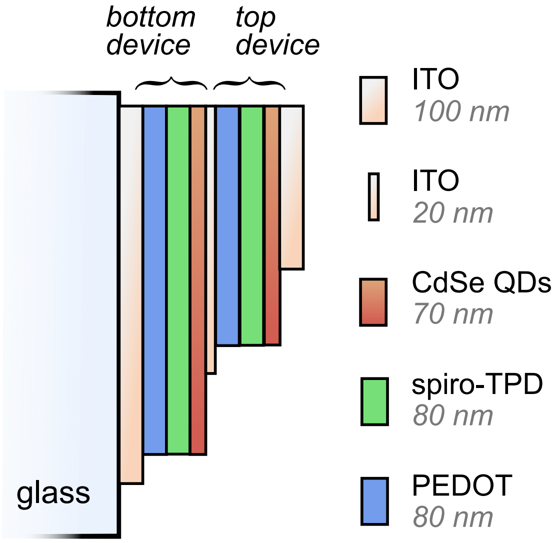

Figure 1-11: Schematic of tandem QD device structure.

diate ITO electrode is kept at 20 nm because thicker ITO films are only necessary for external electrode contacts, which require greater lateral conductivity. The use of the conductive polymer poly(3,4-ethylenedioxythiophene)poly(styrenesulfonate) (PEDOT:PSS) as a planarization layer ensures that the morphology of the top device is the same as the bottom device.

1.3.8 Benefits of a QD planar heterojunction structure

Compared to the more popular bulk heterojunction geometry, we propose that a number of advantages exist for multiple stacks of planar heterojunction cells:

- The planar morphology simplifies charge extraction because carriers do not have to follow a circuitous pathway to the electrodes, potentially encountering dead ends along the way. Improved charge extraction should lead to improved FF.
- Higher V_{OC} and improved FFs should be expected for a bi-layer geometry due to the absence of shunting paths between the anode and cathode.
- In a bi-layer geometry, carriers are driven away from the interface by diffusion,

whereas in a bulk-heterojunction, a built-in electric field is required to drive photocurrent. Alleviating the need for a built-in field allows for the use of a stable and transparent ITO for both anode and cathode.

- Device fabrication is simplified by removing the need for annealing steps often required to control the blend morphology.
- Analysis of device performance and physics of charge generation is simplified without complications from an interpenetrating morphology

The use of quantum dots as the sole absorbing species is advantageous for the following reasons:

- The absorption onset of the device can be changed by simply changing the size of the QDs or the QD material itself
- Characterization and modeling is simplified by not having two materials with overlapping spectra
- Infrared absorption is possible when using smaller bandgap QD materials

With the planar heterojunction tandem device design in Figure 1-11, we have satisfied the three requirements for an effective tandem structure:

- The PEDOT:PSS layer provides the mechanical stability and smooth morphology needed to stack multiple device easily
- The bandgap of the QD layer could, in principle, be chosen to obtain infrared absorption by using a QD material with a smaller bandgap
- The transparent interstitial electrode is compatible with both the top and bottom cell, thus maintaining the optimal performance of the individual cells in the entire tandem structure

Certainly, we acknowledge that stacking more than ten cells could be difficult practically, yet the cost of producing a thin film solar module is dominated by the glass substrate and encapsulant [72]. Additional deposition steps, as long as they are not time consuming, should not affect production costs. In summary, our proposed QD device structure addresses many of the limitations to high efficiency in donor/acceptor photovoltaics by enabling the use of infrared-absorbing semiconductors and tandem devices structures.

1.4 Summary of important results presented in this thesis

In Chapter 5, we present the observation that photocurrent originates from absorption in the QD film. We confirm that the same device structure can accommodate different size QDs by observing a shift in the spectral response of devices with different size QDs. Surprisingly, physical voids in the QD film are pervasive, but do not appear to interrupt the generation of photocurrent or photovoltage. In addition, a large $V_{OC} = 0.8$ V is achieved, which is uncommonly high for a device with symmetric electrodes.

In Chapter 6, we demonstrate an even greater V_{OC} of 1.3 V when the QD film is smooth and complete, accomplished by coating the PDMS stamp with a lower surface energy polymer, parylene-C. The absence of voids in the QD film is found to reduce the current in dark, which is shown to account for the increase in V_{OC}. The magnitude of V_{OC} is exceptionally high, near the detailed-balance limit and much greater than the HOMO/LUMO offset at the spiro-TPD/QD heterojunction, previously believed to be the upper limit to V_{OC} in donor/acceptor heterojunction photovoltaics. An alternative model for V_{OC} is presented that considers the dark current in forward bias as the critical mechanism determining V_{OC}. The origin of low dark current in these structures is believed to result from suppressed recombination at the spiro-TPD/QD heterojunction, observed from photocurrent transient measurements to have a long time constant of at least 0.4 ms. Electroluminescence from the QD layer confirms that hole injection from spiro-TPD into the QD layer and recombination in the QD layer is responsible for current flow in forward bias. Measurement of the voltage dependence of the transient photocurrent decay identifies charge diffusion as the dominant mechanism responsible for photocurrent generation.

In Chapter 7, we describe the first ever successful implementation of a tandem QD structure, using identical bandgap QDs for each cell. The efficiency is double that of the single cell, as expected, and the V_{OC} of 2.67 V is the highest to date for a donor/acceptor solar cell. Finally, we outline the many opportunities and pathways available for improved efficiencies in donor/acceptor photovoltaics.

Chapter 2

Photovoltaic module requirements for widespread adoption

Even though sunlight is the single largest and most readily available energy resource on earth, it nevertheless suffers from two unfortunate drawbacks: relatively low power densities and intermittency. These drawbacks limit its appeal as an energy source and make capturing solar energy on a large scale a difficult problem. In this chapter, we attempt to quantify both the sheer scale of energy demand in the US and the potential for solar energy to become a viable alternative to fossil fuel consumption. We will also discuss why solar cell conversion efficiency requirements are so formidable, why cost considerations are so stringent and why high-throughput manufacturing processes are essential.

2.1 Can we live off of renewables?

Before we begin our discussion of photovoltaics, we should consider the real world impact that photovoltaics might have on society and the natural world. Often one assumes that a new technology will automatically yield fantastic improvements for everyone, but in some cases (especially with purported "green" technologies) the impact can be either insignificant or in fact damaging. For instance, if using photovoltaics for energy generation means converting a large fraction of open space or arable land to solar farms, then we might be better off searching for other renewable sources of energy. Also, if only a small amount of photovoltaics could be produced because of practical manufacturing or material limitations, then the impact would be insignificant and therefore not worth the effort.

With this in mind, we set off to answer the broad question of whether it is *theoretically* possible for the US to displace all of its fossil fuel consumption with solar energy that is generated from land that has already been converted for human use. Although other renewable technologies are certain to play a role in the nation's energy mix in the future and no real storage technology is presently available to handle such a large amount of solar energy generation, the point is to understand the fundamental limits to solar energy deployment.

2.1.1 US energy consumption

We begin by examining the amount of energy consumed in the US. Vast amounts of data on this subject are available at the website for the Energy Information Association (EIA) [1], from which we obtained both the amount of energy consumed by fuel source and by sector.

Our first complication is that each fuel source is measured in a different energy unit. Following the convention set by Professor David J.C. MacKay in his book *Sustainable Energy – without the hot air* [73] – from which we've based much of the methodology for our calculations in this chapter - we will convert each material-specific measurement unit into kilowatt hours per day per person [kWh/day/person]. This unit is the best compromise between the myriad of energy units because it allows for a direct comparison between countries with different population sizes, averages out daily fluctuations in output and can be more easily conceptualized as 1 kWh/day/person being equivalent to one 100W lightbulb turned on for 10 hours a day per person. All the relevant conversion factors are given in Table 2.1.

A second complication lies in how the EIA classifies energy consumption for each sector. The broad categories are given as (a) transportation, (b) industrial, (c) residential and (d) commercial. It's pretty clear how energy is used in transportation,

Table 2.1: Conversion factors for major energy units.

Fuel source	**Name of unit**	**Unit**		**Conversion factor**
Petroleum	million barrels per day	Mbl/day	=	5.66 kWh/day/person
Natural gas	trillion cubic feet per year	Gft^3/yr	=	2.75 kWh/day/person
Coal	million short tons per year	Msh tn/yr	=	5.55 kWh/day/person
Nuclear/ renewables	quadrillion British thermal units per year	PBtu/yr	=	2.67 kWh/day/person
Solar panels	gigawatt peak	GW peak	=	1/60 kWh/day/person

but what's happening to energy going into industrial, residential and commercial sectors? Fortunately, the EIA also provides extremely detailed dissections of fuel usage by application that contain useful specifics like how much petroleum is used for the fabrication of plastics and how much natural gas is directed toward home heating, for example. It turns out that most fuel consumed by the industrial sector is either physically transformed into goods, materials, substances or used as heat energy (not electricity) for the same purpose, while most of the fuel consumed by the residential and commercial sector is for either electriciy or space heating. Therefore, we find it more instructive to use "heating" and "electricity" as sector categories, yet will retain the "industrial" moniker for lack of a better term.

Figure 2-1 displays our estimates, distilled from information provided by the EIA, of the breakdown of energy consumption by fuel and by sector in the US. Out of a total of 281 kWh/day/person, 241 kWh/day/person (or 86%) is consumed in the form of fossil fuels, with petroleum responsible for the largest share and coal and natural gas with roughly equal shares. However, 24% of petroleum is not burnt as fuel, but instead used as raw material for the manufacture of goods and chemicals. Also note that the majority of coal is used to generate electricity. Natural gas consumption is split nearly equally between industrial applications, heating and electricity generation. Almost no petroleum is used to generate electricity. The overwhelming majority of

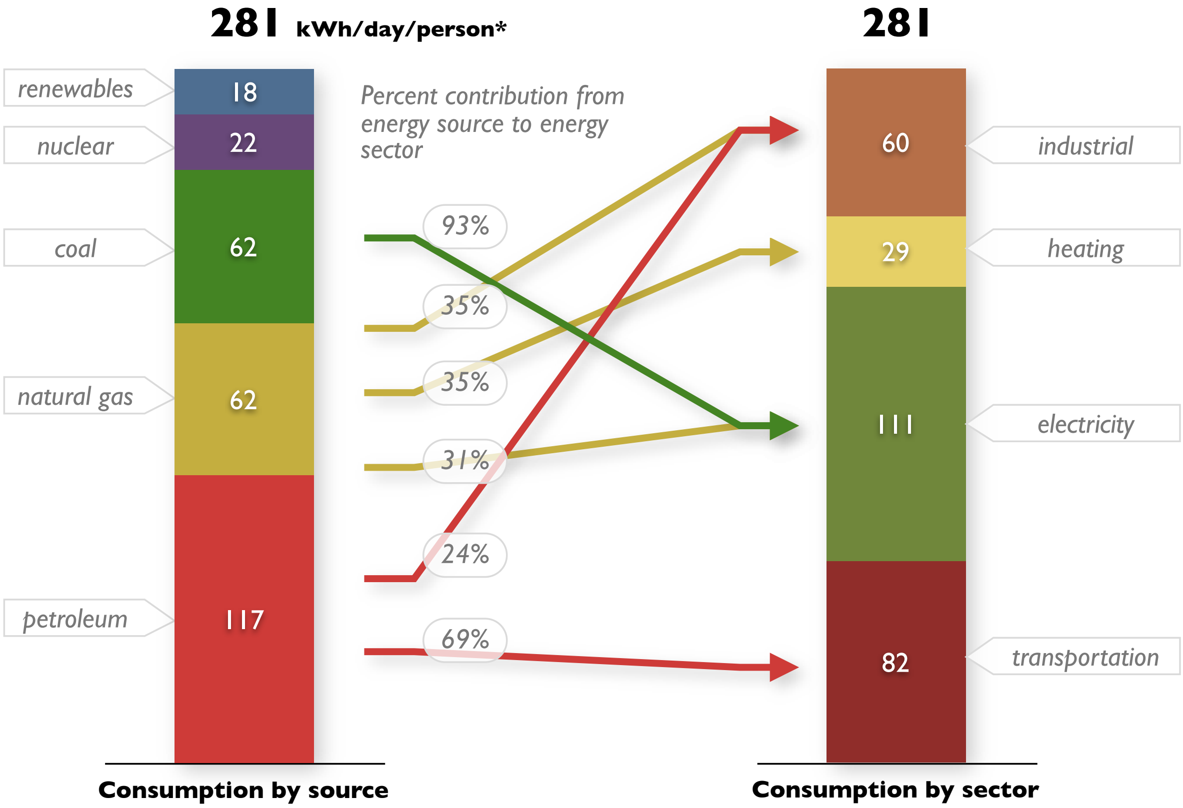

Figure 2-1: Consumption of energy in the US by fuel source and by sector, and percent contribution from fuel source to energy sector.

renewable energy and nuclear power goes toward electricity generation.

2.1.2 How much is useful energy?

Now that we know the staggering magnitude of energy consumed by the average US citizen, we can start to understand whether enough solar energy is available to someday replace all fossil fuel combustion. One common assumption often made in these calculations is that new solar energy installations would have to displace all of the energy presently extracted from fossil fuels. But if we think about how energy would actually be generated and used in a solar economy, many of the inefficiencies of a fossil fuel economy end up going away. Take, for example, the case of electricity generation and distribution. Most electricity is generated by burning coal or natural gas to produce steam that drives a turbine. The process is only 40% efficient in principle, but the EIA data suggests the efficiency is typically 30%. Transmission losses account for another 17% reduction, bringing the the overall efficiency of electricity generation and distribution down to approximately 21%. Another example of energy waste in the fossil fuel economy is the case of internal combustion automobiles, which have an energy efficiency of only about 20%.

In a solar-based economy (where we assume to have some sort of viable energy storage technology), efficiency losses due to combustion do not exist. Electricity is generated close to where it used so transmission losses are near zero. Likewise, automobiles powered by an electric engine and battery have a grid-to-motor efficiency of nearly 90%. Heating buildings and homes is possible with solar water heating and/or electric-powered geothermal heat pumps, which operate by circulating a high heat capacity fluid down into the earth and back up into a home or building, in the process transferring three times as much heat from the earth as used to power the pump. We will (somewhat arbitrarily) assume that a reasonable energy budget for heating is 45% of what is presently used, which can be obtained with a combination of better thermal insulation and a 50% usage rate of geothermal heat pumps (not all locations are suitable for heat pumps). Therefore, the relevant amount of energy to be generated by solar energy is close to the actual amount of useful energy *delivered*

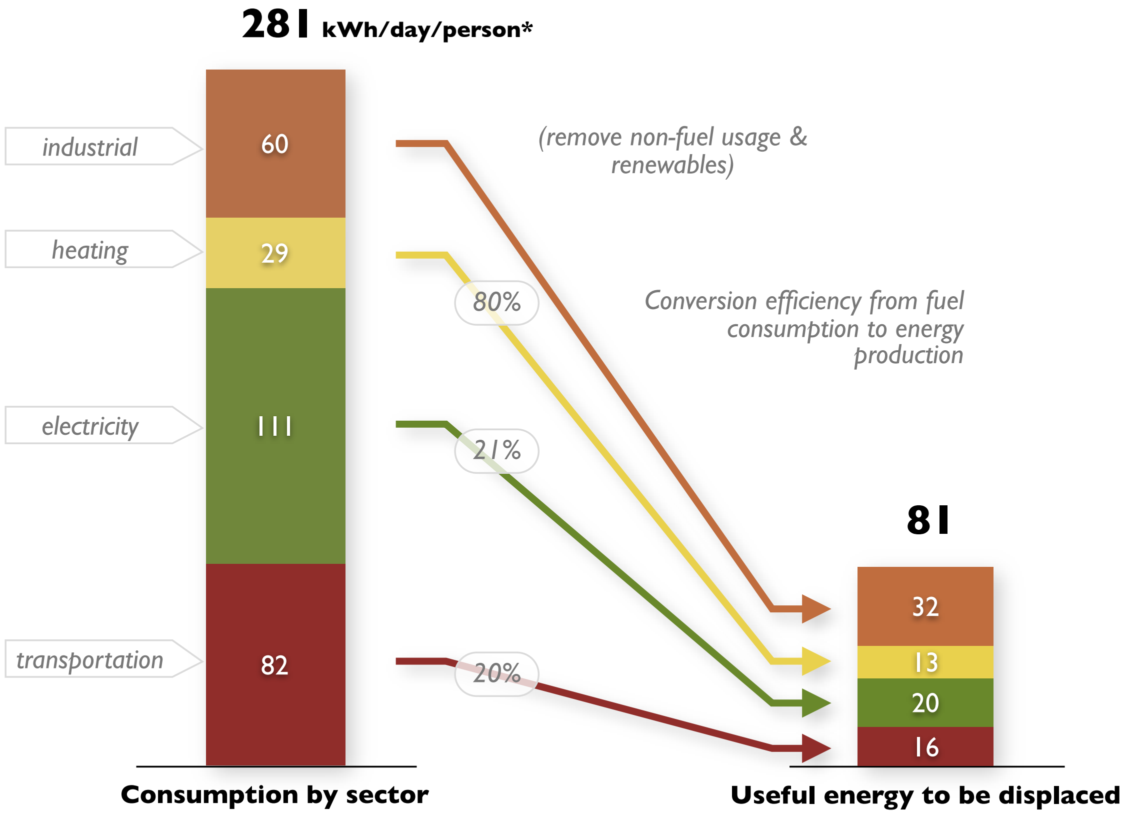

Figure 2-2: The amount of energy consumed in the US by sector and the amount of useful energy that results after efficiency losses, non-fuel usage and renewables are removed.

by fossil fuels, not the energy *contained* in the fossil fuels. In Figure 2-2, we diagram our estimates for the average conversion efficiency loss in each energy sector. Non-fuel usage is also removed. We arrive at an estimated value of 81 kWh/day/person for the amount of fossil-fuel-deliverd useful energy that could in principle be displaced by solar energy. Note that industrial processes become the largest consumer of useful energy, twice as large as transportation. For a detailed table of assumptions used to obtain these numbers, see Appendix A.

2.1.3 Solar potential

The amount of fossil fuel energy to be displaced, though less than 30% of the total energy consumed, is still a massive quantity and, if produced from solar energy, would require covering a broad expanse of the US. Two factors conspire to make solar energy a large-area prospect. First, the average solar insolation (defined as the incident solar energy per day per area) in the US is only 5 kWh/day/m^2. Second, the average efficiency of solar panels is only 15%, resulting in a delivered energy density of 0.75 kWh/day/m^2. Therefore, in order to supply 81 kWh/day/person, we would need 108 m^2/person, which is about the area taken up by six or seven car spaces in a parking lot. Since the total land area of the US is 9,158,960 km^2, which supports a population of 301,139,947 at an average land area per capita of 30,414 m^2/person, then the required coverage area is 32,407 km^2 or 0.35%, which is just bigger than the total area of Massachusetts and Rhode Island, together. Table 2.2 summarizes the above coverage requirements facts.

Our next step is to understand where to put 32,407 km^2 of solar panels. Contrary to some public reports, rooftop space alone is not sufficient, as shown in Table 2.3. Here, we have roughly estimated the available area from land that has already been developed for human use. We assume that solar panels can only be installed on 25% of residential rooftops (many of which are pitched away from the sun) and 60% for flat surfaces (to account for areas that do not have full sunlight)[74]. Other readily available surfaces, like parking and unused land adjacent to highways, dominate the available area in the US – perhaps a commentary on the wastefulness of

Table 2.2: Summary of useful statistics regarding coverage area requirements for solar energy production in the US.

Land area	9,158,960 km^2
Population	301,139,947
Per capita land area	30,414 m^2/person
Fossil fuel energy consumed	281.43 kWh/day/person
Fossil fuel energy delivered	80.71 kWh/day/person
Average solar insolation	5 kWh/day/m^2
Solar panel efficiency	15%
Delivered energy density	0.75 kWh/day/m^2
Required coverage area	32,407 km^2
Per capita required coverage area	107.62 m^2/person
Percent required coverage area	0.35%

our transportation system. Note that the majority of the surfaces in Table 2.3 are located nearby major population centers where the bulk of energy is used. A total of 81,000 km^2 of existing developed land area can be used for energy generation from sunlight, 2.5 times the necessary area to displace 100% of the useful energy produced by combusting fossil fuels.

Converting the available land area to energy, assuming an average insolation of 5 kWh/day/m^2, gives the amount of energy that can be generated by solar photovoltaics, referred to as the solar potential. In Figure 2-3, we plot the solar potential, alongside both the amount of energy consumed in the US and the amount of solar energy production needed to displace all fossil fuel combustion. The main conclusion is that a creative use of space is necessary in order to generate a sufficient amount of energy to power the entire US from sunlight without compromising critical open space or arable land.

2.2 Solar photovoltaic technologies

Having determined how much energy is needed to displace fossil fuels and how much sunlit space is needed to supply that energy, we can now address the question of what type of photovoltaic technology is capable of providing the vast amount photovoltaic

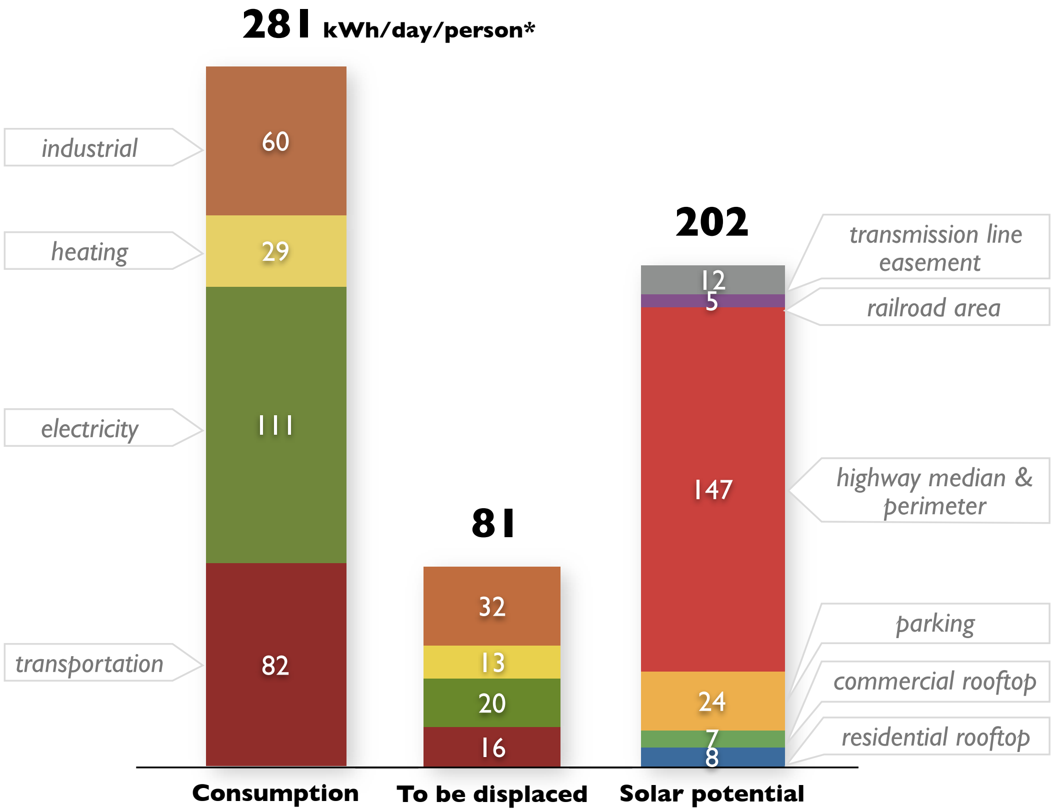

Figure 2-3: Comparison of total energy consumed in the US with the amount of energy that can be provided from solar photovoltaics without including open space or arable land.

Table 2.3: Amount of useable area provided by common built-up surfaces in the US.

Surface	**Area [km^2]**	**Utilization factor**[a]	**Useable area [km^2]**
Residential rooftop	12,821[b]	25%	3,205
Commercial rooftop	4,438[b]	60%	2,663
Parking	15,886[c]	60%	9,532
Highway median & perimeter	98,043[d]	60%	58,826
Railroad area	3,446[e]	60%	2,067
Transmission line easement	7,848[f]	60%	4,709
Total			81,002

---

[a] The percent of surface that can be covered with solar panels, from Navigant consulting [74]

[b] Energy Information Association (EIA)

[c] 250 cars, assuming 4 parking spaces per car and 16 m^2 parking spaces

[d] 3,997,461 highway miles (American Association of State Highway and Transportation Officials), assuming a 50 ft median and embankment width

[e] 140,490 railroad miles (Association of American Roailroads), assuming 50 ft width

[f] 160,000 transmission line miles (Edison Electric Institute), 100 ft width

modules needed to cover 32,407 km^2 of sunlit area. There are two main issues to consider: the cost competitiveness of the solar photovoltaic installation and the ability of the photovoltaic cells to be manufactured easily and rapidly at the scales required for widespread deployment.

2.2.1 Solar photovoltaic installations

First, let's consider the cost breakdown of the entire apparatus associated with a solar photovoltaic installation, diagramed in Figure 2-4. The solar panel or module - an assembly of fifty to a hundred solar photovoltaic cells connected in series and packaged with a protective piece of glass and encapsulation materials - is the main component of the system. These modules are connected in series or parallel with other modules to generate enough electricity to meet the preset system specifications. Typically, modules are responsible for around 43% of the cost of the system. Before the system gets built, an expert must assess the illumination conditions (avoiding shady parts) of the location and design a racking system to hold the modules facing south, at the correct angle in order to maximize energy output. These design costs, together with financing, often equal approximately 25% of the cost of the system. An inverter, which converts the DC output of the modules into grid-compatible AC current, will cost around 4% of the system. Other components like copper wiring, conduit, junction boxes and aluminum racking account for 13% of the system cost. Finally, labor costs for placing the panels and routing the electrical connections will run 15% of the system cost. The above estimates were adapted from estimates provided in discussions with Chet Farris, CEO of Stion Corporation.

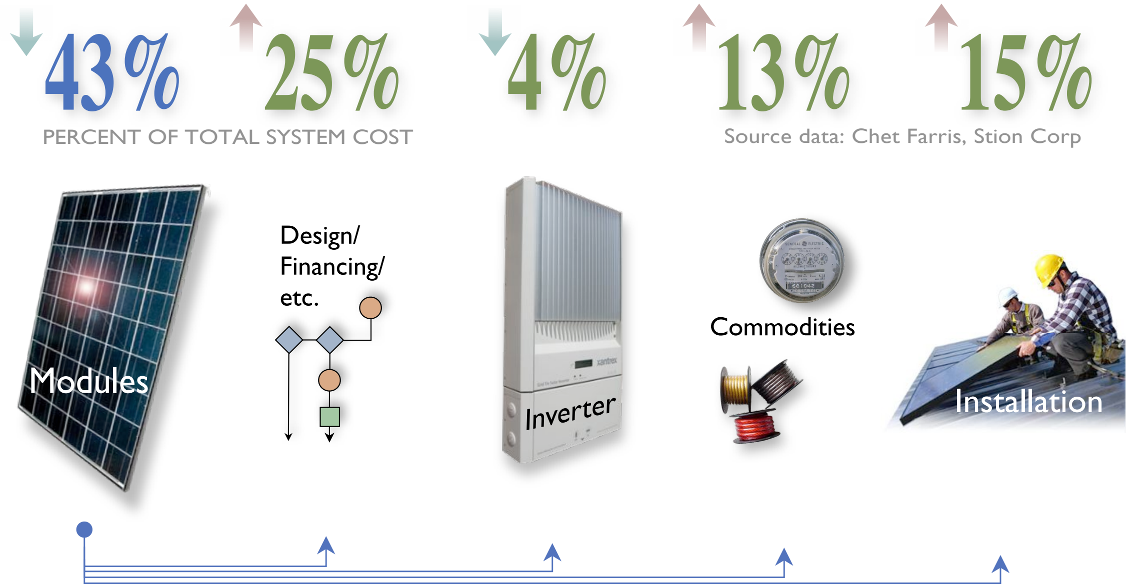

Source data: Chet Farris, Stion Corp

Figure 2-4: Cost breakdown of the major components of a solar photovoltaic installation. Up and down arrows indicated the cost trends with time.

For a discussion of what happens to the cost of a solar installation if some parameter – cost, efficiency, voltage, weight or size – changes, and a breakdown of the ideal module characteristics, see Appendix A.

2.2.2 The cost/efficiency tradeoff

Of all the module specifications discussed in Appendix A, module efficiency has the greatest impact on the cost of a solar installation because it determines the required install area. Design, financing and inverter costs do not change, but commodity and labor costs are heavily dependent on the square footage to be installed. As the installed area increases, more cabling, racking and module connections are required. Because module efficiency and the installed area are inversely proportional, there is a minimum efficiency below which installation costs become prohibitively expensive.

The relationship between the efficiency of the modules and the required install area is

$$\eta_{POWER} = \frac{P_{PEAK}}{Area \times 1000\ \mathrm{W/m^2}} \tag{2.1}$$

where η_{POWER} is the module efficiency, P_{PEAK} is the peak power output specified for the solar installation, $Area$ is the required area and 100 $\mathrm{mW/cm^2}$ is the intensity standard at which P_{PEAK} is determined. The installation cost is comprised of fixed costs and area-dependent costs:

$$Installation\ Cost = Fixed\ Cost + (Area\ Dependent\ Cost) \times Area \tag{2.2}$$

Solving for $Area$ gives

$$Installation\ Cost = Fixed\ Cost + \frac{(Area\ Dependent\ Cost) \times P_{PEAK}}{\eta_{POWER} \times 1000\ \mathrm{W/m^2}}, \tag{2.3}$$

but it's more useful to consider the cost per peak power generated, typically called the cost per Watt

$$\frac{Installation\ Cost}{P_{PEAK}} = \frac{Fixed\ Cost}{P_{PEAK}} + \frac{Area\ Dependent\ Cost}{\eta_{POWER} \times 1000\ \mathrm{W/m^2}} \tag{2.4}$$

which is plotted in Figure 2-5 using a fixed cost of \$0.74/W and an area-dependent cost of \$160/$\mathrm{m^2}$.

Figure 2-5 demonstrates that cost savings begin to diminish above efficiencies of 18%, yet modules below an efficiency of 10% suffer from a large installation cost penalty and below 8% installation costs become prohibitively expensive. This contradicts a frequently espoused motivation for nanostructured photovoltaics - that ease of processing of printable materials will lead to lower cost solar cells and hence lower

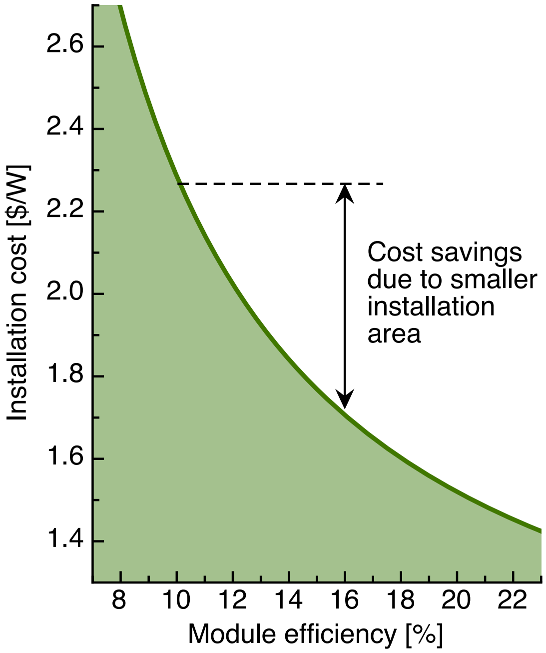

Figure 2-5: Estimated installation cost verses module efficiency.

system costs, even if efficiencies are low. As we can see in Figure 2-6, a plot of the estimated total system cost for the five major solar photovoltaic technologies (nanoscale materials, amorphous silicon (a-Si), cadmium telluride (CdTe), copper indium gallium diselenide (CIGS) and crystalline silicon (c-Si)), nanoscale photovoltaics actually come out to be more expensive overall than c-Si, even though the modules cost half as much.

On the other hand, the data in Figure 2-6 illustrates that simply increasing module efficiency won't necessarily lower overall system costs. This is because of a fundamental tradeoff between cost and efficiency for photovoltaic modules: higher efficiencies often require higher quality materials and more advanced light-trapping techniques that can significantly increase costs. Modules made from a-Si are a notable counter example, with a lower module efficiency yet higher cost. However, a sweet spot emerges for those technologies (CdTe and CIGS) that manage to have low manufacture costs while maintaining adequate efficiencies (12-13%). In these cases, the installation cost penalty for lower efficiency is more than offset by lower module costs. Not surpris-

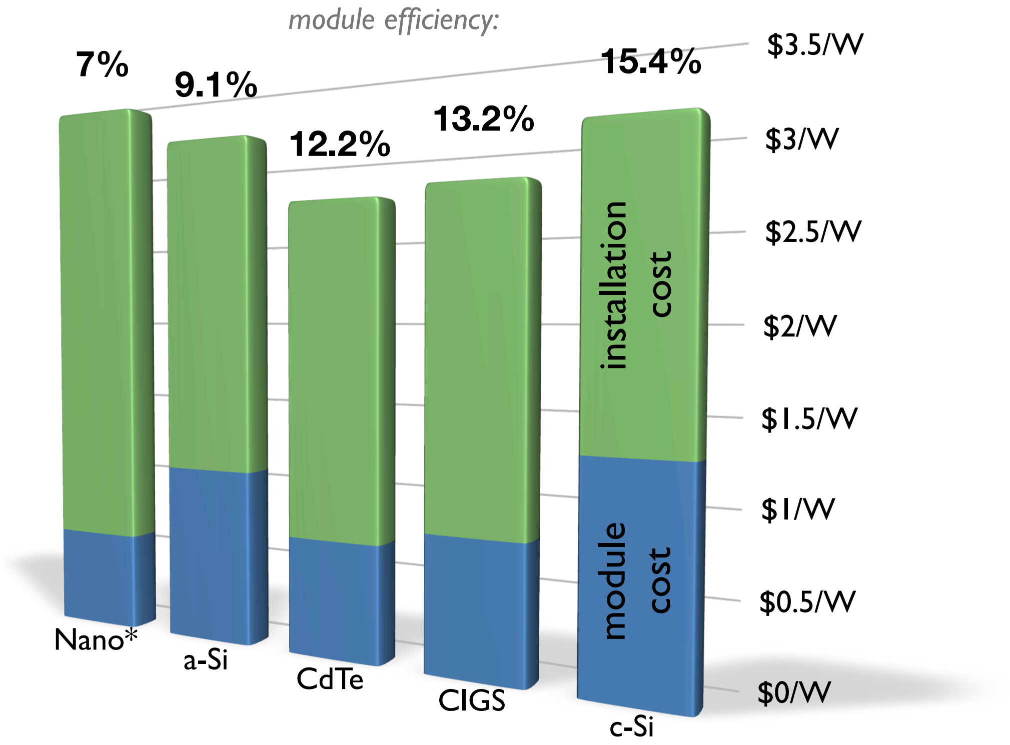

Figure 2-6: Predictions for module efficiency, module cost and installation cost for five major solar photovoltaic technologies in 2015. Adapted from *Solar Photovoltaics*, Deutsche Bank [10]. *Numbers for nanoscale photovoltaics are estimated by us.

ingly, these technologies are growing more rapidly than c-Si and are therefore forecast by some to eventually dominate the solar photovoltaics market.

2.2.3 Module manufacturing throughput

One issue remains in assessing the ability of a solar technology to supply 81 kWh/day/person of energy: can the modules be manufactured and deployed quickly enough to make an impact on energy production within a reasonable time frame? To address this question, we will look at the historical rate of production of modules manufactured in the US, plotted in Figure 2-7.

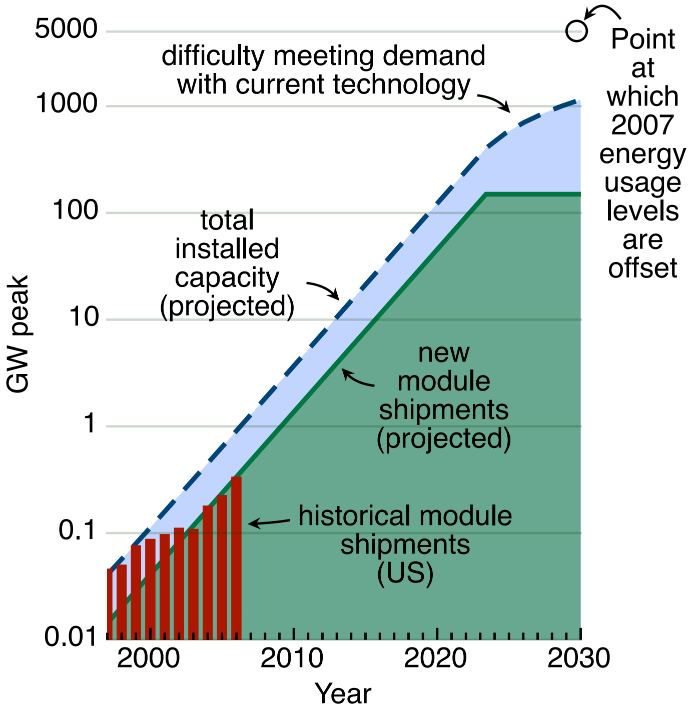

Figure 2-7: Log-linear plot of historical module shipments in the US, with projected shipments in the future and projected total installed capacity. Module shipment data from Ref. [1].

Before examining Figure 2-7, it is worth taking a moment to clarify how we have converted from kWh/day/person to gigawatts GW peak, the customary unit for the power capacity of solar panels. GW peak refers to the power output by a solar panel under illumination from the standard AM1.5G spectrum at an intensity of 1 kW/m^2. It is equivalent to the maximum power obtained at full sun brightness. However, we want to know the average power a solar panel will generate over the course of a day so that we can properly compare it with the average power used per day. We take the value for average solar insolation in the US (5 kWh/day/m^2) and convert to average power (5/24 kW/m^2), which can be directly compared to peak power (1 kW/m^2). Therefore, a solar power plant rated at 1 GW peak will have an average power production of 5/24 GW. If the 1 GW peak power was distributed to each person in the US, a population of 3×10^8 people, everyone would get

$$1 \text{ GW peak} \rightarrow 1/60 \text{ kWh/day/person} = 17\text{Wh/day/person} \tag{2.5}$$

as given in Table 2.1.

From Figure 2-7, the electricity generating capacity from photovoltaic modules in 2007 was 1 GW peak (17 Wh/day/person), roughly a factor of 5000 smaller than (or 0.02% of) the generating capacity needed to supply all of US energy needs. If we take the historical module shipments over the last four years, which have been experiencing an astonishing growth rate of nearly 40%, and extrapolate out into the future, we find that in principle we could supply enough modules to satisfy the nation's energy needs by 2030. This may or not may not be sufficient time to avoid irreversible damage from fossil fuel pollution, depending on the climate expert. However, a number of factors, including changing economic conditions, erratic government subsidy programs and limitations in module manufacturing can conspire to reduce module production below these extrapolations. The EIA, for instance, projects only 5 GW peak by 2030 of electricity generation from solar energy (which we hope is a gross underestimate).

From discussions with manufacturers of c-Si and a-Si modules, we believe that significant manufacturing bottlenecks exist for each major photovoltaic technology, potentially extending the time frame for full deployment considerably beyond 2030. Our rough estimate is that current manufacturing methods cannot sustain more than 100-200 GW peak of module production per year in the US. This best case scenario

Table 2.4: Manufacturing bottlenecks for major photovoltaic technologies.

Technology	**Bottleneck**
nano	low efficiency
a-Si	slow, batch to batch Si deposition
CdTe	tellurium availability
CIGS	indium availability
c-Si	energy intensity & module assembly

would limit energy production from solar photovoltaics to a maximum of only 1 TW peak of 5 TW peak needed by 2030, unless current manufacturing methods could be improved. Note that we've drawn a sharp upper limit to module production, but in reality production would likely approach this value more gradually and therefore further reduce capacity.

Table 2.4 summarizes some of the manufacturing bottlenecks associated with each of the five major photovoltaic technologies. As discussed above, nanoscale photovoltaics suffer from power conversion efficiencies that are patently too low for solar applications. Efficiencies of a-Si photovoltaics are likewise at the low end (around 8-9%), yet the manufacturing outlook is the brightest among existing photovoltaic technologies. Still, costs are high (see Figure 2-6) due to the batch to batch vacuum process used to deposit the a-Si layer. The ultimate production bottleneck however could be the availability of aluminum, out of which the enormous 2 x 4 x 4 m^3 plasma-enhanced chemical vapor deposition chambers are fabricated. The case of CdTe, presently the fastest growing and most cost competitive technology, is constrained by limited resources of tellurium [75]. Potentially upwards of 5-10 GW peak of modules could be produced, but as supply dwindles, the cost of tellurium will begin to infringe on module costs and thus limit production. Similarly, production of CIGS modules could be constrained below the 20 GW peak range by limited resources of indium [75]. Finally, c-Si, the market leader, is the most expensive and least scalable of all the technologies. The energy payback time for c-Si modules is 2 years as opposed to 6 months for thin film [72]. In addition, c-Si modules must be assembled from individual cells, a time-intensive process that can take a full day to complete, even with automated assembly lines.

In summary, while current photovoltaic technologies are far from being constrained by fundamental manufacturing or material supply limitations, in the next 10-15 years, the most promising and cost effective technologies, CdTe and CIGS, will reach their maximum production levels, having supplied less than 30 GW peak of the 5000 GW peak needed to offset all fossil fuel combustion. a-Si and c-Si will similarly reach maximum production levels (although probably in the 100 GW peak range) and cost considerations will leave these technologies vulnerable to other forms of energy generation. Taken as whole, our estimates of module production capabilities lead to the conclusion that no single photovoltaic technology is likely to supply enough capacity within a 20 year timeframe to offset a significant portion of fossil fuel consumption in the US.

2.3 Conclusion

This chapter has attempted to develop four key points regarding market needs among the energy sector for solar photovoltaics:

- Ample space is available from existing developed land areas to supply all of the US with energy produced from sunlight
- In the next decade, current solar technologies will struggle to provide modules at the scale needed to provide all of this energy
- Adequate efficiency (12-14%) is essential in order to keep installation costs under control
- Low module costs must be combined with the use of abundant materials and high-throughput, non energy-intensive manufacturing processes

Our finding that 0.35% of US land area is required to generate 100% of the energy used in 2007 in the US is higher than similar calculation by some promoters of solar energy [74], yet lower than more critical studies [73]. Our second point is rarely discussed since current solar panel production volumes are still scaling rapidly. However, module supply will become an important issue toward the end of this decade. Accomplishing the last two points could have a major impact on how energy is generated in the US in the future.

Chapter 3

Fundamentals of operation and design of donor/acceptor photovoltaics

In the previous chapter, we analyzed energy demand in the US and argued that improvements in manufacturability are needed in order to generate energy on the scale necessary for widespread adoption of solar photovoltaics. In this chapter, we will cover some of the basic opto-electronic properties of a new class of photovoltaics, donor/acceptor photovoltaics, which have been proposed as an easily manufacturable alternative to conventional solar cells. Donor/acceptor photovoltaics employ semiconductors with localized states, often in the form of solution processable conjugated polymers, organic small molecules and/or colloidal quantum dots. We will briefly review the five key attributes that determine a solar cell's efficiency and attempt to develop the basic physics underlying current and voltage generation in donor/acceptor heterojunctions. While there are many interpretations of how these cells operate, we will mostly avoid discussing the myriad of competing theories and instead focus on a simplified example consisting of purely diffusion-driven photocurrent.

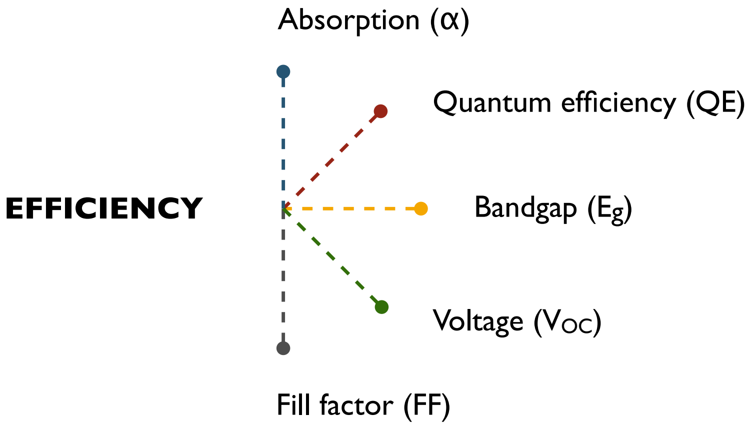

Figure 3-1: The conversion efficiency depends on the both material properties and physical operation of the device.

3.1 Solar conversion efficiency

The efficiency at which a solar cell converts light into electrical energy depends on five key attributes of both the device material properties and physics of operation: the absorption coefficient α of the active absorbing material(s), the efficiency of photon to electron conversion (quantum efficiency QE), the bandgap E_g of the active absorbing material(s), the maximum voltage generated by the device (open-circuit voltage V_{OC}) and the internal resistive properties of the device, obtained by measuring the fill factor FF (Figure 3-1).

Together, these five attributes determine the power conversion efficiency η_P, given by

$$\eta_P = \frac{J_{SC}\, V_{OC}\, FF}{Power\ in} \tag{3.1}$$

where J_{SC} is the current produced under short circuit conditions, which is in turn determined by the absorption, the quantum efficiency and the bandgap. As we will see below, the V_{OC} is also a function of the bandgap.

Unlike traditional inorganic solar cells, the photovoltaic effect in donor/acceptor photovoltaics does not result from the formation of a p-n junction. Instead, photogenerated electrons and holes are produced on opposite sides of the donor/acceptor interface, leading to carrier concentration gradients that help drive photogenerated carriers toward the electrodes. In order to gain an intuitive sense for how this process works, we will arrive at simple estimates of the exciton concentration profile, carrier concentration profile and internal electric field for a simple planar donor/acceptor heterojunction device with typical material properties. These calculations are based on the approximation that pure diffusion is the driving force for photovoltaic action, although drift currents are certain to play a role, but not a dominant one. Finally, we will describe our understanding of how V_{OC} is produced by a donor/acceptor heterojunction based device.

3.2 Absorption of light

We begin with the most fundamental physical process involved in the conversion of light to electricity: the interaction between light and matter. We cover a few important points regarding the nature of the solar spectrum and how light in absorbed in a photovoltaic device.

3.2.1 Black-body radiation

The first key to understanding how to generate power from sunlight is to understand the nature of light itself. Just over a century ago, light was considered to be a propagating electromagnetic field whose properties were governed by Maxwell's equations. The wave theory of light was successful at explaining diffraction and interference, but did not correctly predict the spectral dependence of light emitted from a glowing hot body, termed a black body (because no light is assumed to be reflected or transmitted). Under classical theory, the intensity of emitted light was thought to increase at higher frequencies, in contradiction to experimental observations. In 1901, Max Planck successfully modeled the black body emission spectrum by considering (incorrectly) the walls of the black body to be oscillating in quantized packets of energy.

Planck's law of black-body radiation is

$$E(\nu, T)d\nu = \frac{2h\nu^3}{c^2}\frac{1}{e^{\frac{h\nu}{kT}} - 1}d\nu \tag{3.2}$$

where $E(\nu, T)d\nu$ is the energy per time per area emitted in the frequency range between ν and $\nu + d\nu$, h is Planck's constant, c is the speed of light, k is Boltzmann's constant and T is the temperature of the black body. Later in 1905, Einstein interpreted Planck's model as indicating that light itself was quantized, with the energy of a photon related to the wavelength or frequency of the light wave according to

$$E[\text{eV}] = h\nu = \frac{hc}{\lambda} = \frac{1240}{\lambda[\text{nm}]} \tag{3.3}$$

where $E[\text{eV}]$ is the photon energy in units of electron Volts, λ is the wavelength of light and $\lambda[\text{nm}]$ is the wavelength of light in units of nanometers.

3.2.2 Solar spectrum

The sun is the most famous black-body radiator, with an equivalent temperature of 5777 K. Spectral data provided by the American Society for Testing and Materials (ASTM) is freely available on the web (`http://rredc.nrel.gov/solar/spectra/am1.5/`). The reference spectrum used for photovoltaic performance evaluation is the Air Mass (AM) 1.5 Global (G) 37° south facing tilt at an intensity of 100 mW cm^{-2}, an approximation of the average spectrum for the 48 contiguous states of the United States when the surface normal of the solar cell is pointed toward the sun at an elevation of 41.81° above the horizon. The ASTM data is given in the form of spectral irradiance as a function of wavelength, plotted in Figure 3-2A, along with the ideal black-body spectrum. Spectral irradiance is defined as the incident light energy per second per area per $\Delta\lambda$, the wavelength interval over which the light energy was measured. The units of irradiance are [W m^{-2} nm^{-1}].

In order to illustrate an important point about the risk of plotting spectra in terms of wavelength, we have converted irradiance into photon flux (the number of incident

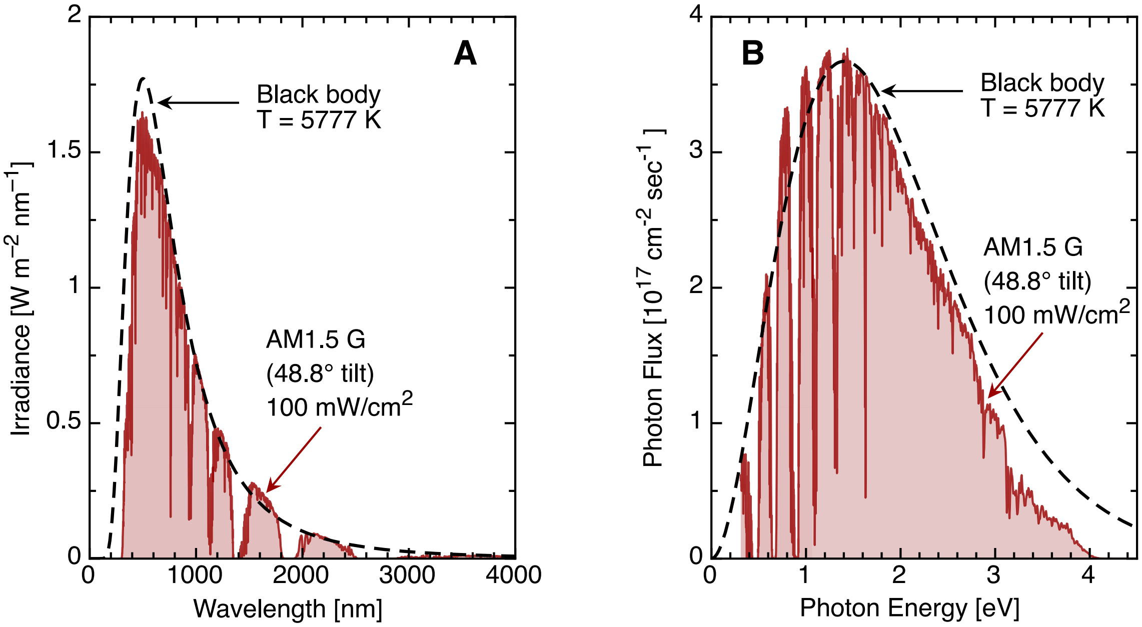

Figure 3-2: The reference solar spectrum used for the evaluation of solar photovoltaics as a function of wavelength (A) or photon energy (B), along with the calculated black-body spectrum at T = 5777 K (dotted line).

photons per second per area, which has units of [sec^{-1} cm^{-2}]). The photon flux is plotted as a function of photon energy in Figure 3-2B. Notice that the two spectra in Figure 3-2 don't look anything like each other. The irradiance peaks at around $\lambda = 495$ nm (sort of an aqua color) whereas the photon flux peaks at around $E = 1.44$ eV, which corresponds to $\lambda = 861$ nm, which is in the near infrared part of the spectrum. What accounts for this difference and which spectrum is correct?

First, the spectral irradiance $I(\lambda, T)$ is not equivalent to the photon flux $F(E, T)$

$$I(\lambda, T) \neq F(E, T) \tag{3.4}$$

because the units of the two functions are different, although both are attempting to describe the same thing. The problem with spectral irradiance is that it depends on the spectral linewidth $\Delta\lambda$ over which the incident power is collected by a monochromator. Consequently, the units of $I(\lambda, T)$ contain a [nm^{-1}] term. This is actually a strange way to bin incident power – by the power per length of the light wave.

Shorter wavelengths end up appearing as if they have higher power densities and the peak of the solar spectrum artificially shifts toward shorter wavelengths. In contrast, $F(E,T)$ is equal to the power detected at a given photon energy over ΔE, the range of photon energies that corresponds to the monochromator linewidth. Therefore, the units of energy in the numerator and denominator cancel, leaving $F(E,T)$ as simply the number of photons at a given photon energy, without any distortion of the true shape of the spectrum. Binning incident power in terms of photon energy makes sense for solar cells and most other optical devices or optical phenomena that do not depend directly on the diffraction of light. Thus, the peak of the solar spectrum is not in the green, but instead in the infrared. Furthermore, it is advisable to plot spectral data as a function of photon energy rather than wavelength in order to avoid potential distortions that can be caused by the use of wavelength as a measurement unit.

3.2.3 Beer-Lambert Law

Photons of a given energy incident on an absorbing material will interact with the molecules in that material over a distance Δx with a probability A_0. The intensity I_0 of light in the material decreases by a factor of $(1 - A_0)$ as it passes through the first layer of molecules, and again by a factor of $(1 - A_0)$ for the second layer, and so on. The total intensity $I(x)$ will decrease with distance inside the film according to

$$I(x) = I_0(1 - A_0)^{x/\Delta x} \tag{3.5}$$

where $x = i \times \Delta x$, and Δx is the thickness of the ith layer of molecules. We can rewrite this equation in a mathematically equivalent form by changing the base to an exponential

$$I(x) = I_0 e^{-\alpha x} \tag{3.6}$$

where α is the absorption coefficient given by

$$\alpha = -\frac{ln(1-A_0)}{\Delta x} \tag{3.7}$$

Taking into account the dependence of α on photon energy gives the well-known Beer-Lambert Law,

$$I(E,x) = I_0 e^{-\alpha(E)x} \tag{3.8}$$

Figure 3-3 shows a plot of light intensity versus thickness for a typical inorganic semiconductor like silicon (Si) (which has an indirect bandgap), a typical quantum-dot (QD) film and a typical conjugated polymer. Knowing α is handy for determining the optimum thickness of the absorbing film in a photovoltaic. A good rule of thumb is that the thickness should be on the order of $1/\alpha$, which is sufficiently thick to absorb 63% of the incoming light on the first pass.

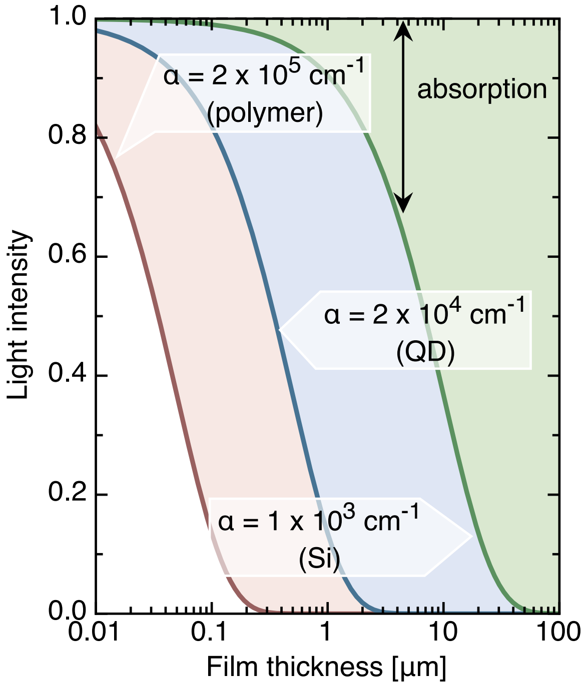

Figure 3-3: Light intensity versus film thickness (log scale) for various absorption coefficients.

3.2.4 Light trapping

For cells whose thickness is less than $1/\alpha$, the intensity profile of light inside the device can become more complicated due to optical interference effects. A strongly reflecting back contact or a large index of refraction offset at one or more interfaces will result in an optical field distribution that is governed by a standing wave pattern within the device rather than a purely exponential decay, resulting in an absorption spectrum that is different from the intrinsic material absorption [76].

In the case where an absorptive film is adjacent to a metal electrode, absorption losses can occur because the optical field is forced to zero at the metal interface. To avoid these losses, an optical spacer layer with index of refraction n and thickness d equal to

$$d = \frac{\lambda}{4n} \tag{3.9}$$

can be inserted between the rear cathode and the absorbing material. Peumans et al. pioneered this effort in small molecule organic cells, demonstrating an improvement in external quantum efficiency (see below for definition) from $\sim$1% to $\sim$10% and an increase in absorption by a factor of four compared to an identical layered stack without a back electrode [40].

An even greater enhancement in absorption can be obtained by increasing the path length of light through the absorptive medium. Either geometrical or wave optic techniques have been studied and are thought to yield enhancements on the order of a factor of $4n^2$. One well known geometrical approach is to use a Lambertian scatterer at the front and/or back of a cell in order to randomly redirect light at an angle through the cell. Alternatively, a V-shape substrate, where the length scale of the grooves is much larger than the thickness of the device, has been used to achieved multiple reflections [35]. Wave optic techniques have also been implemented, such as the use of a photonic crystal at the back of a cell which serves diffract light at a sharp angle across a broad range of wavelengths [6], and surface-plasmon based coupling, which allows for absorption from an external antenna [77, 78].

3.2.5 The Golden rule

One benefit of materials exhibiting localized states, like quantum dots and molecular semiconductors, is that they often have much higher absorption coefficients than materials with long range order like crystalline semiconductors, as shown in Figure 3-3. (In Section 3.3.8, we quantify the benefit gained by increased absorption in donor/acceptor devices in terms of reduced restrictions on charge mobility.)

In quantum mechanics, absorption is thought of as a coupling between the ground states and excited states of a material, perturbed by an electromagnetic field. The probability of transitioning from an initial state with energy E_i to a final state with energy E_f can be approximated by [79]

$$\frac{2\pi}{\hbar}|\langle i|\mathbf{H}'|f\rangle|^2\delta(E_f - E_i \mp E) \tag{3.10}$$

where $\hbar$ is the reduced Planck constant, $|i\rangle$ is the wavefunction of the initial state, $|f\rangle$ is the wavefunction of the final state, $\mathbf{H}'$ is the perturbing Hamiltonian and E is the energy difference between the initial and final state. The delta function describes how energy is absorbed when transitioning from E_f to E_i and emitted when transitioning from E_i to E_f. The term $|\langle i|\mathbf{H}'|f\rangle|^2$ is the coupling strength between the initial and final states and depends on the extent to which the initial and final state wavefunctions overlap. In crystalline semiconductors, the overlap of the initial and final state wavefunctions might be small, for example, if the final state is far-ranging and the initial state is more localized. For quantum confined systems, the overlap between in initial and final state wavefunctions will be greater because both states are confined to the same location, resulting in stronger absorption.

3.2.6 Impurity concentration and cost

Increased absorption can be important for keeping manufacturing costs down for a host of reasons, such as less material usage, shorter film growth times and a higher

Table 3.1: Module cost trends for first, second and third generation PV. *denotes projections by the National Renewable Energy Laboratory (NREL).

PV Technology	**Generation**	**Efficiency** [%]	**Module Cost** [**\$/Watt**]	**Absorption Coefficient** [**cm^{-1}**]
crystalline-Si	I	15	1.40*	5x10^3
amorphous-Si	II	9	0.42*	10^4
CIGS	II	13	0.33*	>10^4
CdTe	II	12	0.28*	5x10^4
Organics	III	*>10?*	*<0.3?*	>10^5

tolerance to impurities. For a film with an impurity density given by

$$D = \frac{N}{L^3} \tag{3.11}$$

where N is the number of impurities in a film of thickness L, we want $N < 1$ in order to prevent loss of charge at an impurity site. Therefore, a film of thickness $L = 1/\alpha$ can tolerate

$$D = N\alpha^3 \tag{3.12}$$

yielding $D = 10^{15}$ cm^3 for an organic semiconductor with $\alpha = 10^5$ cm^{-1} and $N = 1$ versus only $D = 10^9$ cm^3 for c-Si with $\alpha = 10^3$ cm^{-1}. Thus, highly absorbing films can tolerate much higher impurity densities without affecting performance, allowing for more leniency (and less cost) in film qualities and material purification processes. In Table 3.1, module costs are estimated for various photovoltaics by taking into account material costs, capital costs and throughput considerations. Although many factors are involved in determining module costs, projected costs tend to decrease with an increase in the absorption coefficient, indicating that materials with greater absorption tend to have a manufacturing advantage.

3.3 Quantum efficiency

After photoexcitation and the production of free charge, transport of free charge to the electrodes without charge recombination must occur in order to yield photocurrent (Figure 3-4). The external quantum efficiency (EQE) is the number of electrons or holes that arrive at the electrodes per number of incident photons at a single photon energy E_ν:

$$EQE(E_\nu) = \frac{Generated\ electrons}{Incident\ photons\ @\ E_\nu} \tag{3.13}$$

The EQE is a product of both absorption and the efficiency at which absorbed carriers are converted to electrons, called the internal quantum efficiency IQE. The IQE is useful for understanding the efficiency of devices that do not absorb 100% of the incident light. The expression for IQE is

$$IQE(E_\nu) = \frac{Generated\ electrons}{Absorbed\ photons\ @\ E_\nu} \tag{3.14}$$

and we can rewrite the equation for EQE as

$$EQE(E_\nu) = IQE \times Absorption\ @\ E_\nu. \tag{3.15}$$

In principle, the EQE can reach 100%, although practically it is usually peaks around 80% for good quality devices. Reflection, absorption and transport losses can contribute to reduced EQE.

Measurements of EQE are obtained at zero applied bias in order to ensure that charge is generated without being aided or retarded by an external field. Nevertheless, for an ideal photodiode, EQE should be independent of voltage in both reverse bias and forward bias (except for biases approaching the bandgap, as we will see below). Often, the wavelength dependence of photodetectors is given in terms of Responsivity R instead of EQE. R is given by

$$R(\lambda) = \frac{Photocurrent}{Incident\ Power\ @\ \lambda} \tag{3.16}$$

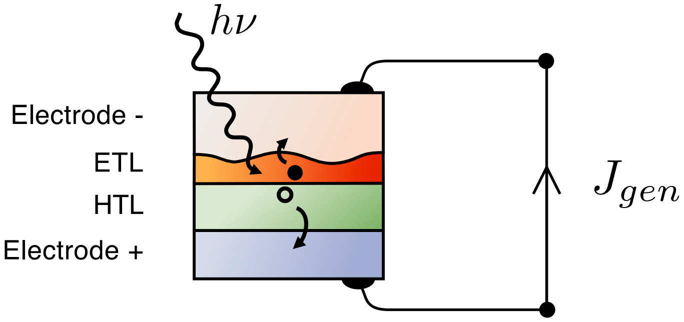

Figure 3-4: Cross section of a photovoltaic device depicting excitation of an electron-hole pair by incident light of energy $h\nu$ and transport of the excited charge toward the electrodes.

with units of [A/W]. Converting between R and EQE can be accomplished using the formula:

$$EQE(\lambda) = \frac{R(\lambda)}{\lambda[\mathrm{nm}]} \times 1240. \tag{3.17}$$

3.3.1 Multistep charge generation

We described earlier how semiconductors with localized states have an advantage associated with increased absorption. Now we'll focus on the charge generation process in these materials, which is inherently more challenging than for crystalline semiconductors. In Figure 3-5, we've drawn a schematic outlining photocurrent generation in a photovoltaic consisting of a donor/acceptor (D/A) heterojunction between a predominantly hole-transporting layer (HTL) and electron-transporting layer (ETL).

Immediately following photoexcitation, the excited electron and hole are located at nearly the same point in space with an initial separation $r_0 = 10 - 100$ Å due to the asymmetric geometrical arrangement of ground and excited state and/or excess thermal energy. A strong coulombic attraction results between the excited charge, the energy of which is given by

$$U_{Ex} = \frac{q^2}{4\pi\epsilon_0\epsilon_i r_0} \tag{3.18}$$

where q is the electron charge, ϵ_0 is the vacuum permittivity and ϵ_i is the dielectric

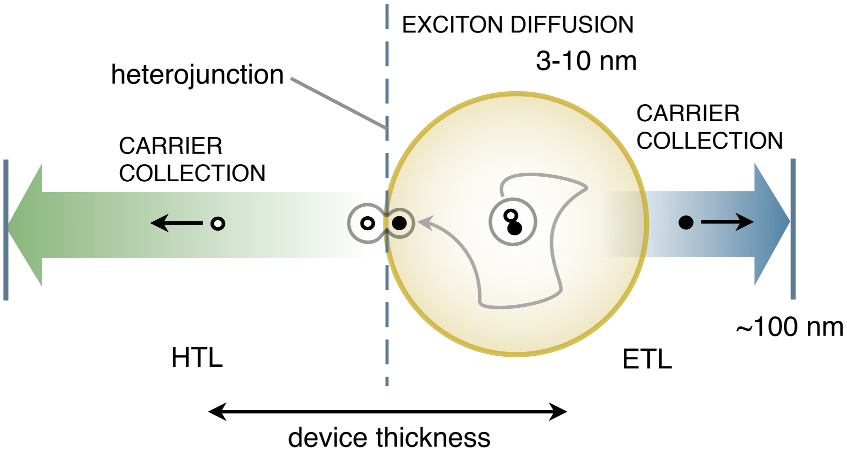

Figure 3-5: The charge generation process for material systems with localized electronic states and a donor/acceptor heterojunction.

constant. For $r_0 = 20$ Å and $\epsilon_i \approx 3 - 4$, the coulombic binding energy $U_{Ex} \approx 0.25$ eV, which is much greater than kT at room temperature and prevents the charge pair from separating into free charge in the bulk. Binding energies can range between 0.1 - 0.5 eV, depending on r_0 and ϵ_i. This bound electron-hole pair, called an exciton, is often mobile and able to diffusive by way of a random walk hopping process toward the D/A heterojunction. Exciton diffusion lengths are notoriously difficult to measure [80], but tend to be in the range of 3 - 10 nm for most organic materials [40]. Upon reaching the heterojunction, either the electron or hole will charge transfer across the interface, depending on the energy level alignment between the ETL and HTL (Figure 3-6). The resulting geminate electron-hole pair is still bound across the interface in what is called a charge transfer state. However, this state is less strongly bound than an exciton in the bulk for two reasons, (1) the extra separation distance afforded by the fact that the two carriers are confined to opposite sides of the heterojunction and (2) the potential energy difference between ETL and HTL is converted during charge transfer to kinetic energy, resulting in a larger r_0 [81]. Once this geminate charge transfer exciton successfully dissociates, the resulting free electron and hole can travel across the bulk of their respective films toward the electrodes in order to produce current flow.

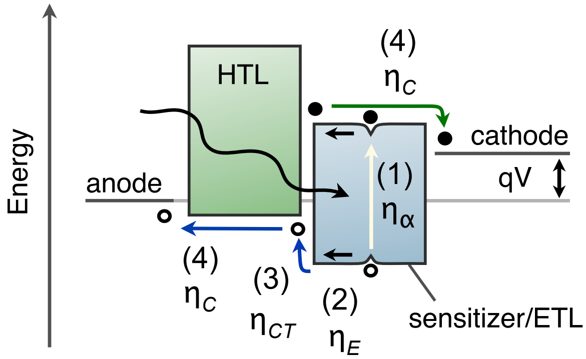

Figure 3-6: Energy band diagram illustrating the four step photogeneration process for a donor/acceptor (D/A) heterojunction.

The band diagram shown in Figure 3-6 displays the four critical charge generation steps outlined above. An expression for the external quantum efficiency can be obtained by multiplying together the efficiency of each photogeneration step [40, 12]

$$\eta_{EQE} = \eta_\alpha \, \eta_{ED} \, \eta_{CT} \, \eta_{CC} \tag{3.19}$$

where η_α is the absorption, η_{ED} is in the efficiency of an exciton diffusing to the heterojunction, η_{CT} is the efficiency of the charge transfer state having resulted in free carriers and η_{CC} is the efficiency of the free carriers reaching the electrodes.

3.3.2 Exciton motion

The most widely studied impediment to high efficiencies in nanoscale materials is the relatively short distance that an exciton can diffuse compared to the characteristic length needed to absorb an appreciable amount of light. For a typical organic molecule, the exciton diffusion length (L_{ED}) is 3 - 10 nm, whereas the typical absorption length ($1/\alpha$) is around 100 nm - more than an order of magnitude away from the condition that $L_{ED} = 1/\alpha$, which would roughly correspond to a quantum efficiency of unity (for a cell with adequate light trapping).

Much theoretical work has been done on the dynamics of exciton motion and dissociation in polymer and small molecule systems [82]. The exciton, being a charge neutral species, can migrate from one molecular site to another irrespective of the surrounding electric field. However, as fields exceed $\sim 10^6$ V/cm (corresponding to 10 V across a 100 nm film), the Coulombic attraction between the electron-hole pair is overcome, leading to field-assisted dissociation in the bulk, also called Onsager dissociation [83]. In the absence of high electric fields, two processes account for the ability of an exciton to hop from one molecule to the next: direct charge transfer (Dexter transfer) or long range energy coupling (Forster transfer or Forster resonant energy transfer). The rate of Dexter transfer is given by

$$r = r_0 e^{-\gamma \Delta x} \tag{3.20}$$

where r_0 is the wavefunction overlap term, γ determines the fall off of the wavefunction overlap with distance and Δx is the separation distance between the two states. The rate of Forster transfer is

$$r = \frac{1}{\tau_{rad}} \left(\frac{R_F}{\Delta x} \right)^6 \tag{3.21}$$

where τ_{rad} is the radiative lifetime and R_F is the Forster radius. In most molecular systems, R_F is on the order of 2 - 6 nm, whereas Dexter transfer is strictly a nearest neighbor phenomenon. In order to further model exciton motion, many groups have investigated more rigorous models which take into account the disordered nature of energetic states in molecular systems, disordered arrangement of molecules in a film and inhomogeneity in molecular-scale polarization [84, 85].

Despite the complexities of the precise mechanisms that govern exciton motion, we can obtain a reasonable picture of how exciton transport affects device performance by making some simple assumptions. Below, we treat excitons as an ensemble of non-interacting particles undergoing diffusion by randomly hopping from one nearby state to the next. We will neglect the dispersion (time dependence) of the diffusion coefficient and differences in transition rates associated with varying energy levels and distances between molecules.

3.3.3 Exciton concentration

In situations with high illumination intensities, it is always important to check if exciton-exciton interaction is likely. We can do this by estimating the density of excitons at a typical intensity of light. Consider a film with an absorption coefficient α and a bandgap E_g under solar illumination. The number of photons per area per second incident on the film roughly equals $\sigma = 1 \times 10^{17}$ s^{-1} cm^{-2} (see Section 3.4 for how we arrive at this number). Multiplying by the fraction of photons absorbed in the first molecular monolayer (of width Δd) and dividing by Δd gives the generation rate G per unit volume. The maximum value for G will occur at the illuminated interface, in the limit where Δd becomes small:

$$G = \lim_{\Delta d \to \infty} \sigma \left(\frac{1 - e^{-\alpha \Delta d}}{\Delta d} \right) = \sigma\alpha. \tag{3.22}$$

For a quantum dot with $\alpha = 10^4$ cm^{-1}, then $G = 1 \times 10^{21}$ s^{-1} cm^{-3}. Assuming all excitons naturally recombine in the bulk without being quenched at an interface, the exciton concentration p per unit volume is obtained by multiplying G by the recombination lifetime τ

$$p = \tau G. \tag{3.23}$$

For a typical quantum dot lifetime of $\tau \approx 20$ ns, we obtain $p \approx 2 \times 10^{13}$ cm^{-3}. How big or small is this number? Assuming a quantum dot occupies a volume of ~(6 nm)^3, then the concentration of dots per volume is $\sim 5 \times 10^{18}$ cm^{-3}. This means that a maximum of only ~0.0004% of dots will be occupied with an exciton at any given instant. In a real device, this concentration will be even lower since most excitons will be dissociated at an interface before recombining in the bulk. We conclude that it is safe to ignore exciton-exciton interactions at typical solar intensities.

3.3.4 Exciton continuity equation

For the case of non-interacting mobile excitons, the continuity equation can be used to obtain the distribution of excitons in a film. Once the exciton distribution is known, we can calculate the percentage of excitons that reach the dissociating heterojunction and ultimately figure out how the external quantum efficiency should vary with thickness.

Taking a closed volume element ∂V, the rate at which excitons are accumulated with time is equal to the number of excitons that are generated minus the number of excitons that recombine, minus the number of excitons that flow out of ∂V [86]:

$$\frac{\partial(p\,\partial V)}{\partial t} = G\,\partial V - R\,\partial V - \int \mathbf{F} \cdot \mathbf{dS} \tag{3.24}$$

where p is the number of excitons, G is the generation rate, R is the recombination rate, $\mathbf{F}$ is the flux of excitons and the integral represents the number of excitons flowing out of the enclosed volume. This equation can be rewritten in differential form as

$$\frac{\partial p}{\partial t} = G - R - \nabla \cdot \mathbf{F} \tag{3.25}$$

In one dimension, the exciton population of the jth layer of molecules can be obtained using the steady state condition

$$\frac{\partial p}{\partial t} = 0 \tag{3.26}$$

together with the flux of excitons leaving the jth layer

$$F_j = D\frac{dp_j}{dx} \tag{3.27}$$

where D is the exciton diffusion coefficient, given by

$$D = \frac{L_{ED}^2}{\tau} \tag{3.28}$$

Using

$$R_j = \frac{p_j}{\tau} \tag{3.29}$$

for the recombination rate, we obtain a second-order linear ordinary differential equation of the form [87, 40]

$$0 = L_{ED}^2 \frac{d^2 p_j}{dx^2} - p_j + \tau G_j \tag{3.30}$$

which is the steady state exciton diffusion equation.

Exciton diffusion in a thick film

To obtain a simple solution to Equation 3.30, we can set $G_j = 0$ for all other layers except for the jth layer. Equation 3.30 becomes

$$0 = L_{ED}^2 \frac{d^2 p_j}{dx^2} - p_j \tag{3.31}$$

which describes the circumstance under which we illuminate only the jth layer and examine the resulting exciton distribution everywhere else, shown in Figure 3-7. Once we have found a solution for each independently illuminated layer, we can add up all the solutions in order to obtain the total exciton population for the fully illuminated film. The solution to Equation 3.30 for the case where the illuminated layer (the jth layer) is located at $x = 0$ and L_{ED} is long compared to length of the film (boundary condition of $p = 0$ at $x = \infty$) is a decaying exponential

$$p_j(x) = \frac{\tau_r G_j}{2} e^{-x/L_{ED}}. \tag{3.32}$$

where τ_r is the radiative or non-radiative exciton lifetime in the bulk. At a distance $x = d$ away from the illuminated layer, Equation 3.32 gives the number of excitons that have not yet radiatively or non-radiatively recombined in the bulk. In other words, the fraction of excitons that have not been lost to recombination is $1 - e^{-d/L_{ED}}$. For example, at $d = L_{ED}/2$, only 39% of excitons will still be in existence.

Exciton diffusion in a thin film

Ideally, we don't want excitons to recombine before they reach a dissociating interface. One might be tempted to think that if we put a dissociating interface at $d = L_{ED}/2$, then we would only be able to harvest the remaining 39% of the excitons. In reality,

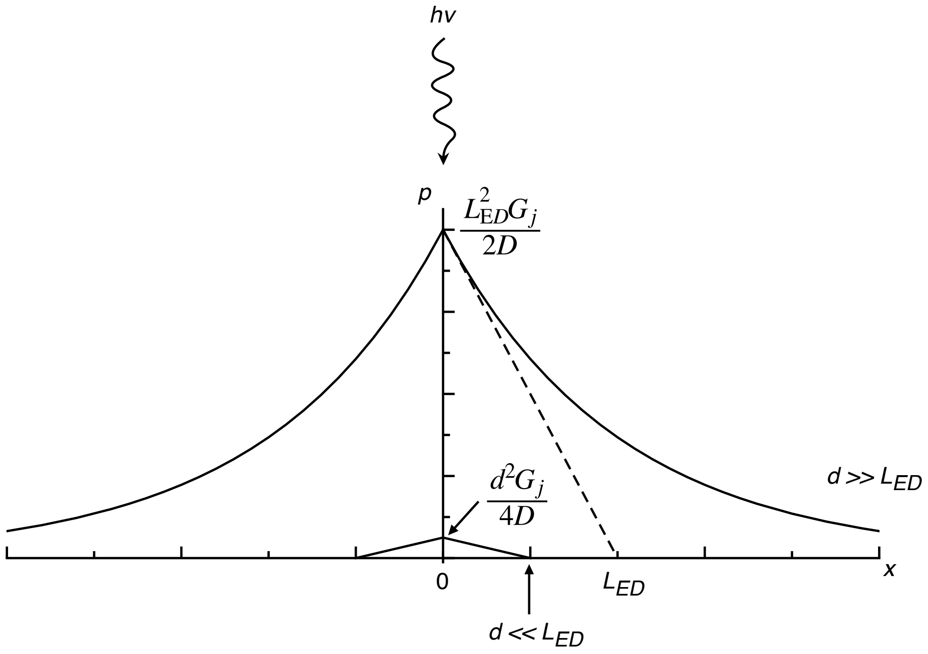

Figure 3-7: Exciton profile p for a thick film device with $d \gg L_{ED}$ and a thin film device with $d \ll L_{ED}$, both illuminated only at the jth molecular layer located at $x = 0$.

making the active film thickness on the order of L_{ED} allows us to capture most of the generated excitons before they recombine. To understand this, let's look at the exciton profile for the case where a dissociating interface is located at $d \ll L_{ED}$.

Assuming that the distance between a dissociating interface and the illumination point is close enough that there is no recombination in the bulk, then Equation 3.31 becomes

$$0 = L_{ED}^2 \frac{d^2 p_j}{dx^2} \tag{3.33}$$

The solution for the boundary condition $p_j(d) = 0$ is then a linearly decreasing function

$$p_j(x) = \frac{\tau_D G_j}{2d}(x - d) \tag{3.34}$$

where τ_D is the time constant for excitons to diffuse to the interface and undergo charge transfer. If τ_D is dominated by the time to diffuse to the interface, τ_D can be related to the exciton diffusion coefficient D by the expression for diffusion velocity

[86]

$$v_{diff} = D\frac{1}{p_j}\frac{dp_j}{dx} \tag{3.35}$$

and by integrating over the time required to reach the interface

$$\tau_D = \int_0^{\tau_D} dt = \int_0^d \frac{1}{v_{diff}}dx = \frac{1}{D}\int_0^d \frac{p_j}{dp_j/dx}dx = \frac{d^2}{2D} \tag{3.36}$$

It is interesting to note that the exciton concentration at $x = 0$ is different than what we found in the previous section, where we assumed that only bulk recombination is taking place. We have

$$p_j(0) = \frac{\tau_r G_j}{2} = \frac{L_{ED}^2 G_j}{2D} \qquad d \gg L_{ED} \text{ (bulk recombination only)} \tag{3.37}$$

$$p_j(0) = \frac{\tau_D G_j}{2} = \frac{d^2 G_j}{4D} \qquad d \ll L_{ED} \text{ (interfacial dissociation only).} \tag{3.38}$$

for the two cases examined so far. The exciton concentration will always be lower for the case of interfacial dissociation because $d < L_{ED}$ and the extra factor of 1/2. This make sense because excitons must be more rapidly destroyed when they dissociate at a nearby interface than when they simply recombine naturally, yet they are generated at the same rate in both cases.

Exciton diffusion in films with thicknesses on the order of L_{ED}

In order to determine $p_j(x)$ in real devices, which often have film thicknesses on the order of L_{ED}, we must solve Equation 3.31 for the boundary condition $p_j(d) = 0$ when some fraction of excitons recombine in the bulk and some dissociate at the interface. The solution can become unwieldy when taking into account additional constraints, like two dissociating interfaces on opposite sides of the absorbing film [87] or the possibility of Forster transfer to an electrode [80]. In addition, interference effects are often present and will modify the exciton profile. Therefore, it is common to use dynamical Monte Carlo modeling in order to describe the exact exciton distribution [88, 84].

3.3.5 Carrier collection

The final step in the charge generation process is carrier collection. The flow of electrons in low mobility materials with localized states and low dopant concentrations can be approximated by the same transport equations that apply to traditional crystalline semiconductors. The transport equations are:

$$\frac{\partial \mathcal{E}}{\partial x} = \frac{q}{\epsilon}(p-n) \qquad \text{(Gauss' law)} \tag{3.39}$$

$$J_e = qn\mu_e\mathcal{E} + qD_e\frac{\partial n}{\partial x} \qquad \text{(Electron current equation)} \tag{3.40}$$

$$\frac{\partial n}{\partial t} = G - R + \frac{1}{q}\frac{\partial J_e}{\partial x} \qquad \text{(Electron continuity equation)} \tag{3.41}$$

where $\mathcal{E}$ is the electric field, ϵ is the dielectric constant, p is the hole concentration, n is the electron concentration, μ_e is the electron mobility, D_e is the electron diffusion coefficient, G is the generation rate and R is the recombination rate.

Electron current is comprised of both drift and diffusion. The solution to the current equation can be solved analytically for a few special cases [89], but usually requires a numerical calculation [90]. In order to get a sense for the relative influence of drift or diffusion in the carrier collection process in donor/acceptor heterojunctions, we can start with the assumption that either drift or diffusion dominates current flow and calculate the supposed carrier concentration and carrier transit time for each process independently.

Carrier concentration and time response of pure drift currents

Using a typical incident photon flux of $\sigma = 1 \times 10^{17}$ s^{-1} cm^{-2} from Section 3.3.3, the current produced is $J = -q\sigma = -16$ mA cm^{-2}, assuming a quantum efficiency of 100%. The electron concentration required to sustain current flow of this magnitude is

$$n = \frac{J_e}{q\mu_e\mathcal{E}_{sat}} = \frac{\sigma d}{\mu_e V_{sat}} \tag{3.42}$$

where d is the thickness of the device and $\mathcal{E}_{sat}$ and V_{sat} are the internal electric field and internal voltage drop, respectively, required to obtain saturated photocurrent.

For a typical mobility of $\mu_e = 10^{-3}$ cm^2 V^{-1} s^{-1}, a thickness of $d = 1/\alpha = 1$ μm and a saturation voltage of $V_{sat} = 0.1$ V, we obtain $n = 10^{17}$ cm^{-3}. This value corresponds to ~2% of quantum dots occupied by an electron, which is a fairly high concentration.

Why did we use such a low value for V_{sat}? In a situation where photocurrent is dominated by drift, we need to be able to saturate photocurrent at a voltage that is much less than the internal voltage driving photocurrent. Otherwise, fill factors will be low (see Section 3.6). Open circuit voltages (V_{OC}) are usually in the range of 0.5-1 V, so a reasonable fill factor (FF) will require saturated photocurrent at only $V_{sat} \sim 0.1$ V (see Sections 3.5 for a definition of V_{OC}).

In the case of pure drift currents, the transit time of electrons across a film is related to μ_e, the voltage drop V across the film and thickness d according to

$$\tau_t = \frac{d}{v_e} = \frac{d}{\mu_e \mathcal{E}} = \frac{d^2}{\mu_e V} \tag{3.43}$$

Assuming an internal voltage of 0.5 V at zero bias, the photocurrent produced for $\mu_e = 10^{-3}$ cm^2 V^{-1} s^{-1} and $d = 1$ μm would have a response time of $\tau_t = 20$ μs.

Carrier concentration and time response of pure diffusion photocurrents

Calculating the carrier concentration under the sole influence of diffusion current is more complicated. Fortunately, the continuity equation for exciton diffusion (which we discussed in Section 3.3.3) is nearly identical to the electron diffusion equation (except for a negative sign). Again, we exclude the possibility of interparticle interactions. We solve the continuity equation for the case of electrons injected at a fixed rate σ at one end ($x = 0$) of a film of thickness d and obtain the distribution of electrons in the film for the boundary condition $n(d) = 0$ at the charge collecting contact (which corresponds to efficient charge extraction).

For a device where the electron diffusion length is much smaller than the thickness of the device ($L_e \ll d$), electrons are lost to recombination before they are able to travel the distance of the film. The electron concentration follows an exponential decay away from the charge generating interface [86]:

$$n = \frac{L_e \sigma}{D_e} e^{-x/L_e} \tag{3.44}$$

where D_e is the electron diffusion coefficient.

For a device where ($L_e \gg d$), all of the injected electrons reach the charge collecting contact. The electron concentration decays linearly with distance away from the charge generating interface [86]:

$$n = -\frac{\sigma}{D_e}(x - d). \tag{3.45}$$

A typical diffusion coefficient $D_e = 2.6 \times 10^{-5}$ cm^2 s^{-1} (which corresponds to $\mu_e = 10^{-3}$ cm^2 V^{-1} s^{-1} in the example above) gives a value of $n(0) = n_0 = 2 \times 10^{17}$ cm^{-3} for the electron concentration at the charge generating interface. Since the average value of n over the thickness of the film is the same as n obtained for drift-dominated current, we cannot distinguish between the contribution from drift or diffusion to carrier collection by simply knowing the amount of charge built-up in the device.

Alternatively, the time required for carriers to traverse the length of a device can be used to distinguish between the relative contribution from drift or diffusion. Integrating over the time for an electron to travel from the interface to the electrode (analogous to exciton diffusion in Equation 3.36) gives the transit time under pure diffusion

$$\tau_t = \frac{d^2}{2D_e} \tag{3.46}$$

which does not depend on bias, unlike the drift transit time (Equation 3.43). For our example device with $d = 1$ μm and $D_e = 2.6 \times 10^{-5}$ cm^2 s^{-1}, we obtain $\tau_t = 200$ μs, an order of magnitude slower than the pure drift case.

When measuring the decay transients of photoexcited carriers, a diffusion-driven photocurrent will flow only as long as a gradient in carrier concentration remains intact. If both drift and diffusion are contributing equally to photocurrent, the time response of the faster drift component will dominate because most carriers will be quickly swept out of the device by the electric field. However, if a large diffusion gradient is present (at least an order of magnitude greater than the baseline carrier concentration), the drift current will not be large enough to degrade the carrier concentration gradient and the slower diffusion component will dominate the decay transients. In addition, only a slight voltage dependence of the decay transient will be observed as long as the electric field strength is less than that required to prevent carriers from diffusing to the electrode.

3.3.6 Effect of device structure

Diffusion of carriers away from a dissociating interface is more likely to be dominant in thin devices with vertically segregated layers than in thicker devices with mixed phases. For thin planar devices, charge carriers can easily form a concentration gradient between the interface (where carriers are produced) and the electrode (where they are extracted). In mixed heterojunctions, free charge carriers are produced throughout the composite film, resulting in a flatter concentration profile and hence a greater reliance on the electric field to generate photocurrent.

Mihailetchi et al. [91] have observed that the magnitude of the photocurrent in polymer blend devices is dependent on the magnitude of the electric field across the electrodes. By using different cathode materials with different work functions, they demonstrated that the photocurrent-voltage characteristics are identical when offset by the built-in voltage drop produced by the electrode work function asymmetry. However, the photocurrent produced using a gold electrode (roughly corresponding to zero built-in electric field) is only 13% lower than when using a lithium fluoride doped aluminum (LiF/Al) electrode, which produces a large built in potential of $\sim$ 1 V. The contribution to photocurrent from diffusion effectively adds a voltage shift of 0.6 V out of a total V_{OC} of 0.9 V. Some believe that some form of vertical phase segregation leads to such a large contribution from diffusion [92].

An even greater role for charge diffusion should be expected for planar donor/acceptor heterojunctions. Many studies consider diffusion to be primarily responsible for charge collection [93, 94, 90, 95, 89]. For example, Ramsdale et al. [93] measured

V_{OC} in a polymer bilayer device for a range of cathode and anode work functions and found that a constant offset of 1 V could be ascribed to diffusion.

3.3.7 Electric field due to space charge

In describing the build up of carriers required to drive charge collection, we've neglected the Coulombic attraction between opposite carriers built up across opposite sides of the heterojunction. How large is the electric field at the heterojunction and will it interfere with charge collection?

We can calculate the electric field and electric potential for photo-excited charges diffusing away from a donor/acceptor heterojunction assuming a triangular distribution of charge shown in Figure 3-8 for the special case where $n_0 = p_0$. The charge distribution of electrons is given by:

$$\rho(x) = \frac{qn_0}{d}x - qn_0 \tag{3.47}$$

and the electric field at the heterojunction ($x = 0$) is

$$\mathcal{E}(0) = \int_0^d \frac{\rho(x)}{\epsilon}dx = -\int_d^0 \frac{\rho(x)}{\epsilon}dx = -\frac{qn_0}{\epsilon}\left[\frac{x^2}{2d} - x\right]_d^0 = \frac{qn_0 d}{2\epsilon} \tag{3.48}$$

where ϵ is the dielectric constant. Using the same example as above with $d = 1$ μm, $n_0 = 10^{17}$ cm^{-3} and $\epsilon = 6 \times 8.85 \times 10^{-14}$ F cm^{-1}, we obtain $\mathcal{E}(0) = 1.5 \times 10^6$ V cm^{-1}. This is a large number for the electric field. It's equivalent to 100 V across a 1 μm film! The potential drop from $x = 0$ to $x = d$ can be calculated from Poisson's equation by integrating the expression for the electric field

$$\phi(0 \to d) = -\int_0^d \mathcal{E}(x)dx = \int_0^d \frac{qn_0}{\epsilon}\left(\frac{(x-d)^2}{2d}\right)dx \tag{3.49}$$

$$= -\frac{qn_0}{\epsilon}\left[\frac{(x-d)^3}{6d} + \frac{d^2}{6}\right]_0^d = -\frac{qn_0 d^2}{6\epsilon} \tag{3.50}$$

Again, for $d = 1$ μm and $n_0 = 10^{17}$ cm^{-3}, we obtain $\phi(d) = 50$ V. Of course, we would never able to build-up enough charge to generate 50 V. We are forced to conclude

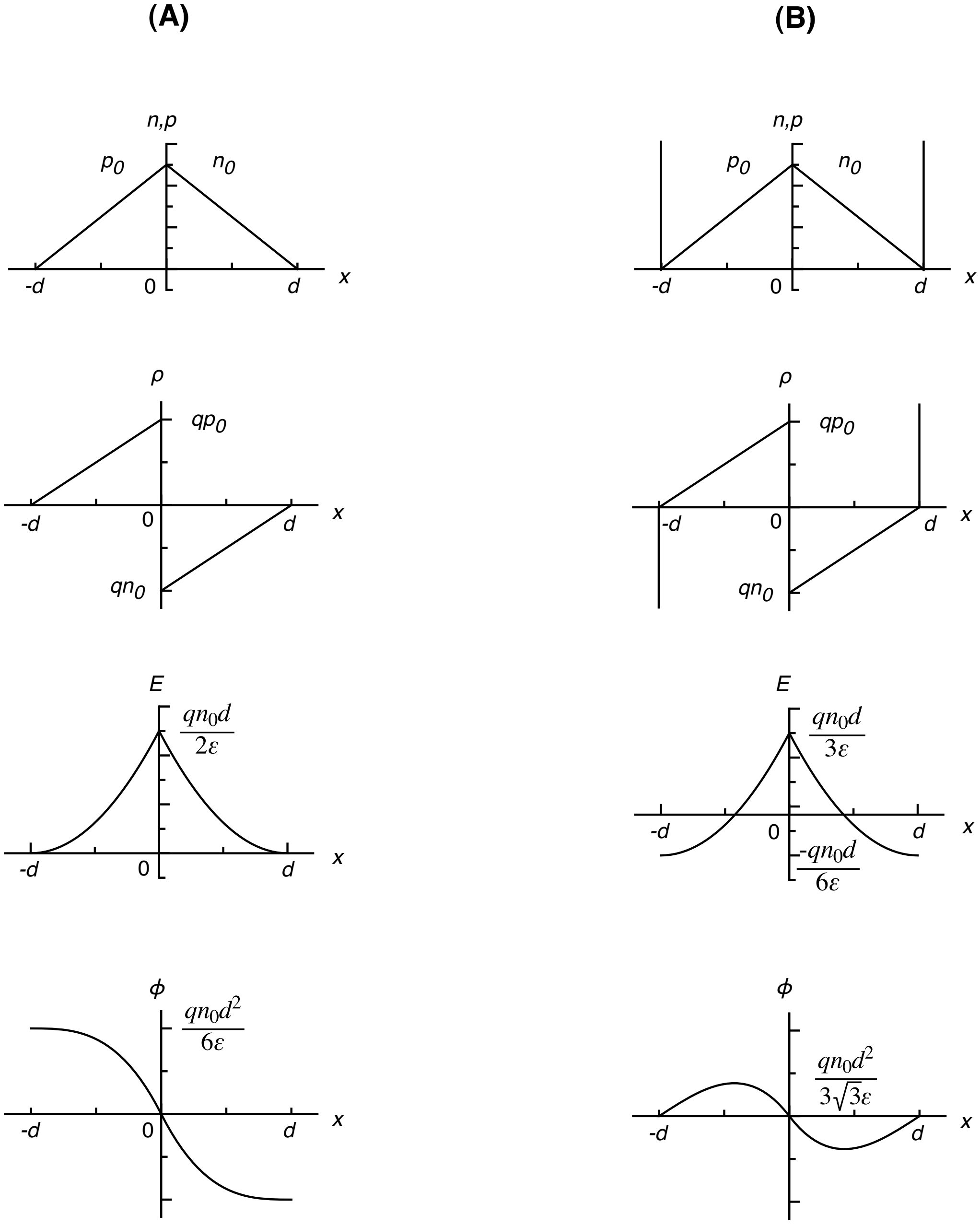

Figure 3-8: Carrier concentration, charge concentration, electric field and electric potential for a donor/acceptor heterojunction under illumination (A) without electrodes and (B) with electrodes under short circuit conditions.

that our example device with $\eta_{QE} = 100\%$ is non-physical. At some point, the internal electric field will limit charge build up and induce drift currents that oppose this voltage drop. In Section 3.5, we will describe why the open-circuit voltage is ultimately limited by the semiconductor bandgap and the dark current.

In a real device with electrodes, the electric field and electric potential will be affected by charge on the two electrodes which sandwich the donor and acceptor layers. At zero bias, charge will accumulate on the electrodes in order to balance out the voltage induced by the build up of photo-excited charge inside the device, as shown in Figure 3-8B. Across the electrodes, the potential drop is forced to zero, resulting in a reduced electric field across the interface and a hump in the electric potential profile. Still, a sizable electric field remains at the heterojunction interface, which indicates that the internal electric field will hinder diffusion, alter the carrier distribution and reduce the charge collection efficiency. For the example device with $d = 1\ \mu\text{m}$ and $n_0 = 10^{17}\ \text{cm}^{-3}$, now we have $\mathcal{E}(0) = 10^6\ \text{V cm}^{-1}$, which remains a very large (and unrealistic) value.

3.3.8 Influence of mobility and absorption coefficient

The question arises as to whether efficient charge collection by diffusion in a planar donor/acceptor heterojunction is physically achievable or simply impossible. Consider the dependencies of Equation 3.50, which relates the carrier concentration and the potential drop across the heterojunction. The carrier concentration (in turn given by Equation 3.45) depends on the diffusion coefficient D_e (or the mobility μ_e) and the thickness depends on the absorption coefficient by $d = 1/\alpha$. Presumably, the dielectric constant ϵ is difficult to modify. Substituting $n_0 = \sigma d/2D_e$ and $d = 1/\alpha$, we can obtain the following criterion for diffusion dominated charge collection:

$$-\phi(0 \rightarrow d) = \frac{qn_0d^2}{6\epsilon} = \frac{q\sigma}{24\epsilon D_e}\left(\frac{1}{\alpha}\right)^3 < 1\ \text{V} \tag{3.51}$$

where $\phi(0 \rightarrow d)$ is the potential drop across each semiconductor film, σ is the incident solar flux and $\phi(0 \rightarrow d)$ is arbitrarily set to be less than 1 V, which we consider to be a plausible voltage drop to overcome. In Figure 3-9, we plot α versus μ_e the equipotential line in Equation 3.51 at three different solar intensities. The region above the equipotential line is where charge collection can flow under pure diffusion without excessive losses due to the internal field produced by built-up space-charge. Therefore, the typical QD diffusion coefficient of $D_e = 2.6 \times 10^{-5}$ cm^2 s^{-1} ($\mu_e = 10^{-3}$ cm^2 V^{-1} s^{-1}) used in the examples above would have to increase to something in the range of $D_e = 2.6 \times 10^{-3}$ cm^2 s^{-1} (or $\mu_e = 10^{-1}$ cm^2 V^{-1} s^{-1}) in order to satisfy Equation 3.51. Likewise, the carrier concentration should always be less than $n_0 = 10^{15}$ cm^{-3}, which corresponds to 0.02% of QDs occupied by a charge carrier.

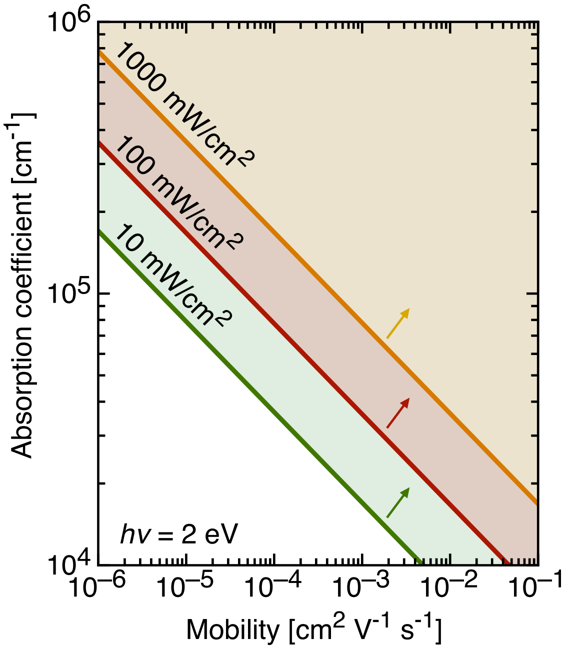

Figure 3-9: Plot of absorption coefficient versus charge mobility at three different solar intensities for the condition that the potential drop due to built-up charge diffusing away from a planar donor/acceptor heterojunction is less than 2 V across the donor and acceptor layers.

On the other hand, the cubic dependence of Equation 3.51 on the absorption coefficient demonstrates the critical advantage gained by highly absorptive materials. Increasing α by only factor of 5 results in more than a two order of magnitude reduction in the potential drop due to built-up space charge. For a given material, the location of α and μ on Figure 3-9 (or simply the factor $\mu\alpha^3$) can be thought of as a figure of merit for carrier collection efficiency.

3.4 Semiconductor bandgap

The bandgap E_g of the absorbing layer in a solar cell affects device efficiency in two important ways: it determines what fraction of the solar spectrum is absorbed and how much voltage can be generated.

3.4.1 Thermal relaxation

The energy level diagram in Figure 3-10 shows light absorbed across a semiconductor bandgap at two frequencies, one with $h\nu > E_g$ and with $h\nu = E_g$. In both cases, an electron and hole are generated, but for $h\nu > E_g$, the electron rapidly lowers its energy to E_g (on the order of picoseconds) by successively coupling to lower and lower energy states. The extra energy $h\nu - E_g$ is lost as thermal energy and, in the absence of other loss mechanisms, the energy of electrons exiting the device will be equal to E_g.

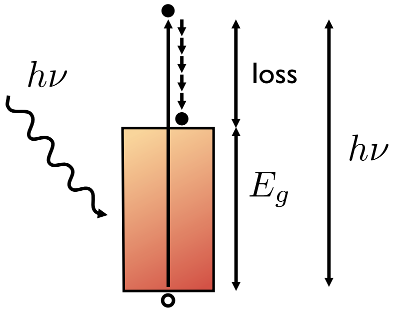

Figure 3-10: Energy band diagram depicting excitation at energies above the bandgap.

For excitation energies lower than E_g, no absorption occurs. This poses a problem for creating an efficient solar cell because the solar spectrum (Figure 3-11A) consists of a broad distribution of photon energies - it's a blackbody radiator at 5777 °C, but missing narrow segments associated with absorption from elements in the earth's

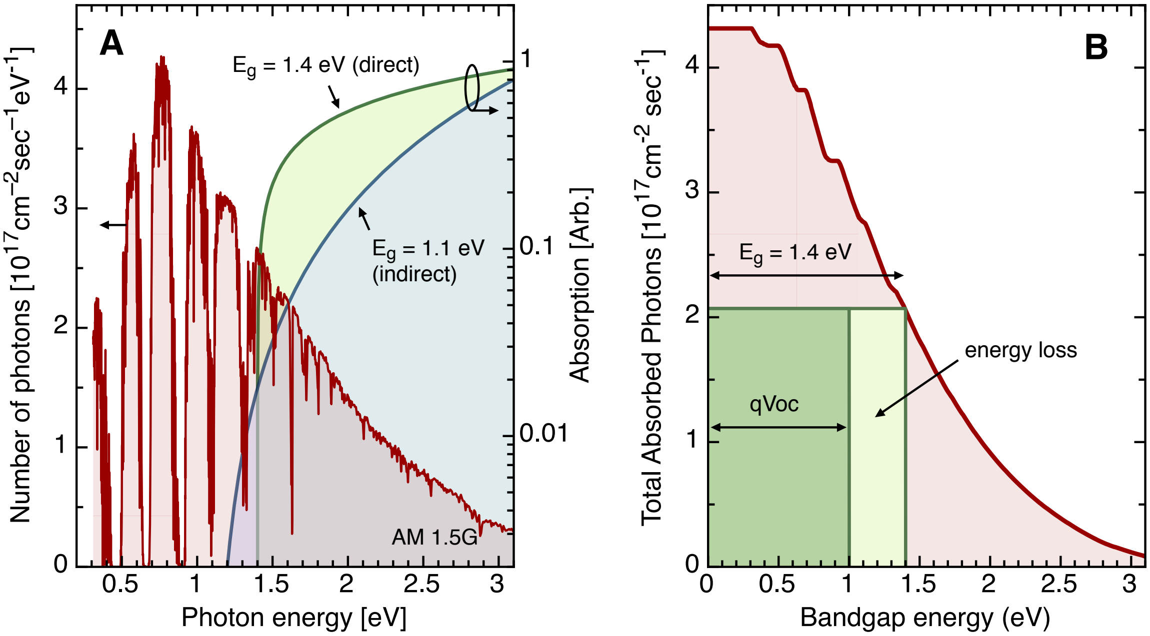

Figure 3-11: Plot of the number of photons versus photon energy for the AM 1.5G standard global spectrum (A), along with the absorption of a direct and indirect bandgap semiconductor. In (B), plot of the total number of photons above a given bandgap energy. The area in green represents the power that can be generated by a semiconductor with bandgap 1.4 eV.

atmosphere like water and oxygen (see Section 3.2.2). One may be tempted to think that a lower bandgap is preferable since the solar spectrum peaks at a photon energy of only 0.75 eV. In fact, a lower bandgap is subject to greater thermal losses due to the relaxation of electrons from $h\nu$ down to E_g. Consequently, an optimum bandgap exists which balances the tradeoff between absorbing the greatest number of photons and retaining the greatest amount of energy from each photon.

3.4.2 Determination of the optimum bandgap

In 1980, Henry [45] developed a simple graphical procedure for determining the optimum bandgap for solar photovoltaics. First, one must calculate the total number of photons with energies above a bandgap E_g by integrating the solar spectrum (Figure 3-11A) from E_g to infinity. Second, the energy produced by a solar cell with bandgap E_g is calculated by multiplying the number of absorbed photons by $E_g - 0.4$ eV (in the next section, we'll explain why we must subtract 0.4 eV). The maximum efficiency is then the ratio between the maximum energy produced for a given E_g and the area under the integrated solar spectrum curve, as shown in Figure 3-11B. The maximum efficiency is 31% for a bandgap of 1.4 eV and reduces to 6% for a bandgap of 0.5 eV or 21% for a bandgap of 2 eV.

3.5 Open-circuit voltage

Along with light absorption and a semiconductor's bandgap, the magnitude of V_{OC} is a third critical factor that determines the theoretical efficiency of a solar cell. There is considerable debate as to the origin of V_{OC} in donor/acceptor photovoltaics, although the consensus is that the maximum V_{OC} is limited by the energy level difference between the highest occupied molecular orbital (HOMO) of the acceptor (HTL) and the lowest unoccupied molecular orbital (LUMO) or the donor (ETL) (see Figure 3-6). One notable exception in the literature is a theoretical study by Nelson et al., who argue that the donor/acceptor energy gap indeed limits V_{OC}, but only when recombination at the donor/acceptor heterojunction is prominent [96]. According to

Nelson, when recombination is low at the interface, the maximum V_{OC} is limited by E_g, as in conventional inorganic photovoltaics. This debate is especially important considering that most donor/acceptor cells exhibit low V_{OC}s, accounting for the single greatest loss mechanism in efficiency. As background, we will cover the basics of how voltage is generated by an idealized semiconductor film and then extend our discussion to include two semiconductor films forming a donor/acceptor heterojunction.

3.5.1 Origin of V_{OC}

A photovoltaic device generates a photocurrent J_{photo} when illuminated. This photocurrent is produced much like a battery produces electrochemical current, except carriers are generated electrochemically whereas a photovoltaic cell generates carriers electro-optically. J_{photo} is dependent on light intensity and typically independent of applied voltage. An applied electric field usually does not influence the rate of photon absorption. In some cases, the rate of dissociation or charge collection can be aided or hindered by an electric field, but we will ignore these effects for now. Most photovoltaics also produce current in dark when bias is applied to the cell. The total current under illumination is referred to as the light current,

$$J_{light}(I, V) = J_{dark}(V) - J_{photo}(I) \tag{3.52}$$

where the dark current J_{dark} depends on voltage V, and the photocurrent J_{photo} depends on intensity I. Since J_{photo} is constant with voltage and J_{dark} increases monotonically with voltage in forward bias, there exists a bias point where J_{dark} and J_{light} are equal and opposite. This bias point is called the open-circuit voltage V_{OC} and is equivalent to the condition where nothing is connected to the external leads of the photovoltaic device. Physically, V_{OC} is the voltage that a photovoltaic induces across itself in order to exactly cancel the generation of photocurrent. The condition for V_{OC} can be written as

$$J_{light}(I, V_{OC}) = J_{dark}(V_{OC}) - J_{photo}(I) = 0 \tag{3.53}$$

Note that V_{OC} will be dependent on intensity and the functional form of the intensity dependence will follow the inverse function of J_{dark}. For example, if J_{dark} follows an exponential voltage law (as do conventional photovoltaics),

$$J_{dark} = J_0 \left(e^{qV/kT} - 1 \right) \tag{3.54}$$

where J_0 is a prefactor, then the condition for V_{OC} is

$$J_0 \left(e^{qV_{OC}/kT} - 1 \right) - J_{photo}(I) = 0 \tag{3.55}$$

Solving for V_{OC} gives

$$V_{OC} = \frac{kT}{q} \ln \left(\frac{J_{photo}(I)}{J_0} + 1 \right) \tag{3.56}$$

Alternatively, if J_{dark} follows a power law with voltage (as do many organic devices) such as

$$J_{dark} = J_0 V^2 \tag{3.57}$$

then V_{OC} will be given by

$$V_{OC} = \sqrt{-\frac{J_{photo}(I)}{J_0}} \tag{3.58}$$

Equations 3.56 and 3.57 accurately describe the light intensity dependence of V_{OC}. However, they do not fully reflect the fact that V_{OC} will eventually saturate at high intensities.

3.5.2 Limit to V_{OC} for a single semiconductor slab

To determine the saturation limit to V_{OC}, we can employ a detailed-balance model that considers the temperature and bandgap of the solar cell. The following discussion is a simplified adaptation of Queisser and Shockley's [44] initial theoretical treatment of the limiting efficiency of a solar cell.

First, consider a simple photovoltaic device consisting of a single semiconducting film (Figure 6.2). In order to function properly, it must have the following three special properties:

- Electrons can only enter and exit the conduction band on one side of the semiconductor (we will assume this happens on the right side) and

- Holes can only enter and exit the valence band on the *other* side of the semiconductor (the left side)

- The semiconductor is contacted on the right by a reservoir of electrons and on the left by a reservoir of holes

In practice, a built-in electronic asymmetry of some sort (such as a p-n junction, heterojunction or Schottky junction) provides this one-way current flow behavior, but the actual device material or geometry does not affect the above requirements.

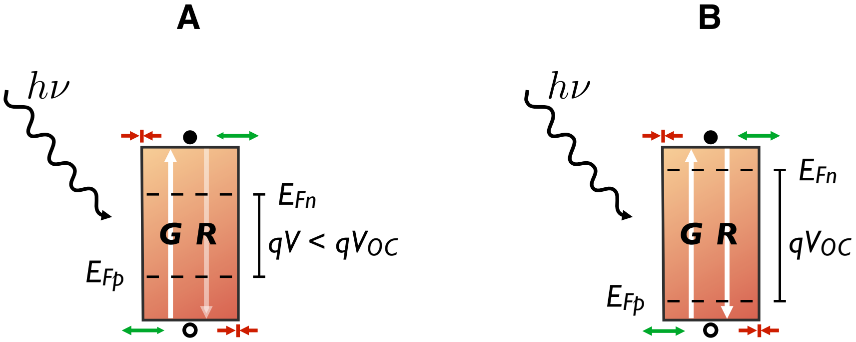

Figure 3-12: Simplified energy band diagram for a photovoltaic device consisting of a single semiconductor film under illumination at an applied bias of (A) $V \leq V_{OC}$ and (B) $V = V_{OC}$. Electrodes are not pictured and are assumed to be perfect reservoirs of electrons and holes on the right and left side of the semiconductor, respectively.

We will make an additional assumption that the carrier concentration in the semiconductor and at the contacts is given by the Boltzmann approximation

$$n \simeq N_c e^{-(E_c - E_{Fn})/kT} \tag{3.59}$$

for electrons, where N_c is effective density of states in the conduction band, E_c is the the energy level of the conduction band, E_{Fn} is the quasi Fermi level for electrons, k

is the Boltzmann constant and T is temperature. For holes

$$p \simeq N_v e^{-(E_{Fp}-E_v)/kT} \tag{3.60}$$

where N_v is effective density of states in the valence band, E_v is the the energy level of the valence band and E_{Fp} is the quasi Fermi level for holes.

Balance of generation and recombination currents

When light illuminates the semiconductor, carriers are generated at a given generation rate G, producing a photocurrent

$$J_{photo}(I) = qG(I)d \tag{3.61}$$

where d is the thickness of the semiconductor layer. When bias is applied to the device, carriers are injected from the electrodes, raising the carrier concentration and the overall recombination rate. In the absence of non-radiative recombination, the only mechanism for current flow is by radiative recombination

$$R = Bnp \tag{3.62}$$

where B is the material-dependent bi-molecular recombination constant. Therefore, the dark current at all voltages is

$$J_{dark}(V) = qR(V)d - qG_0d \tag{3.63}$$

where G_0 is the thermal generation rate and $R(V)$ is the voltage-dependent radiative recombination rate. The term involving G_0 is included because, in the dark and at zero bias, thermally excited carriers will produce a small amount of current. Under illumination, the total current is obtained from Equation 3.52

$$J_{light}(I,V) = qR(V)d - qG_0d - qG(I)d \tag{3.64}$$

Setting $J_{light} = 0$ gives the relationship between generation and recombination at V_{OC}:

$$R(V_{OC}) = G_0 + G(I). \tag{3.65}$$

This equation states that the recombination rate at V_{OC} is determined by the total generation rate. This result is fundamental to all photovoltaics, provided that parasitic leakage currents are small.

Note that the only voltage dependent quantity in the above equation is $R(V)$. Therefore, for a given intensity and a fixed temperature, V_{OC} will depend only on the voltage dependence of R, which is exclusively linked to J_{dark} and not J_{photo}. This is a somewhat non-intuitive result, since it is customary to think of V_{OC} as directly determined by some aspect of the photogeneration process. For example, in donor/acceptor photovoltaics, the energy lost during exciton dissociation (process 3 in Figure 3-6) is widely considered to directly cause a decrease in V_{OC}. Also, the flatband condition (indicating zero electric field) is commonly thought to occur at V_{OC}. In reality, the magnitude of V_{OC} is not correlated to any of the steps in the photogeneration process. Instead V_{OC} can be completely predicted knowing only the voltage dependence of J_{dark}. V_{OC} should be simply thought of as the bias point at which the photocurrent sourced by the semiconductor is subsumed by recombination.

V_{OC} and carrier concentration

An equation for V_{OC} can be obtained by considering the dependence of R on carrier concentration and voltage. In the Boltzmann approximation, carriers in the semiconductor will recombine radiatively across the semiconductor bandgap with a rate of

$$R(V) = Bnp = BN_cN_ve^{-(E_c-E_v-E_{Fn}+E_{Fp})/kT} = Ke^{-(E_g-qV)/kT} \tag{3.66}$$

where we have used the fact that voltage is related to the quasi Fermi levels in the semiconductor by $qV = E_{Fn} - E_{Fp}$ and $K = BN_cN_v$ is a material constant. Notice that once qV exceeds E_g, R will rapidly become very large. Solving for V yields

$$V = \frac{E_g}{q} - \frac{kT}{q} \ln\left(\frac{K}{R}\right) \tag{3.67}$$

From Equation 3.65,

$$V_{OC} = \frac{E_g}{q} - \frac{kT}{q} \ln\left(\frac{K}{G_0 + G(I)}\right) \tag{3.68}$$

For high illumination intensities, $G_0 \gg G(I)$. Using $G(I) = Bnp$, the equation for V_{OC} reduces to

$$V_{OC} = \frac{E_g}{q} - \frac{kT}{q} \ln\left(\frac{N_c N_v}{np}\right) \tag{3.69}$$

where n and p are the photogenerated electron and hole concentrations. Since np is always less than $N_c N_v$, the second term in Equation 3.69 will always be positive, which ensures that the maximum value for V_{OC} is E_g/q at $T = 0$. At a finite temperature, the magnitude of the second term in Equation 3.69 is often ~ 0.4 V.

3.5.3 Limit to V_{OC} in a donor/acceptor heterojunction

In a photovoltaic device consisting of a donor/acceptor heterojunction, the analysis of the maximum V_{OC} is similar to that in the previous section, except for a change in the recombination mechanism, diagramed in Figure 3-13. Under applied bias, hole injection into the hole transport layer (HTL) lowers the quasi Fermi level (E_{Fp}) in the HTL while electron injection into the electron transport layer (ETL) raises the quasi Fermi level (E_{Fn}) in the ETL. If recombination is allowed to take place at the interface, the recombination rate is

$$R(V) = Bnp = BN_{c,ETL}N_{v,HTL}e^{-(E_{c,ETL}-E_{v,HTL}-E_{Fn}+E_{Fp})/kT} = Ke^{-(\Delta E - qV)/kT} \tag{3.70}$$

where $N_{c,ETL}$ is the effective density of states in the conduction band of the ETL, $N_{v,HTL}$ is the effective density of states in the valence band of the HTL, $E_{c,ETL}$ is the energy level of the conduction band in the ETL, $E_{v,HTL}$ is the energy level of the valence band in the HTL and $\Delta E = E_{c,ETL} - E_{v,HTL}$. $R(V)$ is no longer a function of E_g, but instead depends on ΔE, the energy offset at the heterojunction. The equation for V_{OC} becomes

$$V_{OC} = \frac{\Delta E}{q} - \frac{kT}{q} \ln\left(\frac{N_{c,ETL} N_{v,HTL}}{np}\right) \tag{3.71}$$

and the maximum V_{OC} at $T = 0$ is $\Delta E/q$.

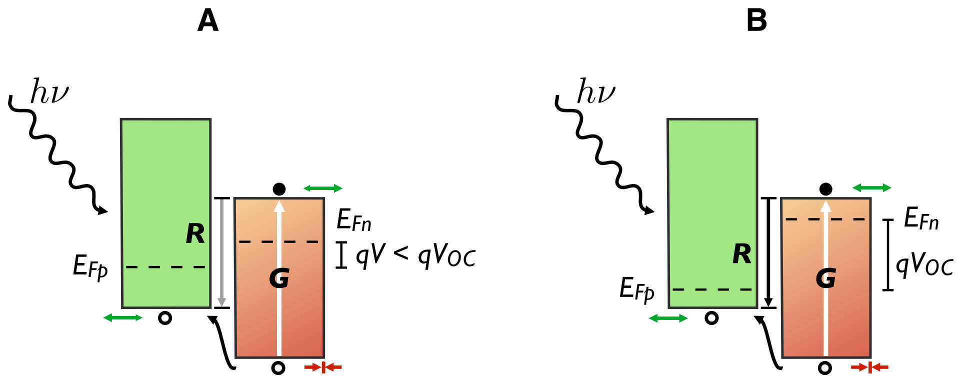

Figure 3-13: Energy band diagram for a photovoltaic device consisting of a donor/acceptor heterojunction under illumination at an applied bias of (A) $V \leq V_{OC}$ and (B) $V = V_{OC}$. Electrodes are not pictured and are assumed to be perfect reservoirs of electrons and holes on the right and left side of the semiconductors, respectively.

3.6 Fill factor

The fill factor is the last major device attribute that determines the efficiency of a solar cell. It reflects the degree to which parasitic resistances or device non-idealities hamper efficient operation of the cell.

The solar cell power efficiency is the ratio of electrical power produced divided by the optical power incident on the device. The efficiency is given by

$$\eta = \frac{Power\ Out}{Power\ In} = \frac{V_{max} J_{max}}{Power\ In} \tag{3.72}$$

where V_{max} and J_{max} are the voltage and current density produced when the load

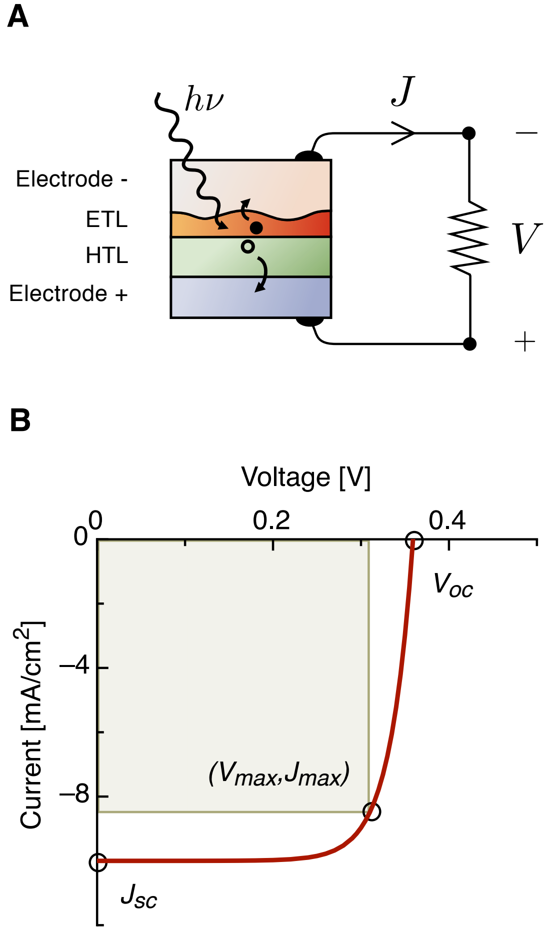

Figure 3-14: A solar cell is connected to a load resistor with the positive terminal attached to the p-type (or HTL) side of the device, as shown in (A). The cell is most efficient at the maximum power point on the i-v characteristic, shown in (B).

impedance connected to the solar cell is chosen such that the output power is maximized. The current and voltage polarity conventions are shown in Figure 3-14A along with a typical i-v characteristic in Figure 3-14B. The fill factor relates V_{max} and J_{max} to the short-circuit current J_{SC} and the open-circuit voltage V_{OC}:

$$FF = \frac{J_{max} V_{max}}{J_{SC} V_{OC}} \tag{3.73}$$

which can be included in the power efficiency equation, giving

$$\eta = \frac{J_{SC}\ V_{OC}\ FF}{Power\ in} \tag{3.74}$$

3.6.1 Equivalent circuit model under illumination

As discussed in section 3.5.1, photocurrent flows in parallel with the diode current and therefore can be modeled as a current source in parallel with a diode in the dark, as shown in Figure 3-15.

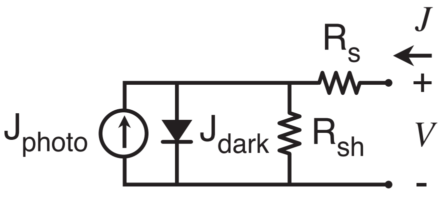

Figure 3-15: Equivalent circuit model for a photovoltaic device under illumination including parasitic resistances.

The parasitic series resistance R_s is the resistance experienced by carriers as they traverse the device from one electrode to the other. R_s should be as close to zero as possible otherwise photocurrent at high intensities will be subject to resistive losses. The parasitic shunt resistance R_{sh} is due to leakage pathways that bypass the built-in rectification of the diode. R_{sh} should be large otherwise it will compromise the flow of photocurrent away from the junction.

3.6.2 Effect of series and shunt resistance on V_{OC}

We used the Quite Universal Circuit Simulator (QUCS), available at `http://qucs.sourceforge.net`, in order to characterize how R_s and R_{sh} effect the i-v characteristics of a solar cell.

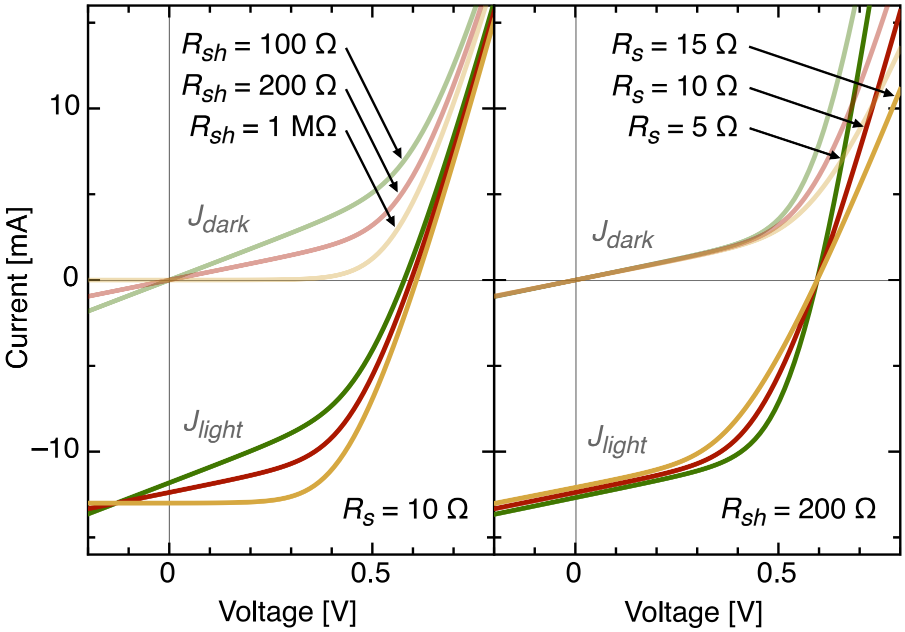

Figure 3-16: Simulated i-v characteristics for a diode in dark and under illumination for varying shunt and series resistances.

From Figure 3-16, we find that both J_{SC} and V_{OC} are adversely affected by reduced R_{sh} while changes to R_s only affect J_{SC} and not V_{OC}. Decreasing R_{sh} creates a pronounced bias dependence below turn-on in dark that translates in light into a bias dependence around 0 V, resulting in a reduced FF. Increasing R_s causes a reduction in the diode current above turn-on. In light, the slope of the light current around V_{OC} is decreased, leading to reduced FF. It is important to note that V_{OC} does not change as R_s is varied. This result can be understood by inspection of the circuit diagram in Figure 3-15. At $J_{light} = 0$, no current flows through R_s, leaving the voltage measured at the contacts equal to the voltage at the diode junction.

3.7 Conclusion

This chapter has attempted to outline some of the major concepts relevant to the physics of operation of donor/acceptor photovoltaics. The purpose of the chapter is to build an understanding of the issues facing photovoltaic devices that rely upon exciton dissociation at an interface and the diffusion of photoexcited carriers. The key points stressed in the chapter are:

- The energy in the solar spectrum peaks at a wavelength of 861 nm, corresponding to a photon energy of 1.44 eV.
- Photogeneration of charge in donor/acceptor photovoltaics occurs via a four step process: absorption, exciton diffusion, exciton dissociation and charge collection.
- In a typical device, the concentration of excitons at the heterojunction interface is around 2×10^{13} cm^{-3}.
- For device thicknesses greater than the exciton diffusion length, the percentage of excitons undergoing dissociation falls off exponentially with thickness.
- The transit time of free charge carriers traveling across a film under pure diffusion is independent of voltage.
- The concentration of photoexcited carriers at the heterojunction interface must remain below 10^{15} cm^{-3} in order to avoid excessive space charge build-up.
- An important figure of merit for an absorbing film in a donor/acceptor solar cell is $\mu\alpha^3$.
- The optimum bandgap of a solar cell is 1.4 eV in the detailed-balance limit.
- V_{OC} is set by the shape of the diode i-v characteristics in dark and not by any aspect of the photogeneration process.

- V_{OC} is limited by the optical bandgap unless recombination at the heterojunction interface is severe, in which case the maximum V_{OC} is limited by the energy level offset at the interface.
- High series resistance can result in reduced fill factors and J_{SC}, but will not affect V_{OC}.

From the analysis presented above, we expect an optimized donor/acceptor solar cell to exhibit strong absorption ($> 10^5$ cm^{-1}), high mobility ($> 10^2$ cm^2 V^{-1} s^{-1}), a bandgap near 1.4 eV, low interfacial recombination, low series resistance and high shunt resistance.

Chapter 4

Fabrication process and characterization techniques

So far we've introduced the basic motivational and theoretical principals underlying quantum-dot and molecular-based donor/acceptor devices. In this chapter, we describe the unique processes developed to fabricate and characterize these devices, including the printing process used to deposit the quantum dot (QD) layer, the growth of a transparent top contact electrode, implementation of a new method to determine the compensation voltage and the measurement of device response time as a function of bias.

4.1 Introduction

The fabrication challenge presented to us is the following: how does one build a reliable and reproducible device structure that incorporates a layer of solution deposited QDs (often with poor uniformity and surface morphology) without shunting through voids in the QD film? A further complication is that the short diffusion length for excitons in the QD film requires film thickness to be on the order of one to ten QD monolayers. At these thicknesses (6-60 nm), film defects or voids are nearly impossible to avoid, especially over large areas. A third complication is that the photocurrent response from such thin films will be weak, requiring a device structure with especially low leakage currents so as to not overwhelm the signal in light.

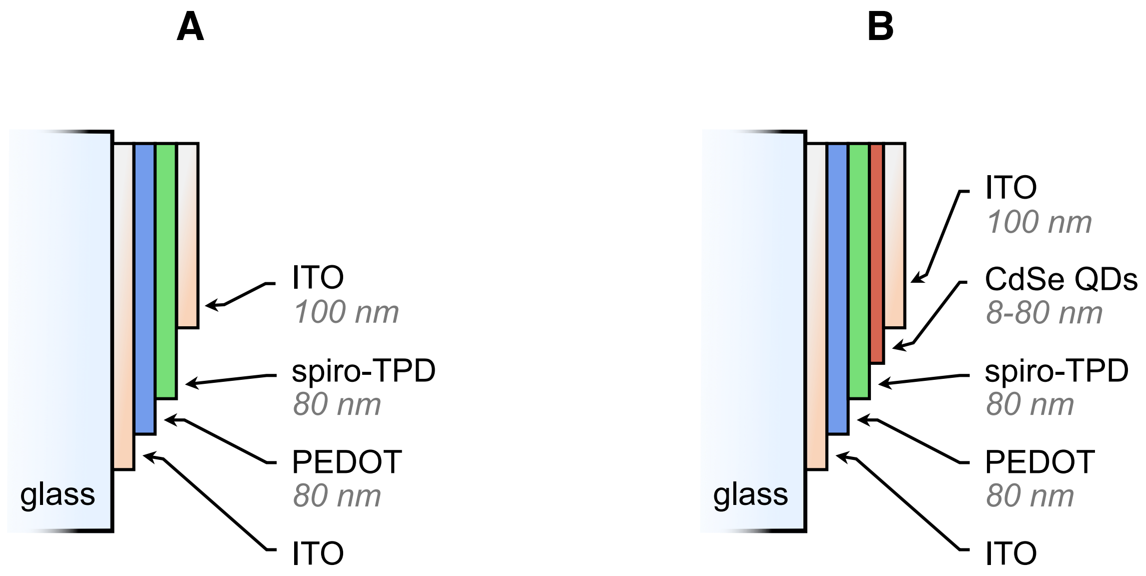

Figure 4-1: Diagram of (A) the control device structure and (B) QD device structure presented in this thesis.

We addressed the challenges mentioned above by first developing a control heterojunction diode without QDs that (a) exhibited low leakage currents and (b) did not absorb in the spectral region where the QDs absorb light (Figure 4-1A). Once a diode with adequate i-v characteristics was obtained, we built a device that included QDs by incorporating them at the heterojunction of the control diode structure. Figure 4-1B shows a schematic of our final and most successful structure. It employs the following sequence of layers:

- a conductive polymer (Poly(3,4-ethylenedioxythiophene) poly(styrenesulfonate) or PEDOT:PSS) as a planarization layer
- a small molecule (N,N′-bis(3-methylphenyl)-N,N′-bis-(phenyl)-9,9-spiro-bifluorene or spiro-TPD) as a hole transport layer
- a colloidally-grown cadmium selenide (CdSe) QD layer that is printed onto spiro-TPD as the absorbing layer

- a sputter-deposited transparent top electrode consisting of indium-tin-oxide (ITO) that function as both the electron transporting layer and top electrode

The end result is a device with diode characteristics that are largely determined by the heterojunction between spito-TPD and ITO and a light sensitivity that is driven by the QDs.

For characterization, we have implemented a state of the art testing set-up that allows for complete device characterization under nitrogen. The set-up is capable of taking i-v characteristics under illumination from an LED, wavelength-dependent photocurrent measurements, bias-dependent photocurrent measurements and photocurrent transient measurements.

4.2 Fabrication

Device fabrication begins with ITO-coated substrates that are cleaned by ultrasonication in micro-90, deionized water, acetone and isopropanol for 5 minutes each, followed by a one second oxygen plasma treatment. The oxygen plasma treatment serves to remove hydrocarbon contaminants and further oxidize the ITO surface, allowing for better wetting by the aqueous solution of PEDOT:PSS.

4.2.1 Spin-coated PEDOT:PSS planarization layer

Two PEDOT:PSS coating options are available from H. C. Stark (`http://www.clevios.com/`), CLEVIOS P VP AI 4083 and CLEVIOS P VP CH 8000. Both PEDOT:PSS variants are designed to be sufficiently conductive for OLEDs and solar cells in the vertical direction, but sufficiently insulating in the lateral direction in order to reduce the occurrence of "cross-talk" in small pixel matrix array displays. CH 8000, with a conductivity two orders of magnitude lower than AI 4083, produces better diode characteristics with lower leakage currents and is used exclusively in devices presented in this thesis, unless stated otherwise.

60 μl of CH 8000 is spin coated onto ITO glass with a micropipette at 3000 rpm

and and acceleration of 10 000 rpm. Removal of the CH 8000 film from the contact pads around the edge of the substrate is perform with a cleanroom swab moistened with deionized water. Next, substrates are transfered to a nitrogen glove box for annealing at 200° C for 10 minutes. The remainder of the device growth occurs in either a nitrogen atmosphere or under vacuum.

4.2.2 Vacuum growth and transfer system

Substrates are placed into a holder that is mated to a shadow mask with the desired mask for the organic film pattern. The substrate holder assembly is directly loaded from the glovebox into a vacuum transfer line, which has a typical base pressure of 9×10^{-9} Torr. High vacuum is achieved in all chambers in the growth system with a turbo pump and separate backing and roughing dry pumps. Movement of substrates along the linear transfer line between chambers is performed with a linear rail, cart and pulley system. Lateral transfer of substrates into each vacuum chamber is accomplished with a linear motion vacuum transfer arm and fork.

4.2.3 Thermally evaporated spiro-TPD hole transport layer

Purified spiro-TPD is obtain from Lumtek (`http://www.lumtek.co.tw`). Thermal evaporation is performed in a custom-built chamber containing six Luxel RADAK furnaces. First, the temperature of the furnace is set to automatically ramp up to 90° C, which is just under the sublimation temperature of spiro-TPD. Unfortunately, the temperature the furnace thermocouple is not the actual temperature inside the spiro-TPD crucible. Therefore, deposition cannot be adequately controlled by monitoring the temperature alone. Instead, a constant rate of deposition can be achieved by maintaining the applied power at a steady value while monitoring the deposition rate indicated by the crystal monitor. Since there is no cooling mechanism, care must be taken to avoid overheating the crucible, otherwise deposition rates may spike and remain elevated for an extended period of time. Typical evaporation rates are 0.2 - 0.3 nm/s and spiro-TPD film thicknesses are 80 nm, unless stated otherwise.

4.2.4 Printed CdSe QD layer

Colloidally-synthesized CdSe QDs were obtained from David Oertel for the work described in Chapter 5 and from Scott Geyer for the work described in Chapter 6. The CdSe is formed by combining cadmium and selenium precursor molecules, together with an organic stabilizing molecule that prevents aggregation of the CdSe nanocrystal as they form. The crystal growth process is temperature activated and can be abruptly halted by lowering the reactant temperature once the desired nanocrystal size is obtained. For a full description of the nanocrystal growth process, see reference ??.

Following spiro-TPD deposition, substrates are transfered back to the nitrogen glove box via the vacuum transfer line where a film of CdSe QDs is deposited onto the spiro-TPD by the non-destructive contact printing method described below.

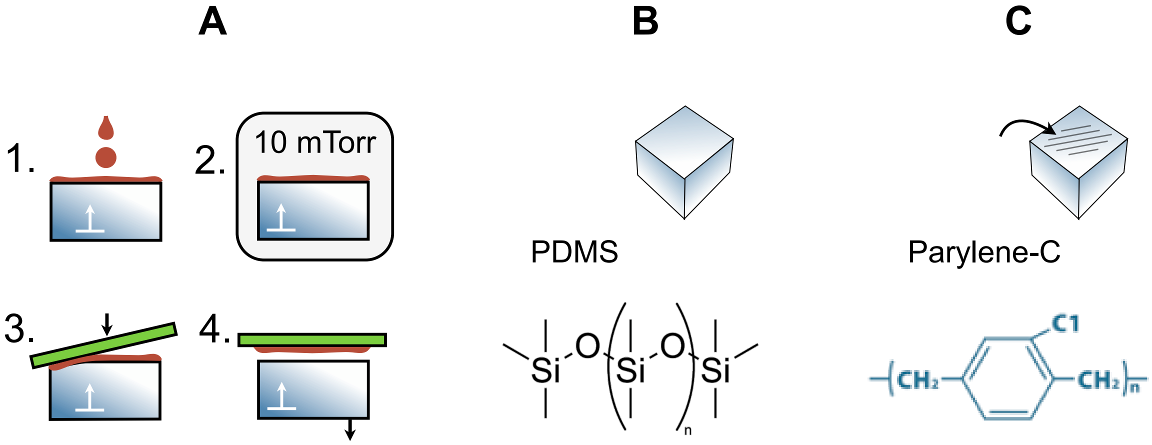

Figure 4-2: Steps involved in the QD printing process (A) using an elastomeric stamp made of PDMS (B) which is optionally coated with an aromatic polymer parylene-C (C).

The elastomeric stamps used for QD printing are made by casting polydimethylsiloxane (PDMS) that is cured at 60°C for two hours to form an optically smooth conformable surface, and then sectioned into 1 cm^2 stamps. 60 μl of a chloroform solution containing CdSe QDs, capped with oleate or trioctylphosphine oxide (TOPO) groups and synthesized according to Jarosz et al. [67], is dispensed on the stamp, spun at 3000 rpm and allowed to dry under vacuum for at least 30 minutes (Figure 4-2), forming a thin QD film coating on top of the stamp. The coated stamp is then pressed against the device stack, making contact first at one edge to minimize air pockets trapped between the stamp and the substrate. The stamp and substrate are then immediately separated, leaving the CdSe film adhered to the spiro-TPD.

4.2.5 Radio frequency sputter deposition of the ITO top electrode

A magnetron sputter deposition chamber contains two electrodes, two magnets, a turbo pump with a variable aperture gate valve and gas flow valve (Figure 4-3).

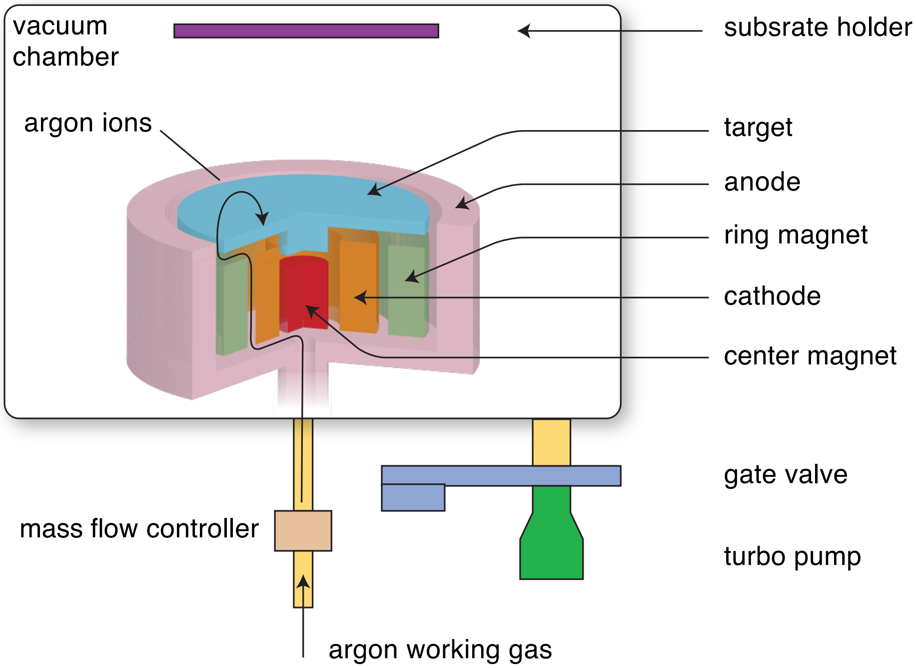

Figure 4-3: Schematic diagram of RF-powered sputter deposition system.

The material to be deposited (the target) is placed on top of the cathode. The chamber is filled with an inert gas such Argon (Ar) and several thousand volts is applied across the electrodes, creating a plasma of equal numbers of positive Ar ions and free electrons. Magnets in the sputtering gun are designed to confine the plasma to the area above the target, sparing the substrate from ion and electron bombardment. When the plasma is struck, emission from the relaxation of excited Ar ions can be seen through the chamber viewport. The positive Ar ions are accelerated toward the target and, upon collision with the surface, dislodge atoms from the target. The free atoms then travel throughout the chamber, coating all surfaces including the substrate. In radio frequency (RF) sputtering, an AC field is applied to the target and electrodes. The AC field is useful for sputtering insulating target materials that will build up charge over a time scale of a couple of microseconds. An AC voltage in the MHz range is faster than this build up, allowing for negative free electrons to neutralize the surface and thereby maintain current flow. The amount of gas in the chamber is controlled by the rate of gas flow into the chamber and the aperture of the gate valve. The gas pressure must be high enough to sustain the plasma, yet low enough that scattering does not prohibit free atoms from reaching the substrate.

In this work, the top ITO contact is RF sputter deposited with argon working gas. A shadow mask is used to define an array of ten patterned electrodes. ITO sputtering is performed at room temperature at a rate of 0.01 nm/s for the first 20 nm in order to minimize damage to the underlying CdSe and TPD films. The remaining 80 nm of the ITO film is grown at 0.07 nm/s.

4.3 Characterization

In order to test the device in nitrogen, we have designed a probe fixture and a masking system with ten individual devices per substrate. Each device is contacted by way of displaced contact pads located on the periphery of the substrate. The probe fixture allows us to contact the device inside the glovebox while keeping the testing instrumentation outside of the glovebox.

4.3.1 Patterning techniques

The bottom ITO layer is patterned with a photolithographic process (described in Appendix B) into two parallel strips down the middle of the substrate and ten contact pads on the periphery. CH 8000 is patterned by hand with a moist swab. The organic and top ITO layers are patterned by shadow masking. The final device area of 1.21 mm^2 is defined by the overlap between the top and bottom ITO electrodes. The tolerance of the masking setup is well withing the limits of the substrate holder/mask holder system, ensuring that the active device area is exactly the same from run to run (Figure 4-5).

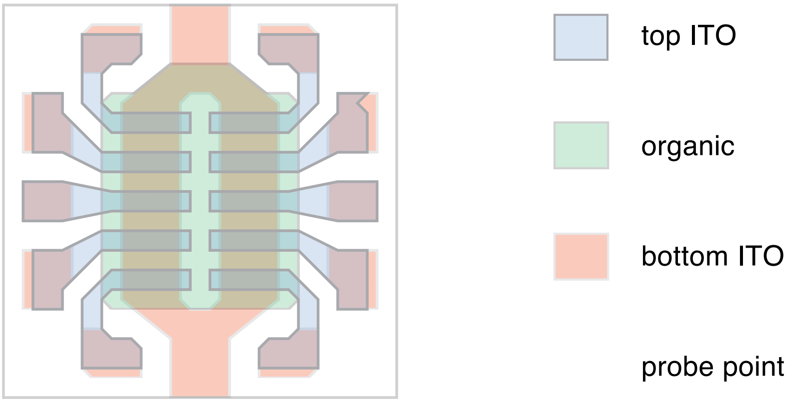

Figure 4-4: Schematic of overlaid patterned layers used to form an array of ten devices on a single glass substrate.

4.3.2 Probe fixture

The probe fixture (Figure 4-6) is designed to house the substrate for testing and to contact the device with spring-loaded gold pins, which are visible in Figure 4-5. The gold pins contact the underlying ITO pads, which in turn are connected to each device's top electrode. In designing the fixture, care was taken to place the sample as close as possible to the front face of the fixture, allowing the sample to be easily viewed and illuminated from all angles. In addition, the process of inserting and removing the sample was made as simple as possible in order to ensure that handling in the

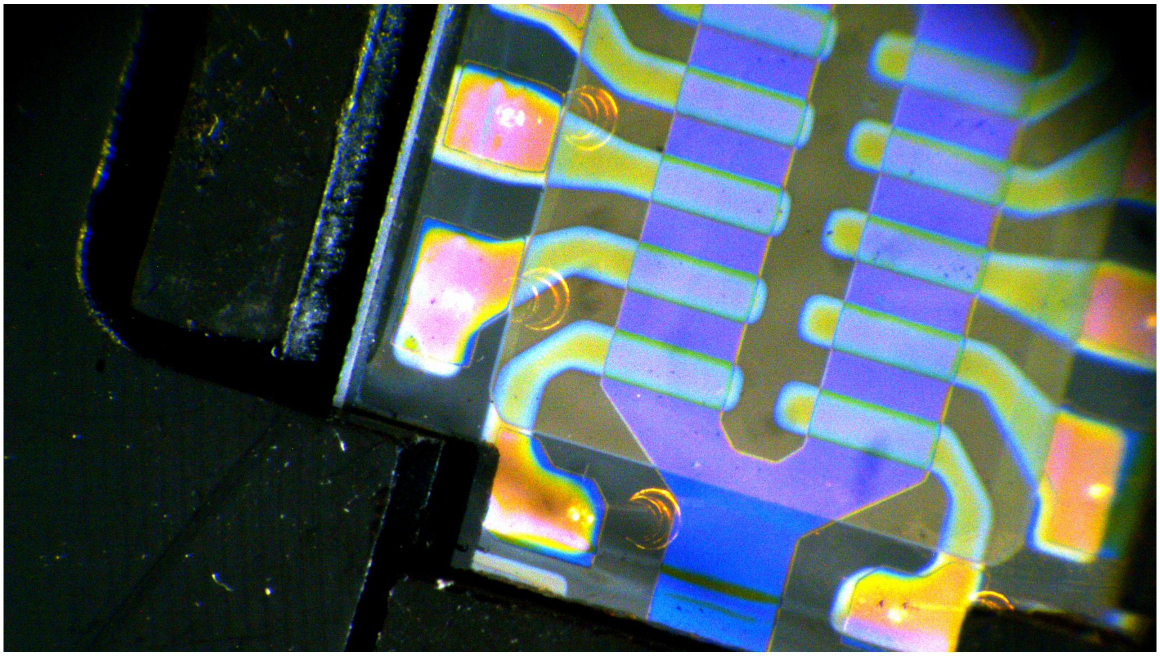

Figure 4-5: Image of a patterned QD device secured in the probe fixture.

glove box would be facile. This was accomplished with a simple latch mechanism and spring loaded pins that serve to keep the fixture door firmly in place when closed.

4.3.3 Glovebox electrical feedthroughs and switch box

Testing all ten pads on a sample located inside a glove box creates a difficult measurement challenge. We have developed a setup that uses a series of BNC electrical feedthroughs along with a Keithley 7000 switch box in order to individually probe each pad on a substrate, as shown in Figure 4-7. The sample is placed in a test box in order to limit electrical noise and provide complete darkness. Voltage is sourced from the source side of a Keithley 6487 and current is measured from the sense side. Note that the HI and LO of the 6487 source and sense are electrically isolated. Since the Keithley 7000 switch box is single pole, double throw (instead of the more convenient double pole, single throw - which is apparently not available from any vendor), we are left with a unfortunate dilemma: under applied voltage, all electrode pads on a substrate will be biased even though current is measured only from one pad. To remedy this problem, we can isolate the BNC shielding between the 6487 and the

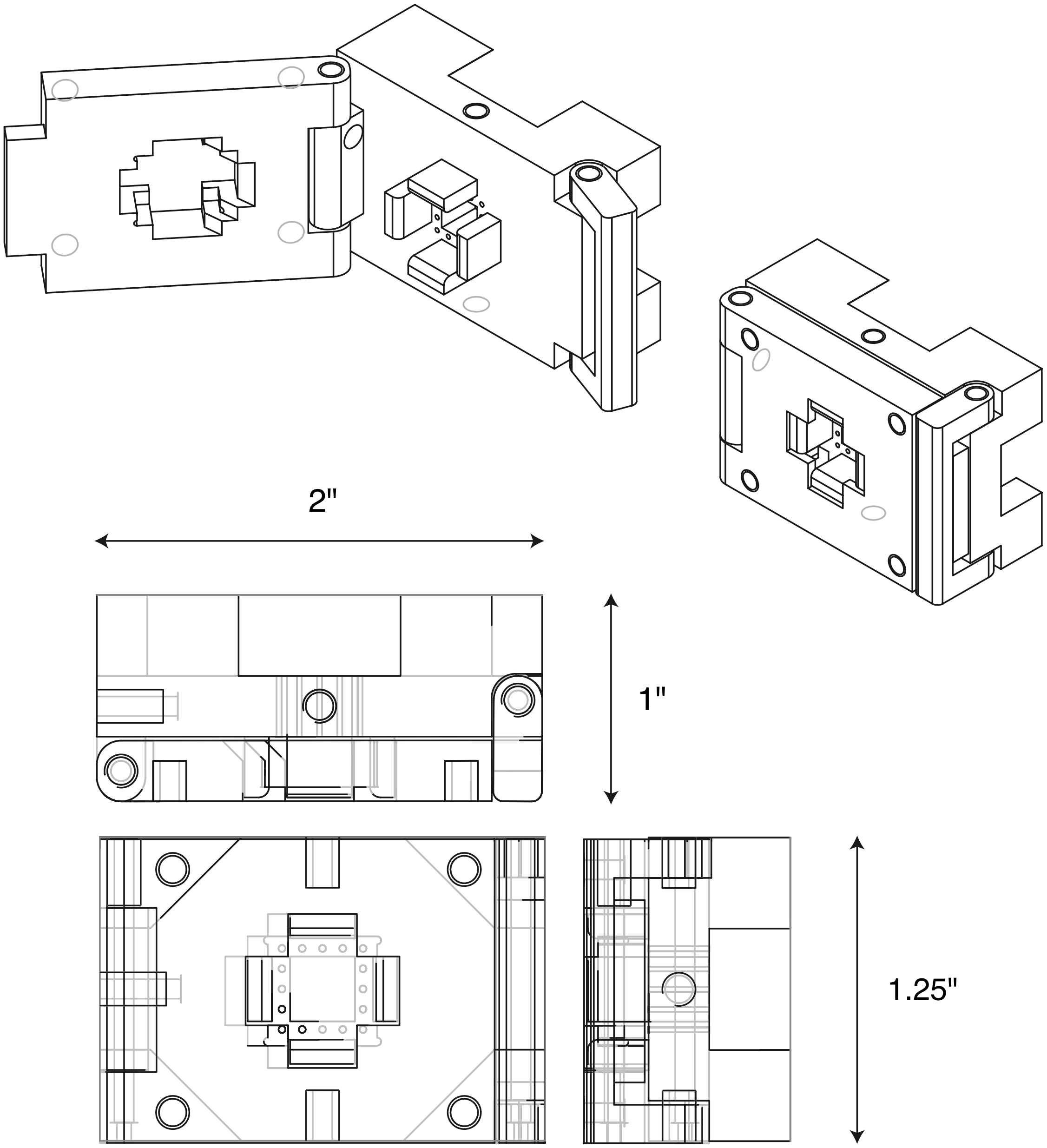

Figure 4-6: Drawings of the probe fixture used to test photodetectors on half-inch substrates.

7000. However, this causes a sizable amount of hysteresis due to the large amount of floating BNC shielding (the BNC cables are 2 meters long). Therefore, we use both configurations depending on the testing situation.

When testing devices such as solar cells that produce a short circuit current, it is not advisable to hook up the sense side of the Keithley 6487 to the common ITO pad of the device. This will result in a measurement of the current from all ten pads regardless of the switch box state.

4.3.4 Current-voltage characteristics under illumination

For i-v measurements in dark and under illumination, we have built a custom LabView interface for the Keithley 6487, which is connected to the device as described above. The light source is a green LED light engine from Lighting Science Group Corp. (formerly Lamina) (`http://www.laminaceramics.com/`, powered by a Keithley 2400 at a drive current of 2 Amperes, unless stated otherwise. The LED is an 0.75” × 1” array that is placed directly on top of the probe fixture and evenly illuminates all pads on the 0.5” substrate. Spectra for the light engine at various drive currents are measured with an Ocean Optics spectrometer and are plotted in Figure 4-8. The spectral peak at a drive current of 2 A is $\lambda = 521$ nm, which corresponds to $E_\nu = 2.38$ eV.

The intensity of the LED is difficult to measure because the emission is not collimated and the proximity of the LED to the test sample does not allow for the insertion of a reference photodiode. Furthermore, our reference photodiodes (Newport 818-UV or Thorlabs FDS100) begin to saturate at intensities near the intensity of the LED at 2 A. Our most reliable calibration method is the following

1. Obtain a QD device with a linear photocurrent response with intensity, measured with a 10 mW green laser (Photonic Products).

2. Measure the photocurrent of the QD device under illumination from the LED at various intensities.

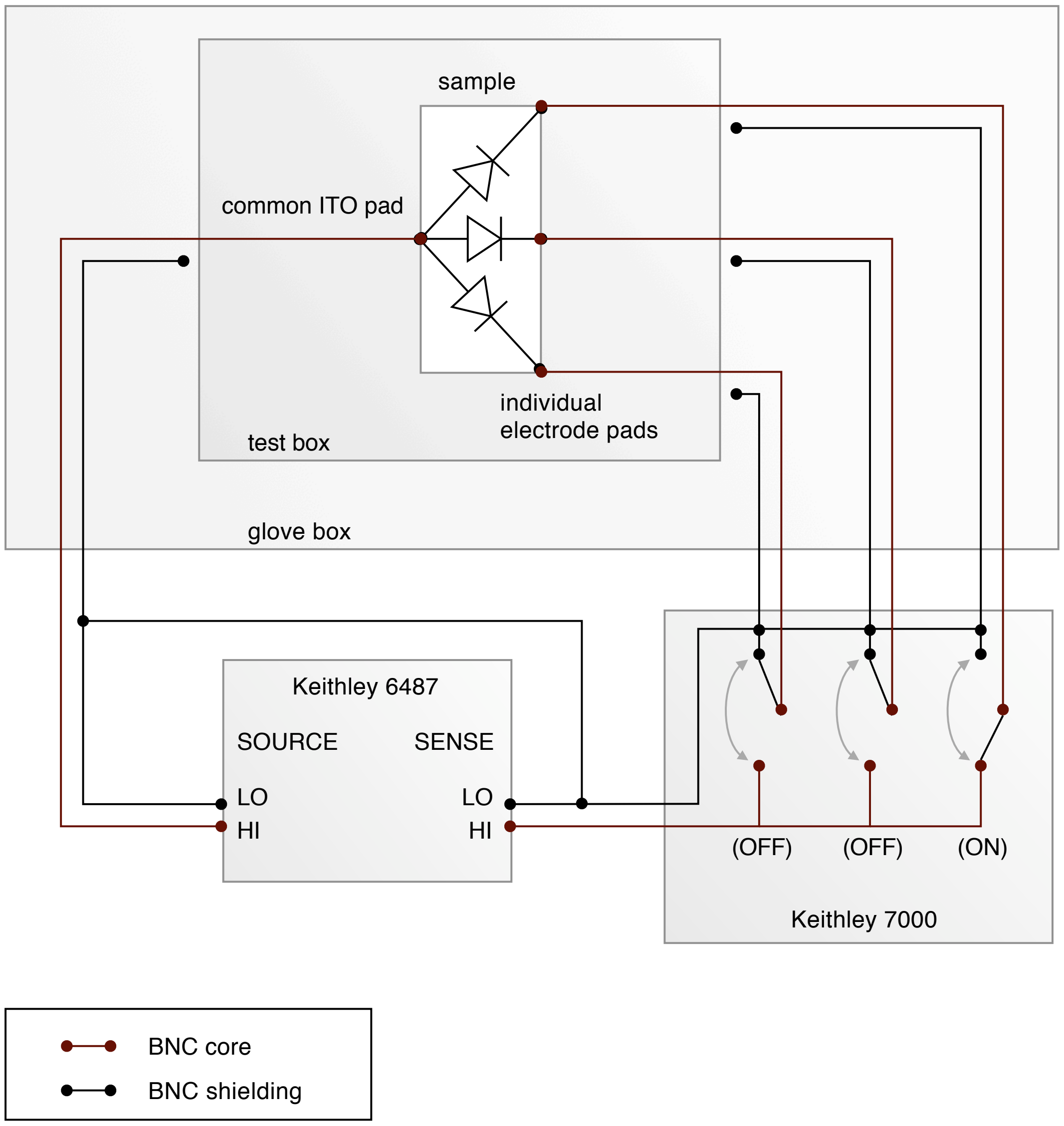

Figure 4-7: Schematic of electrical wiring for i-v measurements and automated switching between pads on a sample located inside our nitrogen-filled testing glove box.

3. Measure the quantum efficiency (QE) of the QD device at a low intensity (see the next section).
4. Calculate the LED intensities by weighing the QD device QE with the shape of the LED emission spectra and scaling the intensity magnitude to match the QE measured at low intensity.

For the green Light Engine LED driven at 2 A, the above procedure results in an intensity value of 50 mW/cm^2, centered at $E_\nu = 2.38$ eV. This intensity is roughly equivalent to the power contained in the visible part of the solar spectrum at one sun.

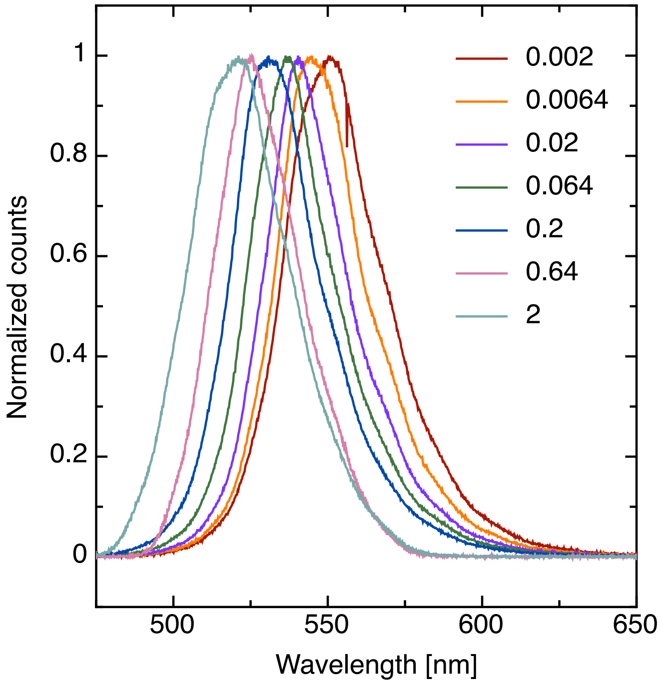

Figure 4-8: Normalized emission spectra at various intensities for the green Light Engine LED used for measuring i-v characteristics under illumination.

4.3.5 Photocurrent spectra

Photocurrent spectra provide two important pieces of information about the operation of a photodetector: wavelength dependence and quantum efficiency. We have built a custom LabView-based program that interfaces with a monochromator and a lock-in amplifier, and coordinates the measurement of photocurrent at wavelengths in the 300 nm to 800 nm range of the electromagnetic spectrum. Quantum efficiency (QE) is obtained by comparing the signal to that of a calibrated reference photodetector.

A narrow wavelength band of light is generated by a white Oriel Instruments Xenon 1 kW arc lamp light source that is chopped by a Stanford Research Systems SR540 Chopper and focused onto an Acton monochromator. The second order diffraction is removed using a series of six low-pass filters with progressively higher cut-off wavelengths. The filter are loaded into a filter wheel that is mounted onto the exit slit of the monochromator. As the monochromator is scanned from lower to higher wavelengths, the filter wheel switches between filters in order to keep the cut-off wavelength greater than 2λ of the first order diffraction. Mounted onto the filter wheel is an optical refocussing assembly that couples light into a fiber optic cable. The fiber optic cable is routed into the glove box and fixed in position above the measurement sample such that the entire substrate is broadly illuminated.

The chopping frequency is output by the chopper to the Stanford Research System SR830 DSP lock-in amplifier's reference channel. The lock-in's circuitry acts as a narrow band filter, measuring only the current from the input signal that is oscillating at the reference frequency. Thus, the lock-in amplifier provides a convenient way to measure photocurrent while excluding electrical noise and stray signal due to the room lights.

Illumination beam spot size: overfill versus underfill

There are two illumination techniques that can be implemented when measuring photocurrent spectra: illuminate the entire device (overfill) or illuminate a small portion of the device (underfill). The benefit of the overfill method is that multiple devices on the substrate can be quickly measured without moving the position of the light source or substrate. The drawback is that the area of the device must be known precisely, otherwise an error in device area will translate into an error in the magnitude of the QE. The benefit of the underfill method is that the illumination spot size is smaller than the device area and therefore the QE is independent of the device area.

The drawback is that it is difficult to align and optimize the position of the incident beam for each electrode pad to be measured. In terms of measurement accuracy, the overfill method has a greater tendency to overestimate the QE because the actual device area may be bigger than the apparent device area, while the underfill method has a greater tendency to underestimate the QE because the illumination beam spot size may extend beyond the actual device area (for devices with small active areas).

For the underfill method, we use a collimating assembly (Princeton Instruments) that focuses light from the fiber optic cable onto a spot size that appears to be less than millimeter in diameter. To test the beam size, we performed the follow experiment:

1. The spot size for our typical photocurrent setup was reduced from a diameter of ~ 0.06 cm to ~ 0.02 cm by increasing the focal distance from the fiber outlet to the first lens from 3" to 4".

2. The spot location was scanned across the substrate and the photocurrent was measured at each location.

3. A camera was set up off angle in order to take an image of the substrate at each location. The distance from the spot to the edge of the device was measured off of the image.

The experiment was performed on a QD device (071120-5-6) and a reference photodetector (ThorLabs FDS-100-CAL). Figure 4-9 shows images of the two device setups.

The photocurrent profile versus spot location, shown in Figure 4-10 does not appear to differ significantly for the QD device or the photodetector. Presumably, the reference photodetector has a sharp edge and the profile we see is due to the broad width of the spot. The photodetector edge appears to be slightly less sharp than the QD device edge. It is not evident why there is an increase in efficiency near the middle of the QD device. The calculated geometrical overlap for two illumination spot radii (assumed to have no blurring) are also shown in Figure 4-10. The apparent spot radius size to the eye is 0.00415 in, while the best approximation of the actual

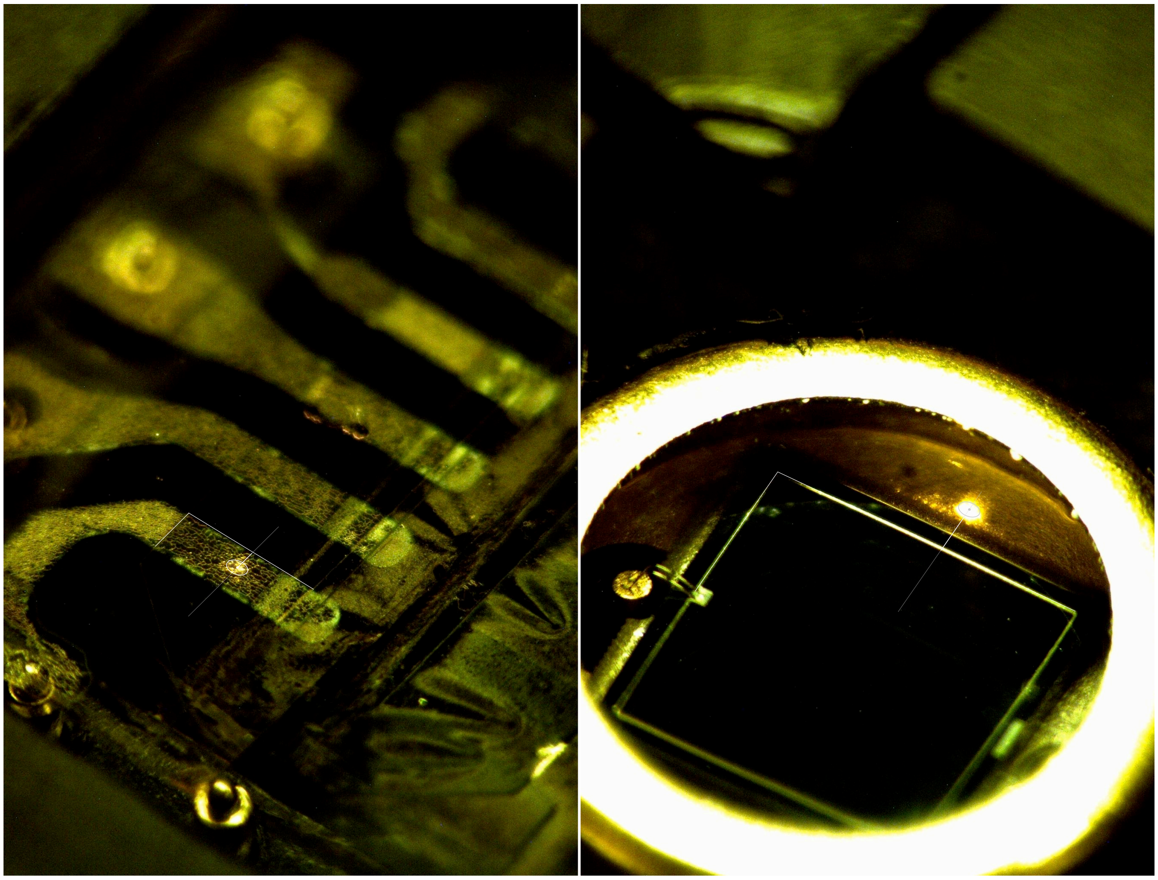

Figure 4-9: QD device substrate with illumination directly on the active pad (left) and ThorLabs detector with illumination reflecting off the side of the casing (right).

spot size is 0.0166 in, four times as large. Note that the long tails of the profile are not captured by the geometrical overlap model because blurring and stray light is not taken into account. These tails are most likely due to stray light and blurring of the actual spot.

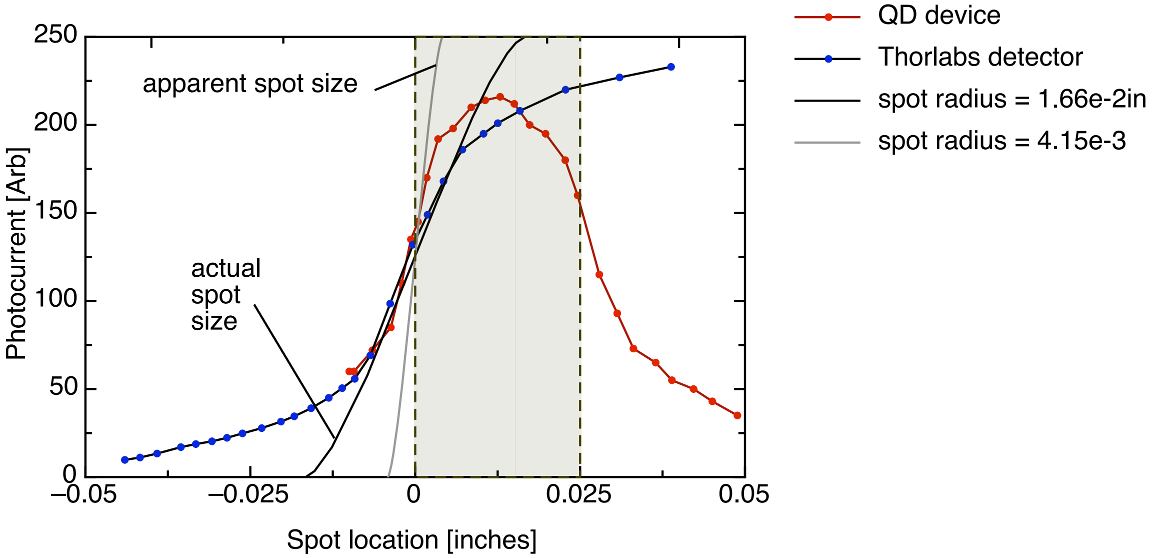

Figure 4-10: Illumination spot location versus distance from top electrode of active device.

To summarize, the spot size is larger than the standard pad size, which will artificially reduce the measured quantum efficiency slightly. In Figure 4-11, we compare QE measurements made with the both the underfill and overfill method. Indeed, the overfill method produces higher efficiencies, although the efficiency at the first absorption peak is similar. Both methods are used for QE throughout the thesis.

4.3.6 Photocurrent-voltage characteristics

At low intensities, weak photocurrent signals can be overwhelmed by the flow of dark current under forward bias. To measure photocurrent signals under applied bias, we measure the photocurrent directly using a lock-in amplifier while applying bias to the device with a Keithley 6487. Illumination is provided by an electrically chopped 10 mW green diode laser (Photonic Products) at $\lambda = 523$ nm. The intensity of

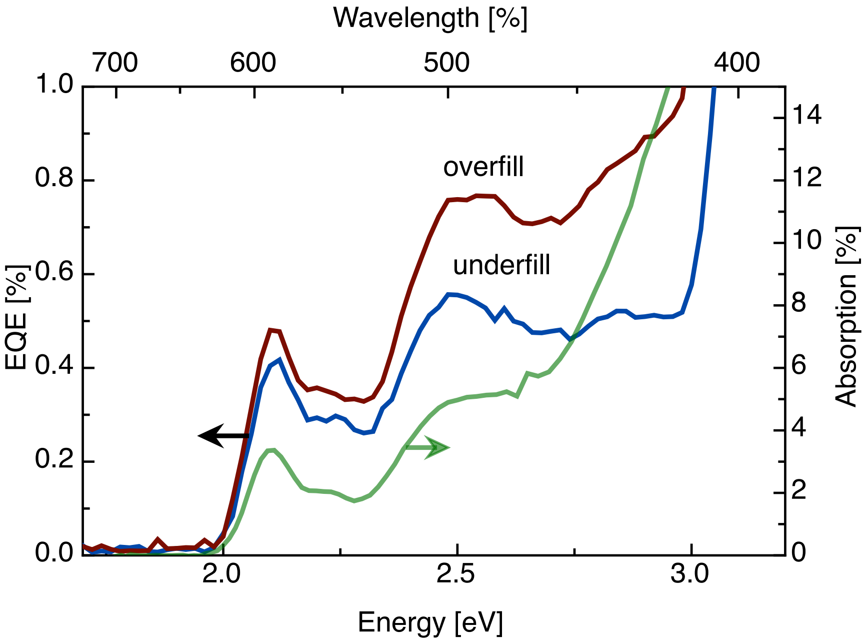

Figure 4-11: EQE measured with overfill and underfill, together with absorption of the whole device stack.

illumination is varied using a Newport circular variable metallic neutral density filter wheel. The experimental setup is shown in Figure 4-12.

The Keithley 6478 is controlled by a LabView routine that applies a voltage to the sample and waits one second for the lock-in to settle and another 0.5 seconds while the lock-in takes a current reading. This process repeats until a full voltage scan is completed. The resulting photocurrent versus voltage characteristics are less sensitive to dark current and other noise than regular i-v measurements.

4.3.7 Photocurrent decay transient measurements

Measuring the time response of a photovoltaic to a pulse of light can be challenging when the photovoltaic response time is fast and the measurement is performed in a glove box. The following criteria must be met in order to ensure the accuracy of the measurement:

- The time response associated with the testing circuit resistances and capacitances must not be slower than the device under test

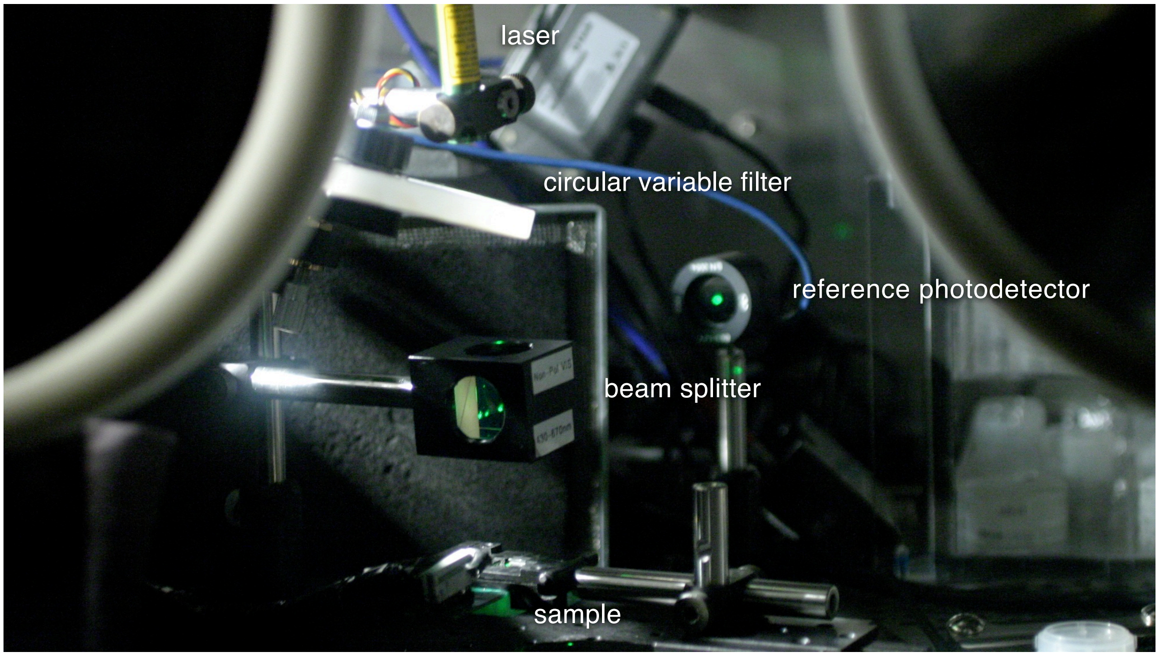

Figure 4-12: Setup for photocurrent-voltage measurements.

- The capacitance of the device under test must not be large enough to dominate the response time
- The light source response time must be faster than the device under test
- Drive electronics for the light source must be faster than the device under test
- The light source must be sufficiently bright to produce a measurable signal
- Signal amplification must be large enough to produce a measurable voltage on the oscilloscope

Figure 4-13 shows the experimental setup used to measure photocurrent decay transients. Illumination from a green LED (Atlas, Lighting Science) is focused onto the sample, which is connected to a 400 Ω load resistor and a DC voltage source (Keithley 6487). A noise filter with R = 1 kΩ and C = 0.1 μF is connected between the DC voltage source and the sample in order to limit noise from the DC voltage source line. Voltage across the load resistor is measured by a differential amplifier

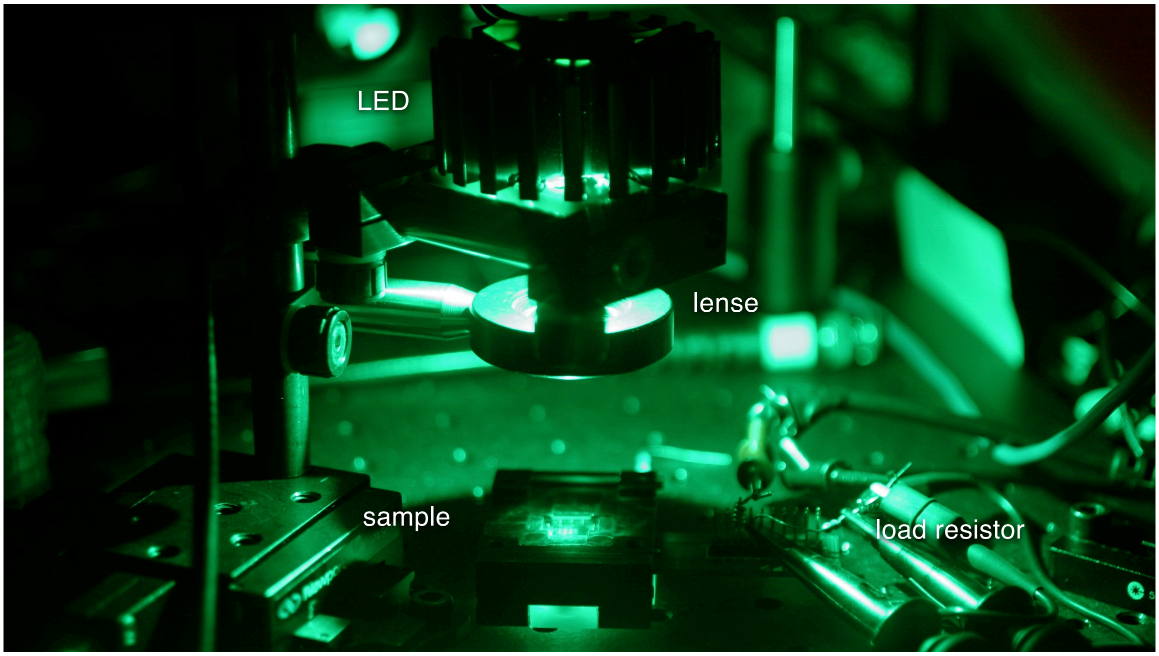

Figure 4-13: Setup for photocurrent decay transient measurements.

(Tektronix ADA400A) and oscilloscope (Tektronix TDS3054C). Voltage to the LED is sourced by a Keithley 2400 and chopped by a power MOSFET driver wired to a function generator (Agilent 33210A).

The circuit diagram in Figure 4-14 was used to simulate the RC time of the setup in order to ensure that the response time of the circuit does not dominate the response time of the measurement. The equivalent circuit of the differential amplifier is drawn to the right of the point at which voltage is measured (labelled Vmeas) and the equivalent circuit of a photovoltaic device is shown to the left of the Vmeas point. The load resistor is labelled R3. The RC time constant of the circuit is predominantly dependent on the capacitance of the diode and the resistance of the load resistor. A capacitance of 400 Ω is chosen as the best compromise between signal intensity and response time.

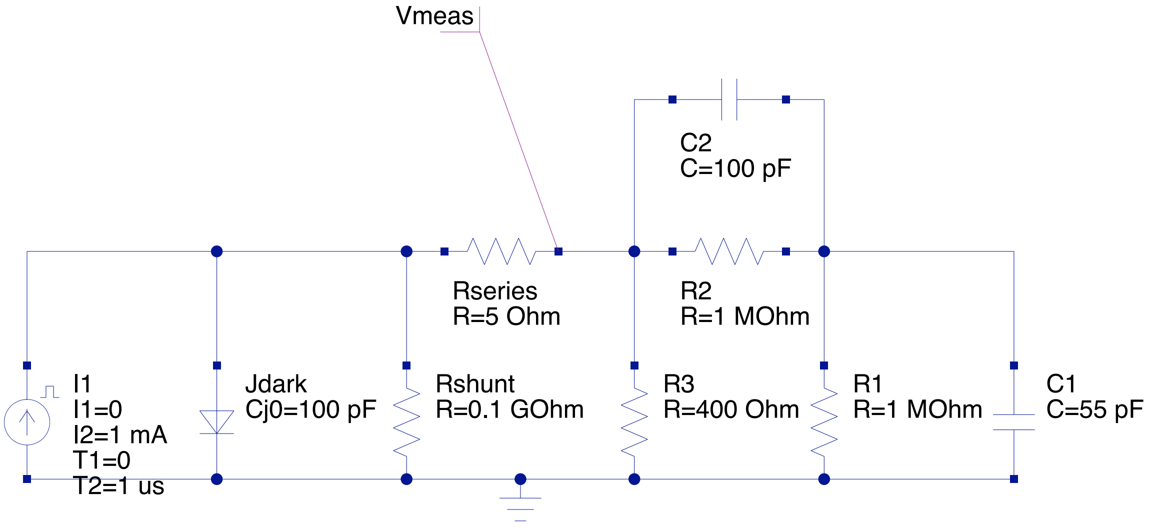

Figure 4-14: Equivalent circuit diagram of a photovoltaic device connected to a load resistor (R3) and a differential amplifier.

We can approximate the capacitance of our device from the formula for a parallel plate capacitor with two dielectric stacks:

$$C = \left(\frac{\epsilon_{r1}\epsilon_{r2}}{\epsilon_{r1} + \epsilon_{r2}} \right) \frac{\epsilon_0 A}{d} \tag{4.1}$$

where ϵ_{r1} and ϵ_{r2} are the relative static permittivities of the two dielectrics, ϵ_0 is the electric constant, A is the area of the device and d is the thickness. For $\epsilon_{r1} = 3$ for organic materials, $\epsilon_{r2} = 6$ for CdSe QDs, $\epsilon_0 = 8.85 \times 10^{-14}$ F cm^{-1}, $A = 0.0121$ cm^2 and $d = 160$ nm, we obtain $C \approx 100$ pF. The simulated decay time constant for a device capacitance of 100 pF and a load resistance of 400 Ω (as shown in Figure 4-14) is ~ 0.2 μs.

To test the fall time of light emitted by the LED, we used a ThorLabs (FDS-100) detector with a quoted response time of 10 ns. The detector gives a decay time constant of 0.1 μs when connected directly to the 50 Ω termination of the oscilloscope and 0.25 μs when connected using the differential amplifier, as in Figure 4-14. The time response limit of our setup appears to be in range of 0.2-0.3 μs.

4.4 Conclusion

The fabrication process of the QD device structure presented in this chapter is noteworthy in three important ways. First, the use of a non-desctructive printing process to deposit the QD layer creates an abrupt, well-defined heterojunction interface between the QD layer and the underlying organic thin film. Second, the use of a transparent top electrode allows for full-transparency below the band-edge of the QDs and is expected to provide enhanced stability compared to low work function metal electrodes often used in donor/acceptor photovoltaics. Third, the fabrication process (after CH 8000 deposition) occurs entirely without exposure to atmosphere, thus minimizing oxygen contamination and experimental variability due to moisture exposure.

The characterization techniques described in this chapter have been implemented nearly from scratch for the purpose of evaluating the devices presented in this thesis. I-v characteristics and QE spectra are standard photovoltaic measurement techniques. However, photocurrent-voltage characteristics are rarely measured in the literature, yet their implementation constitutes a new method to determine the compensation voltage, as we will discuss further in Chapter 6. Measurement of the bias dependence of the photocurrent response time will play important role in understanding recombination dynamics in our QD devices, also discussed in Chapter 6.

Chapter 5

Devices with an incomplete quantum-dot film

The preceding chapter described the fabrication process of a bi-layer photovoltaic device consisting of a planar heterojunction between colloidal cadmium selenide (CdSe) quantum dots (QDs) and a wide band-gap organic hole-transporting thin film of N,N′-bis(3-methylphenyl)-N,N′-bis-(phenyl)-9,9-spiro-bifluorene (spiro-TPD) molecules. This chapter will focus on our initial discovery that working devices with reasonable efficiencies can be achieved even though the active light-absorbing film of printed QDs is shown to be incomplete.

5.1 Introduction

For most of the devices presented in this thesis, the thickness of the QD film is kept as thin as possible. Exciton diffusion lengths are expected be on the order of only a couple of QDs in length (20 - 30 nm) and carrier transport across the QD film has been shown to be limited by the insulating capping groups grafted on the QD exterior [67]. Since the QD absorption coefficient is $\alpha \approx 10^4$ cm^{-1} ($1/\alpha \approx 1$ μm), most of the incident light is transmitted through the 20 - 30 nm thick QD layer. Therefore, high photocurrent densities should not be expected from photovoltaic devices made from these thin layers. Instead, the ratio of the QD photocurrent relative to absorption (which is proportional the internal quantum efficiency (IQE), defined in Chapter 3) is a better metric for evaluating how efficiently charge is generated by the QD film.

In the following discussion, we will demonstrate QD devices with reasonable IQEs of $\sim 10\%$ and external quantum efficiencies (EQE) that follows the absorption profile of the QDs. In addition, we obtain two surprising results: (1) the QD device produces a photovoltaic effect despite voids in the QD layer and (2) the open-circuit voltage (V_{OC}) of 0.8 to 1.3 V is exceptionally large for an architecture with symmetric electrodes. To further investigate the origin of the high V_{OC}, we examine the impact of the printing process on the hole-transport layer (HTL) and construct comparison devices with differing electrodes and molecular absorbing or charge transporting layers. With the evidence presented in this chapter, an argument can be made that both the presence of QDs and the nature of the interface between the QDs and adjacent transport and contact layers are responsible for the observed V_{OC}.

5.2 Morphology of printed QD layer

As discussed in detail in Chapter 4, the device structure (shown in Figure 5-1(a)) consists of the following sequence of films and thicknesses: ITO/poly(3,4-ethylenedioxythiophene) poly(styrenesulfonate) (PEDOT:PSS) (100 nm)/TPD (100 nm)/CdSe/ITO (100 nm). PEDOT:PSS (Baytron P VP CH 8000) is spin cast onto a 0.5 x 0.5 in^2 glass substrate with pre-patterned indium-tin-oxide (ITO) electrodes. The QD layer is deposited from solution using the transfer printing method described in Figure 5-1(e). The procedure is the following: (1) the CdSe suspension is spin cast onto a PDMS stamp and allowed to dry, (2) the TPD-coated substrate and stamp are pressed together and (3) the substrate and stamp are separated.

Unfortunately, the quality of the printed QD film is very poor, as can be seen from AFM images of the surface of the QD film printed on top of TPD (Figure 5-1(d)) and optical micrographs of the completed device (Figure 5-2). On the microscopic level, the valley and mesa morphology observed in the AFM images is consistent with cracking due to tensile stress in the plane of the film during the drying process. Note

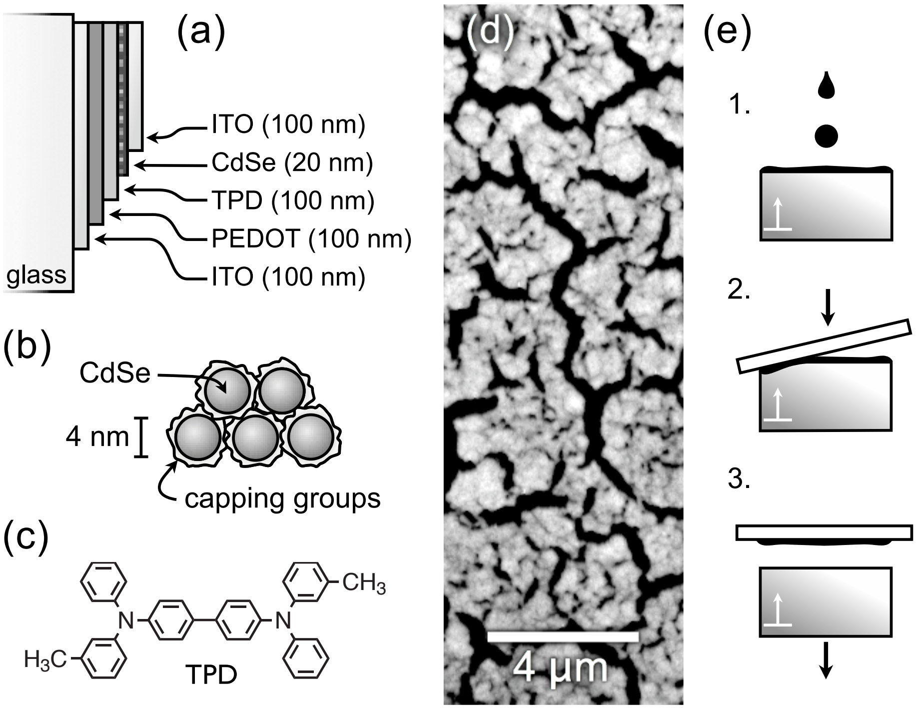

Figure 5-1: Diagram of (a) ITO/PEDOT/TPD/CdSe/ITO device structure, (b) CdSe QDs with organic capping groups and (c) molecular structure of TPD. An AFM image of the printed CdSe film is shown in (d) and a diagram of the steps involved in the printing process is shown in (e).

that the cracked regions are completely void of QDs, leaving the underlying TPD film exposed to the top electrode. To the eye, film defects such as air bubbles, large streaks and particulates are visible, as seen in Figure 5-2. In these optical micrographs, the red coloration of the QD film can be seen around the perimeter of the rectangular pattern of the stamp. In the region where TPD is deposited, light scattered from the QD film and TPD layered stack appears blue. The vertically aligned pads are the top ITO electrodes. The edges of the ITO pads appear brighter, possibly due to thinning effects caused by shadow masking.

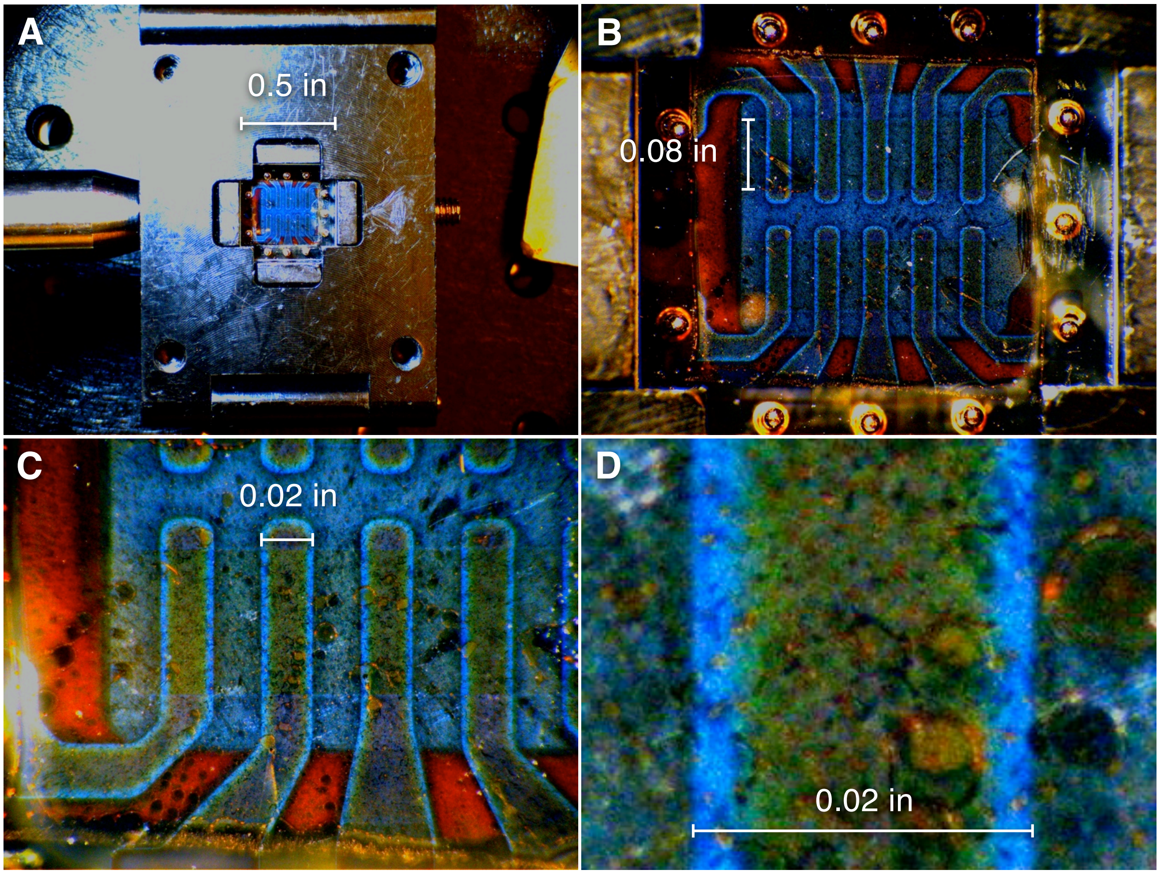

Figure 5-2: Optical micrographs of a sample QD device displaying several types of film defects including voids due to trapped air bubbles, streaking caused by particulates and cracking.

One might think that the images in Figure 5-2 appear to be the result of either aggregates in the QD solution, stray particulates or remnant organics on the surface of the stamp. In reality, care was taken to rinse the surface of the stamps by pre-spinning with chloroform and the QD solution was filtered through a 0.02 μm filter before each deposition. Instead, the observed film morphology is due to the incompatibility between the surface energy of chloroform and that of PDMS. This mismatch in surface energy prevents wetting of the stamp by the chloroform, which results in patchy regions where either no QDs are deposited or excess QDs are built-up and allowed to aggregate.

On the micrometer scale, varying the concentration of QDs in chloroform produces little change in surface morphology, provided the concentration is above a critical value, as shown in Figure 5-3. At a dilution of 500 μl added to a stock solution of QDs, small micron-sized islands of QD form on the surface. However, dilutions ranging from 250 μl to zero dilution result in nearly identical morphologies. A difference in step height of the QD features does occur, ranging from 20 - 40 nm, but isn't well correlated with the concentration of the QD solution. It should be noted that these microscopic images do not fully capture the macroscopic QD film quality (the thickness uniformity and voids over large lengths scales) which may in fact dominate device performance. Despite the apparent poor quality of the QD film, photovoltaic devices have been successfully fabricated from theses films and will be discussed below.

5.3 Devices with varying size QDs

Amazingly, the partial coverage and rough morphology of the QD film does not appear to compromise the film's ability to photogenerate charge, despite the fact that incomplete films in photovoltaic devices are typically rendered useless by parasitic shunting. Below, we demonstrate both working QD photovoltaic devices and the ability to change the onset wavelength of absorption and photocurrent generation by using QDs of varying size.

The *EQE* at zero bias is plotted in 5-4, along with the device absorption for QDs with diameters of 4 nm, 5 nm, and 8 nm, corresponding to first transition

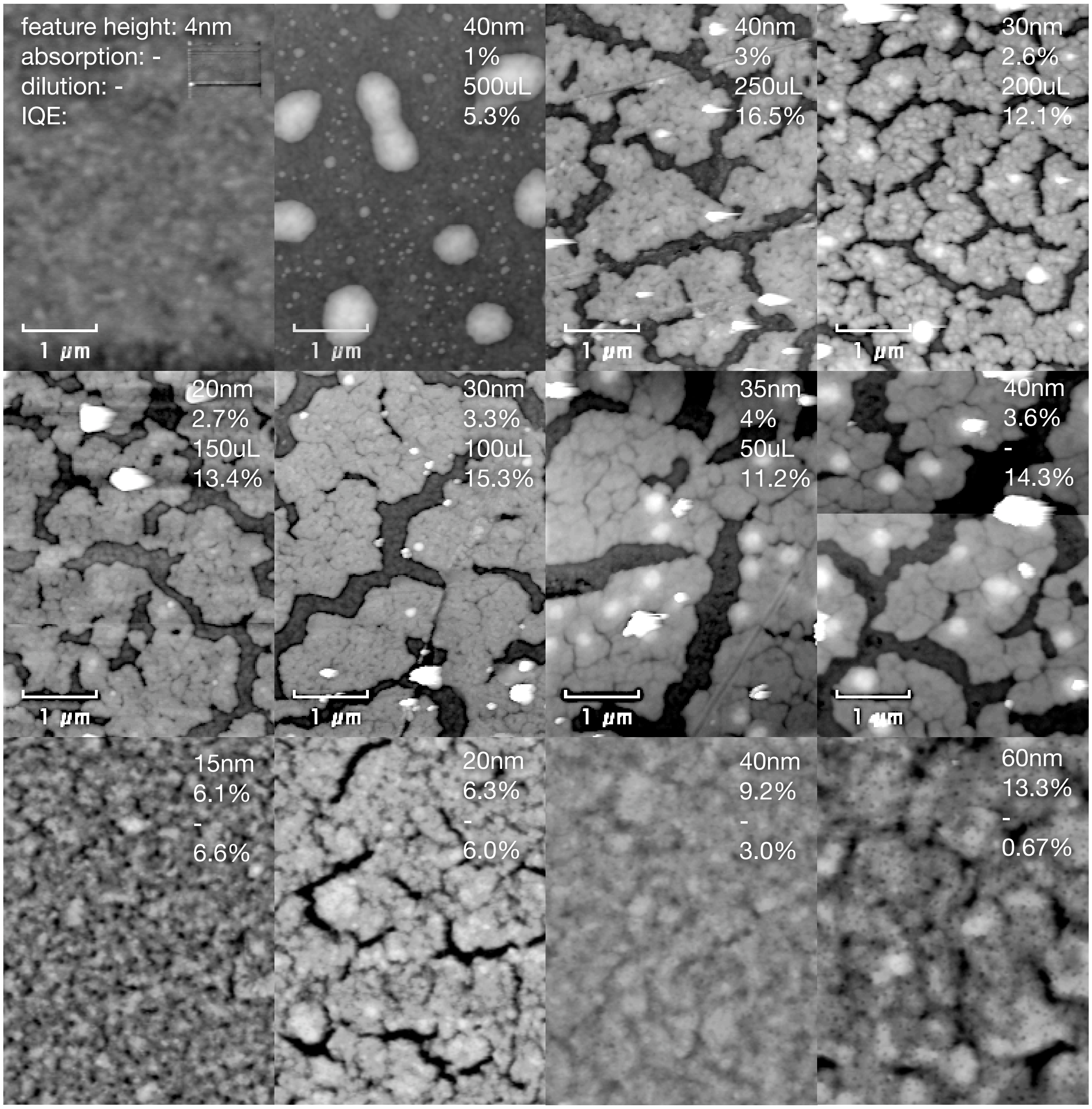

Figure 5-3: AFM images of the surface of QD films deposited on TPD. The top left image is the surface of bare TPD. The QD feature height, QD absorption, dilution of the solution used for deposition, and IQE are labelled for each micrograph.

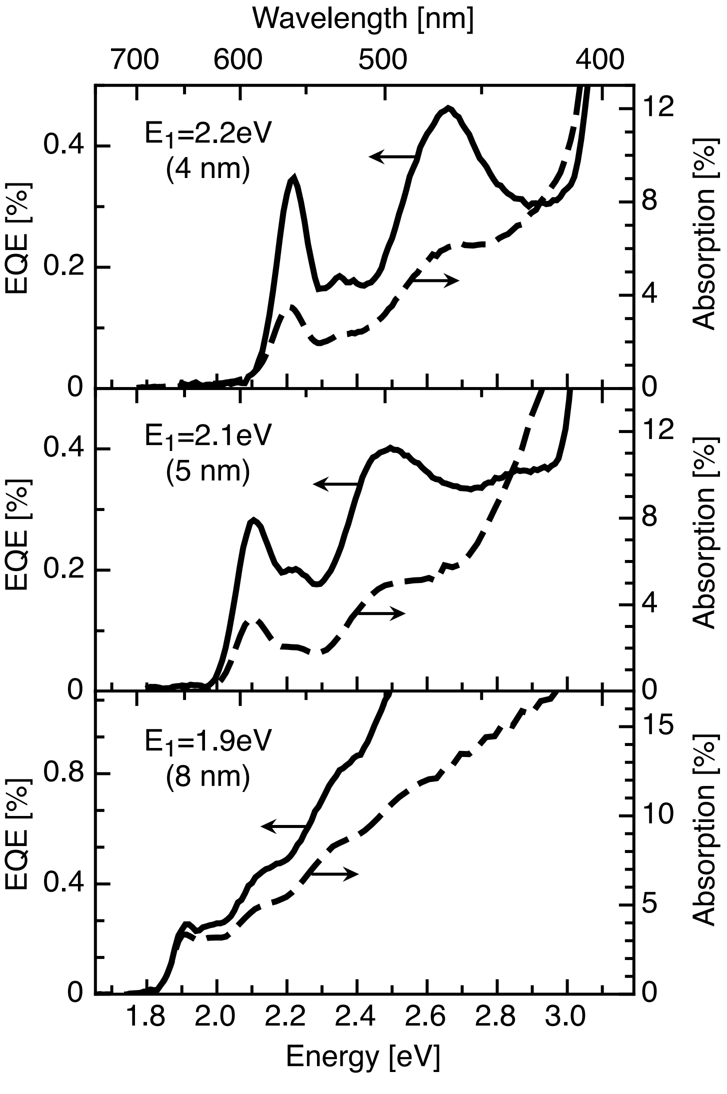

Figure 5-4: Quantum efficiency versus incident photon energy (solid line) and absorption spectra (dotted line) for ITO/PEDOT/TPD/CdSe/ITO devices with QD diameters of 4 nm, 5 nm and 8 nm.

energies (E_1) of 2.2 eV, 2.1 eV and 1.9 eV, respectively. The photocurrent spectrum follows the QD absorption profile below 3 eV, yet is dominated by TPD absorption and photoresponse above 3 eV. The magnitude of the quantum efficiency at the first absorption peak of the QDs is low (∼0.3%), in part due to limited light absorption (∼3%) in the very thin QD films.

From the transmission and reflection spectra of the completed devices we can extrapolate the IQE to be approximately 9.9% at the first absorption peak for the device with E_1=2.2 eV, 8.4% for the device with E_1=2.1 eV and 7.6% for the device with E_1=1.9 eV. The observed decrease in IQE with band-gap may be due to a decrease in electron transfer efficiency at the QD/ITO interface. The energy offset between the electron affinity of the QDs and the work function of ITO is approximately 0.2 eV, 0.1 eV and -0.1eV for E_1=2.2 eV, E_1=2.1 eV and E_1=1.9 eV, respectively. However, we note that none of the devices have been optimized and therefore may not reflect the true trend with band-gap.

5.4 Thickness dependence of QD layer

In Section 5.2, we found that the micron-scale morphology of printed QD films is not strongly affected by the concentration of QDs in solution used for deposition. However, devices made from these same films differ significantly in the amount of light absorbed. Furthermore, a sharp peak in EQE for a QD film absorption of 3 - 4% is observed, along with a monotonic fall-off in efficiency as the QD absorption increases, as shown in Figure 5-5. Both EQE and IQE are measured at the peak absorption peak on the QDs (in this case, E_1 = 2.2 eV). The nominal thickness is determined by (1) measuring the absorption spectrum of a completed QD device (2) extracting the magnitude of QD absorption at E_1 and (3) calculating the nominal thickness using Beer's law and a (previously determined) absorption coefficient of $\alpha = 10^4$ cm^{-1}. The nominal thickness is not an accurate reflection of the actual step height of the QD features, but simply an indication of the amount of QD loading in the sample.

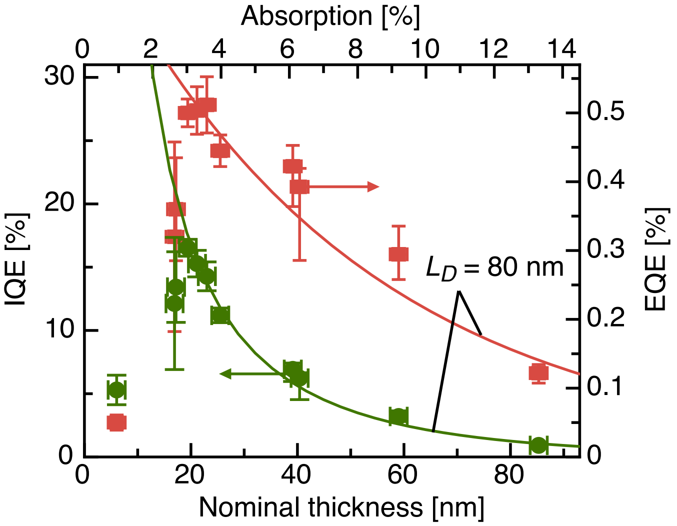

Figure 5-5: External quantum efficiency (EQE) (red squares, right axis) and internal quantum efficiency (IQE) (green circles, left axis) for printed QD photovoltaic devices with varying nominal QD layer thicknesses.

For QD layer thicknesses greater than the charge diffusion length, we expect the charge collection efficiency to fall off exponentially. Assuming charge diffusion is the dominant collection mechanism, a solution to the continuity equation yields an exponentially decreasing carrier concentration with distance away from the charge generating interface (see Section 3.3.5). In Figure 5-5, we fit the EQE for thicknesses greater than 20 nm to an exponential and obtained a diffusion length of $\sim$ 80 nm. However, the fit is not perfect and the decrease in EQE could be fit equally well to a linear decrease. A number of complicating factors confound our analysis of the data in Figure 5-5. For example, data points for thickness greater than 40 nm are obtained from a different device run, which introduces the possibility of a systematic offset in efficiency between the two data sets. In addition, the quoted nominal thickness does not necessarily indicate the length that charge must travel in order to reach an electrode, given the inhomogeneous morphology of the QD film.

5.5 Tolerance to voids in the QD film

The current-voltage characteristics for both ITO/PEDOT/TPD/QD/ITO and a control device without QDs (ITO/PEDOT/TPD/ITO), shown in 5-6, help to explain why voids in the QD film do not interrupt photocurrent generation. Under forward bias, current flow in the dark (J_{dark}, drawn in black) is due to electron injection at the ITO electrode, hole injection at the PEDOT electrode and charge recombination at the junction interface. Under illumination, photocurrent flow (J_{photo}, drawn in grey) occurs by absorption and charge excitation in the QDs, followed by hole transfer to TPD, electron transfer to the ITO electrode and hole migration toward the PEDOT electrode. In the absence of additional current pathways, J_{dark} and J_{photo} must be equal and opposite at V_{OC}. No light response at 532 nm is observed for the device structure which does not contain QDs.

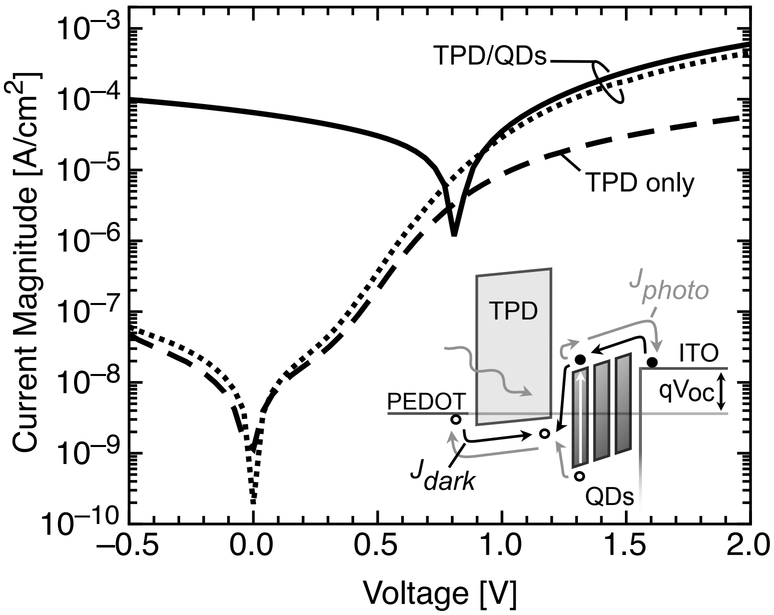

Figure 5-6: Semi-logarithmic plot of the i-v characteristics in the dark (dotted line) and under illumination at wavelength $\lambda = 532$ nm, 50 mW/cm^2 (solid line) for ITO/PEDOT/TPD/QD/ITO (QD diameter of 4 nm) and i-v characteristics for ITO/PEDOT/TPD/ITO (dashed line) in the dark. The inset schematic illustrates the two most prominent current flow pathways at a bias point of V_{OC}, dark current (J_{dark}) and photocurrent (J_{photo}).

In the control structure without QDs, hole injection in forward bias at the PEDOT electrode can support higher current densities than hole injection in reverse bias at the top ITO electrode. With the addition of the QD layer, the forward bias current increases, which can be attributed to a new conduction pathway: electron injection from ITO to the QDs and recombination with holes across the heterojunction interface (see inset, 5-6). Under illumination, charge generated in the QD film contributes to photocurrent (J_{photo}) in both reverse bias and forward bias, as expected based on the favorable alignment of the energy bands. However, one would expect the presence of voids in the QD film to disrupt charge generation because a parasitic recombination pathway should be available for photo-excited holes to transfer from the QDs to the TPD and back to the top ITO electrode, resulting in a loss of photogenerated charge. The relative insignificance of this recombination pathway implies that coupling between holes in the TPD and conducting states in the ITO is inefficient. This result is consistent with the observation of a hole-blocking contact between the ITO and TPD by Shen et al. [97].

5.6 Observation of exceptionally large V_{OC}

The V_{OC} of 0.8 V is significantly higher than expected considering the small work function difference of 0.4 eV between the PEDOT (5.2 eV) and ITO (4.8 eV) electrodes or the energy offset between the electron affinity of the QDs (4.6 eV) and the ionization potential of TPD (5.4 eV), which amounts to an offset of 0.8 eV. Neither a Schottky device model, where the maximum V_{OC} is determined by the difference between electrode work functions [19, 98], nor a donor/acceptor model, where the maximum V_{OC} is determined by the difference between the electron affinity of the acceptor and the ionization potential of the donor [99], can fully account for the observed V_{OC}. Furthermore, it is unlikely that the V_{OC} of 0.8 V is fully saturated given the low photocurrent densities obtained at short circuit.

The high V_{OC} can be ascribed to two factors: low J_{dark} due to the rectifying TPD/ITO heterojunction, and diffusion of photo-excited carriers away from the heterojunction interface [93, 94]. However, a large diffusion current requires a build-up of space charge at the heterojunction interface, which can only be accomplished if rates of recombination are much lower than rates of charge extraction. In our structure, hole transfer at the QD/TPD heterojunction and electron transfer at the QD/ITO heterojunction increase charge build-up (and add to J_{photo}), while recombination at these interfaces decreases charge build-up (and reduces J_{photo}). Therefore, the large V_{OC} must be associated with reduced interfacial recombination relative to rates of charge extraction [100].

The physical mechanism responsible for the favorable balance of charge extraction and recombination rates could be the presence of insulating organic capping groups on the QDs, which serve to passivate the QD surface and suppress parasitic recombination processes. In particular, the spatial separation between electrons and holes confined at the TPD/QD or QD/ITO interface reduces the wavefunction overlap between opposite charge across the heterojunction, resulting in less interfacial recombination, higher carrier concentrations, higher J_{photo} and higher V_{OC}.

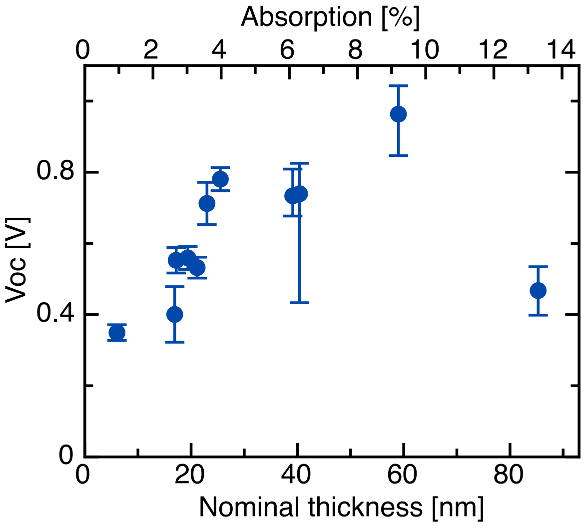

Figure 5-7: Open-circuit voltage (V_{OC}) as a function of the QD absorption and nominal film thickness.

Measurement of the V_{OC} obtained for devices made from QD films deposited from QD solutions of varying concentrations demonstrates that the magnitude of V_{OC} is not inherent to the device structure (Figure 5-7). Instead, V_{OC} remains constant at ~ 0.8 V over a narrow range of thicknesses from 25 - 40 nm and an anomalous data point at 60 nm reaches a 1 V. For QD films with nominal thicknesses below 25 nm, it is possible that the decrease in V_{OC} is due to insufficient surface coverage, allowing voltage to be compromised by the presence of voids, which do not produce voltage. Even though voids in the QD film do not completely shunt the photocurrent at the heterojunction, they may affect the relative rates of recombination or extraction. It is interesting to note that the surface of the QD film corresponding to the device with V_{OC} of 1 V is the only device with a QD film that is more or less free of major cracks and non-uniformities. In the next chapter, we will explore the effect of surface coverage on V_{OC}.

5.7 Thickness dependence of the hole-transport layer

In order to understand the role of the hole-transport layer (HTL) in our device structure, we build a series of devices with different HTL thicknesses ranging from 11 to 103 nm and measure the following properties:

- The current in dark at -0.5 V (J_{dark}) (indicates the level of leakage current)
- The current in light at 0 V (J_{light}) (indicates the efficiency of charge generation)
- V_{OC}
- The compensation voltage (V_0) (indicates the maximum obtainable V_{OC})
- The slope of the normalized light current near 0 V (V_{shunt}) (indicates the magnitude of shunting relative to J_{light})

In Figure 5-8, the i-v characteristics of a device with a spiro-TPD thickness of 80 nm is shown, along with the points on the plot where V_{OC}, V_0 and V_{shunt} are extracted. V_0 is obtained by subtracting J_{dark} from J_{light} and determining the intersection point with the voltage axis. V_{shunt} is obtained by fitting the slope of J_{light} around $V = 0$ and determining the intersection point with the voltage axis. We can also extract

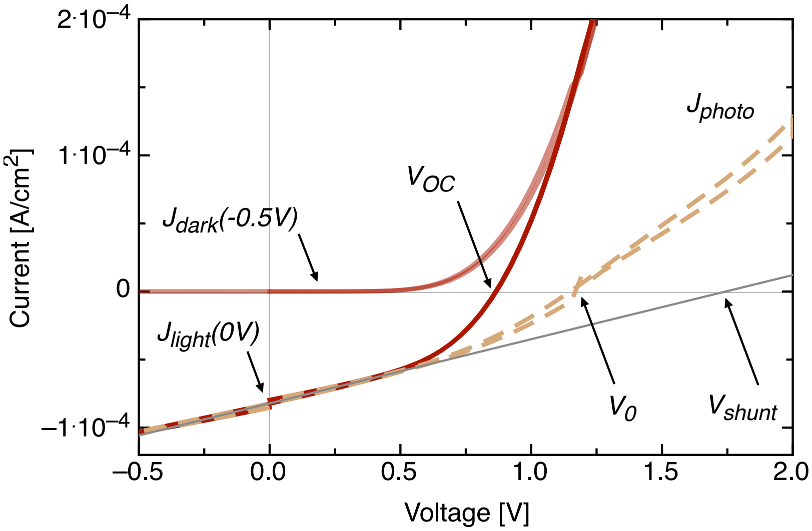

Figure 5-8: I-v characteristics in dark (J_{dark}), in light (J_{light}) and the photocurrent ($J_{photo} = J_{light} - J_{dark}$) for a QD device with a spiro-TPD thickness of 80 nm.

J_{dark} at a bias of -0.5 V as a way of evaluating the magnitude of parasitic leakage currents and J_{light} at a bias of 0 V, which is proportional to the EQE.

In Figure 5-9A, J_{dark} is given as a function of spiro-TPD thickness for devices with and without a QD film (see Figure 4-1 for device structures). We observe behavior that is consistent with damage of the underlying spiro-TPD film during QD deposition. In reverse bias, J_{dark} should be low for a properly functioning diode, as electron injection into spiro-TPD is blocked at the PEDOT:PSS electrode and hole injection into the QDs is blocked at the top ITO electrode. The control device without QDs shows low leakage for all thicknesses except for the thinnest film. However, once QDs are deposited on top of the spiro-TPD films, leakage currents increase by nearly three orders of magnitude, up to spiro-TPD thicknesses of 60 nm. For thicknesses greater than 60 nm, the leakage current is identical to that of the control. There are two likely explanations. First, PDMS is known to swell when exposed to organic solvents. During printing, it is possible that remnant solvent is released from the PDMS stamp and left to partially dissolve the spiro-TPD film. Second, Jen Yu has observed that 30 nm can be removed from the surface of a spiro-TPD

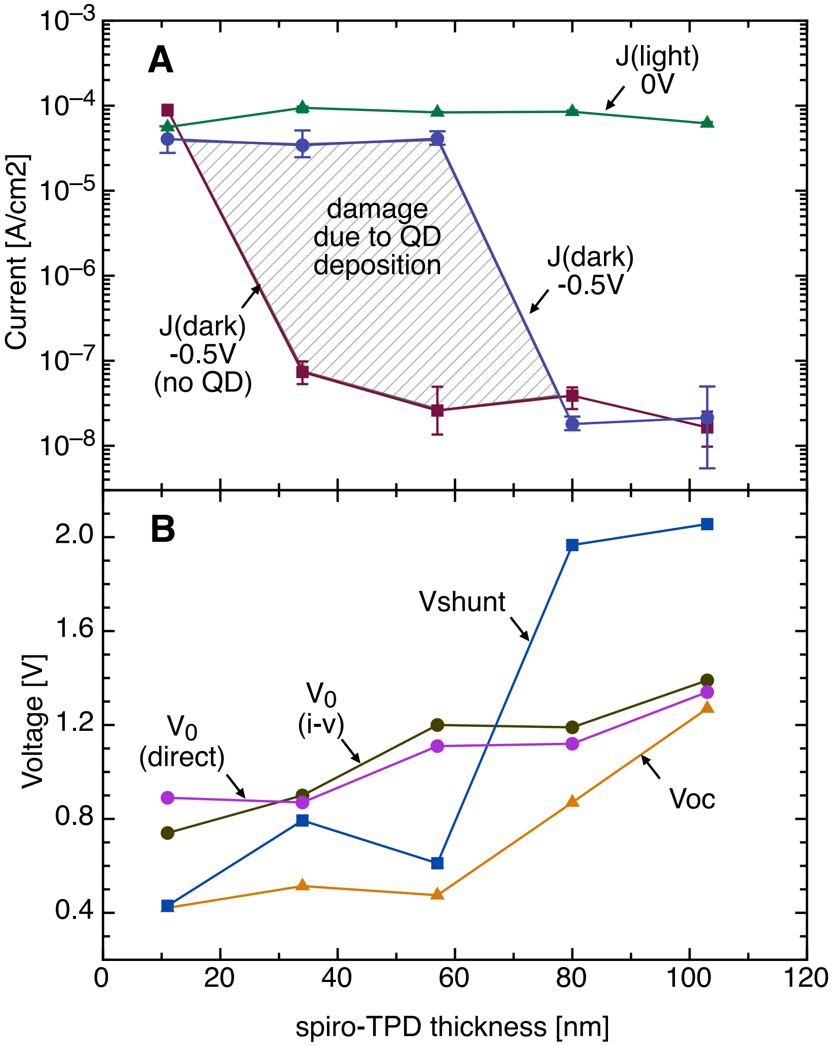

Figure 5-9: Summary of results for devices with varying spiro-TPD thicknesses.

film by contacting and releasing with a PDMS stamp. At voids in the QD film, the PDMS stamp may be able to contact the spiro-TPD, remove portions of the film and subsequently cause leakage through these thinned regions in the spiro-TPD.

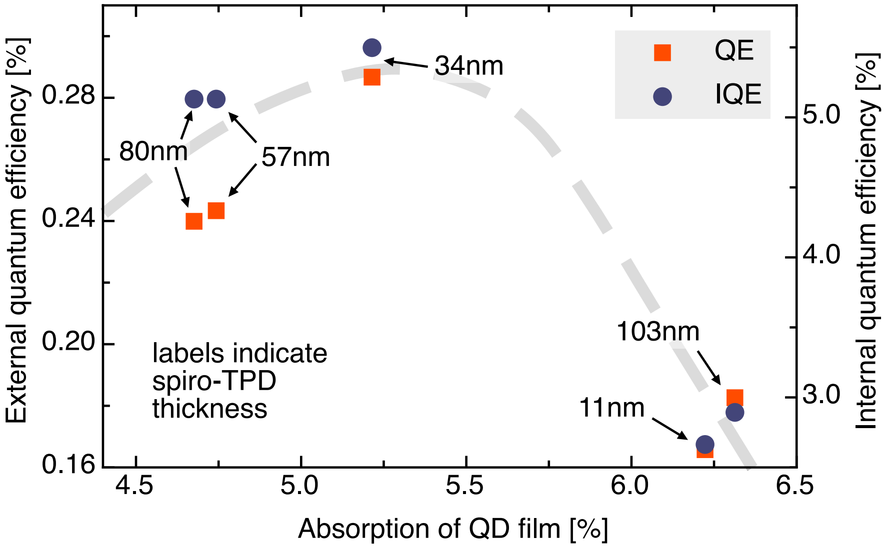

Figure 5-10: Effect of spiro-TPD thickness on the external and internal quantum efficiency, measured at $E_1 = 2.1$ eV.

Measurements of the short-circuit current under illumination (J_{light}) for devices with QD layers demonstrate that changing the spiro-TPD thickness does not affect the photocurrent efficiency. On first inspection, it appears as if J_{light} is reduced for samples with either the thinnest or thickest spiro-TPD film. However, plotting the EQE and IQE versus QD absorption (Figure 5-10) illustrates that the origin of lower efficiency is instead due to unintended variation in the thickness of the QD films. Both the EQE and IQE follow a consistent trend with thickness (similar to that in Figure 5-5) with the 11 and 103 nm spiro-TPD devices having reduced efficiency due to the increased thickness of their respective QD layers.

Eliminating leakage currents appears to be a critical factor in obtaining high V_{OC} and non-shunted devices, as seen in Figure 5-9B. Once the spiro-TPD is made sufficiently thick to avoid film damage and high leakage, both the shunt resistance and V_{OC} increase. The V_{OC} for the device with the thickest spiro-TPD film (103 nm) is now 1.3 V. It is important to note that the resistance of the spiro-TPD layer increases with thickness, but this increase in resistance cannot explain the increase in V_{OC}. From our discussion of the circuit model of the ideal diode in Section 3.6.2, we know that changing the magnitude of the series resistance does not affect V_{OC}.

If reducing leakage currents is so critical to obtaining high V_{OC}, the question remains: can we simply continue to increase the spiro-TPD thickness and obtain increasingly large V_{OC}? To answer this, we can look at the effect of spiro-TPD thickness on the compensation voltage V_0 (the voltage at which the photocurrent goes to zero). V_0 represents the maximum V_{OC} attainable if (1) the dark current is somehow fully suppressed or (2) the illumination intensity is made infinitely bright. We measure V_0 directly (by measuring the photocurrent versus bias with a lock-in) or from the i-v characteristics (by finding the bias point where $J_{light}=J_{dark}$). From Figure 5-9B, it can be seen that V_{OC} approaches V_0 with increasing spiro-TPD thickness. However, at 103 nm, V_{OC} is nearly equal to V_0, and presumably will remain so for even thicker films. In the next chapter, we will investigate V_0 in more detail and explore ways to further increase V_0 and V_{OC}.

5.8 Alternative device structures

Our QD device architecture differs significantly from other popular donor/acceptor photovoltaic structures in the literature. For the first time, we have (1) fabricated a device that employs QDs as the primary absorbing species in a heterojunction configuration and (2) have employed a transparent top ITO electrode. In addition, our use of a transparent HTL is uncommon. In order to understand the origin of high V_{OC}, we have constructed a series of devices which attempt to isolate the particular material or interface that is responsible for the increase in V_{OC}. The following four sets of devices are investigated:

- The electron transport layers (ETLs) 1,4,5,8-naphthalenetetracarboxylic dianhydride (NTCDA) or perylene-3,4,9,10-tetracarboxylic dianhydride (PTCDA) are inserted at the QD/ITO heterojunction in order to evaluate the role of the

QD/ITO heterojunction.

- The top ITO electrode is replaced by silver (Ag) or bathocuproine (BCP)/Ag in order to determine if ITO itself is critical to high V_{OC}
- The QD layer is replaced by bisbenzimidazo[2,1-a:2′,1′-a′]anthra[2,1,9-def:6,5,10-d′e′f′]diisoquinoline-10,21-dione (PTCBI) as an alternative absorbing species in order to determine if the QDs are necessary for high V_{OC}.
- Spiro-TPD is replaced by the more commonly used copper(II) phthalocyanine (CuPc) in order to asses the importance of the HTL.

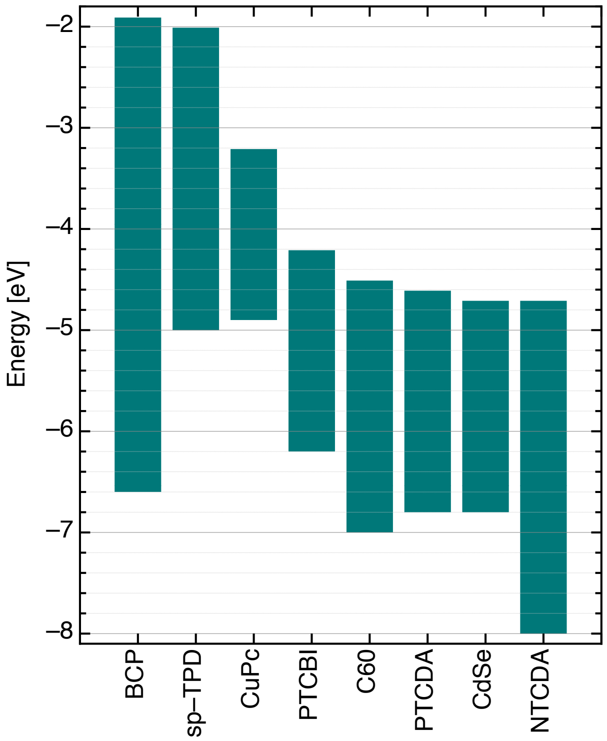

Figure 5-11: Energy levels for the organic molecular semiconductors used to investigate alternative device structures.

In Figure 5-11, we plot the energy levels of the alternative organic molecular semiconductors used in this study. In Table 5.1, we list the complete device structures and their measured compensation voltage V_0 and short-circuit current J_{SC}. In Figure

Table 5.1: Summary of device structures, compensation voltages V_0 and short-circuit currents J_{SC}. Illumination is at an intensity of 50mW/cm^2 and $\lambda = 521$ nm.

Device structure	V_0 **[V]**	J_{sc} **[mA/cm^2]**
ITO top electrode with and without ETL		
ITO/PEDOT:PSS/spiro-TPD/QD/ITO	1.20	6.0e-2
ITO/PEDOT:PSS/spiro-TPD/QD/NTCDA/ITO	0.55	2.5e-2
ITO/PEDOT:PSS/spiro-TPD/QD/PTCDA/ITO	0.90	3.0e-2
Ag electrode with and without ETL		
ITO/PEDOT:PSS/spiro-TPD/QD/NTCDA/Ag	0.40	2.5e-2
ITO/PEDOT:PSS/spiro-TPD/QD/BCP/Ag	1.35	7.0e-4
ITO/PEDOT:PSS/spiro-TPD/QD/PTCDA/Ag	0.50	1.0e-1
ITO/PEDOT:PSS/spiro-TPD/QD/Ag	0.80	2.0e-2
PTCBI as absorbing layer		
ITO/PEDOT:PSS/spiro-TPD/PTCBI/Ag	0.80	5.0e-1
ITO/PEDOT:PSS/spiro-TPD/PTCBI/QD/Ag	0.80	4.0e-1
ITO/PEDOT:PSS/spiro-TPD/PTCBI/QD/ITO	0.80	1.2e-1
ITO/PEDOT:PSS/spiro-TPD/PTCBI/ITO	0.65	2.0e-2
CuPc as HTL		
ITO/PEDOT:PSS/CuPc/C60/BCP/Ag	0.70	2.8e+0
ITO/PEDOT:PSS/CuPc/QD/BCP/Ag	0.48	2.4e-2

5-12, we plot the values of J_{SC} versus V_0 for each structure. We attempt to keep the QD thickness in the 40 nm range. The thickness of the NTCDA and PTCDA ETLs, and BCP is 10 nm. The thickness of the PTCBI absorbing layer is 20 nm. The thickness of CuPc and C60 is 40 nm.

We find that the inclusion of an organic small molecule as HTL, absorber or ETL invariably results in the reduction of V_0. The only device modification that retains the original V_0 is the use of a BCP/Ag electrode as a replacement for ITO. These results imply that the use of any organic molecular semiconductor is incompatible with high V_0, unless the molecular semiconductor has a wide bandgap. PTCDA, PTCBI and CuPc have bandgaps of 2.2, 2 and 1.7 eV, respectively, while spiro-TPD and BCP have bandgaps of 3 and 4.7 eV, respectively (NTCDA is an exception, with a bandgap of 3.3 eV, although this material is extremely conductive and may be adding dopants to the device). When PTCBI is used as an absorbing layer in a device with the same device architecture as our QD structure, V_0 is still significantly reduced. This reduction occurs even though the energy levels and bandgap of PTCBI are similar to those of CdSe QDs. Finally, the inclusion of a QD layer into a standard CuPc solar does not improve V_0 and, in fact, results in a reduction in V_0.

These results are clear evidence that the CdSe QDs are responsible for high V_0, but only when allowed to form a heterojunction with a transport layer or electrode that is compatible with high V_0. Both the QDs themselves and the interfaces between the QDs and the transport or electrode layers must be lacking defects, midgap states, triplet states or recombination centers that can enhance recombination and in turn lower V_0. The presence of QDs alone is insufficient to neutralize interfacial recombination centers responsible low V_0 and V_{OC}. The fact that the energy levels are similar for the QDs that produce high V_0 and the molecular semiconductors that produce low V_0 can be interpreted as evidence that the alignment of energy levels in a donor/acceptor device is less important than the particular recombination mechanism responsible for setting the V_0, the maximum V_{OC}.

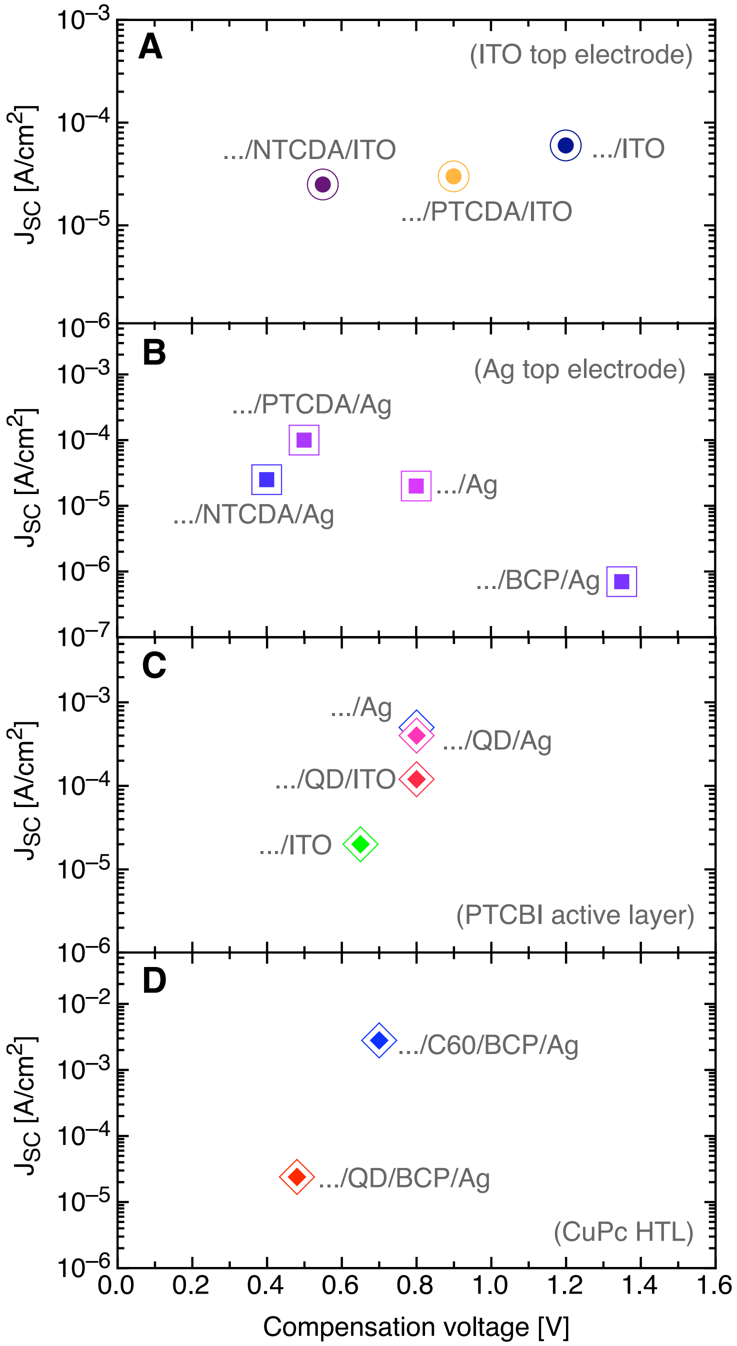

Figure 5-12: Plot of short-circuit current J_{SC} versus compensation voltage V_0 data for devices consisting of (A) ITO/PEDOT:PSS/spiro-TPD/QD/..., (B) ITO/PEDOT:PSS/spiro-TPD/QD/... (C) ITO/PEDOT:PSS/spiro-TPD/PTCBI/... and (D) ITO/PEDOT:PSS/CuPc/....

5.9 Long term stability

The ability to generate a large open-circuit voltage without the need for a low work function electrode should lead to improved reliability in solar applications. Indeed, devices stored either in air or a nitrogen glove box exhibit a remarkable shelf life, with no decay in short-circuit current and only a 10% decay in open-circuit voltage after more than a year. Figure 5-13 shows a device stored in a nitrogen glovebox that is nearly as efficient on the 285th day after being manufactured as on the fourth day. Some reduction in the diode turn-on voltage is observed, as well as a slight increase in J_{SC}.

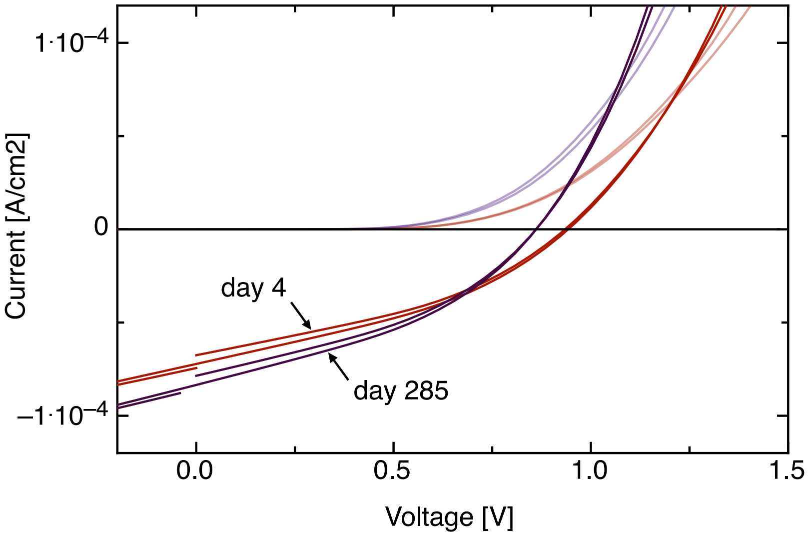

Figure 5-13: I-v characteristics for a typical QD device tested 4 days and 285 days after its date of manufacture.

5.10 Conclusion

The bi-layered heterojunction photovoltaic structure presented in this chapter constitutes our initial attempt to reveal the underlying physics responsible for charge generation in nanostructured photovoltaics containing colloidal QDs. The organic/QD bilayer structure is shown to generate photocurrent from absorption in the QD film and to accommodate different size QDs. Physical voids in the QD film are observed, but do not interrupt the generation of photocurrent or photovoltage. The high V_{OC} and negligible shunting are attributed to the hole-blocking character of the top ITO contact and low rates of interfacial recombination.

In order to increase device efficiency, thicker QD films with improved conductivity and greater absorption must be implemented. Because the QD film is printed and the overall device structure is transparent, advanced multi-layered photovoltaic architectures should be achievable, such as stacked solar cells. Finally, the ability to define the spectral response of the device by choosing the QD size is useful for both stacked solar cells and multi-spectral photodetector arrays.

Chapter 6

High open-circuit voltage in devices with a uniform quantum dot film

The previous chapter presented our result that a high open-circuit voltage (V_{OC}) of 0.8 V can be achieved in quantum-dot (QD) devices even though the QD film is extremely thin and incomplete. In this chapter, we demonstrate that even greater V_{OC} (up to 1.3 V) is obtained when the QD film morphology is smooth and complete. Evidence from the bias dependence of the photocurrent, photocurrent transient measurements and electroluminescence suggests that the high V_{OC} originates from (1) low dark current due to suppressed recombination in the device and (2) a diffusion-driven photocurrent mechanism that is relatively impervious to applied bias. A study of the thickness dependence of the QD layer reveals that charge generation is most efficient when the QD layer is kept optically thin, at a thickness of only 50 nm.

6.1 Introduction

In the introduction to this thesis (Chapter 1), we explained that a major obstacle to commercially viable donor/acceptor heterojunction solar cells is their unfortunately low solar conversion efficiency. The primary cause of low efficiency is low V_{OC}, which is only $\sim 40\%$ of the detailed-balance limit, whereas the quantum efficiency is $\sim 75\%$ and the fill factor is 66% (for one of the best cells listed in Table 1.1, the so-called "bulk-heterojunction" solar cell). At present, the limit to V_{OC} in donor/acceptor photovoltaics is thought to be the energy level offset between the highest occupied molecular orbital (HOMO) and the lowest unoccupied molecular orbital (LUMO) at the donor/acceptor heterojunction, as described in Section 3.5.3.

In this chapter, we present a heterostructure photovoltaic device with a notably large V_{OC} reaching 1.3 V for a bandgap of $E_g = 2$ eV. As in the previous chapter, the device consists of a discrete heterojunction between a thin film of colloidally-grown cadmium selenide (CdSe) quantum dots (QDs) and the wide-bandgap hole-transporting molecular film N,N′-bis(3-methylphenyl)-N,N′-bis-(phenyl)-9,9-spiro-bifluorene (spiro-TPD), shown in Figure 6-1(A).[101] The QD film is responsible for absorption of incident light, while the transparent spiro-TPD film provides hole transport to the PEDOT:PSS electrode. Deposition of the QD film is accomplished using a contact printing method that employs either a bare polydimethylsiloxane (PDMS) stamp (Figure 6-1B) or a PDMS stamp coated with the polymer parylene-C (Figure 6-1C). Atomic force microscopy (AFM) images of the surface of the printed QD films show a cracked surface when films are printed from bare PDMS and a smooth surface for films printed from parylener-C coated PDMS.[71] In order to achieve a high V_{OC} of 1.3 V, we find that the QD layer must form a complete and uniform film, otherwise V_{OC} is limited to ~ 0.8 V by elevated dark current in forward bias. The large V_{OC} is remarkable because it greatly exceeds the energy level offset between the HOMO of the hole donor (QDs) and the LUMO of the hole acceptor (spiro-TPD), expected to be ~ 0.6 eV (Figure 6-7). Furthermore, the built-in potential (Φ_{BI}) between the PEDOT:PSS-coated ITO anode and the top-contact ITO cathode is also much smaller than V_{OC}, at ~ 0.4 eV.

Measurements of electroluminescence from the QD layer, the bias dependence of the photocurrent, and the bias dependence of photocurrent transients lead to the conclusion that the high V_{OC} is due to impeded recombination at the spiro-TPD/QD heterojunction and a diffusion-driven photocurrent mechanism. Our results suggest that efficient QD photovoltaic cells with high V_{OC} are attainable and that the maximum V_{OC} of donor/acceptor photovoltaics in general can be substantially higher than previously thought.

6.2 Morphology of printed QD film

Figure 5-1D illustrates the contact printing process employed to non-destructively deposit the QD film onto the spiro-TPD transport layer. The four steps involved in the printing process are (1) spin cast the QD solution onto the stamp, (2) dry the stamp under vacuum for 30 minutes, (3) bring the substrate and stamp into contact and (4) release. A drawback of this method is that voids in the QD film occur due to de-wetting during spin casting, a result of the surface energy mismatch between PDMS and chloroform. However, coating the surface of the PDMS stamp with an aromatic polymer parylene-C (Figure 5-1C) improves wetting and results in uniform surface coverage, as previously demonstrated by Kim et al.[71].

6.3 The effect of dark current on V_{OC}

A comparison of the current-voltage (i-v) characteristics between QD photovoltaic devices with either cracked films deposited from bare PDMS stamps or smooth films deposited from parylene-C-coated stamps demonstrates the importance of QD film uniformity and the role of dark current on V_{OC}. In Figure 5-6, the i-v characteristics are shown for a device with a cracked QD film and a smooth QD film. Both devices yield diode-like behavior, photocurrent and V_{OC}, yet V_{OC} of the device with a smooth QD film is greater than that of the cracked film by 0.56 V. The device with voids in the QD films functions as a diode due to the hole-blocking nature of the spiro-TPD/ITO junction, as previously identified.[101]

To further explore the role of the dark current in QD devices, we plot the i-v characteristics in dark for a series of devices with different QD film thicknesses for both cracked and smooth QD films, as shown in Figure 6-3. The nominal thicknesses of the

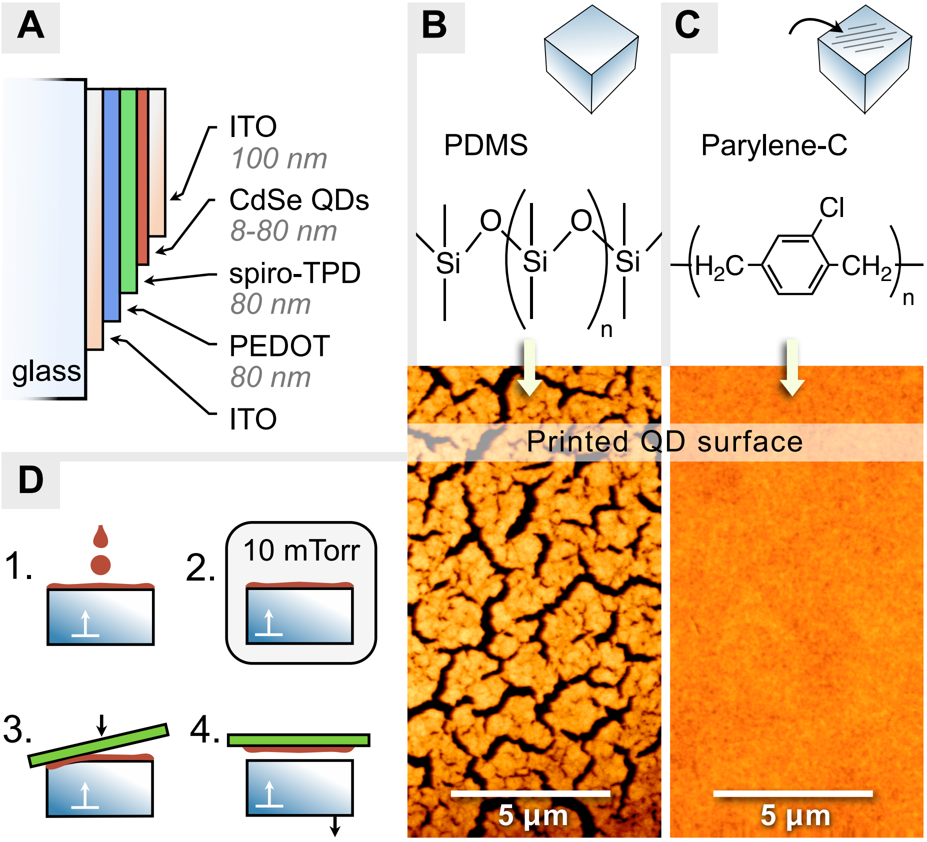

Figure 6-1: The QD device structure is shown in (A). AFM images of the surface morphology of the printed QD film using a bare PDMS stamp (B) and a parylene-coated stamp (C). In (D), the four steps of the printing process.

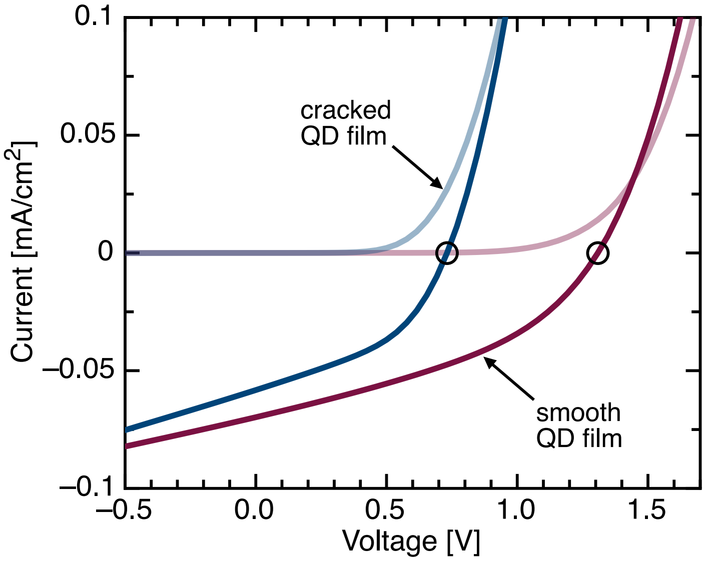

Figure 6-2: Current-voltage characteristics in dark and under illumination with $\lambda = 521$ nm and an intensity of 50 mW/cm^2 for a device with a smooth QD film (40 nm nominal thickness) (solid black line) or a cracked QD film (26 nm nominal thickness) (solid gray line). The open-circuit voltage (V_{OC}) increases from 0.74 V to 1.3 V.

QD films are derived from measurements of the device reflection and transmission in situ, using an absorption coefficient of 10^4 cm^{-1}. Note that for cracked QD films, the quoted nominal thicknesses are not indicative of the actual height of the QD layer, simply the total amount of QD material in the device.

The i-v characteristics display an Ohmic regime at low voltages and a power law dependence ($J \propto V^m$) of $m \approx 6$ above a threshold of 0.6 V. A trap-limited conduction mechanism with $m \approx 6$ is not likely to originate from the bulk of the spiro-TPD film since transport in spiro-TPD has been observed to be space charge limited with $m \approx 2$.[102] Likewise, both hole and electron injection into the device should be efficient: PEDOT:PSS is known to improve charge injection into TPD[103] and the energy barrier for electron injection into CdSe is only 0.2 - 0.6 eV. Trap limited conduction with $m \approx 11$ has been observed in devices with pristine CdSe QD devices,[104, 105] yet we find that devices with and without the QD film display nearly the same the power law dependence, albeit with a reduced threshold voltage for control devices

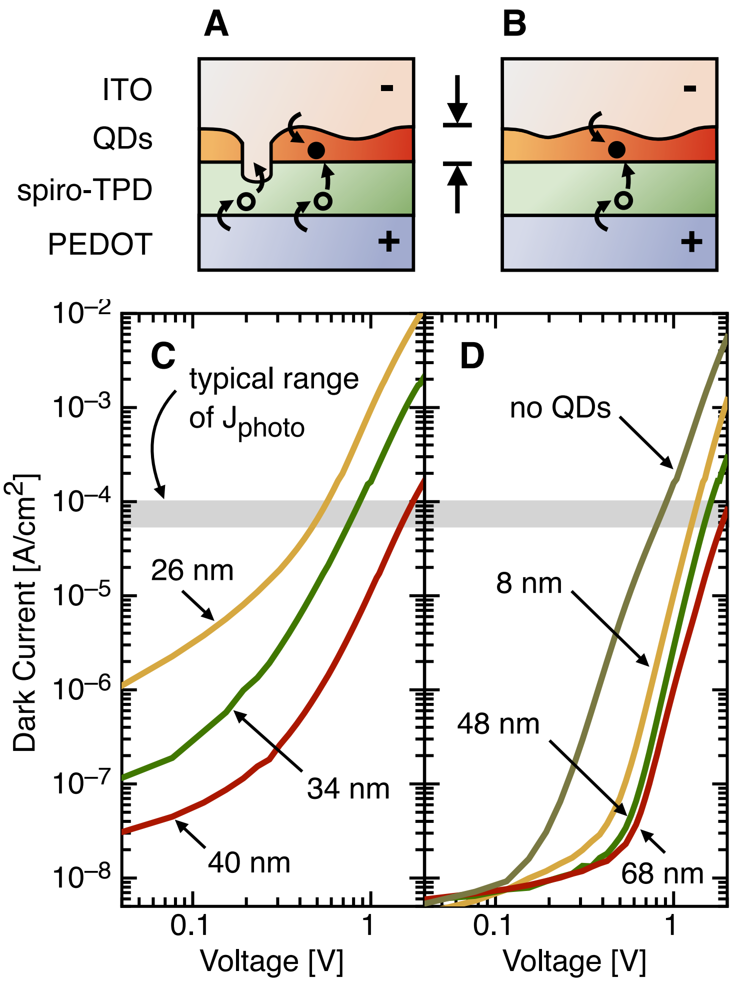

Figure 6-3: Diagram of QD device cross-section for (A) cracked QD films printed without parylene-C-coated stamps and (B) smooth QD films printed with parylene-C. Plot of dark current versus voltage on a log-log scale in forward bias for devices prepared (C) without parylene-C and (D) with parylene-C, where the QD film thickness is given as indicated. In (D), a control device without a QD film. Sizable leakage currents are observed in devices with voids in the QD film, where some portion of the spiro-TPD film is believed to be inadvertently removed or dissolved during the printing process.

without QDs, suggesting that the power law dependence does not originate from the QD film. Increasing the QD thickness leaves the power dependence unchanged, but results in reduced current for both cracked and smooth QD films, which is consistent with higher resistivity across the QD layer and fewer shunting pathways through voids in the QD films. We propose that the power law dependence of the dark current can be assigned to either one of the two only remaining locations for charge build-up: the spiro-TPD/QD heterojunction or the top ITO electrode interface.

At low bias, the device with voids exhibits high Ohmic leakage with a pronounced dependence on QD film thickness (Figure 6-3C). A control device without a QD film does not exhibit leakage to the same extent as devices with a QD film with voids (Figure 6-3D). In addition, such high leakage currents are often observed in devices with spiro-TPD films that are much thinner than the 80 nm thick spiro-TPD films used in this study. Two mechanisms may be responsible for the increased dark current for devices with QD films deposited from bare PDMS stamps. First, PDMS is known to swell when exposed to solvent. When the QD-coated stamp is contacted to the spiro-TPD film, residual solvent held in the PDMS may be released, resulting in partial dissolution of the spiro-TPD. For this reason, the stamps are placed in vacuum for at least 30 min prior to deposition in order to remove residual solvent. Alternatively, we observed (in a separate study) that removal of a 30 nm thick layer from the top of a TPD film occurs when a bare PDMS stamp is brought into contact with a pristine TPD film.[106] Further, blue photoluminescence from the surface of the PDMS stamp is observed after QD deposition onto spiro-TPD, indicating the presence of spiro-TPD on the stamp. In contrast, no luminescence is observed after deposition from parylene-C-coated stamps, indicating that the spiro-TPD layer has not been removed. As shown in Figure 6-3D, devices with QD films printed with parylene-coated stamps exhibit low leakage currents down to less than a monolayer.

The intact and undamaged presence of the spiro-TPD layer leads to low leakage currents and is therefore an important component of improved V_{OC}. A comparison of V_{OC}s obtained from devices deposited from bare PDMS stamps or from parylene-coated stamps illustrates the impact of reduced leakage currents on V_{OC}. In Figure

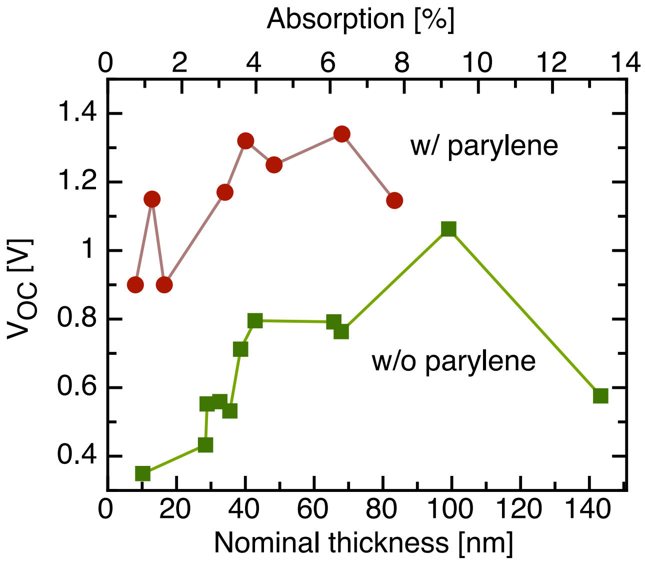

Figure 6-4: Open-circuit voltage (V_{OC}) versus QD layer thickness for devices printed using bare PDMS stamps (■) or parylene coated stamps (●).

6-4, the V_{OC} is substantially higher across a wide range of QD layer thicknesses when a parylene coating is employed. Without parylene, V_{OC} falls off with decreasing QD layer thickness as leakage around voids in the QD films becomes more prominent. With parylene, high V_{OC} is obtained even for QD thicknesses on the order of a monolayer, due to the relatively unaffected integrity of the critical electron-blocking spiro-TPD film.

The relationship between a larger diode turn-on voltage (V_{ON}) in the dark, and an increase in V_{OC} can be understood by considering the fundamental relationship between current in light J_{light} and current in dark J_{dark}

$$J_{light}(I, V) = J_{dark}(V) - J_{photo}(I) \tag{6.1}$$

where J_{dark} is dependent on voltage and the photocurrent $J_{photo}(I)$ is ideally linearly dependent on intensity I and independent of voltage. At V_{OC}, $J_{light}(I, V_{OC}) = 0$ by definition and Equation 6.1 reduces to

$$0 = J_{dark}(V_{OC}) - J_{photo}(I) \tag{6.2}$$

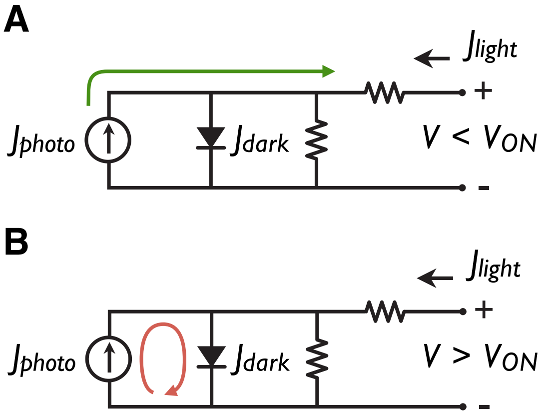

Figure 6-5: Circuit model of an ideal diode under illumination at an applied bias of (A) below diode turn-on and (B) above turn-on.

Therefore, for a given intensity, V_{OC} depends only on the voltage dependence of $J_{dark}(V)$, as long as the production of J_{photo} remains independent of bias. From the ideal diode circuit model in Figures 6-5A and 6-5 B, it is apparent that the diode turn-on voltage V_{ON} in the dark will not affect J_{photo}, yet above V_{ON} J_{photo} will become shunted by the large conductivity of the diode. Although this is the conventional description of V_{OC}, it is somewhat non-intuitive, since V_{OC} in donor/acceptor photovoltaics is often thought to be determined by some aspect of the photogeneration process. In fact, in all cases V_{OC} should be understood as the bias point at which the dark current subsumes the photocurrent sourced by the semiconductor. Along the same line of reasoning, V_{OC} can be thought of as the voltage point at which recombination subsumes the generation of charge.

A comparison of the recombination mechanism in a device with a single semiconductor versus a donor/acceptor heterojunction illustrates the effect of recombination on V_{OC}. In a device consisting of a single semiconductor with a bandgap E_g, current in dark will be due to recombination across the bandgap, as shown in Figure 6-6A, in the absence of other non-radiative or parasitic leakage current pathways. Upon illumination, the quasi Fermi levels for electrons (E_{Fn}) and holes (E_{Fp}) diverge, producing a voltage $qV = E_{Fn} - E_{Fp}$. As the quasi Fermi levels approach the band edge

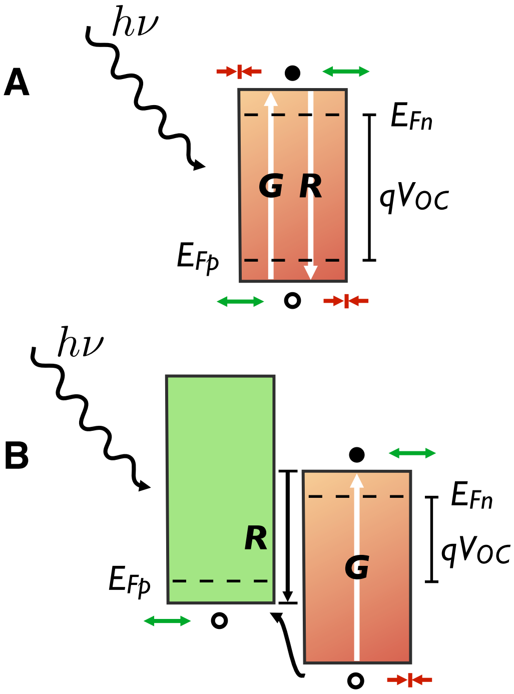

Figure 6-6: Band diagram of a photovoltaic device consisting of (A) a single semiconductor layer and (B) a donor/acceptor heterojunction. The contacts are assumed to be perfect reservoirs for either electrons or holes on the right and left, respectively.

of the semiconductor, recombination (given by $R = Bnp$, where B is the material dependent bimolecular recombination constant) becomes increasingly frequent and eventually results in V_{OC} saturating at $qV_{OC} = E_g$ for $T = 0$ K.[79] At room temperature, a reverse saturation current arises which must be compensated, reducing V_{OC} to 0.3 - 0.4 V below E_g.[44, 45] For the case of a donor/accepter heterojunction shown in Figure 6-6B, recombination is believed to occur across the heterojunction interface, reducing the maximum V_{OC} to $qV_{OC} = E_{Fp,A} - E_{Fn,D}$ where $E_{Fp,A}$ is the quasi Fermi level for holes in the acceptor and $E_{Fn,D}$ is the quasi Fermi level for electrons in the donor. Since the maximum difference in quasi Fermi levels is often significantly less than the bandgap of the donor or acceptor, the magnitude of V_{OC} will likewise suffer. In both cases, the magnitude of the photocurrent is identical, whereas the voltage dependence of the recombination mechanism is the only parameter that is altered.

6.4 First demonstration of V_{OC} greater than the donor/acceptor energy level offset

The observed V_{OC} of 1.3 V for devices consisting of a smooth QD film is significantly higher than the energy level offset between the HOMO of the donor and the LUMO of the acceptor, often considered the theoretical maximum V_{OC} in donor/acceptor photovoltaics, regardless of material system or device geometry.[107, 108, 99] Energy level offsets are difficult to establish, but a plausible range of levels are plotted in Figure 6-7A. The offset between the HOMO of spiro-TPD and the LUMO of CdSe is expected to be between 0.2 eV and 0.9 eV. Such a broad disparity between the measured V_{OC} and the energy level offset at the heterojunction interface forces us to consider an alternative interpretation of the limiting V_{OC} in donor/acceptor photovoltaics. One possible explanation is that a large interface dipole is present at the spiro-TPD/QD heterojunction,[109] which shifts the energy offset at the heterojunction by more than 0.7 eV. It has been shown that a dipole layer can influence V_{OC} in conjugated polymer/titanium dioxide based photovoltaics, although the magnitude of the offset was only 0.25 V.[110] A second possibility is that recombination at the spiro-TPD/QD heterojunction is completely suppressed by the presence of insulating capping groups grafted to the QD surface, resulting in an increase in the diode turn-on voltage and hence a higher V_{OC}. Below, we present bias-dependent time response data that favors the latter interpretation.

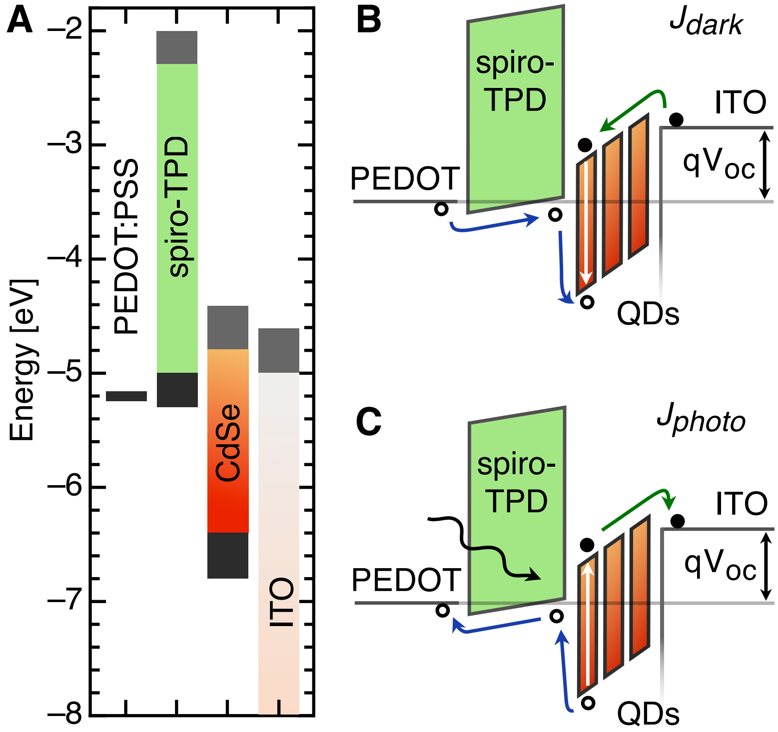

Figure 6-7: (A) Plot of approximate range of HOMO (in black) and LUMO (in gray) energy levels for the QD heterojunction device. The HOMO level of spiro-TPD is approximated from Ref. [[2]], and the LUMO level of CdSe QDs is obtained from Ref. [[3]] and knowledge of the levels of bulk CdSe.[4] The ITO coated glass substrate is omitted. Presumed charge-flow mechanisms for dark current (B) and photocurrent (C) are illustrated in forward bias at open-circuit voltage (V_{OC}).

In Figure 6-7B, the current flow pathway in dark is illustrated for the special case where recombination at the spiro-TPD/QD heterojunction is nonexistent. Under the influence of applied bias, holes are injected into spiro-TPD from the PEDOT:PSS anode and electrons are injected into the QD layer from the top ITO cathode. Electrons and holes are driven toward the heterojunction by the applied electric field and accumulate at the interface while they await recombination. Since the conductivity of spiro-TPD films[2] has been shown to be much higher that of CdSe QD films[67], most of the applied electric field is presumed to be evenly distributed across the QD film. In the absence of recombination across the interface, holes must be further injected into the QD layer in order to recombine with electrons accumulated in the QD film. Upon recombination, the current flow process is complete and, for QDs exhibiting efficient radiative transitions, light is emitted with the spectral characteristic of the QD film.

In Figure 6-7C, the charge-flow mechanism responsible for the generation of photocurrent is illustrated for the case of an applied forward bias equal to V_{OC}. An incident photon with energy between 2 and 3 eV passes through the spiro-TPD and is absorbed by the QD film, producing an exciton that must diffuse toward the spiro-TPD/QD heterojunction in order to dissociate. Interfacial charge separation results in a free hole on spiro-TPD and a free electron in the QD film. At an applied bias approaching V_{OC}, electron and hole transport to the electrodes must contend with a considerable external electric field aligned to oppose charge extraction. In turn, carrier collection must rely on concentration gradients that serve to drive charge away from the heterojunction interface via diffusion, similar to both conjugated polymer and organic small molecule bilayer donor/acceptor structures.[90, 89]

6.5 Electroluminescence from the QD film

In the discussion above, we argued that V_{OC} is set by the diode turn-on voltage V_{ON} and that V_{ON} in our structure is higher than expected because holes must overcome a large potential step barrier between spiro-TPD and the QDs. Under this circumstance, current flow above V_{ON} should be accompanied by electroluminescence with a spectral dependence that is characteristic of the QD film. In the following (Figures 6-8 and 6-9), we show that electroluminescence is indeed sharply peaked and red in color, as expected from CdSe emission with a quantum confined bandgap of 2 eV.[57]

Electroluminescence has previously been observed in QD devices with similar or-

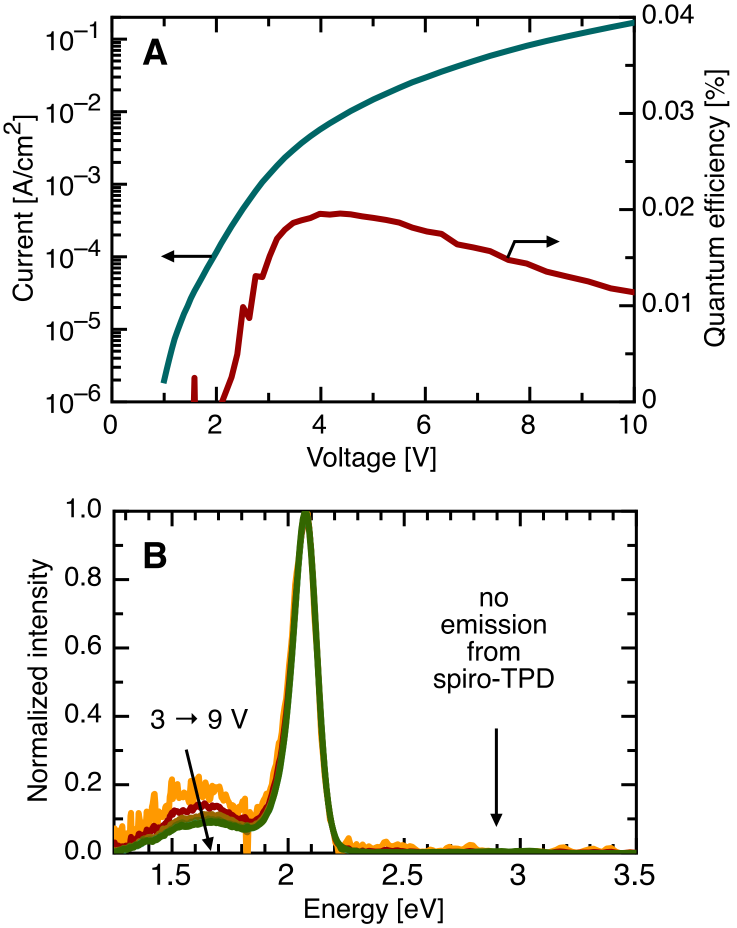

Figure 6-8: Log-log i-v characteristics (left axis) and electroluminescence quantum efficiency (right axis) are shown in (A). In (B), normalized emission spectra at an applied bias of 3 to 9 V.

ganic/QD planar heterojunction architectures.[71, 111] In these devices, an electron transport layer tris-(8-hydroxyquinoline) aluminum (Alq_3) and a magnesium:silver cathode are required to achieve optimized electroluminescence efficiencies. The emission mechanism is attributed to carrier accumulation and exciton formation on the Alq_3 side of the Alq_3/QD interface, followed by energy transfer to the QDs and recombination in the QDs. This process is believed to be more efficient than direct charge injection and recombination on the QDs, but results in emission from both the QD film and Alq_3. Under high applied bias, the width of the region where excitons form on the Alq_3 widens beyond the energy transfer radius and emission from Alq_3 alone becomes more prominent.

Here, i-v characteristics and emission spectra are shown in Figure 6-8 for the photovoltaic device structure presented in this work (Figure 6-1), which does not contain Alq_3. The QD layer thickness is 40 nm. Onset of emission occurs above 2 V and the spectral characteristic follows the narrow emission expected from the QDs, without a detectable signal from between 2.5 and 3 eV, where spiro-TPD is known to emit. Even under high applied bias, no emission from spiro-TPD is discernible, indicating that exciton formation on spiro-TPD does not occur. A small contribution from defect states at lower energies, centered near 1.6 V, is observed. The absence of emission from spiro-TPD and the presence of emission from the QD film implies that direct charge injection and recombination in the QD layer is exclusively responsible for electroluminescence. However, because of the low efficiency of electroluminescence, reaching 0.02% at 4 V, we cannot rule out the possibility that some fraction of holes may contribute to current flow in forward bias by some other conduction mechanism, for example, by recombining across the spiro-TPD/QD interface. Even so, low electroluminescence quantum efficiencies can result from many causes, such as non-radiative recombination in the QDs, trapping at defect states or Onsager dissociation due to the presence of a high electric field, which may be as high as 1×10^6 V cm^{-1} at 4 V. Therefore, we conclude that the observation of electroluminescence from the QD layer agrees with, but does not conclusively prove, the interpretation that the forward bias conduction requires hole injection from spiro-TPD to the QDs.

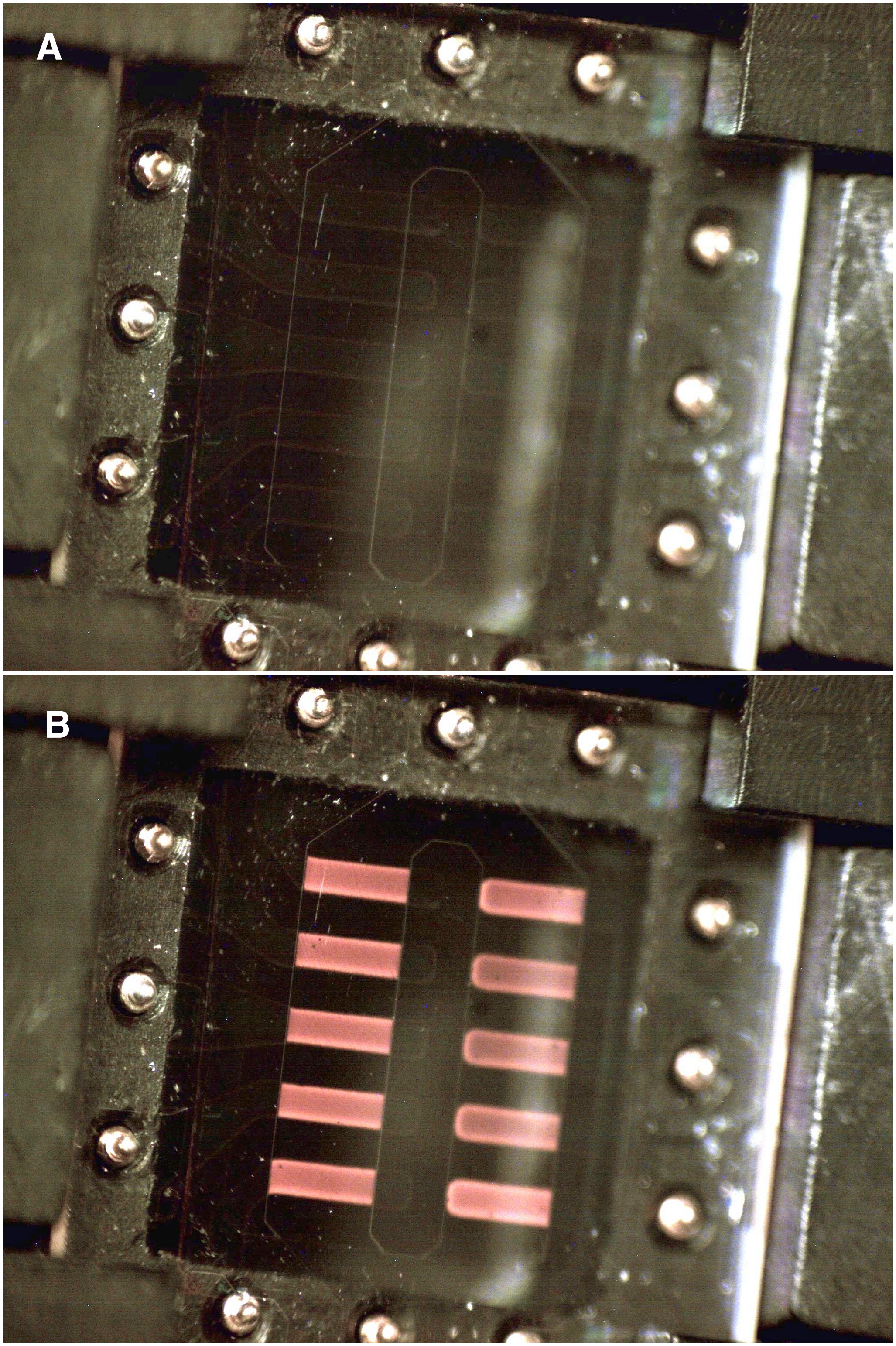

Figure 6-9: Images of QD device at an applied bias of (A) 0 V and (B) 4 V.

6.6 Bias-dependent photocurrent transients

In Figure 6-7C, we drew the band diagram of the QD device under applied forward bias assuming a substantial electric field drop across the QD film. The question arises: how do free carriers extract themselves from the interface and travel to the electrodes notwithstanding an opposing electric field? In this section, we present photocurrent decay measurements that support the view that charge diffusion plays a major role in photocurrent generation.

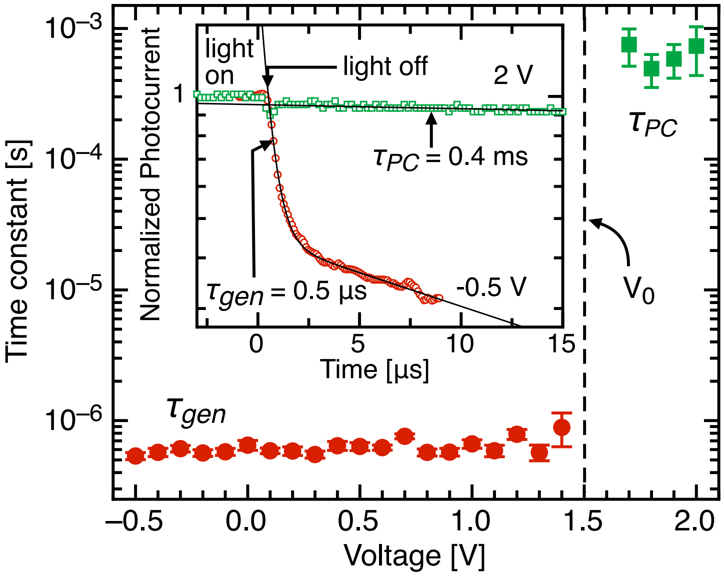

Figure 6-10: Photocurrent decay time constant plotted versus voltage for a QD device with a QD film thickness of 80 nm, illuminated with $\lambda = 521$ nm at an intensity of 50 mW/cm^2. The inset shows the normalized photocurrent transient curve for negative photocurrent (measured at -0.5 V) and positive photocurrent (measured at 2 V).

Photocurrent decay transients in response to an abrupt step function light pulse are shown in Figure 6-10. At a voltage of -0.5 V, the decay transient follows an initial single exponential decay with a time constant associated with the photocurrent generation $\tau_{gen} = 0.5$ s, which is defined as the photocurrent with negative polarity. A second, slower decay mode emerges after the initial fast decay, but is attributed to the low pass RC filter connected between the DC voltage source and the sample.

The measured time constant follows a weak bias dependence up until 1.5 V, at which point the photocurrent signal diminishes to zero. Above 1.5 V, the photocurrent signal switches polarity – becoming positive – and the device acts as a photoconductor. The decay constant τ_{PC} associated with photoconduction (positive photocurrent) displays a multimode decay with a nearly three order of magnitude longer decay ranging from 0.4 ms out to 1 ms.

A number of possible mechanisms could lead to the decay of the photo-excited carrier population. The rate equation for the population of electrons in the QD layer can be written as

$$\frac{\partial n}{\partial t} = G - R_{Int} - R_{Bulk} - T \tag{6.3}$$

where n is the electron concentration, G is the net rate of free carrier generation (which encompasses exciton generation, geminate recombination, dissociation and bi-molecular recombination), R_{Int} is the interfacial recombination rate, R_{Bulk} is the recombination rate due to space charge in the bulk and T is the carrier collection rate associated with transport to the electrodes. First, we can rule out G as a contributing factor to the photocurrent decay on the basis that exciton diffusion and dissociation must be faster than radiative geminate recombination, which is on the order of $\tau \approx$ 30 ns for CdSe QDs.[112] Second, R_{Int} is likely too slow to limit excited carrier extraction, observed to be on the order of 1 ms to 10 μs in conjugated polymer donor/acceptor systems.[110, 113] Third, R_{Bulk}, which becomes more prominent at high carrier concentrations, can compete with carrier collection at high intensities. To ensure that R_{Bulk} is not dominant, a device is chosen with an external quantum efficiency (EQE) that remains constant over the range of intensities achievable with of our setup (Figure 6-12). Finally, T could be dominated by the transport rate of either holes across spiro-TPD or electrons across the QD layer. Given the relatively high hole mobility of spiro-TPD ($\mu \approx 10^{-4}$ cm^2 V^{-1} s^{-1})[2] versus the electron mobility of CdSe QDs ($\mu \approx 10^{-4}$ to 10^{-6} cm^2 V^{-1} s^{-1}),[104] the response time should be limited by electron transit across the QD layer. Indeed, an increase in time response is observed with thicker QD films.

6.7 Interpretation of transient results

The weak bias dependence of the photocurrent decay time constant and sharp step increase above V_0 are consistent with a diffusion-driven carrier collection model and can not be explained by a field-driven collection mechanism. Below, we argue that the long time constant measured at voltages above V_0 places a lower bound of 400 μs to 1 ms on the recombination lifetime of carriers at the spiro-TPD heterojunction interface. The long interfacial lifetime, in turn, permits the build up large concentration gradients that serve to drive diffusion of photo-excited carriers away from the interface.

In the steady state, the continuity equation (Equation 6.3) becomes

$$0 = G - R_{Int} - R_{Bulk} - \frac{\partial}{\partial x}(n\mu\mathcal{E} + D\frac{\partial n}{\partial x}) \tag{6.4}$$

where the transport rate has been separated into drift and diffusion components, n is the electron concentration, μ is the electron mobility, $\mathcal{E}$ is the electric field, D is the electron diffusivity. First, consider the possibility that carriers are solely propelled by a built-in potential Φ_{BI}, perhaps as a result of an induced dipole at the spiro-TPD/QD interface. If R_{Bulk} is negligible, then $n = G/\tau$ and $\mathcal{E} = (V - \Phi_{BI})/d$ where τ is the transit time of photogenerated carriers across the QD film, given by

$$\tau = \frac{1}{\mu}\frac{d^2}{|\Phi_{BI} - V|} \tag{6.5}$$

and d is the thickness of the QD film (assuming the field-drop is exclusively across the QD layer, for simplicity). If Φ_{BI} is singularly responsible for photocurrent, then $\Phi_{BI} = V_0$ in Figure 6-10. Two inconsistencies then arise between the above equation and the measured transit times. First, as V approaches V_0, we would expect τ to slow down considerably, following a $1/V$ dependence. Instead, τ_{gen} remains nearly constant as V approaches V_0. Second, τ should be symmetric around V_0, unlike in Figure 6-10 where τ changes abruptly above V_0.

In contrast, the diffusion of photo-excited carriers away from a heterojunction

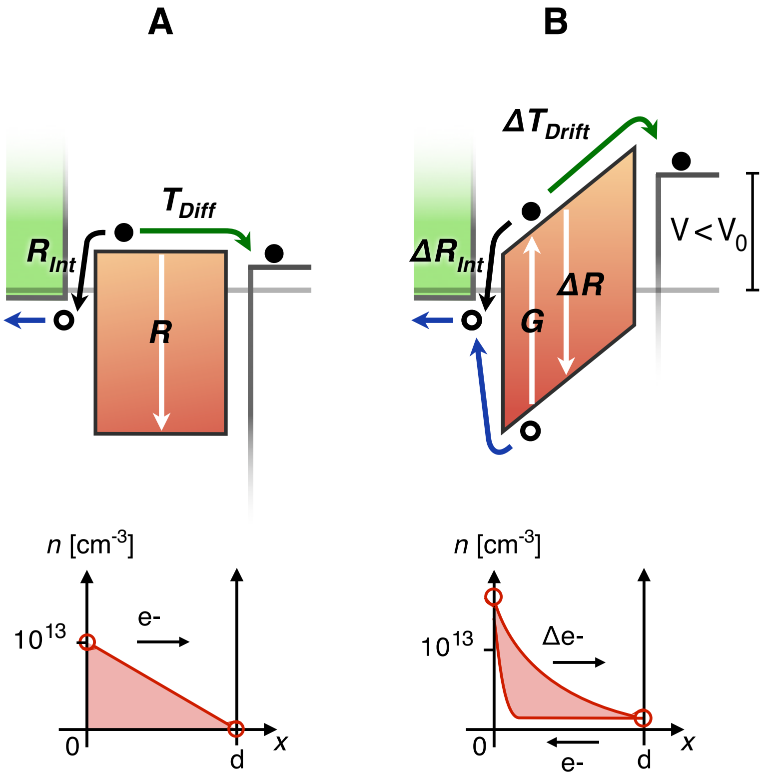

Figure 6-11: Band diagram and electron carrier concentration in the QD film at (A) zero electric field ($V = \Phi_{BI}$) and (B) an opposing electric field ($\Phi_{BI} < V < V_0$).

interface is not explicitly bias-dependent. At the flat band condition, the continuity equation becomes

$$0 = D\frac{\partial^2 n}{\partial x^2} \tag{6.6}$$

when R_{Int}, R_{Bulk} and G are small within the QD film. Applying boundary conditions $n \approx 0$ at the collecting electrode and a surface generation rate g_s at the heterojunction interface gives a linear carrier concentration profile[86]

$$n = -\frac{g_s}{D}(x - d) \tag{6.7}$$

as shown in Figure 6-10A. The time required for carriers to diffuse across the QD layer is obtained by integrating the diffusion velocity[86]

$$v_{diff} = D\frac{1}{n}\frac{dn}{dx} \tag{6.8}$$

from $x = 0$ to d, which yields

$$\tau = \frac{d^2}{2D} \tag{6.9}$$

which reveals that τ is not dependent on bias. Our observation of a slight increase in τ with increasing bias can be understood as a shift in the average distribution of carriers toward the interface as the electric field acts to counteract diffusion (Figure 6-11B). From the measured $\tau = 0.6\ \mu\text{s}$, we obtain $D = 5.3 \times 10^{-5}\ \text{cm}^2\ \text{s}^{-1}$, which corresponds to $\mu = 2 \times 10^{-3}\ \text{cm}^2\ \text{V}^{-1}\ \text{s}^{-1}$, assuming the Einstein relation holds.[114] We note that this value is higher than expected for the electron mobility in QD films,[104] perhaps due to the possibility that our transient decay measurements selectively capture electrons at the higher end of the distribution of thermal velocities.

Under an applied electric field, a steady state drift current component flows in parallel with the transient photocurrent signal, but does not significantly influence the photocurrent process below V_0 (Figure 6-11B). Injected carriers raise the baseline carrier concentration across the QD film and accumulate at the heterojunction interface until they recombine with holes, either across the interface or with holes that are injected into the QD film from spiro-TPD. The magnitude of the drift current is therefore determined by either $R_{Int} = Bn_{QD}(0)p_{TPD}(0)$, (where B is the bimolecular recombination constant, $n_{QD}(0)$ is the concentration of electrons on the QD side of the heterojunction and p_{TPD} is the concentration of holes on the spiro-TPD side) or $R_{Bulk} = p_{QD}(0)/\tau_{rec}$ (where τ_{rec} is the excited state lifetime of the QDs).

Once V exceeds V_0, R_{Int} and/or R_{Bulk} become too large to support further accumulation of charge at the heterojunction interface, recombination outcompetes carrier collection and the photocurrent reverses polarity. The direction of photocurrent is now aligned with the electric field and the device operates in the photoconduction regime. The rate equation for photo-excited carriers in the accumulation layer is then

$$\frac{\partial n'}{\partial t} = G - \Delta R_{Int} - \Delta R_{Bulk} + \Delta T_{Drift} \tag{6.10}$$

where n' is the photo-excited carrier concentration, ΔR_{Int} is the excess recombination rate, ΔR_{Bulk} is the excess bulk recombination rate and ΔT_{Drift} is the photoconductive injection and drift transport term. The time constant associated with ΔR_{Int} is presumed to be relatively slow since electron and holes must couple across organic ligands surrounding the QDs in order to recombine. In contrast, both ΔR_{Bulk} and ΔT_{Drift} should operate on short times scales since recombination and drift transport are both fast processes. However, ΔR_{Bulk} and ΔT_{Drift} are competing rates and therefore a slight difference between the two can yield a slow change in the overall carrier population. Consequently, attributing the photoconduction decay constant τ_{PC} to ΔR_{Int}, the longest decay process, can be misleading. Still, the measured value of $\tau_{PC} \approx 0.8$ ms places a lower bound on the charge carrier lifetime in the accumulation layer, which is nonetheless notably longer than that of other donor/acceptor systems. For instance, transient photovoltage (TPV) measurements give a carrier lifetime of $\sim$10 μs at 0.6 V in conjugated polymer blend photovoltaics[113] and ~ 30 μs at 0.6 V in polymer/titanium dioxide bilayer photovoltaics.[110] Furthermore, these lifetimes are observed to decrease exponentially with increasing voltage, which suggests that, at comparable voltages, the carrier lifetime at the spiro-TPD/QD interface may be many orders of magnitude longer than in polymer based photovoltaics.

6.8 Bias-dependent photocurrent

Above, we interpreted the bias-dependence of photocurrent decay transients as evidence that long carrier lifetimes at the heterojunction interface permit the build-up of a carrier concentration gradient across the QD film, in turn driving photocurrent against an applied electric field. As a next step, we investigate the magnitude and intensity dependence of the photocurrent as a function of bias in order to establish if the voltage dependence is compatible with a diffusion-driven model of carrier collection.

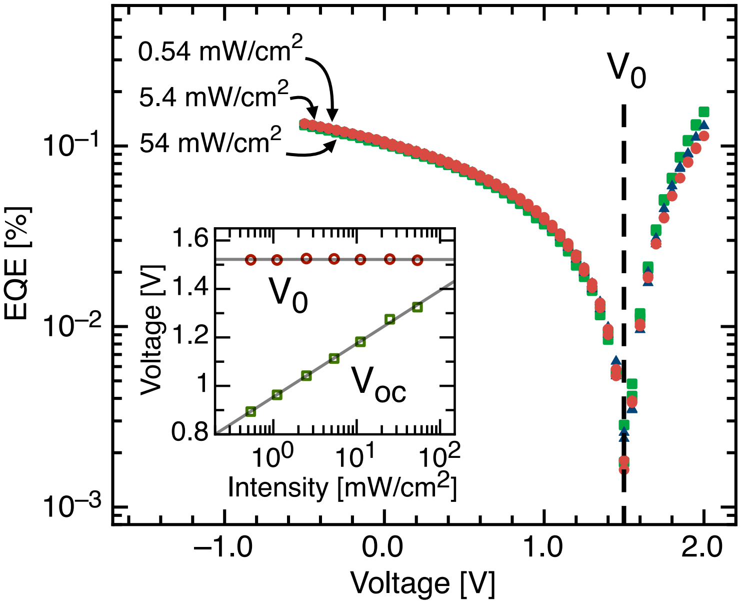

Figure 6-12: Log-linear plot of the external quantum efficiency (EQE) versus voltage for QD devices printed with parylene-C-coated stamps at illumination intensities as indicated with $\lambda = 532$ nm. The cross-over from negative photocurrent to positive photocurrent is marked as the compensation voltage (V_0). The inset shows the dependence of V_0 and V_{OC} on illumination intensity.

Photocurrent versus voltage characteristics have been used to help identify the role of drift, diffusion and exciton dissociation efficiency in conjugated polymer-fullerene bulk heterojunction cells[91, 115] In these cells, the voltage needed to set $J_{photo} = 0$, defined as the compensation voltage V_0, indicates the point where the built-in electric field is zero, and the photocurrent bias dependence signifies the degree to which exciton dissociation is affected by the electric field.[116] Measurements of photocurrent as a function of bias at various intensities for our spiro-TPD/QD bilayer devices, plotted in Figure 6-12, demonstrate that J_{photo} indeed exhibits bias dependence and V_0 is independent of intensity, yet as we will shown below, this behavior is entirely consistent with a diffusion-driven photocurrent mechanism and not necessarily the result of a built-in electric field.

To interpret the origin of the intensity-independence of V_0, we can again consult the continuity equation. In steady state, at an applied voltage V_0, the rate at which excess carriers generated by light enter and leave the accumulation region near the spiro-TPD/QD interface is given by

$$0 = G - \Delta R_{Int}(V_0) - \Delta R_{Bulk}(V_0) + \Delta T_{Drift}(V_0) - \Delta T_{Diff}(V_0) \tag{6.11}$$

where $\Delta R_{Int}(V_0)$ is the excess recombination rate at the spiro-TPD/QD interface at V_0, $\Delta R_{Bulk}(V_0)$ is the excess recombination rate in the QD bulk at V_0, $\Delta T_{Drift}(V_0)$ is the rate at which excess injected carriers reach the accumulation region near the interface and $\Delta T_{Diff}(V_0)$ is the rate at which excess carriers diffuse away from the interface. For the above equality to hold for all intensities, each term must be linear with intensity. We can simplify the expression by noting that $\Delta T_{Drift}(V_0) = \Delta T_{Diff}(V_0)$ by definition at V_0. Therefore, the rate equation at V_0 reduces to

$$0 = G - B\Delta n_{QD}(V_0)\Delta p_{TPD}(V_0) - \frac{\Delta p_{QD}(V_0)}{\tau_r} \tag{6.12}$$

where B is the bimolecular recombination constant, $\Delta n_{QD}(V_0)$ is the concentration of photo-excited electrons on the QD side of the heterojunction, $\Delta p_{TPD}(V_0)$ is the concentration of photo-excited holes on the spiro-TPD side of the heterojunction, $\Delta p_{QD}(V_0)$ is the concentration of photo-excited holes that are injected across the heterojunction from spiro-TPD to the QD layer and τ_r is the carrier lifetime of injected holes in the QD layer. While the bulk recombination term is linear with intensity, the bimolecular term is not, implying that B must be small in order to maintain the intensity independence of V_0. Also note that in the absence of interfacial recombination and with a modest (linear) voltage dependence for ΔT_{Drift} and ΔT_{Diff}, the voltage dependence of Δp_{QD} will dominate in Equation 6.11 and therefore determine the magnitude of V_0.

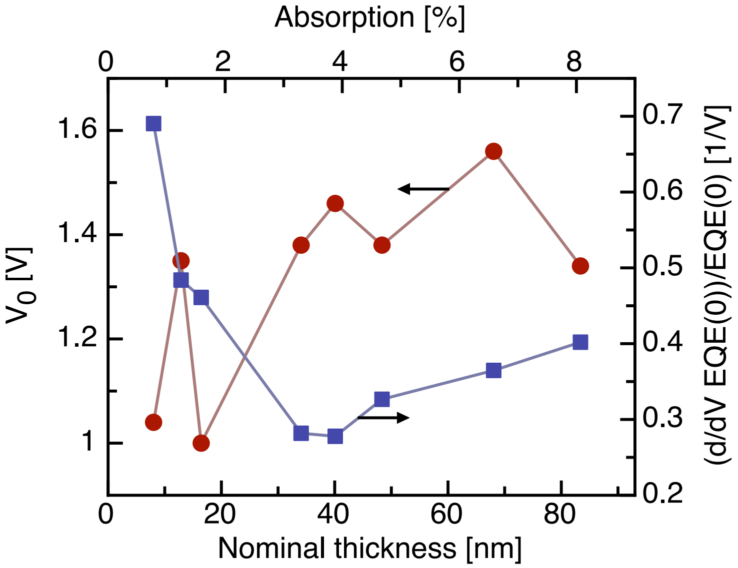

Figure 6-13: Compensation voltage (left axis) and the slope of the EQE-voltage characteristics about V=0 (right axis) for a series of devices with QD layers printed with parylene-C coated stamps and different QD layer thicknesses.

The thickness dependence of the photocurrent-voltage characteristics adds additional insight into the physical mechanisms at play in bilayer spiro-TPD/QD cells. In Figure 6-13, V_0 is shown to vary slightly with thickness, implying that the strength of the electric field has a modest effect on hole injection from spiro-TPD into the QD layer, believed to be the limiting mechanism for diode turn-on and hence V_0. The normalized slope of the photocurrent-voltage curve at $V = 0$, also plotted in Figure 6-13, indicates that the electric field strength can influence the photocurrent generation process. Ideally, field-independent photocurrent generation should yield a slope of zero. For devices with QD films less than 40 nm thick, however, the slope increases for thinner QD films with a 1/d dependence and roughly corresponds to a slight reduction in V_0. Above 40 nm, the slope begins to increase, due to transport losses in the QD layer (to be discussed below). At $d = 83$ nm, V_0 decreases as transport losses limit charge diffusion. At $d = 68$ nm, V_0 is maximized at 1.56 V, reaching an optimum balance between electric field strength and transport losses.

6.9 Dependence of EQE and IQE on QD layer thickness

Despite high V_{OC}, the efficiency is severely constrained by the thinness of the QD layer, which must be kept extremely thin in order to limit resistive losses. Shown in Figure 5-4, the absorption at the first excitonic peak (2.1 eV) is only 3.5%, for a device with 40 nm QD layer, resulting in an EQE of 0.7%. At these absorption levels, the QD layer is optically thin and the complete device appears entirely transparent to the eye. However, the internal quantum efficiency (IQE) is relatively high for a QD film, near 20%, although the IQE decreases above 2.7 eV because of absorption in the spiro-TPD film.

From the i-v characteristics obtained under monochromatic illumination, we can estimate the AM1.5G power conversion efficiency (η) by integrating the external quantum efficiency (EQE) with the American Society for Testing and Materials (ASTM) G173-03 solar spectrum (Table 6.1). The internal monochromatic power efficiency (η_{Int}) gives an indication of the potential efficiency in the event that absorption losses could be overcome.

The restrictions imposed by transport losses in the QD film are exhibited by the thickness dependence of the EQE and IQE, plotted in Figure 6-15. The EQE and IQE reach their maximum values at thicknesses corresponding to very low optical absorption, which severely limits the maximum attainable η for QD films of this type. In the proceeding discussion, we present a simple model that accounts for the general trend of the EQE and IQE with thickness. The model takes into account the effect of exciton diffusion, transport losses in the QD film and the possibility of one or more damaged QD monolayers adjacent to the top ITO electrode.

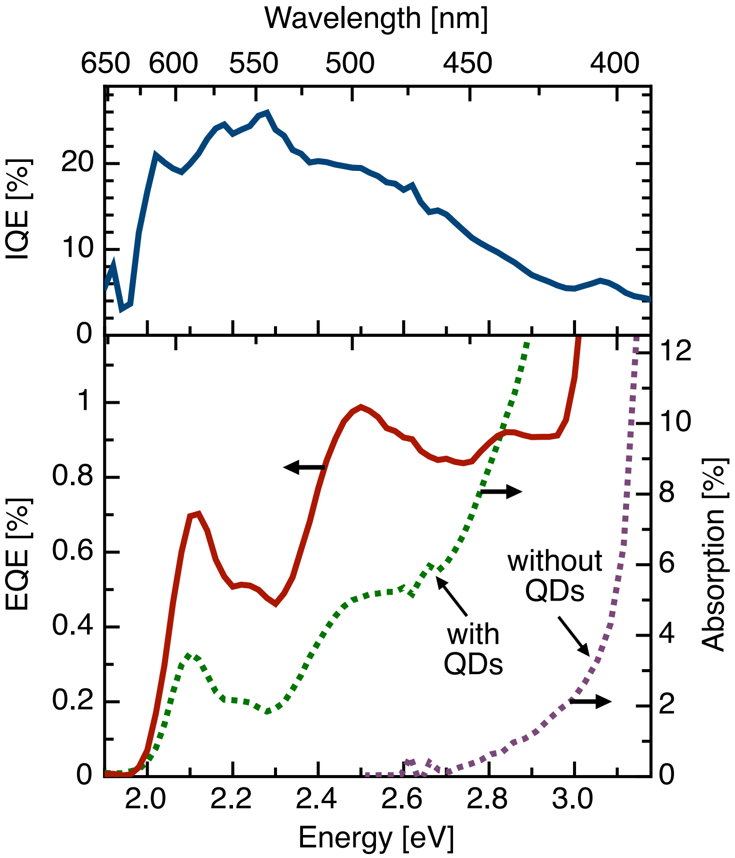

Figure 6-14: Plot of external quantum efficiency (EQE) and device absorption versus photon energy and wavelength, and internal quantum efficiency (IQE) for a device with a QD film printed from a parylene-coated stamp and a nominal QD film thickness of 34 nm.

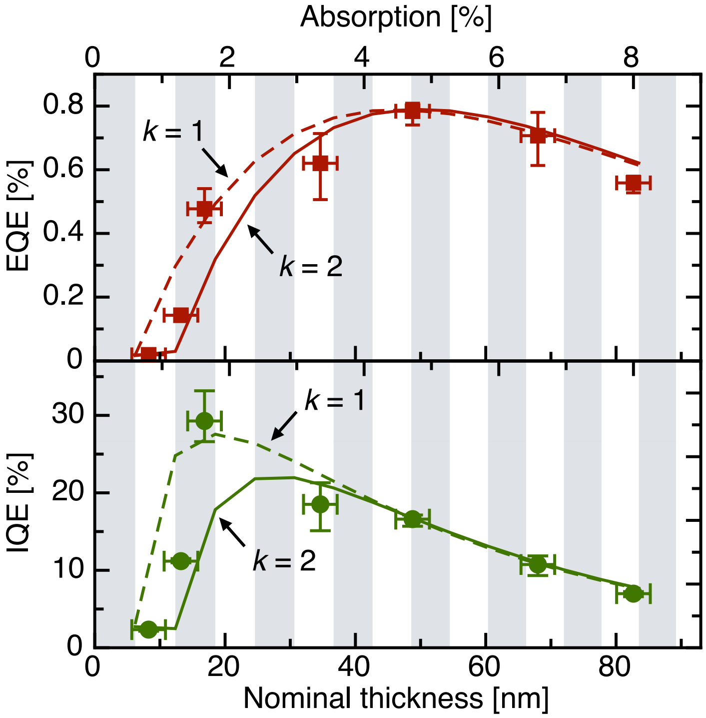

Figure 6-15: External quantum efficiency (EQE) (top) and internal quantum efficiency (IQE) (bottom) at $\lambda = 590$ nm versus nominal QD film thickness and device absorption at $\lambda = 590$ nm for devices with smooth QD films printed with parylene-C. The data is fitted to a model which takes into account either one ($k = 1$) or two ($k = 2$) low-efficiency QD monolayers adjacent to the top ITO electrode. Nominal thicknesses are calculated assuming an absorption coefficient of 10^4 cm^{-1} at $\lambda = 590$ nm.

Table 6.1: Summary of conversion efficiencies for devices with varying QD layer thicknesses.

Absorption[a] [%]	**Thickness**[b] **[nm]**	J_{SC}[c] **[A/cm^2]**	V_{OC}[c] **[V]**	FF[c]	η_{Int}[d] [%]	η[e] [%]
1.2	8	1.23e-5	0.90	0.34	0.60	2.8e-3
1.6	13	1.47e-5	1.15	0.30	0.62	3.7e-3
2.1	16	5.84e-5	0.90	0.31	1.56	0.012
2.9	34	8.07e-5	1.17	0.42	2.71	0.029
3.9	40	6.90e-5	1.32	0.40	1.86	0.027
4.6	48	7.28e-5	1.25	0.38	1.50	0.025
6.9	68	6.77e-5	1.34	0.34	0.90	0.023
8.0	83	3.62e-5	1.15	0.29	0.30	8.8e-3

---

[a] QD Absorption at $\lambda = 521$ nm

[b] Nominal QD thickness obtained at $\lambda = 590$ nm for $\alpha = 10^4$ cm^{-1}

[c] Measured at $\lambda = 521$ nm and 50 mW/cm^2

[d] Internal monochromatic power efficiency at $\lambda = 521$ nm and 50 mW/cm^2

[e] Solar conversion efficiency under an equivalent intensity of 136 mW/cm^2 at AM 1.5 G

The EQE is the product of four charge generation processes, given by[40, 12]

$$\eta_{EQE} = \eta_\alpha \, \eta_{ED} \, \eta_{CT} \, \eta_{CC} \tag{6.13}$$

where η_α is the absorption, η_{ED} is exciton diffusion efficiency, η_{CT} is the charge transfer (interfacial dissociation) efficiency and η_{CC} is the carrier collection efficiency.

Beginning with absorption in the QD layer, an absorption coefficient $\alpha = 10^4$ cm^{-1} gives an absorption efficiency per QD monolayer $\eta_{\alpha_i} = 0.994$. Assuming all other processes have a constant efficiency of 64% results in a monotonically increasing EQE and and a flat IQE (Figure 6-16). However, it is likely that photogeneration in the monolayer closest to the ITO electrode is compromised due to ion bombardment during sputtering. Treating the monolayer adjacent the ITO electrode as having a uniquely low efficiency accurately predicts the fall in IQE at thicknesses of one and two monolayers (Figure 6-17). Properly treating the effect of exciton diffusion on EQE requires solving the exciton continuity equation and assuming knowledge of the boundary conditions at both QD film interfaces.[87] In order to keep the model simple and more general, we make the crude assumption that the exciton transfer efficiency from QD to QD follows an exponential decay with distance

$$\eta_{ED_0} = e^{-\Delta x/\gamma_{ex}} \tag{6.14}$$

were Δx is the width of one monolayer and γ_{ex} is the characteristic exciton diffusion length. Including η_{ED} with $\gamma_{ex} = 43$ nm forces the EQE to asymptotically approach $\sim 2.6\%$, which corresponds to the EQE contribution from the first 43 nm of the QD film (Figure 6-18). Adding additional thickness to the QD film beyond 43 nm will not result in reduced EQE unless the carrier collection efficiency is taken into account. Again, we assume a crude formula for electron transfer between QDs, given by

$$\eta_{CC_0} = e^{-\Delta x/\gamma_n} \tag{6.15}$$

where γ_n is the characteristic electron diffusion length. Including η_{CC} with $\gamma_n = 68$ nm replicates the observed decrease in EQE and IQE (Figure 6-19). The full model can be summarized with the following equation for the EQE of a device with j QD monolayers

$$\eta_{EQE}(j) = \left(\sum_{i=1}^{j-k} \eta_{\alpha_i} \eta_{CT} (\eta_{ED_0})^i + \sum_{l=1}^{k} \eta'_{EQE} \right) (\eta_{CC_0})^j \tag{6.16}$$

where the first summation term represents the efficiency of the properly functioning QD layers and the second summation term represents the efficiency of the damaged QD layers. The carrier collection term is factored in after the number of carriers generated from each monolayer is tabulated. The dramatic decrease in EQE and IQE with increasing thickness suggests that charge-carrier losses are pervasive, with fewer carriers able to successfully cross the bulk QD film as thickness is increased. Given a peak IQE at a QD thickness of only 3 monolayers, corresponding to an absorption of only 1.6%, it is clear that further work is needed to optimize η_{ED}, η_{CC} and η_{α}.

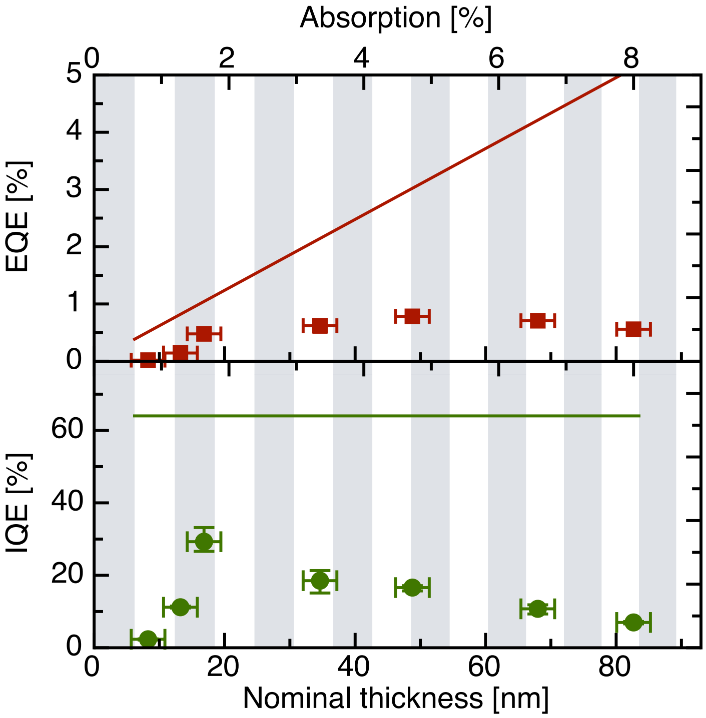

Figure 6-16: External quantum efficiency (EQE) (top) and internal quantum efficiency (IQE) (bottom) versus nominal QD film thickness and device absorption. The data is fitted to a model which only considers η_α for $\alpha = 10^{-4}$ cm^{-1} and assumes all other processes have an efficiency of 64%.

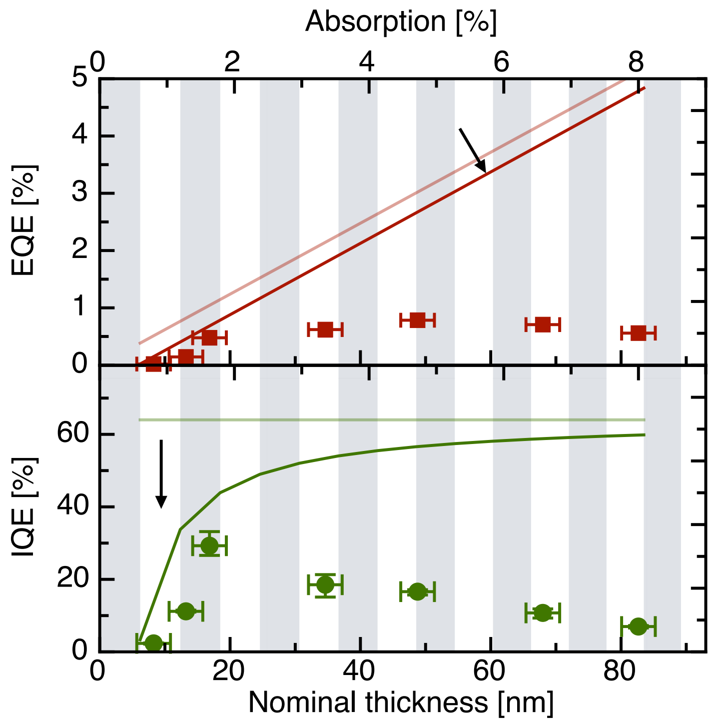

Figure 6-17: External quantum efficiency (EQE) (top) and internal quantum efficiency (IQE) (bottom) versus nominal QD film thickness and device absorption. The fit shows the effect of including one low-efficiency QD monolayer adjacent to the top ITO electrode.

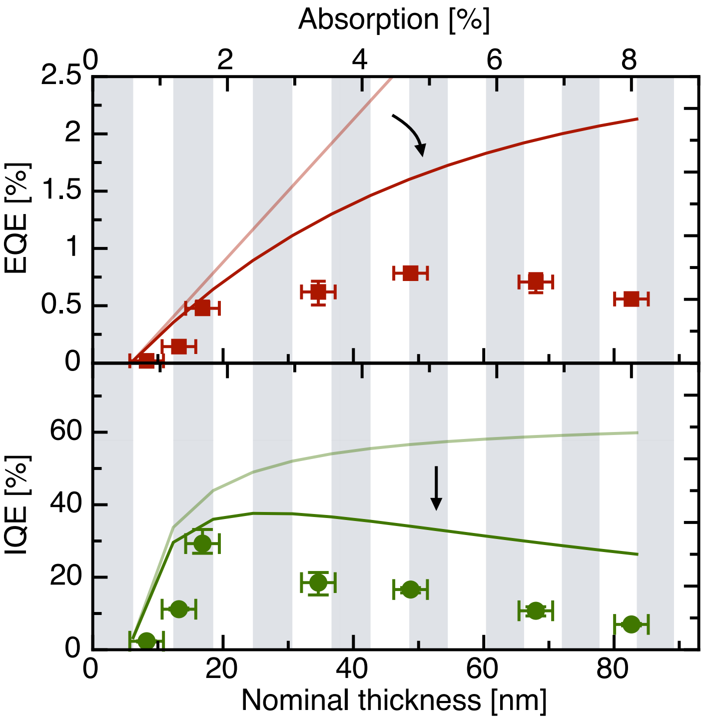

Figure 6-18: External quantum efficiency (EQE) (top) and internal quantum efficiency (IQE) (bottom) versus nominal QD film thickness and device absorption. The fit shows the effect of including $\gamma_{ex} = 43$ nm.

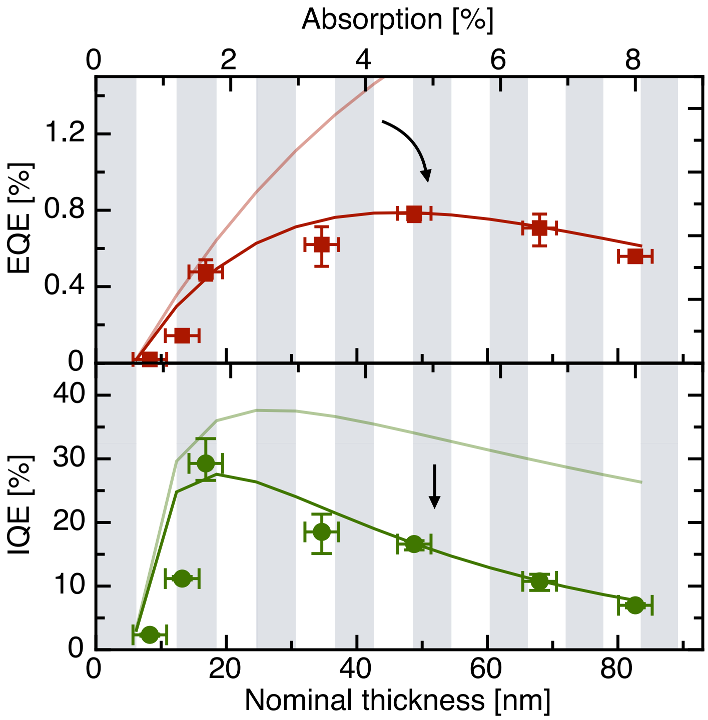

Figure 6-19: External quantum efficiency (EQE) (top) and internal quantum efficiency (IQE) (bottom) versus nominal QD film thickness and device absorption. The fit shows the effect of including $\gamma_n = 68$ nm.

6.10 Conclusion

The high V_{OC} demonstrated in devices with a smooth QD film is the first observation of V_{OC} exceeding the HOMO/LUMO offset in donor/acceptor heterojunction photovoltaic cells. The measured V_0, which represents the maximum obtainable V_{OC}, is only 0.44 V less than the QD bandgap, near the theoretical maximum V_{OC} at room temperature. Overcoming the HOMO/LUMO offset implies that other donor/acceptor photovoltaics, such as polymer bulk heterojunction and small-molecule photovoltaics, may have theoretical efficiencies that are much higher than previously thought, provided that interfacial recombination rates can be reduced. The top ITO electrode structure represents a critical step toward improved long-term stability due to the absence of a low work function cathode, and opens up the potential for new applications, such as light-activated touch screens and tinted power-generating windows. Finally, we envision the incorporation of chemical treatments[63] to improve transport and/or new QD materials will result in improved conversion efficiencies.

In summary, we demonstrate an improved V_{OC} in a bilayer heterojunction photovoltaic device consisting of a CdSe QD film that is printed with a parylene-coated PDMS stamp. The enhanced device characteristics stem from reduced dark current associated with the elimination of voids in the QD film. A high V_{OC} and photo-induced V_0, which exceed the HOMO/LUMO offset at the spiro-TPD/QD heterojunction, are attributed to a low diode turn-on voltage due to suppressed recombination at the spiro-TPD/QD heterojunction. Measurement of the voltage dependence of the transient photocurrent decay identifies charge diffusion as the dominant mechanism responsible for photocurrent generation. Electroluminescence from the QD layer confirms the role of hole injection from spiro-TPD into the QD film and recombination in the QD film as a conduction mechanism in forward bias. Solar conversion efficiencies are shown to be limited by low absorption in the QD film, which must remain optically thin in order to minimize transport losses. Further work is needed to improve transport and enhance absorption in the QD film.

Chapter 7

Tandem structures and future work

Most of the discussion in this thesis has focussed on the implementation of a quantum dot (QD) solar cell comprised of an organic/QD heterojunction sandwiched between a top and bottom electrode. We found that the efficiency of the cell is absorption limited because the thickness of the QD layer must be kept sufficiently thin in order to accommodate short exciton and electron diffusion lengths, a common occurrence for donor/acceptor solar cells. In this section, we demonstrate a proof-of-principle device that consists of two identical QD solar cells, one grown on top of the other, forming a double tandem cell. This tandem cell represents an important alternative to a bulk heterojunction as a method of solving the exciton diffusion bottleneck in donor/acceptor heterojunction solar cells. We also detail the many potential opportunities for improving the efficiency QD heterojunction solar cells.

7.1 Introduction

As described earlier in this thesis, a number of approaches to overcoming the exciton diffusion bottleneck in donor/acceptor solar cells, including bulk-heterojunction geometries (Section 1.2) and light-trapping techniques (Section 3.2.4) have been extensively investigated, often yielding impressive gains in efficiency over simple devices with discrete layers [117]. A third approach involves stacking multiple discrete layered devices in tandem in order to transform an otherwise optically thin device into one with significant absorption [38, 39]. The individual devices are connected in series, imparting extra open-circuit voltage V_{OC} with each added cell, yet maintaing the same short-circuit current J_{SC}. The challenge, then, is to ensure that each subcell in the stack produces the same current, which can be accomplished by setting the thickness of each subcell appropriately. The correct subcell thickness must be derived from optical interference and exciton diffusion modeling [46]. Another challenge involves the choice of interstitial electrode layer(s) used to provide the series connection between the top and bottom cell. Three requirements for an effective interstitial electrode layer are:

- Transparency
- Mechanical stability suitable for fabrication of the top cell without damaging the bottom cell
- Electron work function level compatibility with high V_{OC} and J_{SC} for both the cathode of the bottom cell and anode of the top cell

Given that the performance of most donor/acceptor solar cells is highly dependent on the choice of metal cathode [91], the first and third requirements have proven to be a significant obstacles [43]. In most cases, a thin layer of Au or Ag clusters is used as the interstitial layer, although metal oxides in combination with poly(3,4-ethylenedioxythiophene) poly(styrenesulfonate) (PEDOT:PSS), have also been successfully employed [48, 118, 41]. Unlike most donor/acceptor heterojunction devices architectures, the QD heterojunction device presented in this thesis is a natural candidate for a tandem structure because the anode and cathode are both fully-transparent indium-tin-oxide (ITO), and the PEDOT layer provides mechanical planarization of the bottom cell for fabrication of the top cell.

As a proof-of-concept, we have fabricated a tandem cell consisting of two stacked QD devices, a diagram of which is shown in Figure 7-1. The device growth process proceeds exactly as outlined for a single device in Section 4, except that a thin layer (20 nm) of ITO is deposited as the intermediate cathode.

We find that V_{OC} of the stacked device is nearly double ($V_{OC} = 2.67$ V) that of the individual cell ($V_{OC} = 1.48$ V), and the overall solar conversion efficiency more than doubles, from $\eta_P = 0.018\%$ to $\eta_P = 0.037\%$ (Table 7.1). Although absorption losses are still limiting the conversion efficiency, the successful implementation of a tandem structure establishes the potential for greater efficiency improvements by using the simple technique of stacking an increasing number of cells.

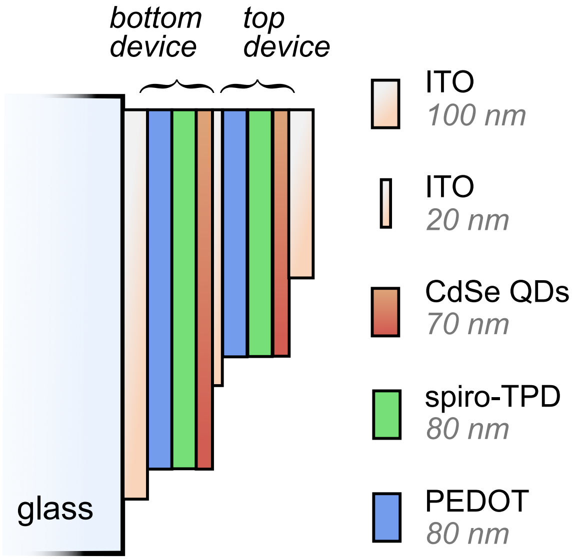

Figure 7-1: Schematic of tandem QD device structure.

7.2 Proof-of-concept device

The current-voltage (i-v) characteristics, plotted in Figure 7-2, show a near doubling in V_{OC}, turn-on voltage (V_{ON}) the compensation voltage (V_0) (or maximum V_{OC}). The doubling in V_{OC} verifies that a tandem structure has been achieved, with both top and bottom devices acting properly. The fill factor is low, as expected for a 70 nm film where transport losses impart a strong bias dependence to the photocurrent. The cause of a slightly increased J_{SC} in the double cell is unknown, although we should note that variations in J_{SC} from device to device are not uncommon. The V_{OC} of 2.67

V is much greater than any other published value for donor/acceptor photovoltaics [119].

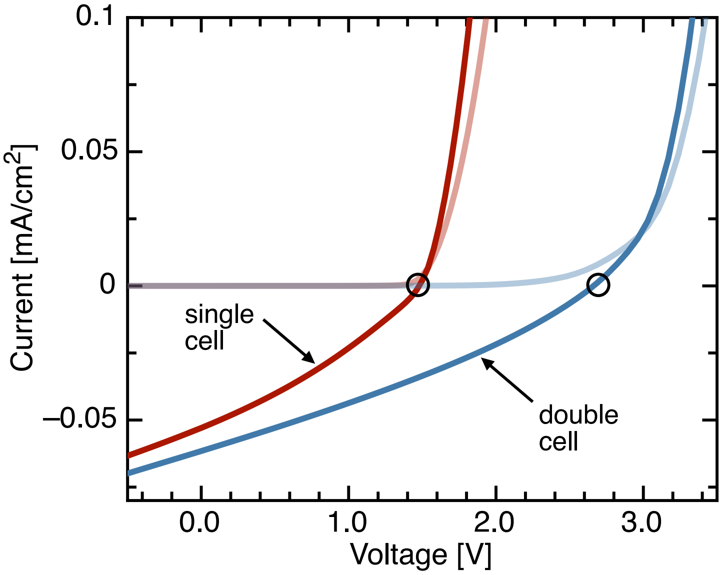

Figure 7-2: Current-voltage characteristics under an illumination intensity of 50 mW/cm^2 at $\lambda = 521$ nm for a single cell QD device and a double cell device.

In situ absorption spectra of the single and stacked devices show a doubling in absorption, indicating that the top QD layer has been deposited successfully (Figure 7-3). The external quantum efficiency (EQE) and internal quantum efficiency (IQE) of the single cell show somewhat lower-than-usual values (IQE $\sim$ 20% should be achievable) possibly due to the excessive thickness of the QD layer. Further work is need to optimize both the efficiency of the individual cells and improve the masking scheme in order to allow for more than two stacked cells.

7.3 Opportunities for future work

At least a two order of magnitude improvement in efficiency is required in order for the QD devices structures presented here to approach commercial viability. We've argued that single-bandgap tandem structures can provide a pathway toward higher

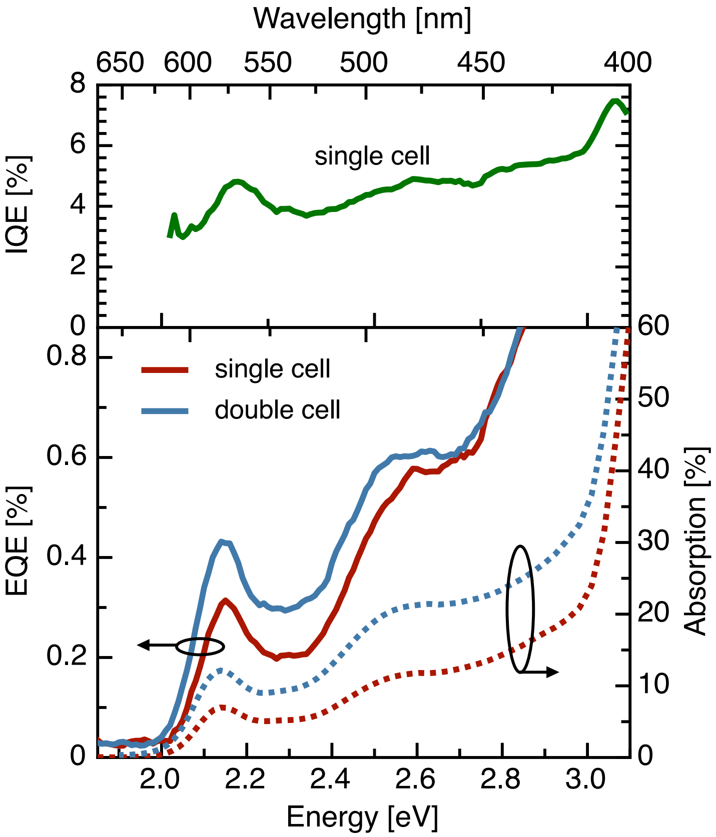

Figure 7-3: External quantum efficiency (EQE) and absorption for a single cell and double cell QD device, and internal quantum efficiency (IQE) for the single cell device.

Table 7.1: Solar conversion efficiencies for single and double cell QD devices.

Device	J_{SC}[a] **[A/cm^2]**	V_{OC}[a] **[V]**	FF[a]	η_P[b] [%]
Single cell	3.3e-5	1.48	0.32	0.018
Double cell	4.7e-5	2.67	0.31	0.037

---

[a] Measured at $\lambda = 521$ nm and 50 mW/cm^2

[e] Solar conversion efficiency under an equivalent intensity of 136 mW/cm^2 at AM 1.5 G

efficiency for devices that are absorption-limited. In order to approach that limit, the internal monochromatic power efficiency of each constituent cell needs to be close to the theoretical limit, for example, $\eta_{Int} \approx 80\%$ at $h\nu = 2$ eV. Our best internal power efficiency is close to 3%, meaning that a factor of ∼25 improvement is desired. At best, the fill factor can be improved by a factor of 2, leaving the remaining factor of 12.5 to be accomplished by solving transport losses across the QD layer, damage to the top QD monolayers due to ITO deposition and the inherent inefficiency of the QDs themselves due to nonradiative decay. Below, we will outline a few of the many routes toward more efficient QD films, most involving improved surface passivation and improved dot to dot coupling. In addition, our QD core material, CdSe (the prototypical QD material) whose bandgap is ∼2 eV, is far from the optimal bandgap of 1.4 eV. Other QD materials have have properties that are more compatible with solar energy conversion. Finally, more sophisticated device architectures can be integrated into our QD structure, such as light-trapping and improved transport layers.

7.3.1 Modifying capping groups

Many groups have shown that the capping groups surrounding the QD core influence the opto-electronic functionality of the QD layer. The challenge is to properly passivate nonradiative surface states while maintaining strong overlap between wavefunctions of neighboring dots. The three broad categories of QD surface modification can result in improved performance:

Inorganic QD shell: Employing an inorganic shell in place on native ligands can increase the quality of passivation. Porter et al. [120] have shown that the photogeneration efficiency of CdSe QD films in lateral devices is enhanced when zinc sulfide (ZnS) shells are used to cap the QD core, without seriously affecting the film mobility. However, in order to obtain high efficiencies, the extra organic ligands must be removed by a thermal anneal at 300°C or a methanol treatment. The challenge is to incorporate the ligand removal process prior to transfer of the QD film onto the spiro-TPD without damaging the stamp or strongly adhering the QDs to the stamp.

Chemical post-treatments: Using chemical treatments to exchange native ligands with more electrically compatible ligands can increase film conductivity and reduce nonradiative processes. Oertel el al. [69] found that post-deposition treatment of CdSe QD films with n-butylamine greatly increases the QD film EQE in photovoltaic devices. Barkhouse et al. [121] similarly found a large increase in EQE with ethanethiol post-treatment. In our initial efforts, we had varying success transferring QD films after post-treatments.

Post deposition physical treatments: Another way to remove unwanted ligands from the QD film is to do so after the QDs have been transfered onto the hole-transport layer. UV ozone or oxygen plasma treatments may be able to remove ligands from the QD film without damaging underlying layers.

7.3.2 Choosing viable QD materials

Among the multitude of materials investigated in the fifties and sixties, amorphous silicon (a-Si), copper indium gallium (di)selenide (CIGS) and cadmium telluride (CdTe) are the only commercially viable thin film solar materials to have emerged. Both CIGS and CdTe rely on a heterojunction with cadmium sulfide (CdS) which was found to be critical for high efficiency [122]. One of the promises of QD technology is to expand the material base available for solar photovoltaics by lifting the restrictions imposed by traditional film deposition methods, such as the need for a CdS heterojunction, columnar grain structure and surface state passivation. The remaining requirements for QD systems are outlined well by Wadia et al. [75]:

Non-toxic: There is debate about the need for non-toxic materials. An argument can be made that an encapsulated module is not an environmental risk as long the module is recycle at its end of life. However, the manufacture of modules using toxic materials can impose additional costs and increase the environmental impact at the manufacturing cite.

Earth abundant: Material availability is a critical problem for CdTe and CIGS, but copper zinc tin sulfide (CZTS), lead sulfide (PbS), nickel sulfide (NiS), cuprous oxide (Cu_2O), zinc phosphide (Zn_3P_2), cupric oxide (CuO), copper sulfide (CuS_2) and iron pyrite (FeS_2) are readily abundant and have yet to be fully explored as potential QD solar cell candidates [75].

Infrared absorbing: QD semiconductors with a bandgap close to 1.4 eV have a theoretical efficiency of 31% as opposed to a 2 eV material, like CdSe QDs, which has a theoretical efficiency of 20%. For multiple-bandgap tandem cells, materials need to be identified with bandgaps near 0.7 eV, 1.2 eV and 1.8 eV.

Balanced electron/hole mobilities: Throughout this work, we assume the QD film has only one active interface: the spiro-TPD/QD heterojunction. However, the QD/ITO heterojunction may also be capable of dissociating excitons. In this case, transport of holes across the QD film is required in order to produce photocurrent. An ideal absorbing material would have comparable electron and hole mobilities so that both the front and back side of the QD film could contribute equally to the photocurrent, thus enhancing the QD internal quantum efficiency.

7.3.3 Improving device architectures

Optimizing device architectures has not been a focus of this thesis, yet a large set of possible improvements could dramatically effect the device efficiency:

Light-trapping techniques: Internally efficient devices that are absorption-limited can benefit from geometric or optical light-trapping techniques (Section 3.2.4). Adding a simple rear reflector will add almost a factor of two to the external conversion efficiency.

Highly passivated QDs at interface: If high V_{OC} is indeed due to suppressed recombination at the spiro-TPD interface, we may be able to print a thin highly passivated QD layer at the interface, followed by a thicker QD layer with shorter ligands, better conductivity and a longer exciton diffusion length. The bulk of absorption would occur in the high-conductivity region, but recombination at the interface would remain suppressed, thus retaining high V_{OC} while improving absorption and charge transport.

Doped transport layers: The use of doped transport layers, either with tertbutyl pyridine, a lithium salt ionic dopant and a chemical dopant (used for solid state dye-sensitized cells) [123] or a tetrauoro-tetracyano-quinodimethane (F_4-TCNQ) (used in p-i-n solar cells) [30] can improve V_{OC}, FFs and charge transport by helping to shield internal electric fields.

Electron transport layers: Protection of the QD film during deposition of the ITO top electrode could alleviate damage to the QD film. A transparent organic electron transport layer such as C60 or an exciton blocking layer such as bathocuproine (BCP) could serve as a sacrificial layer and help preserve the integrity of the surface of the QD film.

Metal-oxide transport layers: Transition metal oxide anodes or cathodes such as the n-type titanium dioxide (TiO_2) [124] or the p-type tungsten oxide (WO_2) [125] have been shown to enable improved fill factors in conjugated polymer devices. Metal oxides are also more robust than organic films and can withstand thermal annealing and chemical treatments. The challenge is to recreate the rectified junction that forms between spiro-TPD and ITO, which is essential for achieving high V_{OC} and non-shunted device characteristics.

Ten stacked cells: Currently, stacking more than two cells is complicated by the fact that the intermediate electrode must be patterned, as well as the top and bottom electrodes. Alternatively, one could blanket deposit each layer in the device stack and use a laser cutter to define the device as the final step. This technique would make stacking additional cells almost trivial, since each addition cell would only require an extra hour or so, with our current setup. Potentially more ten cells could be easily stacked using this process.

7.4 Conclusion

The fabrication of the first ever tandem QD solar cell and the achievement of the highest V_{OC} (2.67 V) to date for a donor/acceptor solar cell represents a major step toward the goal of high efficiency QD based photovoltaics. The simple discrete layered organic/QD heterojunction structure, which employs ITO for both anode and cathode, naturally accommodates tandem structures without loss of J_{SC} or V_{OC}. This result implies that as long as the internal power efficiency of a single QD solar cell can be made to reach a certain value, the external power efficiency of QD tandem structures should be able to approach the same efficiency. Further work is needed to optimize the internal efficiency of individual QD devices and improve the masking process in order to accommodate tandem structures with more than two stacked cells.

A number of potential material improvements, new processing techniques and new devices structures are suggested which may lead toward improved efficiency.

Chapter 8

Conclusion

8.1 Summary

The broad goal of this thesis has been to explore the use of colloidal quantum dots (QDs) as the primary photoactive species in a photovoltaic device. As a first background exercise, the issues governing adoption of solar cell technologies were studied in order to gain an understanding of the real world market needs for an emerging solar photovoltaic technology. We found that the scale of energy demand is enormous, most likely overwhelming the projected supply of photovoltaics within the next 20 years. Material availability, scalability and high efficiency are the three essential requirements for an emerging solar technology to exceed the capacity of existing photovoltaic technologies.

Next, we set out to develop a device structure that could, in principle, meet the three seemingly daunting goals mentioned above. We proposed a simple planar heterojunction device consisting of organic small molecules and colloidal QDs. The simplicity of the device design and the ability of some QD materials to absorb infrared light were the two primary factors motivating the planar QD device architecture. In order to solve the problem of low absorption, a symmetric electrode structure was chosen so that multiple cells could be easily stacked together. In order to construct the device, a new fabrication process involving printing the quantum dots onto an organic film was implemented. In addition, the innovative use of a transparent indium tin oxide (ITO) top electrode enabled the successful realization of the symmetric electrode structure.

Our initial findings revealed low efficiencies, but were encouraging for three reasons. First, the device operated as a photovoltaic even when the QD film was made extremely thin and incomplete. Such a tolerance to voids in the active film has the potential to be tremendously useful for scientist attempting to characterize the photosensitivity of nanometer-scale thin films or materials that exhibit nanoscale range phenomena. In addition, without the need to worry about voids, material waste can be minimized in devices that require additional thickness simply to avoid shunting (a problem with cadmium telluride cells, for example). Second, the open-circuit voltage (V_{OC}) was found to be much higher than expected for a device with symmetric electrodes. Third, the device stability was exceptional, with some devices nearly unchanged after more than a year of storage.

An improvement in uniformity and completeness of the QD film was accomplished by using a lower surface energy polymer, parylene-C, coated on the PDMS stamp used for QD deposition. The resulting devices produced V_{OC}s greater than 1.3 V, the first observation of V_{OC} higher than the HOMO/LUMO gap in a donor/acceptor heterojunction device. This result led us to perform a number of measurement to help understand the origin of the high V_{OC}. Measurement of the voltage dependence of the transient photocurrent decay identified charge diffusion as the dominant mechanism responsible for photocurrent generation. Electroluminescence from the QD film confirmed that recombination in the QD film is in part responsible for dark current flow in forward bias. Measurement of the quantum efficiency versus bias demonstrated that the quantum efficiency is independent of intensity. In order to explain these results and the magnitude of V_{OC}, we employed a model that describes the maximum V_{OC} as dependent on only one quantity: the energy level separation over which recombination takes place. We concluded that recombination at the spiro-TPD/QD heterojunction must be strongly suppressed, leaving V_{OC} limited by recombination in the QD layer itself. Photocurrent transient decay rates measured at an applied bias of 2 V support this conclusion, revealing a long carrier recombination lifetime greater than 0.4 ms.

Finally, an attempt was made to improve absorption by fabricating a tandem structure consisting of two identical stacked devices. A doubling in efficiency was observed, signaling the successful implementation of the first proof-of-concept tandem QD heterojunction device. A host of material improvements and device structure improvements were proposed that should result in large enhancements in efficiency.

8.2 Looking forward

Our demonstration of V_{OC} in a donor/acceptor photovoltaic device that is not limited by the energy gap across the heterojunction is a stark illustration of the need to reassess the current theoretical understanding of the photovoltaic effect in donor/acceptor systems, develop new design rules for obtaining efficient donor/acceptor photovoltaics and arrive at better ways to predict the maximum theoretical efficiency of donor/acceptor photovoltaics.

We've attempted to explain the magnitude of V_{OC} by equating the maximum theoretical V_{OC} to the maximum energy separation between the electron and hole quasi Fermi levels, an assumption borrowed from the physics of inorganic solar cells. A number of valid questions can be raised about this interpretation. For example, how does one draw the quasi Fermi levels across the entire device under applied bias? How can we account for the recuperation of the energy lost during exciton dissociation and charge transfer?

To illustrate the latter question, we have drawn the band diagram for a typical donor/acceptor device structure consisting of two semiconductors with identical bandgaps E_g and energy levels offset by energy ΔE_1 (Figure 8-1A). In this structure, the conventional description of the origin of V_{OC} would predict that the maximum $qV_{OC} = E_g - \Delta E_1$, where ΔE_1 is the energy lost during charge dissociation at the interface. Now consider the hypothetical device structure presented in Figure 8-1B, consisting of multiple heterojunction layers with cascading energy levels offset in energy by ΔE_2, all of the same bandgap E_g and surrounded by wide bandgap

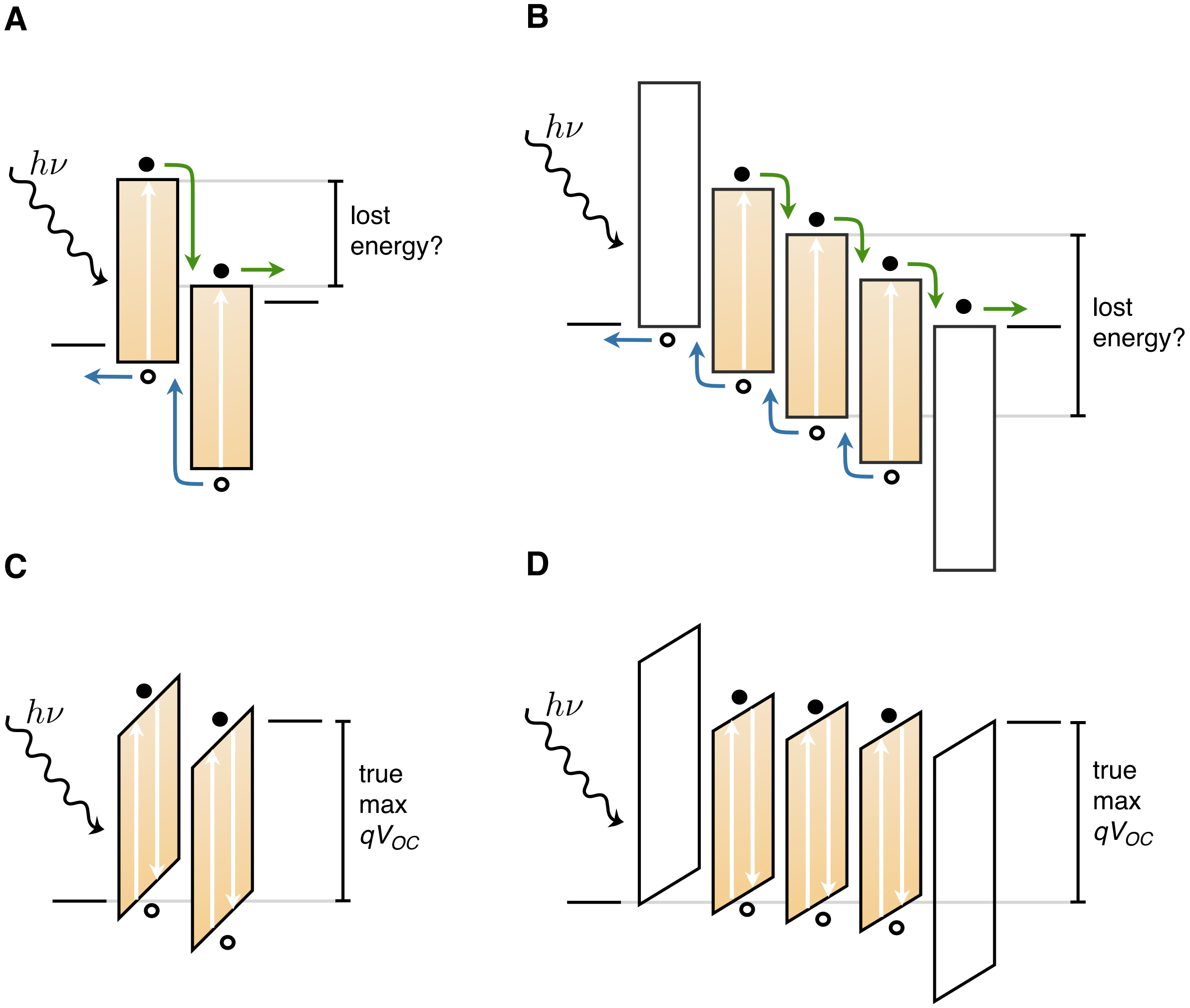

Figure 8-1: Band diagram for a hypothetical device with cascading energy levels at (A) zero bias and (B) V_{OC}.

charge-transporting layers at the contacts. A fundamental contradiction arises when the conventional description is applied to this structure. Since the energy lost at each interface is ΔE_2, the total electron and hole energy lost for each layer is $4\Delta_2$. If the energy levels are chosen such that $4\Delta_2 = E_g$ (as drawn in Figure 8-1B), then this device should produce a maximum $V_{OC} = 0$ according to the conventional description. But if $V_{OC} = 0$, then $J_{SC} = 0$, which doesn't make sense – the cascading energy levels should efficiently drive electrons and holes to their appropriate electrodes, resulting in a strong photocurrent. Furthermore, one would expect this structure to display a particularly high V_{OC} since reversing the direction of charge flow is hindered by both the presence of the blocking layers at the electrodes and the cascading energy levels. The conventional description of the link between exciton energy loss and V_{OC} is clearly broken since it fails to accurately predict V_{OC} for device structures with more than one heterojunction.

In contrast, our interpretation – that V_{OC} is determined by the energy level separation in the region where recombination occurs – predicts that the maximum V_{OC} is E_g/q when recombination occurs in the bulk or $(LUMO - HOMO)/q$ for interfacial-dominated recombination. However, illustrating the band diagram at V_{OC} (shown in Figures 8-1A & B) is problematic because it is unclear how to accurately draw the quasi Fermi levels, which are typically flat at V_{OC}. Further theoretical work is needed to clarify the behavior of the quasi Fermi levels at applied bias.

Perhaps the most important question is whether the high V_{OC} is compatible with high exciton separation efficiency? In other words, is there a fundamental trade-off between V_{OC} and the short circuit current (as observed in solid state dye-sensitized cells employing an insulating interstitial layer at the heterojunction [126])? A more complete device modeling effort and further experimentation should shed light on these issues. In particular, solving the transport equations using the carrier lifetimes obtained in Chapter 6 will help us understand how the relationship between charge separation and charge recombination lifetime is related to the charge separation efficiency and the maximum V_{OC}. Measurement techniques such as transient open-circuit voltage decay [127] and photo-induced charge extraction by linearly increasing voltage (CELIV) [128] can be used to verify carrier lifetimes, while transient absorption spectroscopy (TAS) [129, 113] and photoinduced absorption (PIA) [64] can give information about the charge separation dynamics.

Another important question to consider is the following: will a well-passivated donor/acceptor heterojunction with suppressed recombination – believed to be the cause of high V_{OC} in our QD device – result in enhanced V_{OC} in bulk heterojunction geometries? Surface passivation could be studied, for example, by covering the surface of the porous titanium dioxide TiO_2 with insulating organic capping groups in interpenetrating TiO_2/polymer devices [31]. Alternatively, organic molecules with greater steric hindrance might be engineered to restrict interfacial recombination in small molecule devices.

Looking forward, new design rules for donor/acceptor photovoltaics should be adopted based on the notion that high V_{OC} can be obtained by suppressing interfacial recombination. The first and foremost implication of this work is that new material sets with large HOMO/LUMO offsets should be not be excluded outright. Instead, the relative rates of dissociation versus recombination should be given greater priority. In addition, suppression of recombination at the device contacts should also be taken into consideration. Employing wide bandgap transport layers at the contacts could be one way to

- reduce recombination at the electrodes
- avoid the presence of midgap states located near the charge transfer state, which could enhance interfacial recombination
- help block shunting that may occur through the absorbing film(s).

Finally, employing only a single absorbing layer or multiple absorbing layers with the same bandgap could have advantages when building tandem structures. Since the V_{OC} of a cell with multiple bandgaps is determined by the smallest bandgap, avoiding absorption from higher bandgap materials will result is less wasted voltage that could otherwise be harnessed using a multiple bandgap tandem structure.

As a final thought, I hope that others in the field will benefit from our assessment that high efficiency is a critical requirement for all emerging photovoltaic technologies, even those that anticipate to be low cost. I believe that the techniques used to achieve high V_{OC} presented in this thesis can be applied to other QD device types and other types of donor/acceptor photovoltaics in order to increase conversion efficiencies beyond the presently observed limits.

Appendix A

Ideal module specifications

What happens to the cost of a solar installation if some parameter - cost, efficiency, voltage, weight or size - changes? Consider the case of 50 V modules (typical for thin film), as opposed to 25 V modules (typical for crystalline silicon (c-Si)). Ten 50 V modules can be connected in series to produce 500 V, the upper voltage limit allowed under current regulations, while twenty 25 V modules must be connected in series in order to obtain the same voltage. However, connecting twenty modules in series can be difficult for installers because of two reasons. First, a parallel connection is easier than a series connection since a parallel connection simply requires connecting the end of a string to a junction box, while a series connection requires connecting the correct input and output on each panel. Second, a string of low voltage modules connected in series can be upwards of 10-15 m long and might not fit easily on a roof without being broken up into sections, resulting in more complicated wiring, longer install times and potential wiring errors. The alternative is to use shorter strings at only 250 V, for example, but this requires using higher amperage cabling at a higher cost.

Other parameters are similarly important. The weight of a module must be less than 16 kg - the weight that one person can carry - or else a crane is required. On the other hand, the size of a module should be as big as possible, reducing the number of connections and wiring. In addition, the way modules are secured to the racking system can influence system cost. For example, c-Si modules are often made with

Table A.1: Desired module specifications according to a survey of installers. Typical c-Si and thin film modules specs are give as a comparison.

Module attribute	**Desired specs**	**Comment**	**c-Si**	**Thin film**
Efficiency	18%	most important cost factor	14.1%	10.07%
Area	0.9 m2	large as possible	1.28 m^2	0.72 m^2
Weight	14.4 kg	not greater than 16 kg	15.5 kg	11.4 kg
Power	162 W	above 160 W	180 W	72.5 W
Voltage	55 V	not greater than 60 V	35.6 V	67.9 V
Voltage (V_{OC})	69 V	not greater than 75 V[a]	44.4 V	90 V
Current	2.9 A	low as possible[b]	5.06 A	1.07 A
Fuse current	15 A	high as possible	15 A	10 A
Framing	frameless	efficient clips	frame	frameless

---

[a] V_{OC} should be even multiple of (inverter voltage x 85%)
[b] I_{SC} should be even multiple of (fuse current x 85%)

an aluminum frame which keeps the front glass and the module backing secured. The modules are then attached to the racking with bolts and the entire apparatus must be grounded with extra cabling. However, modules consisting of two laminated pieces of glass can be connected with clips to the racking system, resulting in a quicker installation procedure and fewer grounding connections. We've summarized the desirable physical attributes in Table A.1, along with typical thin film and c-Si module parameters.

We are grateful to the installers and those familiar with installations, listed in Table A.2, who provided the above information.

Table A.2: Sources for desired module specifications provided in Table A.1.

Frank Wang	Stion Corporation
Albert Brown	Stion Corporation
Anthony Fotopolous	Conergy
David Levy	-
Jordan Sapp	3rd Rock Systems & Technologies, Inc.
Kevin Crystie	Helios Energy, LLC
Michael Rogol	Photon Consulting
MJ Shiao	Solar Design Associates, Inc.
Paul Lyons, P.E.	Zapotec Energy, Inc.
Rick Lavezzo	SunEdison, LLC

Appendix B

Procedure for pattering ITO-glass substrates

This document describes the procedure developed by John Kymissis for photolithographically patterning ITO-coated glass substrates, beginning with large 13" x 13" ITO-glass sheets. Following this procedure results in $4\frac{2}{3}$" x $4\frac{2}{3}$" patterned ITO glass slides that can then be cut into one inch or half inch substrates with the dicing saw. The $4\frac{2}{3}$" glass fits perfectly into our 170 x 90 mm pyrex crystallization dishes, which is useful when etching the ITO and stripping off the resist film. The 13" x 13" ITO-glass sheets and pyrex beakers are generally kept in the cabinet in the instrument room.

B.1 Supplies

- 13" x 13" ITO-glass sheet
- Diamond scribe
- 2 containers suitable for developing resist
- Acid-resistant wafer tweezers
- Sodium carbonate
- 2 170 x 90 mm pyrex crystallization dishes

- ITO etchant
- Hot plate
- Butyl gloves
- Face shield
- Isopropanol
- Ohmmeter

B.2 Procedure

1. Cut 13” x 13” sheets to size
    (a) Roughly measure out and mark $4\frac{2}{3}$” x $4\frac{2}{3}$” sized pieces
    (b) Scribe and break by hand
2. Pre-clean ITO-glass
    (a) Wipe with texwipe wetted with 2% micro90 in H_2O
    (b) Rinse with H_2O and then with isopropanol
    (c) Blow dry
    (d) UV-ozone for 5 minutes
3. Lamination
    (a) Mark ITO side
    (b) Turn on laminator and set temperature to 110C at speed = 1
    (c) Wait until roller is heated (display with say “ready”) and press “run” to laminate
    (d) Cut sample out of film, leave 1 cm margin around edge
4. Exposure and development
    (a) Mix up developer: 1% sodium carbonate in H_2O (10 g in 1l)
    (b) Fill second tank with H_2O
    (c) Place sample in drawer, safe from UV exposure
    (d) Set exposure to 14 units on the photolith machine
    (e) Press start and leave room until UV lamp is extinguished

    (f) Place sample under glass plate and apply vacuum
    (g) Expose samples
    (h) Cut top film around edge of sample
    (i) Remove top and bottom films, leaving middle resist layer
    (j) Develop in sodium carbonate bath until reflection of room lights can be seen in developed areas
    (k) Rinse in H_2O when developed
    (l) Dispose of developer in the drain and rinse containers

5. Etching
    (a) Using butyl gloves and face sheild, fill pyrex dish with stock ITO bath
    (b) Apply medium heat (setting = 3)
    (c) Etch sample for 15 minutes
    (d) Remove with acid resistant tweezers and rinse with water in fume hood sink
    (e) Blow dry and test conductivity of etched ITO regions
    (f) Carefully pour ITO etch into a large beaker using a funnel and then pour etch back into its original jar using funnel
    (g) Thoroughly rinse pyrex dish, let dry and return dish to instrument room

6. Stripping
    (a) Fill the other pyrex dish with isopropanol
    (b) Strip remaining photoresist
    (c) Rinse pyrex dish with isopropanol, let dry and return dish to instrument room

Appendix C

Procedure for cutting patterned ITO-glass using the dicing saw

This document describes the procedure for cutting half inch substrates out of a $4\frac{2}{3}$" x $4\frac{2}{3}$" piece of patterned ITO glass. Most supplies are located in the second from the top cabinet drawer closest to the dicing saw. The wafer-mounting film is located in the larger cabinet drawer and should be kept wrapped in black plastic to minimize UV exposure. To release substrates from the mounting film after cutting, place under UV lamp for 20 minutes. Consult the dicing saw manual located next to the saw for more detailed information. Please wear eye protection when operating the saw.

C.1 Supplies

- Wafer-mounting film
- Razor blade
- Scrap piece of ITO-glass
- Dicing saw blades suitable for cutting glass
- Adjustable wrench
- Allen wrench 5/16"
- Tweezers

- 3 pinned blade holder disassembly tool
- Ohmmeter
- Eye protection

C.2 Procedure

1. Laminate glass sample to wafer-mounting film
    (a) Cut out segment of mounting film
    (b) Tear end to separate plastic backing film from adhesive layer
    (c) Place adhesive layer face up on counter
    (d) Hold glass, ITO side up, at a 45° angle above the film
    (e) Press the glass onto the film and slowly slide both over the edge of the counter, applying pressure at the counter edge where the glass and film intersect
    (f) Avoid air bubbles between the glass and film
    (g) Trim film with razor as close as possible to the edge of the glass
2. Inspect saw
    (a) Consult log book to see if a Si or glass blade is installed.
    (b) Always remove plastic safety window and inspect blade, regardless of whether you need to change the blade or not. Check to ensure that the blade is not broken and that the holding nut is secure.
3. Change blade
    (a) Unscrew the holding nut with an adjustable wrench by turning the shaft with a hex wrench.
    (b) Remove washer
    (c) Use blade removal wand to extract blade holder piece
        i. Turn on vacuum pump
        ii. Turn on vacuum to blade removal wand by flipping switch under front left side of dicing saw
        iii. Place wand flush against saw holder piece and pull out saw holder piece
        iv. Turn off vacuum to wand
        v. Turn off vacuum pump

    (d) Open blade holder piece with 3 pin tool
    (e) Remove blade with tweezers, replace, reassemble holder piece, remount onto shaft, remount washer, tighten nut and fasten window

4. Programing dicing saw
    (a) Press and turn “Stop” button to turn on dicing saw
    (b) Press “Program,” chose a parameter, enter value given in the table below and press “Enter.” Units are in Mils

Parameter	Description	Value
Mode	substrate shape and cutting sequence	30
1st Index	length between cuts in y-direction	495
2nd Index	length between cuts in x-direction	495
Height	thickness of mounting film	3
Thickness	thickness of substrate and mounting film	43.5
Angle	angle between cutting directions	90
Speed	Mils/sec	150
*	substrate dimension in y-direction	4666
Dia	substrate dimension in x-direction	4666

    (c) Press “Reset”

5. Start saw
    (a) Turn on vacuum pump
    (b) Turn on nitrogen until resistance on multimeter drops
    (c) Press “Spindle” to start saw

6. Zero chuck
    (a) Put metal gauge disk on chuck
    (b) Press “Lock” to turn on vacuum to chuck
    (c) Press “Chuck Zero”
    (d) Press “Unlock” to release vacuum
    (e) Remove gauge disk

7. Make a test cut for reference

   (a) Laminate mounting film to a test piece of ITO glass
   (b) Place test sample on chuck and press “Lock”
   (c) Press “Align” and “Single Cut” to make one test cut down middle of sample
   (d) Turn on monitor
   (e) Move horizontal reference line on screen to center of previous cut by pressing “up” or “down” on side of camera housing.
   (f) Press “Fast” and “Left” to move chuck away from blade
   (g) Press “Unlock” and remove test sample

8. Align and cut substrates
   (a) Mount new sample
   (b) Press “Align”
   (c) Align patterned markers on substrate with reference line on monitor
   (d) Press “Autocut” to automatically cut all streets and then rotate chuck by 90^o
   (e) Repeat alignment and press “Autocut”

9. Remove sample and shut down system
   (a) Press “Standby” to stop saw
   (b) Press “Unlock” and remove sample
   (c) Turn off vacuum pump
   (d) Turn off nitrogen
   (e) Turn off monitor
   (f) Press “Stop” to turn off system

Appendix D

Contributions associated with this thesis

D.1 Publications

1. D.C. Oertel, M.G. Bawendi, A.C. Arango, and V.Bulovic. Photodetectors based on treated CdSe quantum-dot films. *Applied Physics Letters*, 87(21), Nov. 2005.
2. J.C. Ho, A.C. Arango, and V.Bulovic. Lateral organic bilayer heterojunction photoconductors. *Applied Physics Letters*, 93(6), Aug. 2008.
3. T.P. Osedach, S.M. Geyer, J.C. Ho, A.C. Arango, M.G. Bawendi, and V.Bulovic. Lateral heterojunction photodetector consisting of molecular organic and colloidal quantum dot thin films. *Applied Physics Letters*, 94(4), Jan. 2009.
4. A.C. Arango, D.C. Oertel, Y.Xu, M.G. Bawendi, and V.Bulovic. Heterojunction photovoltaics using printed colloidal quantum dots as a photosensitive layer. *Nano Letters*, 9(2):860863, Feb. 2009.

D.2 Patents

1. Phototransistor for Chemical Sensing, M.I.T. Case No. 10470, September 2003

2. Light Emitting Devices Including Semiconductor Nanocrystals, MIT Assignment 11452, February 2005
3. Electro-Optical Device, M.I.T. Case No. 12769, June 2007
4. Photovoltaic Device Including Semiconductor Nanocrystals, M.I.T. Case No. 12770, June 2007
5. Photovoltaic Device Employing Charge Cascade Layer(s), M.I.T. Case No. 12951, January 2008

Bibliography

[1] Department of Energy (DOE) Energy Information Administration (EIA). http://www.eia.doe.gov/.

[2] T.P.I Saragi, T Fuhrmann-Lieker, and J Salbeck. Comparison of charge-carrier transport in thin films of spiro-linked compounds and their corresponding parent compounds. *ADVANCED FUNCTIONAL MATERIALS*, 16(7):966–974, May 2006.

[3] Brooke Carlson, Kurtis Leschkies, Eray S Aydil, and X. Y Zhu. Valence band alignment at cadmium selenide quantum dot and zinc oxide (10(1)over-bar0) interfaces. *J Phys Chem C*, 112(22):8419–8423, Jan 2008.

[4] T.C. Chiang, K.H. Frank, H.J. Freund, A. Goldmann, F.J. Himpsel, U. Karlsson, R.C. Leckey, and W.D. Schneider. *Electronic Structure of Solids: Photoemission Spectra and Related Data*, volume 23a of *Group III*. Springer, Berlin, 1989.

[5] B O'Regan and M Gratzel. A low-cost, high-efficiency solar-cell based on dye-sensitized colloidal tio2 films. *Nature*, 353(6346):737–740, Jan 1991.

[6] Peter Bermel, Chiyan Luo, Lirong Zeng, Lionel C Kimerling, and John D Joannopoulos. Improving thin-film crystalline silicon solar cell efficiencies with photonic crystals. *Optics Express*, 15(25):16986–17000, Jan 2007.

[7] G YU, J GAO, JC HUMMELEN, F WUDL, and AJ HEEGER. Polymer photovoltaic cells - enhanced efficiencies via a network of internal donor-acceptor heterojunctions. *Science*, 270(5243):1789–1791, Jan 1995.

[8] CW TANG. 2-layer organic photovoltaic cell. *Applied Physics Letters*, 48(2):183–185, Jan 1986.

[9] NC Greenham, XG Peng, and AP Alivisatos. Charge separation and transport in conjugated-polymer/semiconductor-nanocrystal composites studied by photoluminescence quenching and photoconductivity. *Physical Review B*, 54(24):17628–17637, Jan 1996.

[10] Steve O'Rourke, Peter Kim, and Hari Polavarapu. Solar photovoltaics. Technical report, Deutsche Bank Global Markets Research, 2007.

[11] Travis Bradford, Sorin Grama, Eric Wesoff, and Alok Bhargava. The futre of thin film solar. Technical Report 1, Greentech Media Inc., Prometheus Institute, August 2007.

[12] Fan Yang and Stephen R. Forrest. Photocurrent generation in nanostructured organic solar cells. *Acs Nano*, 2(5):1022–1032, MAY 2008.

[13] Paul W. M. Blom, Valentin D. Mihailetchi, L. Jan Anton Koster, and Denis E. Markov. Device physics of polymer : fullerene bulk heterojunction solar cells. *Advanced Materials*, 19(12):1551–1566, JUN 18 2007.

[14] DL Morel, AK Ghosh, T Feng, EL Stogryn, PE Purwin, RF Shaw, and C Fishman. High-efficiency organic solar-cells. *Applied Physics Letters*, 32(8):495–497, Jan 1978.

[15] P Peumans and SR Forrest. Very-high-efficiency double-heterostructure copper phthalocyanine/c-60 photovoltaic cells. *Applied Physics Letters*, 79(1):126–128, Jan 2001.

[16] B P Rand, J G Xue, F Yang, and S R Forrest. Organic solar cells with sensitivity extending into the near infrared. *Applied Physics Letters*, 87(23):233508, Jan 2005.

[17] I Gur, NA Fromer, ML Geier, and AP Alivisatos. Air-stable all-inorganic nanocrystal solar cells processed from solution. *Science*, 310(5747):462–465, Jan 2005.

[18] KL Mutolo, EI Mayo, BP Rand, SR Forrest, and ME Thompson. Enhanced open-circuit voltage in subphthalocyanine/c-60 organic photovoltaic cells. *Journal of the American Chemical Society*, 128(25):8108–8109, Jan 2006.

[19] Joseph M. Luther, Matt Law, Matthew C. Beard, Qing Song, Matthew O. Reese, Randy J. Ellingson, and Arthur J. Nozik. Schottky solar cells based on colloidal nanocrystal films. *Nano Letters*, 8(10):3488–3492, OCT 2008.

[20] Peng Wang, Agnese Abrusci, Henry M. P Wong, Mattias Svensson, Mats R Andersson, and Neil C Greenham. Photoinduced charge transfer and efficient solar energy conversion in a blend of a red polyfluorene copolymer with cdse nanoparticles. *Nano Letters*, 6(8):1789–1793, Jan 2006.

[21] V Shrotriya, G Li, Y Yao, T Moriarty, K Emery, and Y Yang. Accurate measurement and characterization of organic solar cells. *Advanced Functional Materials*, 16(15):2016–2023, Oct 2006.

[22] J.Y Kim, S.H Kim, H.-H Lee, K Lee, W Ma, X Gong, and A.J Heeger. New architecture for high-efficiency polymer photovoltaic cells using solution-based titanium oxide as an optical spacer. *Advanced Materials*, 18(5):572–576, Mar 2006.

[23] Christopher R McNeill, Agnese Abrusci, Jana Zaumseil, Richard Wilson, Mary J McKiernan, Jeremy H Burroughes, Jonathan J. M Halls, Neil C Greenham, and Richard H Friend. Dual electron donor/electron acceptor character of

a conjugated polymer in efficient photovoltaic diodes. *Applied Physics Letters*, 90(19):193506, Jan 2007.

[24] Fan Yang, Kai Sun, and Stephen R. Forrest. Efficient solar cells using all-organic nanocrystalline networks. *Advanced Materials*, 19(23):4166–+, DEC 3 2007.

[25] Yun-Yue Lin, Tsung-Hung Chu, Chun-Wei Chen, and Wei-Fang Su. Improved performance of polymer/tio2 nanorod bulk heterojunction photovoltaic devices by interface modification. *Applied Physics Letters*, 92(5):053312, Jan 2008.

[26] Yasuo Chiba, Ashraful Islam, Yuki Watanabe, Ryoichi Komiya, Naoki Koide, and Liyuan Han. Dye-sensitized solar cells with conversion efficiency of 11.1%. *Jpn J Appl Phys 2*, 45(24-28):L638–L640, Jan 2006.

[27] Henry J. Snaith, Adam J. Moule, Cedric Klein, Klaus Meerholz, Richard H. Friend, and Michael Gratzel. Efficiency enhancements in solid-state hybrid solar cells via reduced charge recombination and increased light capture. *Nano Letters*, 7(11):3372–3376, NOV 2007.

[28] Stuart S Williams, Meredith J Hampton, Vignesh Gowrishankar, I-Kang Ding, Joseph L Templeton, Edward T Samulski, Joseph M DeSimone, and Michael D McGehee. Nanostructured titania-polymer photovoltaic devices made using pfpe-based nanomolding techniques. *Chem Mater*, 20(16):5229–5234, Jan 2008.

[29] Peter Peumans, Soichi Uchida, and Stephen R Forrest. Efficient bulk heterojunction photovoltaic cells using small-molecular-weight organic thin films. *Nature*, 425(6954):158–162, Sep 2003.

[30] Christian Uhrich, David Wynands, Selina Olthof, Moritz K Riede, Karl Leo, Stefan Sonntag, Bert Maennig, and Martin Pfeiffer. Origin of open circuit voltage in planar and bulk heterojunction organic thin-film photovoltaics depending on doped transport layers. *Journal of Applied Physics*, 104(4):043107, Jan 2008.

[31] A C Arango, S A Carter, and P J Brock. Charge transfer in photovoltaics consisting of interpenetrating networks of conjugated polymer and tio2 nanoparticles. *Appl Phys Lett*, 74(12):1698–1700, Jan 1999.

[32] Johann Boucle, Punniamoorthy Ravirajan, and Jenny Nelson. Hybrid polymer-metal oxide thin films for photovoltaic applications. *Journal of Materials Chemistry*, 17(30):3141–3153, 2007.

[33] P Peumans, V Bulovic, and SR Forrest. Efficient photon harvesting at high optical intensities in ultrathin organic double-heterostructure photovoltaic diodes. *Applied Physics Letters*, 76(19):2650–2652, Jan 2000.

[34] H Hänsel, H Zettl, G Krausch, R Kisselev, M Thelakkat, and H.-W Schmidt. Optical and electronic contributions in double-heterojunction organic thin-film solar cells. *Advanced Materials*, 15(24):2056–2060, Dec 2003.

[35] Seung-Bum Rim, Shanbin Zhao, Shawn R Scully, Michael D McGehee, and Peter Peumans. An effective light trapping configuration for thin-film solar cells. *Applied Physics Letters*, 91(24):243501, Jan 2007.

[36] Viktor Andersson, Kristofer Tvingstedt, and Olle Inganas. Optical modeling of a folded organic solar cell. *Journal of Applied Physics*, 103(9):094520, Jan 2008.

[37] Mukul Agrawal and Peter Peumans. Broadband optical absorption enhancement through coherent light trapping in thin-film photovoltaic cells. *Optics Express*, 16(8):5385–5396, Jan 2008.

[38] M HIRAMOTO, M SUEZAKI, and M YOKOYAMA. Effect of thin gold interstitial-layer on the photovoltaic properties of tandem organic solar-cell. *Chemistry Letters*, (3):327–330, March 1990.

[39] A Yakimov and SR Forrest. High photovoltage multiple-heterojunction organic solar cells incorporating interfacial metallic nanoclusters. *Applied Physics Letters*, 80(9):1667–1669, Jan 2002.

[40] P Peumans, A Yakimov, and SR Forrest. Small molecular weight organic thin-film photodetectors and solar cells. *Journal of Applied Physics*, 93(7):3693–3723, April 2003.

[41] Jin Young Kim, Kwanghee Lee, Nelson E Coates, Daniel Moses, Thuc-Quyen Nguyen, Mark Dante, and Alan J Heeger. Efficient tandem polymer solar cells fabricated by all-solution processing. *Science*, 317(5835):222–225, Jan 2007.

[42] A Hadipour, B de Boer, and P. W. M Blom. Device operation of organic tandem solar cells. *Organic Electronics*, 9(5):617–624, Jan 2008.

[43] Tayebeh Ameri, Gilles Dennler, Christoph Lungenschmied, and Christoph J Brabec. Organic tandem solar cells: A review. *Energ Environ Sci*, 2(4):347–363, Jan 2009.

[44] William Shockley and Hans J. Queisser. Detailed balance limit of efficiency of p-n junction solar cells. *Journal of Applied Physics*, 32(3):510–519, 1961.

[45] CH HENRY. Limiting efficiencies of ideal single and multiple energy-gap terrestrial solar-cells. *Journal of Applied Physics*, 51(8):4494–4500, 1980.

[46] JG Xue, S Uchida, BP Rand, and SR Forrest. Asymmetric tandem organic photovoltaic cells with hybrid planar-mixed molecular heterojunctions. *Applied Physics Letters*, 85(23):5757–5759, Jan 2004.

[47] J Drechsel, B Männig, F Kozlowski, M Pfeiffer, K Leo, and H Hoppe. Efficient organic solar cells based on a double p-i-n architecture using doped wide-gap transport layers. *Applied Physics Letters*, 86(24):244102, Jan 2005.

[48] Kenji Kawano, Norihiro Ito, Taisuke Nishimori, and Jun Sakai. Open circuit voltage of stacked bulk heterojunction organic solar cells. *Applied Physics Letters*, 88(7):073514, Jan 2006.

[49] Gilles Dennler, Hans-Jurgen Prall, Robert Koeppe, Martin Egginger, Robert Autengruber, and Niyazi Serdar Sariciftci. Enhanced spectral coverage in tandem organic solar cells. *Applied Physics Letters*, 89(7):073502, Jan 2006.

[50] MA REED, JN RANDALL, RJ AGGARWAL, RJ MATYI, TM MOORE, and AE WETSEL. Observation of discrete electronic states in a zero-dimensional semiconductor nanostructure. *Physical Review Letters*, 60(6):535–537, February 1988.

[51] V. Ryzhii, editor. *Intersubband Infrared Photodetectors*, volume 27. World Scientific, 2003.

[52] J FAIST, F CAPASSO, DL SIVCO, C SIRTORI, AL HUTCHINSON, and AY CHO. Quantum cascade laser. *Science*, 264(5158):553–556, April 1994.

[53] KF Brennan and J Haralson. Invited review - superlattice and multiquantum well avalanche photodetectors: physics, concepts and performance. *Superlattices and Microstructures*, 28(2):77–104, August 2000.

[54] R ROSSETTI, S NAKAHARA, and LE BRUS. Quantum size effects in the redox potentials, resonance raman-spectra, and electronic-spectra of cds crystallites in aqueous-solution. *Journal of Chemical Physics*, 79(2):1086–1088, 1983.

[55] CB MURRAY, DJ NORRIS, and MG BAWENDI. Synthesis and characterization of nearly monodisperse cde (e = s, se, te) semiconductor nanocrystallites. *Journal of the American Chemical Society*, 115(19):8706–8715, September 1993.

[56] AP Alivisatos. Perspectives on the physical chemistry of semiconductor nanocrystals. *Journal of Physical Chemistry*, 100(31):13226–13239, August 1996.

[57] S Coe, WK Woo, M Bawendi, and V Bulovic. Electroluminescence from single monolayers of nanocrystals in molecular organic devices. *Nature*, 420(6917):800–803, DEC 26 2002.

[58] WU Huynh, JJ Dittmer, N Teclemariam, DJ Milliron, AP Alivisatos, and KWJ Barnham. Charge transport in hybrid nanorod-polymer composite photovoltaic cells. *Physical Review B*, 67(11), March 2003.

[59] WU Huynh, XG Peng, and AP Alivisatos. Cdse nanocrystal rods/poly(3-hexylthiophene) composite photovoltaic devices. *Advanced Materials*, 11(11):923–+, August 1999.

[60] WU Huynh, JJ Dittmer, and AP Alivisatos. Hybrid nanorod-polymer solar cells. *Science*, 295(5564):2425–2427, March 2002.

[61] WU Huynh, JJ Dittmer, WC Libby, GL Whiting, and AP Alivisatos. Controlling the morphology of nanocrystal-polymer composites for solar cells. *Advanced Functional Materials*, 13(1):73–79, January 2003.

[62] BQ Sun, E Marx, and NC Greenham. Photovoltaic devices using blends of branched cdse nanoparticles and conjugated polymers. *Nano Letters*, 3(7):961–963, July 2003.

[63] Keith W Johnston, Andras G Pattantyus-Abraham, Jason P Clifford, Stefan H Myrskog, Dean D Macneil, Larissa Levina, and Edward H Sargent. Schottky-quantum dot photovoltaics for efficient infrared power conversion. *Applied Physics Letters*, 92(15):151115, Jan 2008.

[64] DS Ginger and NC Greenham. Photoinduced electron transfer from conjugated polymers to cdse nanocrystals. *Physical Review B*, 59(16):10622–10629, April 1999.

[65] M Drndic, MV Jarosz, NY Morgan, MA Kastner, and MG Bawendi. Transport properties of annealed cdse colloidal nanocrystal solids. *Journal of Applied Physics*, 92(12):7498–7503, December 2002.

[66] BA Ridley, B Nivi, and JM Jacobson. All-inorganic field effect transistors fabricated by printing. *Science*, 286(5440):746–749, October 1999.

[67] M. V. Jarosz, V. J. Porter, B. R. Fisher, M. A. Kastner, and M. G. Bawendi. Photoconductivity studies of treated cdse quantum dot films exhibiting increased exciton ionization efficiency. *Phys. Rev. B*, 70(19):195327, Nov 2004.

[68] Herbert Stanley Allen. *Photo-electricity; the liberation of electrons by light, with chapters on fluorescence & phosphorescence, and photo-chemical actions & photography,*. London, New York [etc.] Longmans, Green and co., 1913, 1913.

[69] D. C. Oertel, M. G. Bawendi, A. C. Arango, and V. Bulovic. Photodetectors based on treated cdse quantum-dot films. *Appl. Phys. Lett.*, 87(21):213505, Nov 2005.

[70] T. S Mentzel, V. J Porter, S Geyer, K MacLean, Moungi G Bawendi, and M. A Kastner. Charge transport in pbse nanocrystal arrays. *Physical Review B*, 77(7):075316, Jan 2008.

[71] LeeAnn Kim, Polina O. Anikeeva, Seth A. Coe-Sullivan, Jonathan S. Steckel, Moungi G. Bawendi, and Vladimir Bulovic. Contact printing of quantum dot light-emitting devices. *Nano Letters*, 8(12):4513–4517, DEC 2008.

[72] K Knapp and T Jester. Empirical investigation of the energy payback time for photovoltaic modules. *Sol Energy*, 71(3):165–172, Jan 2001.

[73] David JC MacKay. *Sustainable energy - without the hot air.* UIT Cambridge Ltd., 2009.

[74] J. Paidipati, L. Frantzis, H. Sawyer, and A. Kurrasch. Rooftop photovoltaics market penetration scenarios. Technical report, Navigant Consulting, Inc, 2008.

[75] Cyrus Wadia, A. Paul Alivisatos, and Daniel M Kammen. Materials availability expands the opportunity for large-scale photovoltaics deployment. *Environ Sci Technol*, 43(6):2072–2077, Jan 2009.

[76] Matt Law, Matthew C Beard, Sukgeun Choi, Joseph M Luther, Mark C Hanna, and Arthur J Nozik. Determining the internal quantum efficiency of pbse nanocrystal solar cells with the aid of an optical model. *Nano Letters*, 8(11):3904–3910, Nov 2008.

[77] J. K Mapel, M Singh, M. A Baldo, and K Celebi. Plasmonic excitation of organic double heterostructure solar cells. *Applied Physics Letters*, 90(12):121102, Jan 2007.

[78] T. D Heidel, J. K Mapel, M Singh, K Celebi, and M. A Baldo. Surface plasmon polariton mediated energy transfer in organic photovoltaic devices. *Applied Physics Letters*, 91(9):093506, Jan 2007.

[79] Jenny Nelson. *The physics of solar cells*. Imperial College Press, 2003.

[80] Shawn R Scully and Michael D McGehee. Effects of optical interference and energy transfer on exciton diffusion length measurements in organic semiconductors. *Journal of Applied Physics*, 100(3):034907, Jan 2006.

[81] P Peumans and SR Forrest. Separation of geminate charge-pairs at donor-acceptor interfaces in disordered solids. *Chemical Physics Letters*, 398(1-3):27–31, Jan 2004.

[82] Conor Madigan. *Theory and Simulation of Amorphous Organic Electronic Devices*. PhD thesis, Massashusetts Institute of Technology, 2006.

[83] L Onsager. Initial recombination of ions. *Physical Review*, 54:554–557, Oct 1938.

[84] C Madigan and V Bulovic. Modeling of exciton diffusion in amorphous organic thin films. *Physical Review Letters*, 96(4):046404, Jan 2006.

[85] Conor Madigan and Vladimir Bulovic. Exciton energy disorder in polar amorphous organic thin films: Monte carlo calculations. *Physical Review B*, 75(8):081403, Jan 2007.

[86] Jesus delAlamo. *Integrated Microelectronic Devices: Physics and Modeling*. Prentice Hall, 2009.

[87] AK GHOSH and T FENG. Merocyanine organic solar-cells. *Journal of Applied Physics*, 49(12):5982–5989, 1978.

[88] PK Watkins, AB Walker, and GLB Verschoor. Dynamical monte carlo modelling of organic solar cells: The dependence of internal quantum efficiency on morphology. *Nano Letters*, 5(9):1814–1818, Jan 2005.

[89] D Cheyns, J Poortmans, P Heremans, C Deibel, S Verlaak, B. P Rand, and J Genoe. Analytical model for the open-circuit voltage and its associated resistance in organic planar heterojunction solar cells. *Physical Review B*, 77(16):165332, Jan 2008.

[90] JA Barker, CM Ramsdale, and NC Greenham. Modeling the current-voltage characteristics of bilayer polymer photovoltaic devices. *Physical Review B*, 67(7):075205, Jan 2003.

[91] V. D Mihailetchi, L. J. A Koster, and P. W. M Blom. Effect of metal electrodes on the performance of polymer:fullerene bulk heterojunction solar cells. *Applied Physics Letters*, 85(6):970, Jan 2004.

[92] Baoquan Sun, Henry J Snaith, Anoop S Dhoot, Sebastian Westenhoff, and Neil C Greenham. Vertically segregated hybrid blends for photovoltaic devices with improved efficiency. *Journal of Applied Physics*, 97(1):014914, Jan 2005.

[93] CM Ramsdale, JA Barker, AC Arias, JD MacKenzie, RH Friend, and NC Greenham. The origin of the open-circuit voltage in polyfluorene-based photovoltaic devices. *Journal of Applied Physics*, 92(8):4266–4270, Jan 2002.

[94] BA Gregg. Excitonic solar cells. *J Phys Chem B*, 107(20):4688–4698, Jan 2003.

[95] BA Gregg. The photoconversion mechanism of excitonic solar cells. *Mrs Bull*, 30(1):20–22, Jan 2005.

[96] Jenny Nelson, James Kirkpatrick, and P Ravirajan. Factors limiting the efficiency of molecular photovoltaic devices. *Physical Review B*, 69(3):11, Jan 2004.

[97] Y. L. Shen, D. B. Jacobs, G. G. Malliaras, G. Koley, M. G. Spencer, and A. Ioannidis. Modification of indium tin oxide for improved hole injection in organic light emitting diodes. *Adv. Mater.*, 13(16):1234–1238, Aug 2001.

[98] Keith W. Johnston, Andras G. Pattantyus-Abraham, Jason P. Clifford, Stefan H. Myrskog, Sjoerd Hoogland, Harnik Shukla, Ethan J. D. Klem, Larissa Levina, and Edward H. Sargent. Efficient schottky-quantum-dot photovoltaics: The roles of depletion, drift, and diffusion. *Applied Physics Letters*, 92(12):122111, MAR 24 2008.

[99] Barry P. Rand, Diana P. Burk, and Stephen R. Forrest. Offset energies at organic semiconductor heterojunctions and their influence on the open-circuit voltage of thin-film solar cells. *Physical Review B*, 75(11):115327, MAR 2007.

[100] J. Nelson, J. Kirkpatrick, and P. Ravirajan. Factors limiting the efficiency of molecular photovoltaic devices. *Phys. Rev. B*, 69(3):035337, Jan 2004.

[101] A C Arango, D C Oertel, Y Xue, M G Bawendi, and V Bulovic. Heterojunction photovoltaics using printed colloidal quantum dots as a photosensitive layer. *Nano Lett*, 9(2):860–863, 2009.

[102] Tim P Osedach, Scott M Geyer, John C Ho, Alexi C Arango, Moungi G Bawendi, and Vladimir Bulovic. Lateral heterojunction photodetector consisting of molecular organic and colloidal quantum dot thin films. *Applied Physics Letters*, 94(4):043307, Jan 2009.

[103] H Mu, W Li, R Jones, A Steckl, and D Klotzkin. A comparative study of electrode effects on the electrical and luminescent characteristics of alq3/tpd oled: Improvements due to conductive polymer (pedot) anode. *Journal of Luminescence*, 126(1):225–229, Sep 2007.

[104] DS Ginger and NC Greenham. Charge injection and transport in films of cdse nanocrystals. *Journal of Applied Physics*, 87(3):1361–1368, Jan 2000.

[105] RAM Hikmet, DV Talapin, and H Weller. Study of conduction mechanism and electroluminescence in cdse/zns quantum dot composites. *Journal of Applied Physics*, 93(6):3509–3514, Jan 2003.

[106] Jennifer J. Yu. *Improving OLED technology for displays*. PhD thesis, Massashusetts Institute of Technology, 2008.

[107] CJ Brabec, A Cravino, D Meissner, NS Sariciftci, T Fromherz, MT Rispens, L Sanchez, and JC Hummelen. Origin of the open circuit voltage of plastic solar cells. *Adv Funct Mater*, 11(5):374–380, Jan 2001.

[108] M.C Scharber, D Mühlbacher, M Koppe, P Denk, C Waldauf, A.J Heeger, and C.J Brabec. Design rules for donors in bulk-heterojunction solar cells—towards 10 *Advanced Materials*, 18(6):789–794, Mar 2006.

[109] Kazuhiko Seki and Antoine Kahn. *Conjugated Polymer and Molecular Interfaces*. CRC Press, 2001.

[110] Chiatzun Goh, Shawn R Scully, and Michael D McGehee. Effects of molecular interface modification in hybrid organic-inorganic photovoltaic cells. *Journal of Applied Physics*, 101(11):114503, Jan 2007.

[111] P. O Anikeeva, C. F Madigan, J. E Halpert, M. G Bawendi, and V Bulovic. Electronic and excitonic processes in light-emitting devices based on organic materials and colloidal quantum dots. *Physical Review B*, 78(8):085434, Jan 2008.

[112] Gautham Nair and Moungi G Bawendi. Carrier multiplication yields of cdse and cdte nanocrystals by transient photoluminescence spectroscopy. *Physical Review B*, 76(8):1–4, Aug 2007.

[113] C. G Shuttle, B O'regan, A. M Ballantyne, J Nelson, D. D. C Bradley, J De Mello, and J. R Durrant. Experimental determination of the rate law for charge carrier decay in a polythiophene: Fullerene solar cell. *Applied Physics Letters*, 92(9):093311, Jan 2008.

[114] J van de Lagemaat. Einstein relation for electron diffusion on arrays of weakly coupled quantum dots. *Physical Review B*, 72(23):235319, Jan 2005.

[115] VD Mihailetchi, LJA Koster, JC Hummelen, and PWM Blom. Photocurrent generation in polymer-fullerene bulk heterojunctions. *Physical Review Letters*, 93(21):216601, Jan 2004.

[116] R. A Marsh, C. R McNeill, A Abrusci, A. R Campbell, and R. H Friend. A unified description of current-voltage characteristics in organic and hybrid photovoltaics under low light intensity. *Nano Lett*, 8(5):1393–1398, Jan 2008.

[117] RAJ Janssen, JC Hummelen, and NS Saricifti. Polymer-fullerene bulk heterojunction solar cells. *Mrs Bull*, 30(1):33–36, Jan 2005.

[118] Jan Gilot, Martijn M Wienk, and René A. J Janssen. Double and triple junction polymer solar cells processed from solution. *Applied Physics Letters*, 90(14):143512, Jan 2007.

[119] M. Magdalena Mandoc, Welmoed Veurman, L. Jan Anton Koster, Bert de Boer, and Paul W. M Blom. Origin of the reduced fill factor and photocurrent in mdmo-ppv : Pcnepv all-polymer solar cells. *Advanced Functional Materials*, 17(13):2167–2173, Jan 2007.

[120] Venda J Porter, Scott Geyer, Jonathan E Halpert, Marc A Kastner, and Moungi G Bawendi. Photoconduction in annealed and chemically treated cdse/zns inorganic nanocrystal films. *J Phys Chem C*, 112(7):2308–2316, Jan 2008.

[121] D. Aaron R Barkhouse, Andras G Pattantyus-Abraham, Larissa Levina, and Edward H Sargent. Thiols passivate recombination centers in colloidal quantum dots leading to enhanced photovoltaic device efficiency. *Acs Nano*, 2(11):2356–2362, Jan 2008.

[122] MD Acher and R Hill, editors. *Clean Energy from Photovoltaics.* World Scientific Publishing Company, London, 2001.

[123] Henry J Snaith, Lukas Schmidt-Mende, and Michael Grätzel. Light intensity, temperature, and thickness dependence of the open-circuit voltage in solid-state dye-sensitized solar cells. *Physical Review B*, 74(4):1–6, Jul 2006.

[124] A C Arango, L R Johnson, V N Bliznyuk, Z Schlesinger, S A Carter, and HH Horhold. Efficient titanium oxide/conjugated polymer photovoltaics for solar energy conversion. *Advanced Materials*, 12(22):1689–+, November 2000.

[125] Seungchan Han, Won Suk Shin, Myungsoo Seo, Dipti Gupta, Sang-Jin Moon, and Seunghyup Yoo. Improving performance of organic solar cells using amorphous tungsten oxides as an interfacial buffer layer on transparent anodes. *Organic Electronics*, 10(5):791–797, Jan 2009.

[126] Brian C O'Regan, Klaas Bakker, Jessica Kroeze, Herman Smit, Paul Sommeling, and James R Durrant. Measuring charge transport from transient photovoltage rise times. a new tool to investigate electron transport in nanoparticle films. *J Phys Chem B*, 110(34):17155–17160, Jan 2006.

[127] BC O'Regan and F Lenzmann. Charge transport and recombination in a nanoscale interpenetrating network of n-type and p-type semiconductors: Transient photocurrent and photovoltage studies of tio2/dye/cuscn photovoltaic cells. *J Phys Chem B*, 108(14):4342–4350, Jan 2004.

[128] A. J Mozer, N. S Sariciftci, L Lutsen, D Vanderzande, R Österbacka, M Westerling, and G Juška. Charge transport and recombination in bulk heterojunction solar cells studied by the photoinduced charge extraction in linearly increasing voltage technique. *Applied Physics Letters*, 86(11):112104, Jan 2005.

[129] I Montanari, AF Nogueira, J Nelson, JR Durrant, C Winder, MA Loi, NS Sariciftci, and C Brabec. Transient optical studies of charge recombination dynamics in a polymer/fullerene composite at room temperature. *Applied Physics Letters*, 81(16):3001–3003, Jan 2002.